



universität
wien

DIPLOMARBEIT

Titel der Diplomarbeit

„Gamma-ray Spectroscopy at Volcanoes“

Verfasserin

Stefanie Kauer

angestrebter akademischer Grad

Magistra der Naturwissenschaften (Mag. rer. nat.)

Wien, 2012

Studienkennzahl lt. Studienblatt:

A 416

Studienrichtung lt. Studienblatt:

Geophysik

Betreuerin / Betreuer:

Ao. Univ. Prof. Dr. Bruno Meurers

Danksagungen

Das Verfassen meiner Diplomarbeit ist mir durch die Unterstützung einer Vielzahl von Menschen ermöglicht worden. Ganz besonders möchte ich mich bei folgenden Personen und Organisationen bedanken:

Zuallererst möchte ich mich bei der Geologischen Bundesanstalt (insbesondere der Fachabteilung Geophysik) für die Bereitstellung der für diese Arbeit notwendigen Daten und Programme bedanken. Für die Betreuung meiner Diplomarbeit und die ständige Unterstützung möchte ich mich bei meinem operativen Betreuer an der Geologischen Bundesanstalt, Mag. Robert Supper, bedanken. Weiters gilt mein Dank auch HR Mag. Klaus Motschka und Dr. Edmund Winkler, die immer wieder geduldig meine Fragen beantwortet haben.

Die Messungen über den Äolischen Inseln wurden durch die finanzielle Unterstützung des Austrian Science Fund (FWF), contract P15515-TEC "Improved Modeling and Interpretation of Complex Geophysical Data Applied to the Eolian Volcanic Province" (COMVOLC) und des National Institute of Advanced Industrial Science and Technology (AIST), Japan, ermöglicht. Dafür möchte ich mich an dieser Stelle bedanken. Weiters gilt mein Dank auch dem Secretaría de Marina - Armada de México für die Unterstützung der Messungen über der Insel Socorro.

Für die Übernahme dieses Themas bedanke ich mich recht herzlich bei Ao. Univ. Prof. Dr. Bruno Meurers.

Ich möchte ich mich auch bei meinen Eltern für die finanzielle Unterstützung während meines Studiums bedanken.

Dank gilt auch meinen Studienkolleginnen Anna Zöchbauer und Jutta Rasel, die mich während meines gesamten Studiums begleitet haben und mir immer mit Rat und Tat zur Seite gestanden sind.

Ganz besonders möchte ich mich auch bei meinem Lebensgefährten Martin Gruber bedanken, der für jedes Problem (insbesondere Computer-Problem) immer eine Lösung parat hatte.

Stefanie Kauer
Alser Straße 16/7
1090 Wien

”Hiermit erkläre ich, dass ich diese Arbeit selbständig verfasst habe, dass ich die verwendeten Quellen und Hilfsmittel vollständig angegeben habe und dass ich die Stellen der Arbeit – einschließlich Tabellen, Karten und Abbildungen –, die anderen Werken oder dem Internet im Wortlaut oder dem Sinn nach entnommen sind, auf jeden Fall unter Angabe der Quelle als Entlehnung kenntlich gemacht habe.”
Wien, im Januar 2012

Stefanie Kauer

Abstract

Volcanic regions are often associated with rough topography and large inaccessible areas. The use of airborne gamma-ray spectroscopy when surveying volcanic regions is therefore especially interesting, as it reflects the radiometric properties of surface geology over a large area.

The objective of my work was to reprocess and interpret radiometric data with new processing algorithms, and to correlate the processing results with geological mapping results. Data was derived from airborne gamma-ray measurements at the Aeolian Islands (Italy), acquired in 2002 and 2004, and data of the volcanic island Socorro (Mexico), acquired in 2009. Datasets from all surveys were processed with up-to-date radiometric processing-software, which implies recently invented methods for spectral noise reduction and offers various options to improve the outcome of data processing. Processed radiometric data was then interpolated to a regular grid and loaded into a GIS project for interpretation. Interpretation of radiometric data was performed with the main intention of comparing it with geologic maps. Furthermore, the influence of detector size, survey altitude and flight-line spacing on the resolution of gamma-ray data could be observed.

The best results could be achieved for the island of Socorro. Some of the main geologic units could be clearly identified on the basis of radioelement distribution. Furthermore, very interesting results could be achieved from the comparison of radiometric results with two geologic maps (a map of the whole island by *E.A. Carballido-Sanchez* and a map of the easily accessible Lomas Coloradas area by *W. Bohrson* and *M. Reid*). With the combined use of radioelement maps, ternary maps and a satellite image of the island, it was possible to confirm the studies of *W. Bohrson* and *M. Reid*, which were restricted to the southern part of Socorro Island. In contrast, the radiometric results in some parts disagree with the classification of *E.A. Carballido-Sanchez*. Main differences are three peralkaline trachyte domes, a cinder cone and a large lava flow, which all have been assigned to the Lomas Coloradas basalts by *E.A. Carballido-Sanchez* and which could be interpreted as postcaldera silicic products by means of radiometric data. However, some other geologic units, which had been delineated by *E.A. Carballido-Sanchez*, could not be identified by means of radiometric data alone. Interpreting radiometric data of Socorro Island was particularly interesting, as only few geophysical and geological data existed from the island, especially from the hardly accessible area to the north. Data from the airborne geophysical survey of the Geological Survey of Austria therefore yields a good basis for reworking the few pre-existing geologic maps.

Data from the gamma-ray survey over the Aeolian Islands showed a large range in quality. The measurements in 2002 were impaired by bad weather conditions with occasional heavy rainfall, which had strong influence on data quality. Compared to data from the survey in 2004, the rainfall caused strong attenuation of gamma-rays and increased the amount of noise. Due to bad quality, radiometric data from the survey in 2002 was not interpreted and only compared with the results of the Vulcano-Lipari

survey in 2004.

The survey in 2004 yielded good results for the islands of Vulcano and Lipari. It was possible to determine characteristic gamma-values for the main geologic units on the basis of the radioelement-distribution maps. As a lot of detailed geologic information exists of the two islands, interpretation of radiometric data was rather a comparison with the well-known geology and a testing of the applicability of gamma-ray spectroscopy as an additional mapping tool. It was interesting to see the relation between ground concentrations of radioelements and degree of magma differentiation and SiO_2 content, respectively. K concentration increases with increasing SiO_2 content and U and Th concentrations increase with increasing degree of magma differentiation. Volcanic rocks on Vulcano and Lipari Island show a general tendency of increasing SiO_2 content for more recent products and therefore the ground concentrations of the three radioelements are positively correlated for all geologic units on the islands and the relative concentrations remain approximately constant.

Data of the islands of Salina, Panarea and Stromboli could not be interpreted reasonably, due to low radioactivity, low data density and high survey altitude.

Kurzfassung

Vulkangebiete sind oftmals durch raue Topographie und große, unzugängliche Bereiche gekennzeichnet. Aerogeophysikalischer Gamma-Strahlen-Spektroskopie Messungen eignen sich daher besonders gut zur Untersuchung von Vulkangebieten, weil sie die radiometrischen Eigenschaften des Oberflächengesteins über ein breites Gebiet wiedergeben.

Im Rahmen dieser Arbeit sollten Radiometrie-Daten mit neuen Processing-Algorithmen prozessiert und interpretiert und anschließend mit den Ergebnissen von geologischen Kartierungen verglichen werden. Die dafür verwendeten Daten stammen von aerogeophysikalischen Messungen über den Äolischen Inseln (Italien) aus den Jahren 2002 und 2004 und von der Vulkaninsel Socorro (Mexiko) aus dem Jahr 2009. Alle Datensätze wurden mit neuester radiometrischer Processing-Software prozessiert, die unter anderem aktuelle Methoden zur spektralen Noise-Reduktion und verschiedenste Möglichkeiten zur Verbesserung der Processing-Resultate beinhaltet. Die prozessierten Daten wurden anschließend auf ein regelmäßiges Gitter interpoliert und für die weitere Interpretation in ein GIS Projekt geladen. Das Haupt-Augenmerk der Interpretation lag auf der Vergleichbarkeit mit geologischen Karten. Weiters konnten die Auflösbarkeitsgrenzen der Gamma-Strahlen-Spektroskopie in Bezug auf Detektorgröße, Flughöhe und Linienabstand beobachtet werden.

Die detailliertesten Ergebnisse konnten für die Insel Socorro erzielt werden. Aufgrund der Radioelement-Verteilung konnten einige geologische Einheiten eindeutig identifiziert werden. Vor allem der Vergleich der Radioelement-Karten mit zwei geologischen Karten der Insel (eine Karte der gesamten Insel von *E.A. Carballido-Sanchez* und eine

Karte des leicht zugänglichen Lomas Coloradas Gebietes von *W. Bohrson* und *M. Reid*) brachte interessante Ergebnisse hervor. Mit Hilfe von Radioelement-Karten, Ternär-Plots und einem Satellitenbild der Insel war es möglich, die Untersuchungsergebnisse von *W. Bohrson* und *M. Reid* zu bestätigen, die sich leider nur auf den Südtteil der Insel beschränkten. Im Gegensatz dazu widersprechen die Ergebnisse der radiometrischen Untersuchung teilweise der Einteilung von *E.A. Carballido-Sanchez*. Die wichtigsten Unterschiede sind drei peralkaline Trachyt-Dome, ein Aschekegel und ein großer Lavafluss, die von *E.A. Carballido-Sanchez* den Lomas Coloradas Basalten zugeordnet wurden und die auf Grund der radiometrischen Untersuchungen als saure peralkaline Eruptionsprodukte interpretiert werden können. Dennoch konnten auch einige von *E.A. Carballido-Sanchez* abgegrenzte geologische Einheiten, auf Basis der Radiometrie-Daten allein, nicht identifiziert werden. Die Interpretation der Radiometrie-Daten von Socorro war besonders interessant, weil bisher nur wenige geophysikalische und geologische Daten der Insel existierten, vor allem aus dem schlecht zugänglichen Bereich im Norden der Insel. Der aerogeophysikalische Datensatz der Geologischen Bundesanstalt bildet daher eine gute Grundlage für die Überarbeitung der wenigen existierenden geologischen Karten der Insel.

Die Gamma-Strahlen Daten der Äolischen Inseln hatten sehr unterschiedliche Qualität. Während der Messungen im Jahr 2002 herrschten schlechte Wetterbedingungen mit teils kräftigem Regen. Dieser wirkte sich stark auf die Qualität der Messergebnisse aus. Zusätzlich zu der stark dämpfenden Wirkung war auch ein viel höherer Noise, im Vergleich zu den Daten aus dem Jahr 2004, zu beobachten. Auf Grund der schlechten Qualität wurden die Radiometrie-Daten aus dem Jahr 2002 nicht interpretiert und lediglich mit den Ergebnissen des Vulcano-Lipari-Surveys von 2004 verglichen.

Der Survey im Jahr 2004 lieferte für die Inseln Vulcano und Lipari sehr gute Ergebnisse. Es war möglich, charakteristische Gamma-Werte für die geologischen Einheiten der Inseln, anhand der Radioelement-Verteilung, zu bestimmen.

Da bereits viel über die Geologie der beiden Inseln bekannt ist, war die Interpretation der Radiometrie-Daten mehr ein Vergleich mit bereits vorhandenen, detaillierten geologischen Karten und ein Test der Anwendbarkeit der Gamma-Strahlen-Spektroskopie als unterstützende Methode zur konventionellen geologischen Kartierung. Weiters konnte ein interessanter Zusammenhang zwischen den Radioelement-Konzentrationen und dem SiO_2 -Gehalt des Gesteins, beziehungsweise dem Grad der Magma-Differentiation beobachtet werden. Die K-Konzentration im Gestein steigt mit steigendem SiO_2 -Gehalt, während die U- und Th-Konzentration im Gestein mit erhöhtem Grad der Magma-Differentiation ansteigt. Die vulkanischen Gesteine auf Lipari und Vulcano zeigen die generelle Tendenz von steigendem SiO_2 -Gehalt für jüngere Eruptionsprodukte und daher sind die Bodenkonzentrationen der Radioelemente für alle geologischen Einheiten positiv korreliert und die relativen Konzentrationen sind für alle geologischen Einheiten in etwa konstant.

Die Daten der Inseln Salina, Panarea und Stromboli konnten leider auf Grund zu geringer Radioaktivität, zu geringer Datendichte und zu großer Flughöhe nicht sinnvoll interpretiert werden.

Contents

Abstract	iii
Kurzfassung	iv
1 Introduction	1
2 Gamma-rays in general	3
2.1 Principles of radioactivity	3
2.1.1 Radioactive decay processes	4
2.1.2 Quantities and units	5
2.2 Sources of gamma-radiation	6
2.2.1 Natural sources of gamma-radiation	7
2.2.2 Radiochemistry and geochemistry of potassium, uranium and thorium	8
2.2.3 ^{40}K , ^{238}U and ^{232}Th in fertilizers	14
2.2.4 Disequilibrium	14
2.2.5 Sources of background radiation	15
2.2.6 Interaction of gamma-rays with matter	16
3 Airborne gamma-ray measurements	19
3.1 Detection of gamma-radiation	20
3.1.1 The gamma-ray spectrometer	20
3.1.2 The effect of flying altitude on spatial resolution and on the measured count rates	21
3.1.3 Gamma-ray Spectra	22
3.2 Calibration flights	25
3.2.1 High-altitude cosmic- and aircraft-background flights	26
3.2.2 Ground calibration using radioactive pads	26
3.2.3 Calibration range flights	26
4 Processing and Interpretation	27
4.1 Processing of gamma-ray spectrometric data	27
4.1.1 Spectral noise reduction/ spectral smoothing:	27
4.1.2 Dead time/ life time correction	28
4.1.3 Energy calibration	29

4.1.4	Aircraft and cosmic background removal	29
4.1.5	Radon background removal	34
4.1.6	Stripping/ channel interaction correction	35
4.1.7	Height correction	36
4.1.8	Reduction to elemental concentrations	41
4.1.9	Levelling the data	41
4.2	Data Processing with Praga 4 radiometric processing software	42
4.2.1	Setting the project	42
4.2.2	Channel to energy calibration	43
4.2.3	Principal component analysis and spectrum restoration (smoothing)	43
4.2.4	Standard window based processing	44
4.2.5	Radon detection and removal	45
4.3	Basic models	45
4.3.1	Physical models	45
4.3.2	Statistical models	46
4.4	Data presentation and interpretation	47
4.4.1	Gridding	47
4.4.2	Pseudo-colour radioelement maps	48
4.4.3	Ternary radioelement maps	48
4.4.4	Georeferencing and map projections	49
4.4.5	Integration with other datasets	49
4.4.6	Creating Shapefiles	50
4.4.7	Statistical analysis	51
4.4.8	Reassignment of geologic units	51
4.4.9	Reconsideration of results with ternary radioelement diagrams	51
5	Gamma-rays and Volcanoes	55
5.1	Volcán Evermann, Socorro Island, Mexico	55
5.1.1	Geophysical survey at Socorro	59
5.1.2	Processing of gamma-ray spectrometer data	60
5.1.3	Description of Geologic Units	68
5.2	The Aeolian Archipelago	86
5.2.1	Vulcano	88
5.2.2	Lipari	90
5.2.3	The airborne geophysical survey of the GSA	93
5.2.4	Processing of gamma-ray spectrometer data	95
5.2.5	Description of Geologic Units	109
6	Discussion and Conclusion	125
A	Geologic units and radioelement concentrations of Socorro Island	131
B	Geologic units and radioelement concentrations of Vulcano Island	135
C	Geologic units and radioelement concentrations of Lipari Island	137

Chapter 1

Introduction

The beauty of volcanoes has always attracted people. Therefore it's not surprising, that some of the largest volcanic areas are densely populated and frequently visited by tourists. In order to protect population and visitors of volcanic regions against volcanic hazards, it's very important to supervise the volcanic activity and to estimate the consequences of a potential eruption. Therefore, our knowledge on structure and surface geology of volcanoes has to be improved. This knowledge helps us in understanding the eruption mechanisms and the behaviour of volcanoes.

The intention of the European Community project TOMAVE was to investigate the physical structure of Italian volcanoes with the help of airborne and ground based geophysical techniques. These surveys were conducted by the Geological Survey of Austria (GSA) in the years 1998-2000 [Supper et al. 2001]. The airborne survey included magnetic-, VLF- (very low frequency) and gamma-ray measurements. The ground geophysical survey included geoelectric and magnetic measurements.

Further airborne surveys over the Aeolian Islands were conducted in the years 2002 and 2004 in the frame of the project COMVOLC and as a cooperation work of the GSA and the Geological survey of Japan. Another aero-geophysical dataset of a volcanic island was collected in 2009 in the frame of a groundwater-study over Socorro Island (Mexico).

Volcanic regions are often associated with rough topography and large inaccessible areas. The use of airborne gamma-ray spectroscopy when surveying volcanic regions is therefore especially interesting, as it reflects the radiometric properties of surface geology over a large area. Gamma-rays which are detected at airborne survey height are emitted only by approximately the upper 30 cm of rock. Igneous rocks show a general tendency of increasing radioelement concentration with degree of magma differentiation. Furthermore, felsic volcanic rocks often show very high radioelement concentrations compared to average crustal abundances. Gamma-ray spectroscopy, although hardly applied, could therefore be an appropriate technique for studying and deriving knowledge on the magmatic evolution and the different eruption phases.

Gamma-ray spectroscopy has been used for many years for mineral exploration and geological- and environmental mapping [e.g. IAEA 2003]. Also the use of gamma-ray spectroscopy for characterization of volcanic products has gained in importance, espe-

cially in the frame of research studies concerning distribution of natural radionuclides, petrochemical classification of volcanic rocks and radioactive heat production.

Several borehole-, laboratory- and in situ- gamma-ray studies on volcanic rocks can be found from scientists all over the world, but only few studies have been carried out on airborne gamma-ray spectroscopy at volcanoes. In fact, only one airborne radiometric study on volcanic and plutonic rocks could be found, which has been carried out in Central Anatolia by *I. Aydin* [Aydin et al. 2006].

Some ground-radiometric studies of the Aeolian Islands have been performed by *P. Chiozzi*, and *I. Gehring* tried to reconstruct volcanostratigraphy of La Fossa di Vulcano with the help of gamma-ray measurements.

Hence, it can be said, that the radiometric surveys of the GSA at Socorro and at the Aeolian Islands have been the first detailed airborne gamma-ray spectrometric surveys at the respective islands. The airborne dataset of GSA showed good quality with regard to gamma-response, survey altitude, and flight-line density. The dataset had already been processed several years ago, but it became apparent, that a reprocessing with modern radiometric processing software was necessary.

Therefore, the intention of this work is to reprocess gamma-ray spectrometric data of Socorro and the Aeolian Islands with up-to-date radiometric processing software, test the applicability of gamma-ray spectroscopy at volcanoes and interpret the processing results in terms of comparing them with geologic maps. Interpretation of gamma-ray spectrometric data requires a thorough understanding of decay processes and deposition- and relocation-processes. Prior to discussing processing and interpretation techniques, a short introduction to gamma-rays, the principles of radioactivity and the natural sources of gamma-radiation will therefore be given.

Chapter 2

Gamma-rays in general

2.1 Principles of radioactivity

At the time when first works were done on radioactive decay processes, the nucleus of the atom - being the source of radioactivity - was not even completely understood. However, it is important to understand the chemical construction of the matter.

Atoms consist of a positively charged nucleus, composed of protons and neutrons, and negatively charged electrons, arranged in discrete electron shells surrounding the nucleus. The number of protons (Z , also called atomic number) defines the element itself, the number of neutrons can vary within the same element. Nuclides of the same element, but with a different number of neutrons, are called isotopes. Protons and neutrons are heavy particles and have approximately the same mass of $1.6 \times 10^{-27} \text{ kg}$. Since electrons have about 1/1800 of the mass of protons and neutrons, almost the entire mass of the atom is contained in the nucleus. The atomic mass number (A) is therefore the nucleon number, thus the sum of protons and neutrons. [Riedel 2004]

Two different forces act within the nucleus: The Coulomb-force (protons repel other protons) and the much stronger nuclear force, keeping the nucleus together. Atoms with more than 20 protons need to have more neutrons than protons to be stable, because the nuclear force is only effective over very short distances ($< 3 \times 10^{-15} \text{ m}$). [Demtröder 2009]

Atoms with more than 83 protons are unstable and decay to more stable nuclei by the emission of particles and radiation [e.g. Telford et al. 1990, Riedel 2004]:

- **α -particles** are He -nuclei (two protons and two neutrons). α -decay results in elements with an atomic number reduced by 2 and a mass number reduced by 4:
$${}^A_Z E_1 \rightarrow {}^{A-4}_{Z-2} E_2 + {}^4_2 He$$

Because they have both, a charge and a mass, they can be easily stopped by a sheet of paper or a few centimetres of air.
- **β -particles** are electrons ejected from the nucleus when a neutron splits into a proton and an electron. The proton remains in the nucleus, so the element moves

up one place in the Periodic Table: ${}_Z^A E_1 \rightarrow {}_{Z+1}^A E_2 + {}_{-1}^0 e$

Since β -particles have virtually no mass and only a charge, they can travel up to one meter in air and are blocked by a thin metal sheet.

- **γ -radiation** is a high energetic electromagnetic radiation. It represents excess energy of the new nucleus which is left after α - or β -decay. γ -rays show discrete energy spectra, each energy being characteristic of the source isotope. The atomic number and the mass number do not change during γ -decay. Thus, the element remains the same and only its energy state changes. Since γ -rays have neither mass nor charge, they can travel hundreds of meters in air and 30 to 50 cm in rock. Therefore, γ -rays are the only alternative for the airborne measurement of radioactivity. Gamma-rays are the same kind of electromagnetic radiation like X-rays. The only difference is the energy range. Electromagnetic radiation of energy lower than 40 keV is called X-rays, electromagnetic radiation of higher energy is denoted as γ -rays. [IAEA 2003]
- Another type of nuclear transmutation is **electron- or K-capture**. An electron from the innermost electron shell is captured by a proton from the nucleus, forming a neutron and a neutrino. Thus, the atomic number of the element decreases by one, what is quite opposite to the β -decay. [Telford et al. 1990]

The highest atomic number of naturally occurring elements is $Z = 92$, which belongs to uranium. All elements with higher atomic number, called transuranium elements, do not occur in nature because of their short half-lives (on a geologic scale). Though, they can be synthesised via nuclear reactions. [Riedel 2004]

Apart from the heavy elements, also some of the elements with lower atomic number are radioactive (${}_1^3 H$, ${}_6^{14} C$, ${}_{19}^{40} K$, ${}_{37}^{87} Rb$). These elements only disintegrate via β -decay. [Riedel 2004]

2.1.1 Radioactive decay processes

Radioactive decay is a spontaneous and statistical process, what means that the probability that any nucleus decays is constant over time. Thus it's impossible to determine the moment at which a certain nucleus disintegrates. The rate of disintegration is independent of temperature, pressure or type of chemical binding of the radioactive nuclide. Each radioactive substance shows a characteristic rate of disintegration, being proportional to the number of nuclei present. This law can be described by the following relation [Riedel 2004]:

$$\frac{dN}{dt} = -\lambda N$$

N ... number of radioactive nuclei present at time t

λ ... decay-constant, being characteristic of each unstable nuclide type

N_0 ... number of radioactive nuclei present at time $t = 0$

N_t ... number of not yet disintegrated nuclei at time t

$$\int_{N_0}^{N_t} \frac{dN}{N} = - \int_0^t \lambda dt \quad \Longrightarrow \quad \ln \frac{N_0}{N_t} = \lambda t \quad \Longrightarrow \quad N_t = N_0 e^{-\lambda t}$$

The degree of stability of an unstable nuclide is described by its half-life $t_{1/2}$, which can be calculated by:

$$\frac{N_{t_{1/2}}}{N_0} = \frac{1}{2} = e^{-\lambda t_{1/2}} \quad \Longrightarrow \quad \ln \frac{1}{2} = -\lambda t_{1/2} \quad \Longrightarrow \quad t_{1/2} = \frac{\ln 2}{\lambda} = \frac{0.693}{\lambda}$$

Half-life values of radioactive nuclei vary enormously, from 10^{-9} seconds to 10^{14} years [Riedel 2004]. ^{40}K , ^{232}Th and ^{238}U are elements with long half-lives in the order of the age of the Earth.

Some radionuclides have more than one daughter nuclide. For example, ^{40}K (the only radioactive isotope of K) decays with a probability of 0.89 by β -decay to ^{40}Ca and with a probability of 0.11 by electron capture to ^{40}Ar . [Minty 1997]

A lot of radioactive disintegrations proceed in chains. A radioactive nuclide decays to a daughter product, which is also radioactive and decays again to a radioactive nuclide until the process is terminated by a stable isotope. The consecutive links of the decay chain can either have the same mass number (β -decay) or the mass number is reduced by four (α -decay). [Riedel 2004]

If the number of daughter isotopes decaying in a fixed time is the same as the number of daughters being created by the parent isotope, the system is said to be in equilibrium. It usually takes several half-lives to reach equilibrium. If a radioactive decay series is in equilibrium, then the amount of source isotopes can be determined by measuring the amount of one of its daughter isotopes. [Telford et al. 1990]

2.1.2 Quantities and units

The *activity* of a radioactive substance is defined as the number of disintegrations per unit time interval. The SI unit is Becquerel (Bq), whereas 1 Becquerel corresponds to one disintegration per second. The former unit of activity was Curie (Ci), which corresponds to the activity of 1 g of ^{226}Rn and $1 \text{ Ci} = 3.7 \times 10^{10} \text{ Bq}$.

To describe the radionuclide content of rocks, an often used quantity is the *specific activity* (activity per unit mass). It describes the number of nuclear disintegrations per unit time per unit mass, $\text{Bq/kg} = \text{s}^{-1}\text{kg}^{-1}$.

The contamination of the Earth's surface by fall-out of man-made nuclides is usually described by the *surface activity* (activity per unit area), which is given in Becquerel per square metre ($\text{Bq/m}^2 = \text{s}^{-1}\text{m}^{-2}$).

The *absorbed dose* is the mass specific energy which is transferred to a body by ionizing radiation. The SI unit is Gray (Gy), with $1 \text{ Gy} = 1 \text{ m}^2/\text{s}^2 = 1 \text{ J/kg}$.

The *absorbed dose rate* is defined as the ratio of an incremental dose to a time interval,

with the SI unit $Gy/s = m^2/s^3$. To describe the terrestrial radiation in air, the absorbed dose rate is usually given in nGy/h.

To express the biological effects of radiation on a human body, the matter (tissue) and the type of radiation (α -, β -, γ -rays) have to be specified. This is realised by multiplying the absorbed dose by a dimensionless radiation quality factor q . The resulting quantity is called *dose equivalent* and has the SI unit Sievert (Sv). The tolerance threshold for radiation workers is 20 mSv/a, the average exposure to natural radioactivity in Austria and Germany is between 2 and 3 mSv/a.

[IAEA 2003], [Riedel 2004]

2.2 Sources of gamma-radiation

The sources of gamma-radiation can be divided into three different classes, differing in their type of origin [IAEA 2003]:

- **Naturally occurring nuclides:** Naturally occurring radionuclides can be assumed to be on Earth since its genesis and have been decaying continually ever since. Because of their long half-lives in the order of the age of the Earth, they are still relatively abundant. This group of radionuclides includes ^{40}K , ^{232}Th , ^{235}U and ^{238}U . Their relative abundance in the Earth's crust causes a terrestrial radiation with a typical gamma dose rate of 20 - 100 nGy/h. Most of the naturally occurring gamma rays are radiated by those isotopes and their daughter isotopes, respectively. [IAEA 2003]
- **Man-made nuclides:** Enforced nuclear reactions enabled the creation of artificial nuclides. Most of these man-made nuclides are unstable and have rather short half-lives. Artificial radioactive isotopes gained high importance for medical purposes and nuclear power generation. [Riedel 2004]
Fallout from nuclear weapon tests and power plant accidents has caused a considerable contamination of the environment with artificial radionuclides, especially on the northern hemisphere. The most persistent radionuclide from nuclear fallout is ^{137}Cs , with a half-life of 30.17 years. [IAEA 2003]
- **Nuclides of extra-terrestrial origin:** Cosmic radiation is caused by high-energy particles, originating from the sun or outside our solar system. This primary radiation interacts with particles in the atmosphere and produces cosmogenic radionuclides, which give rise to a secondary radiation of gamma-rays and particles. The cosmic-ray dose rate at sea level is about 32 nGy/h and increases with altitude, doubling every 2000 m. [IAEA 2003]

Humans are exposed to external and internal irradiation, caused by natural and man-made sources. External sources of radiation are for example cosmic rays, terrestrial radiation, radionuclides in building materials, X-ray examinations and nuclear fallout. Internal sources of radioactivity can be found in our food or water and

in the air we breathe. Especially radon gas contributes significantly to our annually absorbed radiation dose. [IAEA 2003]

2.2.1 Natural sources of gamma-radiation

The majority of the terrestrial radiation results from radionuclides of the decay chains of ^{238}U and ^{232}Th and from the decay of ^{40}K . While potassium is a major component of the Earth's crust, uranium and thorium are only minor components. The regional distribution of these elements can have a wide range, depending on the composition of rocks and soils. Local and regional variations in rock composition result in different gamma-responses. Therefore, the measurement of gamma-radiation provides a good idea about the concentration of radioelements, making gamma-ray spectroscopy a useful tool for mapping mineralogical and geochemical properties of the upper 30 cm of rock and soil. In geology, the radioelement concentration in rocks and soils is usually given as mass concentration in % for potassium and in ppm for uranium and thorium, with $1 \text{ ppm} = 10^{-6} \text{ g/g} = 1 \text{ g/ton}$. The related specific activity of the radioelements can be found in table 2.1:

1% K in rock	=	313 Bq/kg	^{40}K
1 ppm U in rock	=	12.35 Bq/kg	^{238}U or ^{226}Ra
1 ppm Th in rock	=	4.06 Bq/kg	^{232}Th

Table 2.1: Conversion of radioelement concentration to specific activity [IAEA 2003]

If the concentrations of K, U and Th are known, the dose rate can be calculated for a certain locality in consideration of the following aspects [Kemski et al. 1996]:

- For terrestrial gamma-ray exposure, only nuclides located in the upper 30 cm of rocks or soils have to be considered.
- The calculation requires equilibrium in the U and Th decay series, which is, at least in the U series, not always present.
- A mean soil composition has to be considered, including mean density, water content, and concentrations of different minerals.
- This kind of calculation only makes sense at regional scale.

The fluctuation range of the local dose rate can be significant. An UNSCEAR ¹ - report [cp. Kemski et al. 1996] from 1993 quotes values taken from measurements in 40 countries, varying between 1 and 1300 nGy/h for local values and between 24 and 160 nGy/h for mean values of the countries. The effective exposure to humans can

¹UNSCEAR: United Nations Scientific Committee on the Effects of Atomic Radiation

differ significantly from these values. People living in industrialised countries spend a good portion of their lives in buildings, whose building materials contain natural radionuclides. Mean values of the exposure to humans caused by the radiation of buildings vary between 20 and 190 nGy/h. [Kemski et al. 1996]

2.2.2 Radiochemistry and geochemistry of potassium, uranium and thorium

As mentioned before, potassium, uranium and thorium are the only elements with isotopes of sufficient concentrations and gamma-ray energies to be measured at airborne survey height. Some properties of those three elements are listed in the following table:

Isotope	Abundance [%]	Half-life [years]	Decay type	Energy [MeV]
${}_{19}K^{40}$	0.012	1.3×10^9	β , k-capture	1.46
${}_{90}Th^{232}$	100	1.39×10^{10}	α, β, γ	0.03 - 2.62
${}_{92}U^{238}$	99.284	4.5×10^9	α, β, γ	0.4 - 2.5

Their properties and their behaviour in rocks and minerals will be closer discussed in the following section.

Potassium:

With 2-2.5 weight %, potassium is one of the major elements of the Earth's upper crust [IAEA 2003]. Apart from the isotopes ${}^{39}K$ (93.26%) and ${}^{41}K$ (6.73%), 0.012 % of naturally occurring potassium appear as the radioactive isotope ${}^{40}K$. 11 % of ${}^{40}K$ decay to ${}^{40}Ar$ by electron-capture, emitting a single gamma-ray photon with an energy of 1.46 MeV. If the gamma-ray flux of ${}^{40}K$ is measured, the total amount of K can be estimated, because ${}^{40}K$ appears as a fixed proportion of K [cp. Billings 1998]. In a chemical bond, potassium serves as kation (negative ion) and plays an important role in the formation process of rock forming silicates [Kemski et al. 1996].

Potassium occurs mainly in alkali-feldspars and micas in felsic rocks. It has only a low content in mafic rocks (basalt) and a very low content in ultramafic rocks (dunite, peridotite). The K content varies between 0.004 % for ultrabasites and more than 5 % for granites and claystones [Kemski et al. 1996]. The major hosts of potassium are potassic feldspars and micas [Dickson & Scott 1997].

Since potassium is soluble under most conditions, there is a general tendency for the potassium concentration in rocks or soils to decrease during weathering. After being released by its host, potassium can be taken up in the formation of K-bearing minerals or absorbed into clays [Dickson & Scott 1997].

The following table lists minerals with relatively high content of potassium [IAEA 2003]:

K Minerals	Chemical Formula	%K
Rock forming silicate minerals		
Feldspars	$(K, Na)AlSi_3O_8; (Na_x, Ca_{1-x})Al_{2-x}Si_{2+x}O_8 (x = 0 - 1)$	
Alkali-feldspar	$(K, Na)AlSi_3O_8$	13
Microcline	$KAlSi_3O_8$	13
Orthoclase	$KAlSi_3O_8$	13
Sanidine	$KAlSi_3O_8$	13
Leucite	$KAlSi_2O_6$	17
Nepheline	$(K, Na)AlSiO_4$	23
Biotite	$K(Mg, Fe)_3AlSi_3O_{10}(OH)_2$	8
Muscovite	$KAl_2AlSi_3O_{10}(OH)_2$	8
Phlogopite	$KMg_3AlSi_3O_{10}(OH)_2$	8
Hornblende	$(K, Na)_{0-1}(Na, Ca)_2(Fe, Mn, Mg, Ti, Al)_5(Si, Al)_8(OH, F)_2$	1
Other K-minerals		
Alunite	$KAl_3(SO_4)_2(OH)_6$	
Glaucosite	$(K, Ca, Na)_{<1}(Al, Fe^{3+}, Fe^{2+}, Mg)_2[(OH)_2/Al_{0.35}Si_{3.65}O_{10}]$	
Sylvite	KCl	

Mean potassium contents of rocks and soils are listed in the following table [cp. Kemski et al. 1996]:

Rock type	K concentration [%]		
	Mean	Min.	Max.
Acidic igneous rocks	3.2	2.5	5.4
Intermediate igneous rocks	2.8	1.7	3
Alkaline igneous rocks	0.6	0.58	0.75
Ultrabasites	0.004	0.001	0.09
Sandstone	1.48	0.01	6.7
Claystone	2.81	0.49	4.3
Carbonates	0.31	0.02	1.5
Soil	1.68	0.05	9.5

Uranium:

Natural uranium has an average abundance of 2-3 ppm in the Earth's crust and occurs with the radioisotopes ^{234}U (0.0056 %), ^{235}U (0.7202 %) and ^{238}U (99.2672 %). ^{234}U is only a daughter product within the ^{238}U decay chain, while ^{235}U and ^{238}U are mother nuclides, which both show long disintegration series that terminate in stable isotopes of ^{206}Pb and ^{207}Pb , respectively [Kemski et al. 1996]. Since ^{235}U is relatively rare and the gamma-ray energies in its decay series are too low to be detected at airborne survey height, only ^{238}U is of interest in airborne gamma-ray spectroscopy. No gamma-ray is emitted directly by the decay of ^{238}U and thus we rely on the gamma-ray emission of its radioactive daughter nuclide ^{214}Bi , which emits gamma-rays of several different energies. The strongest energy peak is at 1.76 MeV and also the peak at 0.609 MeV is of interest in airborne surveying [cp. Billings 1998]. ^{214}Bi has a half-life of approximately 20 min. Since ^{214}Bi appears far down in the ^{238}U

decay chain, there are several sources of disequilibrium and an accurate estimation of U requires therefore consideration of disequilibrium conditions. Figure 2.1 lists the ^{238}U decay series [Minty 1997].

Nuclide	Half-life	Major radiation energy (MeV) and intensity*		
		α	β	γ
^{238}U ↓	4.468x10 ⁹ y.	4.15 (23%) 4.19 (77%)	–	–
^{234}Th ↓	24.1 d.	–	~0.103 (19%) 0.191 (81%)	0.063 (3.5%) 0.093 (4%)
^{234}Pa ↓	1.18 m	–	2.29 (98%)	0.765 (0.30%) 1.001 (0.60%)
99.86% ^{234}Pa → ^{234}U 0.14% ^{234}Pa → ^{234}Pa ↓	6.7 h	–	0.53 (66%) 1.13 (13%)	0.10 (50%) 0.70 (24%) 0.90 (70%)
^{234}U ↓	2.48x10 ⁵ y.	4.72 (28%) 4.77 (72%)	–	0.053 (0.2%)
^{230}Th ↓	7.52x10 ⁴ y.	4.62 (24%) 4.68 (76%)	–	0.068 (0.6%) 0.142 (0.07%)
^{226}Ra ↓	1602 y.	4.60 (5.5%) 4.78 (94.5%)	–	0.186 (4%)
^{222}Rn ↓	3.825 d.	5.49 (~100%)	–	0.510 (0.07%)
99.98% ^{218}Po → ^{214}Pb 0.02% ^{218}Po → ^{218}At ↓	3.05 m	6.11 (100%)	0.33 (100%)	–
^{214}Pb → ^{214}Bi ↓	26.8 m	–	1.03 (6%)	0.295 (19%) 0.352 (36%)
^{214}Bi ↓	2 s	6.65 (6%) 6.70 (94%)	0.67 (94%)	–
^{214}Bi ↓	19.7 m	5.61 (100%)	3.26 (100%)	0.609 (47%) 1.120 (17%) 1.764 (17%)
99.96% ^{214}Bi → ^{214}Po 0.04% ^{214}Bi → ^{210}Tl ↓	164 μs	7.83 (100%)	–	0.799 (0.014%)
^{214}Po → ^{210}Pb ↓	1.32 m	–	2.3 (100%)	0.296 (80%) 0.795 (100%) 1.31 (21%)
^{210}Pb ↓	~22 y.	3.7 (1.8 x10 ⁻⁸ %) 0.064 (15%)	0.017 (85%) 0.064 (15%)	0.047 (4%)
^{210}Bi ↓	5.02 d.	4.93 (60%) 4.89 (34%) 4.59 (5%)	1.155 (100%)	–
~100% ^{210}Bi → ^{210}Po ~0.00001% ^{210}Bi → ^{206}Tl ↓	138.3 d.	5.30 (100%)	–	0.803 (0.0011%)
^{210}Po → ^{206}Pb ↓	4.19 m	–	1.520 (100%)	–
^{206}Pb	Stable	–	–	–

* Intensity refers to percentage of disintegrations of the nuclide itself, not to the original parent of the series

Figure 2.1: Uranium decay series [Minty 1997]

The chemical properties of uranium are related to its natural valence states (+4 and +6), whereas U^{4+} appears under reducing conditions in insoluble minerals and U^{+6} appears under oxidising conditions as highly soluble species [Dickson & Scott 1997]. Because of its large ionic radius, uranium can only be found as trace elements in the main rock forming minerals. There is a general tendency for the uranium content to increase from light-coloured felsic minerals (feldspars, quartz) to the dark-

coloured mafic minerals (pyroxene, micas) [Kemski et al. 1996]. During magmatic differentiation uranium is preferentially attached to minerals of the late magmatic and pegmatitic crystallisation. In rock forming minerals, uranium can be found alongside of fissures and grain boundaries, particularly in granites and pegmatite. Uranium enrichment is often caused by chemical precipitation from aqueous solutions, what, in turn, is often caused by a change from an oxidising to a reducing milieu or by changes of the pH-value or in temperature. [Kemski et al. 1996]

The most abundant uranium minerals are listed in the following table [IAEA 2003]:

Uranium Minerals	Chemical Formula	% UO_2 /ppmU
Minerals with uranium as major constituent		
Uranite (Pitchblende)	UO_2	
Betafite	$(U, Ca)(Nb, Ta, Ti)_3O_9nH_2O$	
Huttonite	$ThSiO_4$	100-20000 ppm
Uranospherite	$(BiO)(UO_2(OH)_3$	
Thorite, Uranothorite	$ThSiO_4, (Th, U)SiO_4$	1-35%
Thorianite, Uranothorianite	$ThO_2(Th, U)O_2$	5%
Common accessory rock forming minerals		
Zircon	$ZrSiO_4$	5%
Xenotime	YPO_4	5%
Monazite	$(REE, Th)PO_4$	100-20000 ppm
Allanite	(Ca, Al, Fe, Mg) silicate	10-2000 ppm
Apatite	$Ca_5(PO_4)_3(F, Cl, OH)$	5-200 ppm
Sphene	$CaTiSiO_5$	10-500 ppm

The uranium content of some felsic and mafic minerals is listed in the following table [modified after Kemski et al. 1996]:

Minerals	Chemical Formula	²³⁸ U [ppm]	
		Min.	Max.
mafic:			
Olivine	(Mg, Fe) ₂ SiO ₄	0.01	
Augite	(Ca, Mg, Fe, Ti, Al)(Al, Si) ₂ O ₆	0.01	40
Hornblende	(Ca, Na) _{2–3} (Mg, Fe, Al) ₅ (Si, Al) ₈ O ₂₂ (OH) ₂	1	30
Biotite	K(Mg, Fe) ₃ AlSi ₃ O ₁₀ (OH, F) ₂	1	40
felsic:			
Muscovite	KAl ₂ (AlSi ₃ O ₁₀)(OH, F) ₂	2	8
Plagioclase	CaAl ₂ Si ₂ O ₈	0.2	5
Potassic feldspar	KAlSi ₃ O ₈	0.2	3
Quartz	SiO ₂	0.1	5

Mean uranium contents of rocks and soils are listed in the following table [cp. Kemski et al. 1996]:

Rock type	U concentration [ppm]		
	Mean	Min.	Max.
Acidic igneous rocks	3.5	3	20
Intermediate igneous rocks	1.5	1	8
Alkaline igneous rocks	0.8	0.3	1
Ultrabasites	0.05	0.01	0.1
Sandstone	1.6	0.5	3
Claystone	3.7	1.5	8
Carbonates	1.8	0.3	2.3
Soil	3.2	1	20

Thorium:

The average abundance of Thorium in the Earth's crust is 8-12 ppm [IAEA 2003]. There are six natural radioisotopes of thorium, whereas ^{232}Th is the most abundant and has the longest half-life. It disintegrates in a long chain that terminates with the stable isotope ^{208}Pb . ^{228}Th is a daughter nuclide in the same decay chain and has a half-life of 1.9 years. ^{234}Th ($t_{1/2} = 24.1$ days) and ^{230}Th ($t_{1/2} = 75400$ years) are daughters of the ^{238}U decay chain, ^{231}Th ($t_{1/2} = 25.4$ hours) and ^{227}Th ($t_{1/2} = 18.2$ days) are daughter products of the ^{235}U decay chain. [Kemski et al. 1996] The measured gamma-ray peak in the thorium series at 2.62 MeV is actually caused by the decay of ^{208}Tl , which has a half-life of 3.1 min. On average, it takes about 40 years to reach equilibrium in the Th decay series. [Dickson & Scott 1997] Figure 2.2 lists the ^{232}Th decay series [Minty 1997].

Nuclide	Half-life	Major radiation energy (MeV) and intensity*		
		α	β	γ
^{232}Th	1.39×10^{10} y.	3.95 (24%) 4.01 (76%)	–	–
\downarrow				
^{228}Ra	5.75 y.	–	0.055 (100%)	–
\downarrow				
^{228}Ac	6.13 h	–	2.11 (100%)	0.34 (15%) 0.908 (25%) 0.96 (20%)
\downarrow				
^{228}Th	1.913 y.	5.34 (28%) 5.42 (71%)	–	0.084 (1.6%) 0.214 (0.3%)
\downarrow				
^{224}Ra	3.64 d.	5.45 (5.5%) 5.68 (94.5%)	–	0.241 (3.7%)
\downarrow				
^{220}Rn	55.6 s	6.30 (~100%)	–	0.55 (0.07%)
\downarrow				
^{216}Po	0.145 s	6.78 (100%)	–	–
\downarrow				
^{212}Pb	10.64 h	–	0.580	0.239 (47%) 0.300 (3.2%)
\downarrow				
^{212}Bi	60.5 m	6.05 (70%) 6.09 (30%)	2.25 (100%)	0.040 (2%) 0.727 (7%) 1.620 (1.8%)
\downarrow				
^{212}Po	304 ns	8.78 (100%)	–	–
\downarrow				
^{208}Tl	3.1 m	–	1.80 (100%)	0.511 (23%) 0.583 (86%) 0.860 (12%) 2.614 (100%)
\downarrow				
^{208}Pb	Stable	–	–	–

* Intensity refers to percentage of disintegrations of the nuclide itself, not to the original parent of the series

Figure 2.2: Thorium decay series [Minty 1997]

Because of its large ionic radius and its oxidation state (mainly +4) thorium is only present as a trace element in the main minerals. Because uranium has a very similar ionic radius, uranium and thorium can substitute each other in the crystal lattice of their host mineral. In the same way, thorium can also replace zirconium and cerium and hence the thorium content in accessory minerals can increase up to several percent. In the magmatic cycle, thorium can be enriched during differentiation and is especially attached to late crystallising minerals. [Kemski et al. 1996]

Thorium is present in the rocks huttonite, thorite and uranthorite, in accessory minerals and as trace elements in the major rock forming minerals [IAEA 2003]. Generally, it is insoluble except in acid solutions. Thorium that is freed during the weathering process can be taken up into clays and iron oxides. [Dickson & Scott 1997] The most abundant thorium minerals are listed in the following table [IAEA 2003].

Thorium Minerals	Chemical Formula	% ThO_2
Minerals with thorium as major constituent		
Huttonite	$ThSiO_4$	80
Thorite, Uranothorite	$ThSiO_4, (Th, U)SiO_4$	50, < 50
Cheralite	$(Th, Ce, Ca)(SiO_4PO_4)$	30
Thorianite, Uranothorianite	$ThO_2(Th, U)O_2$	80, < 80
Common accessory rock forming minerals		
Zircon	$ZrSiO_4$	0.01-1
Xenotime	YPO_4	0.4-1
Monazite	$(REE, Th)PO_4$	10
Allanite	(Ca, Al, Fe, Mg) silicate	0.1-1
Apatite	$Ca_5(PO_4)_3(F, Cl, OH)$	0.001-0.1
Sphene	$CaTiSiO_5$	0.001-0.01
Epidote	$CaFe^{3+}Al_2O.OH(Si_2O_7)(Si_2O_4)$	0.005-0.05

Mean thorium contents of rocks and soils are listed in the following table [cp. Kemski et al. 1996]:

Rock type	Th concentration [ppm]		
	Mean	Min.	Max.
Acidic igneous rocks	12.6	10	90
Intermediate igneous rocks	3.9	2	10
Alkaline igneous rocks	1.9	0.5	2
Ultrabasites	0.4	0.01	0.5
Sandstone	1.7	1	9
Claystone	12.2	10	17
Carbonates	1.1	0.1	3
Soil	10.3	4.2	23

Radium:

The chemistry of radium should also be considered because it can be a source of disequilibrium both within the ^{238}U and the ^{232}Th decay series. All known radium

isotopes are radioactive, but in a geological frame only ^{226}Ra is of interest. Its half-life of 1600 years is in the range of geological accumulation and depletion processes. Within a hydrous environment, radium nuclides can be mobilised and detached from their long-lived mother nuclides. [Kemski et al. 1996]

2.2.3 ^{40}K , ^{238}U and ^{232}Th in fertilizers

Natural radionuclides can also be brought to the environment by fertilizers, which are often used in agriculture. Plant growth benefits from elements like nitrogen, phosphorus and potassium, and therefore these elements are contained in fertilizers. Radionuclides of the ^{232}Th and ^{238}U decay series can be intercalated in phosphate rocks, giving them relatively high radionuclide concentrations (30 - 260 ppm U in phosphate rocks). [Ghosh et al. 2008]

The ^{238}U content of fertilizers therefore depends on the phosphate content and is directly related to the P_2O_5 concentration in various fertilizers [Harb et al. 2008]. The content of ^{40}K in fertilizers depends on the potassium content of the fertilizers, as ^{40}K appears as a fixed percentage of potassium.

In airborne surveying it therefore has to be considered, that the radioelement concentrations of fertilizers affect the soil radioelement concentration of agriculturally used areas.

2.2.4 Disequilibrium

In open systems, like the zones of interaction between pedosphere, atmosphere and hydrosphere, the nuclides of the natural decay chains are not always in equilibrium. If one or more daughter isotopes of a decay series are removed or added to the system, the system is no longer in equilibrium and estimates of the parent isotope from measuring one of its daughters are simply wrong. There are no disequilibrium problems with potassium, because the measured γ -radiation is directly produced by the decaying source isotope and also in the thorium decay series, disequilibrium is rather uncommon. However, disequilibrium in the U decay series is a common source of error in gamma-ray spectroscopy. [Minty 1997]

According to *B.R.S. Minty* [Minty 1997], there are at least 5 positions in the ^{238}U decay series where fractionation can lead to disequilibrium: ^{238}U can be selectively leached relative to ^{234}U , ^{234}U can be selectively leached relative to ^{238}U , ^{230}Th and ^{226}Ra can be selectively leached relative to the other isotopes in the chain and eventually ^{222}Rn (radon gas) is very mobile and can escape into the atmosphere from soil and rock fissures.

The time needed to restore equilibrium is about ten times the half-life of the disturbed member and can take up to millions of years.

Estimates of the uranium concentration in rocks from gamma-ray spectroscopy require equilibrium conditions that are not always present. Therefore the inaccuracy is ex-

pressed by the term "equivalent uranium" (eU). The same expression is also used for thorium (eTh), although it rarely occurs out of equilibrium. [Minty 1997]

2.2.5 Sources of background radiation

Background radiation refers to radiation not originating from natural decay processes in rocks or soils. It has no geological significance and therefore has to be removed. There are at least four different sources of background radiation [e.g. Billings 1998]:

- **Aircraft and spectrometer background** is due to trace amounts of radionuclides in the helicopter and in the spectrometer. This component of background is constant. A small amount of background radiation is also caused by people in the helicopter. The human body contains approximately 0.02 % potassium, most of it in the muscles. The radioactive isotope ^{40}K makes up 0.012 % of potassium and causes human exposure. A person weighing 70 kg contains about 140 g potassium and causes an equivalent dose of 200 $\mu\text{Sv/a}$ [Burnham 2011].
- **Atmospheric radon:** Radon gas (^{222}Rn) is a radioactive daughter of ^{238}U and can escape from soils and rock fissures into the atmosphere. Radon gas and particularly its radioactive daughter products ^{214}Bi and ^{214}Pb are the main source of background. The degree of background depends on air temperature and pressure, air movements and wind patterns.
- **Cosmic rays** of high energy interact with molecules in the upper atmosphere and cause a complex background spectrum. Cosmic background has a constant energy distribution within the lower atmosphere and shows decreasing amplitude with decreasing altitude.
- **Nuclear fallout** from atomic explosions and nuclear tests or accidents causes some ^{137}Cs background with a single photopeak at 0.662 MeV. This kind of background is particularly present on the northern hemisphere.

Testing the influence of a person in the helicopter

Due to the fact that people radiate gamma-rays, an attempt was made to test the influence of a person on the detected count-rates of a gamma-spectrometer. Several different measurements were made: A background measurement with the spectrometer alone in a room, a measurement with a person sitting at a distance of 1.5 m to the spectrometer, a measurement with a person sitting on top of the spectrometer, a measurement with the spectrometer on top of a person lying on the floor, a measurement with the spectrometer on top of a person sitting on a chair and a background measurement with the spectrometer on the top of a chair. All measurements were averaged over a time interval of 300 s to get better statistical significance.

The person sitting 1.5 m away from the spectrometer had no influence on the detected

count rates, or if there was an influence, it was smaller than the standard deviation of the background measurements. The person sitting on top of the spectrometer caused a small reduction of the detected count rates of 4.7 %, 3.2 %, 8.8 % and 9.8 % for the TC-, K-, U-, and Th-windows, respectively. In this case, the human body probably shielded the gamma-rays originating from the ceiling. Compared to the background measurements, the measurements with the spectrometer on top of a person showed reduced count rates. The measurements on the floor showed a reduction of the detected count-rates of 22.2 %, 25.1 %, 22.1 % and 25.7 % for the TC-, K-, U-, and Th-windows, respectively. The measurements on the chair showed a reduction of the detected count-rates of 16.6 %, 18.9 %, 15.1 % and 25.2 % for the TC-, K-, U-, and Th-windows, respectively. In these cases, the human body probably shielded the gamma-rays originating from the floor.

The following table lists the results of the measurements. The values in [cps] refer to average values over several test series:

	TC [cps]	K [cps]	U [cps]	Th [cps]
floor				
Background	7619 ± 73	1797 ± 17	389 ± 14	217 ± 10
Person at 1.5 m	7603 ± 77	1799 ± 39	400 ± 11	232 ± 30
Person sitting on Spec.	7258 ± 64	1740 ± 21	359 ± 13	201 ± 5
Spec. on top of person	5920 ± 11	1347 ± 55	307 ± 13	166 ± 2
chair				
Background	7170 ± 57	1652 ± 10	382 ± 31	210 ± 3
Spec. on top of person	5978 ± 27	1340 ± 7	324 ± 1	157 ± 2

2.2.6 Interaction of gamma-rays with matter

Gamma-rays are part of the electromagnetic spectrum and travel at the speed of light. They have a discrete energy (E), frequency (f), and wavelength (λ), and are related by

$$E = hf = \frac{hc}{\lambda}$$

with h ... Planck's constant 6.6261×10^{-34} Js

and c ... velocity of light

[IAEA 2003]

The loss of energy when gamma-rays pass through matter is a complex process. There are three different ways in which gamma-rays interact with matter [e.g. Minty 1997, Billings 1998, IAEA 2003]:

- **The photoelectric effect:** An incident gamma-ray photon loses all of its energy, when being absorbed by a bound atomic electron. A part of the energy of the photon is used by the electron to overcome its binding to the atom; the remaining energy is converted to kinetic energy of the electron. This effect predominates at

low energies (≤ 200 keV) and depends on the atomic number of the absorbing material.

- **Compton scattering:** The incident gamma-ray photon loses only part of its energy to a bound atomic electron and is deflected in its path. The energy loss depends on the scattering angle and is a maximum at 180° . This effect predominates at moderate energies and is the dominant interaction process for gamma-rays of naturally occurring minerals when passing through rock, water or air. Thus the electron density of the material between source and detector influences the attenuation of γ -ray energies.
- **Pair Production:** An incident photon is completely absorbed within the electrostatic field of a nucleus, which results in the production of an electron-positron pair. The required energy for this process must be greater than the rest mass of the electron-positron pair (1.02 MeV). If the energy of the incident photon was greater than 1.02 MeV, the excess energy is converted into kinetic energy of the electron-positron pair.

Photons of moderate energy lose their energy through successive Compton scattering events until their energy is low enough that they can be absorbed by an electron through the photoelectric effect.

The distance a gamma ray can travel through a material until it loses half of its energy is called half-thickness and can be computed as follows:

$$\Delta x = \frac{\log 2}{\mu} \approx \frac{0.693}{\mu} \quad \mu = \text{attenuation coefficient}$$

[Formula: Billings 1998]

In air the half-thickness for gamma-ray energies between 0.609 (Rn) and 2.62 MeV (Th) is about 100 m, in rocks and soils it is generally less than 15 cm [Billings 1998]. Since a gamma-ray photon loses about half of its energy with each scattering event, it can be assumed that the gamma-ray photons detected at airborne survey height have been scattered only once or even not at all.

Chapter 3

Airborne gamma-ray measurements

Airborne geophysical measurements flown by a helicopter were first applied in Canada in the 1960's and were performed mainly for mineral exploration and geologic mapping. Recently, this geophysical technique has also been used for groundwater exploration and geologic hazard mitigation (landslides, volcanoes). The Geological Survey of Austria uses airborne geophysics since 1982. The system has been improved for several times and meanwhile it's one of the world's most modern and complex systems of this kind [Motschka 2001]. The instrumentation consists of an EM-bird, a Cs-Magnetometer, nine sodium-iodide crystals (eight downward-looking crystals and one upward-looking crystal), a passive microwave soil moisture sensor and additionally a GPS and a Radar- and Laser-altimeter. Usually, in an airborne geophysical survey all of these instruments record simultaneously.

Airborne gamma-ray surveys are flown at approximately constant ground clearance and along parallel profiles ("flight lines") with constant line spacing. It is also quite common to fly "tie lines" perpendicular to the "flight lines" and at larger line-spacing, which are then used to correlate the data and minimise differences at the intersection points. The survey height largely depends on topography and is usually a compromise between the requirements of the different geophysical methods being used. A typical survey height would be 80 m, but rough topography sometimes forces the pilot of the helicopter to fly at higher altitude. Line spacing depends on the survey height and should be a compromise between costs and the desired spatial resolution. Typical line spacing would be 50-200 m. Spatial resolution also depends on the speed of the helicopter (usually between 30-60 m/s) and on the sampling-rate of the instruments. A gamma-ray spectrometer with a sampling time of 1 s therefore reaches a sample distance of 30 m. [Motschka 2001]

Because the physical state of the air between source and helicopter strongly influences propagation and attenuation of gamma-rays, it's necessary to exactly determine the position of the helicopter (flight path, altitude) and additionally to measure air pressure, air temperature and air humidity. Usually, the exact navigation of the helicopter is realised by a GPS receiver, but during the whole survey a video camera additionally records the flight path. The videos are used for verification of the laser values relative to the vegetation, which are then used for vegetation correction of

altitude. Comparing the videos with topographic maps allows controlling of the accuracy of the GPS receiver and serves as a backup in the case of missing satellite signals. Sensors which measure air temperature and humidity are also attached to the helicopter. For determining the flight altitude, three different instruments (laser altimeter, radar altimeter and barometric altimeter) are mounted in the helicopter, which measure simultaneously. [Motschka 2001]

3.1 Detection of gamma-radiation

3.1.1 The gamma-ray spectrometer

Modern gamma-ray spectrometers are enhancements of the scintillation meter or scintillation counter [Telford et al. 1990]. They consist of at least one large, thallium-activated sodium iodide NaI(Tl) crystal which is connected to a 256 channel spectrometer. The energy range between 0.2 and 3.0 MeV is assigned to the channels 1-255, channel 256 measures the cosmic background radiation (3.0-6.0 MeV) [e.g. Motschka 2001]. Therefore, each channel, except for the cosmic channel, records gamma-rays within an 11.7 keV energy-range. Currently, the typical survey equipment would contain eight 4.2 litre NaI(Tl) crystals looking "downward" for detection of radiation from the ground and one 4.2 litre "upward looking detector", which records the background radiation.

If an incident gamma-ray interacts with the material of the crystal, photons of visible light are produced that induce the ejection of electrons from the photocathode of an attached photomultiplier [IAEA 2003]. The electrons are accelerated towards a series of dynodes, which increase the number of electrons by secondary emission of electrons from their surface. During this process, the number of electrons is amplified by about 10^6 [Billings 1998].

Finally, a cloud of electrons strikes the anode, inducing a negative voltage pulse as output. Gamma-ray spectrometers or "pulse height analyzers" separate the characteristic gamma-rays of potassium, uranium and thorium by making use of the fact, that the intensity of the light pulse and hence the amplitude of the output voltage pulse is proportional to the energy of the incident gamma-ray [Telford et al. 1990]. The number of gamma-rays emitted by the decay of those three elements and the total radioactivity are monitored in four relatively broad spectral windows within the following energy-ranges:

Window	Nuclide	Energy Range [MeV]
Total Count	-	0.400-2.810
Potassium	^{40}K (1.460 MeV)	1.370-1.570
Uranium	^{214}Bi (1.765 MeV)	1.660-1.860
Thorium	^{208}Tl (2.614 MeV)	2.410-2.810

Table 3.1: Standard gamma-ray energy windows recommended for natural radioelement mapping [cp. IAEA 2003]

3.1.2 The effect of flying altitude on spatial resolution and on the measured count rates

In airborne gamma-ray spectroscopy, radiometric data is measured by counting pulses originating from the ground under the helicopter. Figure 3.1 demonstrates that a radioactive source need not necessarily lie directly beneath the aircraft. The area from which the pulses may originate is theoretically infinite. [Billings 1998]

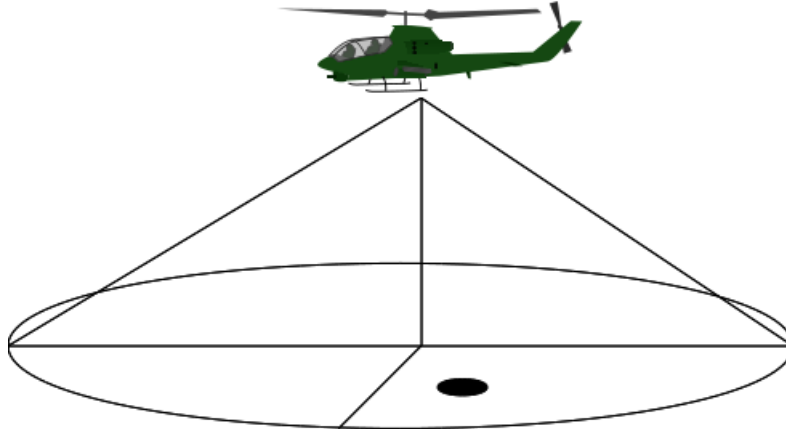


Figure 3.1: Effect of flying altitude on spatial resolution

R.L. Grasty [Grasty et al. 1979] calculated a relation between detector height and radius of the circle centred below the aircraft, which contributes to the signal. The following equation describes the percentage of the total detected gamma-ray photons, which originate from within a circle of radius r . The equation is valid for a spherical detector above a flat uniformly radioactive infinite source:

$$P = 100 * [1 - \cos\theta \frac{E_2(\mu \frac{h}{\cos\theta})}{E_2(\mu h)}]$$

μ = linear attenuation coefficient
 h = aircraft altitude
 θ = half-angle of the cone

$E_2(\mu h)$ is the exponential integral of the second kind, sometimes called King's function:

$$E_2(\mu h) = \int_1^\infty \frac{e^{-\mu h x}}{x^2} dx$$

[Formula: Grasty et al. 1979]

The previous equation disregards the movement of the helicopter during the integration time. Taking the movement of the aircraft into account, the area from which the pulses originate would rather be elliptical.

S.D. Billings [Billings 1998] calculated the radius of a circle, which contributes 90 % of the signal as a function of detector height (Fig. 3.2). The height of the helicopter also influences the count rates recorded, which decrease with increasing height. A model computed by *S.D. Billings* [Billings 1998] can be seen in Fig. 3.3.

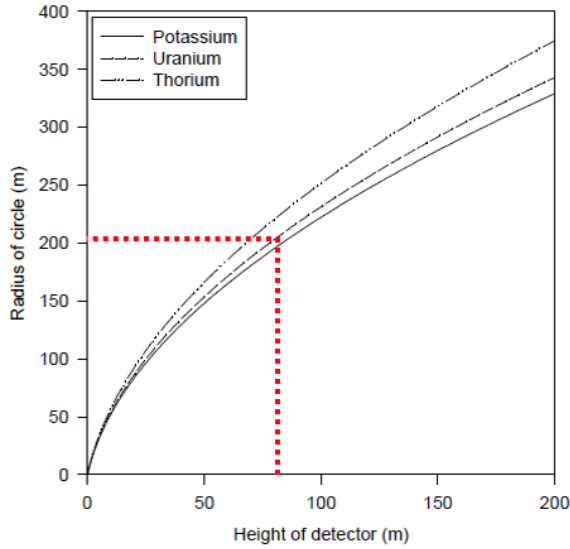


Figure 3.2: Radius of the circle that contributes 90% of the signal as a function of detector height [Billings 1998]

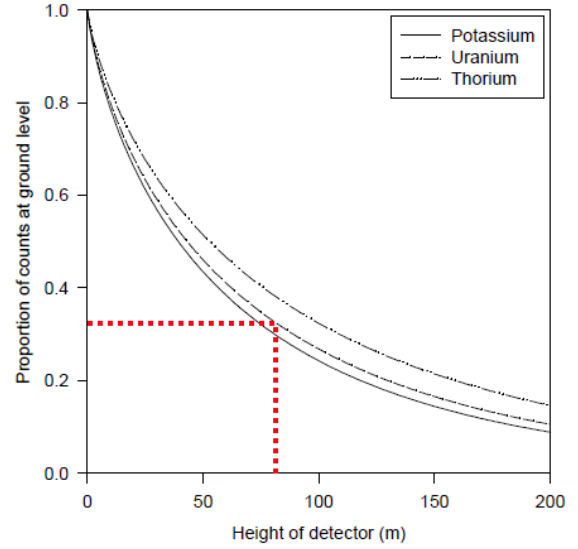


Figure 3.3: Reduction in the observed signal with height [Billings 1998]

3.1.3 Gamma-ray Spectra

^{40}K , ^{238}U and ^{232}Th each have characteristic line spectra, which represent the theoretical energy distribution of emitted photons at the source. Examples of theoretical line spectra are shown in the figures 3.4, 3.6 and 3.8 [Minty 1997].

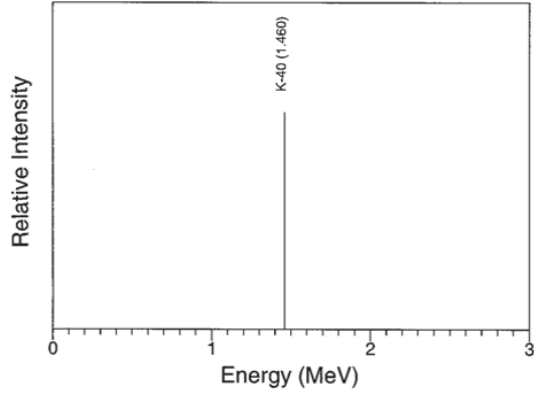


Figure 3.4: Potassium line spectrum [Minty 1997]

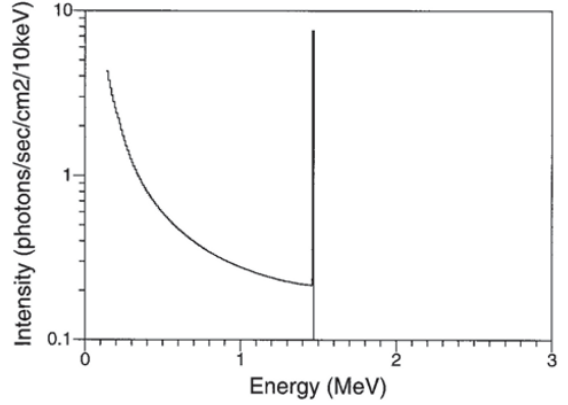


Figure 3.5: Simulated potassium flux at 300m altitude [Minty 1997]

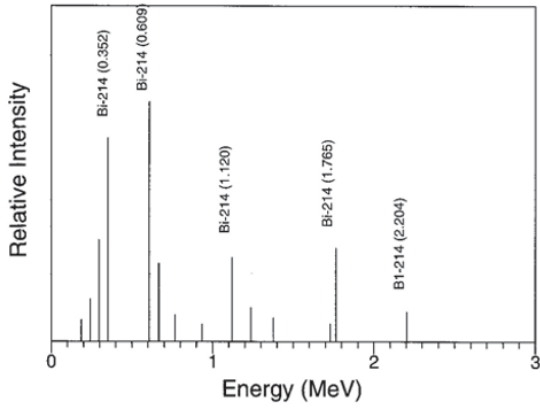


Figure 3.6: Uranium line spectrum [Minty 1997]

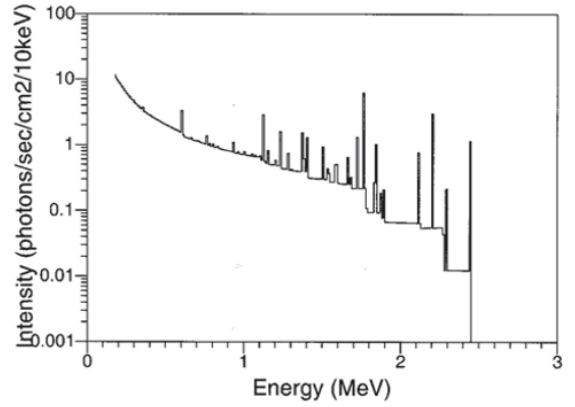


Figure 3.7: Simulated uranium flux at 300m altitude [Minty 1997]

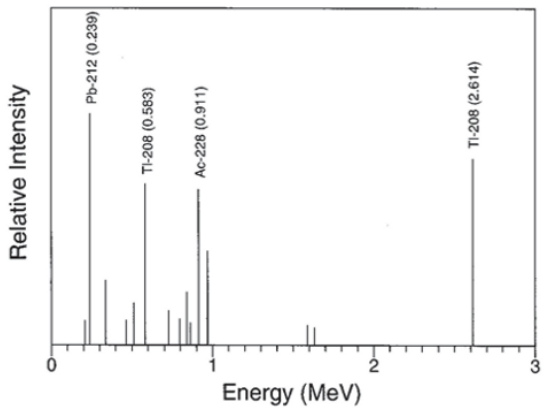


Figure 3.8: Thorium line spectrum [Minty 1997]

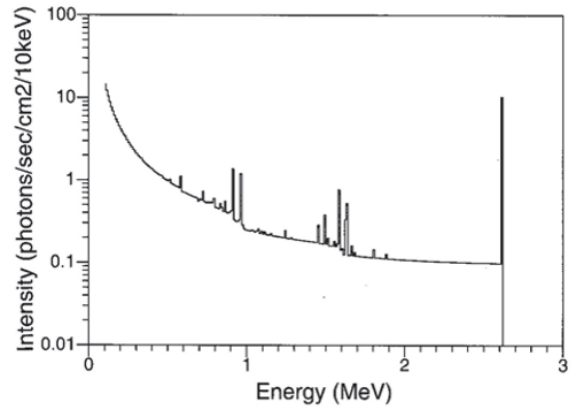


Figure 3.9: Simulated thorium flux at 300m altitude [Minty 1997]

These theoretical spectra are modified in many ways. As shown in subsection 1.2.5

(Interaction of gamma-rays with matter), scattering events between the source and the detector reduce the energy of the scattered photons and cause the build-up of a continuum of energies. Unscattered photons of each radioelement within the decay series generate sharp peaks at the respective energies. The simulated gamma-ray flux of K, U and Th at 300 m altitude is shown in figures 3.5, 3.7 and 3.9 [Minty 1997].

”The relative contribution of scattered and unscattered photons to the gamma-ray flux at airborne altitude depends on the source geometry (thickness and lateral extent) and on the amount of attenuating material between the source and the detector.” [Minty 1997] The gamma-ray flux spectra shown in figures 3.5, 3.7 and 3.9 are further modified, because the measured spectra are also functions of the detector response. This results in spectrum photopeaks of approximately Gaussian shape.

The following aspects influence the ratio of scattered and unscattered gamma-rays:

- **Source type:** In spectra of broad sources there is a larger build-up of the Compton continuum, in contrast to spectra of point sources. This results from the higher number of Compton scattering events within broad sources. [Minty 1997]
- **Source thickness:** Again, because of a larger number of scattering events within the sources, increasing source thickness leads to a greater build-up of the Compton continuum and a reduction of the photopeaks relative to the Compton-background. This effect dominates at lower energy levels, because gamma-rays of lower energy are more easily attenuated than gamma-rays of high energy. [Minty 1997]
- With increasing **electron density** and thus with increasing attenuation, the photopeaks are reduced relative to the energy continuum because of an increasing number of scattering events. [Minty 1997]
- Increasing **detector height** leads to decreasing total-count rates. A change of detector height of 10 meters will affect the measured radiation by about 7%. [IAEA 2003]

The airborne detector, namely the detector response, modifies the shape of the spectrum considerably. The following aspects influence the detector response [Minty 1997]:

- The **detector efficiency** is the probability, that a photon emitted from the source will be detected, thus will interact with the spectrometer. The detector efficiency increases with increasing detector size and decreases with increasing energy of the photons. The previous relation is one reason for the higher count-rates in lower energy channels.
- The **detector resolution** refers to the ability of the detector to distinguish between two gamma-rays of only slightly different energy. This is usually defined as the full width of a photopeak at half of the maximum amplitude (FWHM) divided by the photopeak energy. Typical spectrometer resolution would be 10 % for the ^{137}Cs photopeak at 0.662 MeV and 7% for the ^{208}Tl peak at 2.615 MeV.
- **Dead time** is the time required for the spectrometer to process a signal. During this time, no other incident gamma-rays can be detected. Thus, dead time should

be as small as possible.

- **Other factors** related to the airborne detector are escape events, accidental summing and the characteristic Compton edge. It may happen that a photon is only partially absorbed and then escapes the detector, resulting in a detected energy somewhat lower than that of the incident photon ("Compton scatter escape"). The highest energy resulting from this process of scatter escapes is called the "Compton edge".

In each pair-production event two gamma-ray photons with energy of 0.51 MeV are produced. If one of these or both escape from the detector, "escape peaks" at energies 0.51 or 1.02 MeV lower than that of the incident photons are produced (pair production escape).

Environmental Effects:

Air temperature and pressure, humidity, precipitation, soil moisture, dense vegetation and thickness of any non-radioactive overburden all influence the results of gamma-ray measurements. As mentioned above, attenuation of gamma-rays in the source, the material between source and detector and in the detector itself significantly affects the measured radiation. Therefore, non-radioactive overburden and dense vegetation both have the effect of reducing the radiation, which reaches the detector. According to *B.R.S. Minty* [Minty 1997], just 2 cm of barren overburden reduce the radiation output from the Earth's surface by 35 %.

Changing air temperature and pressure can change the air density by up to 30 % and thus affect attenuation and height correction factors. Rainfall and soil moisture change the soil density (or actually the wet density) and generally reduce the radiation output from the Earth's surface. A 10% increase in soil moisture usually decreases the radiation output by about the same amount. However, the effect on the uranium output can be controversial. The radioactive precipitation of radon gas (a daughter of ^{238}U) attached to dust particles in the lower atmosphere can lead to a significant increase in uranium ground concentration.

Topography can seriously affect the results of airborne gamma-ray measurements, because the spectrometers are calibrated for a 2π (infinite, flat) surface- and source-geometry. Deviations from the 2π surface will cause errors in the concentration estimates.

[Minty 1997, IAEA 2003]

3.2 Calibration flights

As mentioned in the previous section, the shape of spectra from airborne gamma-ray spectrometric measurements is affected by many factors. The spectra have to be corrected for effects not originating from natural terrestrial sources. Some of these corrections require calibration flights to determine cosmic- and aircraft-background, height attenuation coefficients and sensitivity coefficients, among others. These are

briefly described in the following section.

3.2.1 High-altitude cosmic- and aircraft-background flights

High-altitude cosmic- and aircraft-background calibration flights are usually flown off-shore in an area where atmospheric radon is at a minimum. The helicopter ascends vertically and spectra are measured at different heights like 1000, 1500, 2000, 2500, 3000 and 3500 m above sea level. Ideally, the measured spectra should only contain background, since no gamma-rays are radiated from the sea surface. The aircraft background is constant, the cosmic background increases with altitude. The actual calculation to determine the background is described in subsection 4.1.4. [IAEA 2003]

3.2.2 Ground calibration using radioactive pads

The spectra of K, U and Th partly overlap and therefore stripping ratios have to be determined to correct the spectral count rates for the effects of the other elements. The calibration procedure requires the measurement of spectra over concrete calibration pads (1m x 1m x 0.3m) with known concentrations of radioelements. Usually four pads are used; three of them have anomalous concentrations of K, U and Th, respectively, and the fourth pad serves as background pad. One after another, the pads are mounted beneath the helicopter and samples should be accumulated over ten minutes. The calculation of the "stripping ratios" is described in subsection 4.1.6. [IAEA 2003]

3.2.3 Calibration range flights

A calibration range is a strip of land with well known elemental concentrations of ground sources, used to compute sensitivity coefficients. Furthermore, the calibration flight is flown at different survey altitudes to determine the response of the spectrometer to changes in altitude (height attenuation coefficients).

If the ground concentration of radioelements is known, the sensitivity coefficients can be computed by dividing the background- and stripping-corrected count rates at nominal survey height by the ground concentration of the calibration range. In later processing the sensitivity coefficients are used to transform the count rates to ground concentrations.

To compute the height attenuation coefficients, the calibration range is flown at different altitudes, which would be typical for a survey (e.g. between 60 m and 300 m). If the background is known and the spectra have been background- and stripping-corrected, the elemental attenuation coefficients can be derived from an exponential regression of each channel count rate against height.

[IAEA 2003]

Chapter 4

Processing and Interpretation

4.1 Processing of gamma-ray spectrometric data

The role of processing is to improve the signal-to-noise-ratio of the observed data, to apply different corrections and to reduce the airborne count rates to estimates of the ground concentrations of K, U and Th. The following processing steps have to be carried out in the same succession as they are described here [Minty et al. 1997, IAEA 2003, Praga Manual]:

4.1.1 Spectral noise reduction/ spectral smoothing:

[IAEA 2003, Praga Manual]

This recent development in gamma-ray processing has improved the quality of processed data dramatically. Two methods are currently used for spectral noise reduction. The intention of these methods is to find the dominant spectral shapes of the raw spectra and reduce the noise to a minimum. With the help of principal component type analysis (PCA) radiometric spectra are analysed for correlated (signal) and non-correlated (noise) spectrum signatures by calculating principal eigenvectors. These are in fact combinations of detector responses to radionuclides present in the survey area. In gamma-ray spectrometry the detector response of the specific radionuclides stays approximately the same over the whole survey area, while the response to variations in the gamma-ray attenuation does change. In PCA, the whole dataset is converted into a single $N \times N$ (N = number of spectrum channels) covariance matrix (NASVD) or into signal and noise covariance matrices (MNF). The covariance matrix is then transformed into a set of N eigenvectors, which represent the dominant shapes of the whole dataset. In the next step, the spectra are reconstructed with only a part of the eigenvectors (usually the first 9-11, depending on the number of radionuclides present in the survey area).

- **NASVD** (Noise-Adjusted Singular Value Decomposition) smoothing: The ob-

served spectra are transformed into orthogonal spectral components and the components are then sorted according to the degree to which they contribute to the shape of the spectra. Signals correlate from channel to channel, random noise does not. In this way, noise can be removed by reconstructing the spectra from low-order components, which contain the bulk of the signal. The difference to the standard PCA method is that the spectra are normalized to unit variance in each channel before PCA is applied. The noise is then assumed to have equal variance across the whole spectrum and the computed eigenvectors are sorted by decreasing signal variance.

- **MNF** (Maximum Noise Fraction) smoothing: This method includes two linear transformations of the data, which are combined to a single transformation. It does not make any a-priori expectations about the noise, but calculates noise directly from the difference between two consecutive spectra. In the first step the noise is decorrelated and normalized to equal error variance in each channel. Thus, the data is "noise-whitened". In the second step, a standard principal component transformation is applied to the data.

The spectral noise reduction techniques have to be handled with care. Both can as well introduce false anomalies and remove real anomalies where spectral shapes are not well represented in the data.

4.1.2 Dead time/ life time correction

[Minty et al. 1997]

Gamma-ray spectrometers use a two-stage measurement technique. The nominal sample time (usually 1 s) is divided into the time the spectrometer requires for the detection of gamma-rays and the time required for measuring the energy of the detected pulses. The time devoted to the processing of the signal is called dead time. During this time, no other incident pulses can be processed and are automatically rejected. Thus, the total counting time is reduced by the dead time, which has typical values of 5-15 $\mu\text{s}/\text{pulse}$. The resulting time available to detect gamma-radiation is called life time and is automatically computed in modern spectrometers. The influence of equipment dead time on the observed count rates can be corrected as follows:

$$N = \frac{n}{1 - Ct}$$

N ... corrected count rate [cps] = [counts per second]

n ... observed count rate [cps]

C ... total count rate over all channels [cps]

t ... equipment dead time per pulse

"The dead time correction is usually very small, but can be significant in areas of high radioactivity or during some calibration procedures." [Minty et al. 1997] High radioactivity results in an increasing number of counts and thus, the proportion of the nominal sample time required for the spectrometer to compute the energy increases.

4.1.3 Energy calibration

[Minty et al. 1997]; [IAEA 2003]

Energy drift in the measured spectra is a serious source of error. In an energy calibrated spectrometer, each channel is related to a discrete energy window. For a standard spectrometer which measures energies between 0.2 and 3.0 MeV digitised into 255 channels, each channel is related to an energy window with a range of approximately 11.7 keV. Older spectrometers may drift up to 2-4 channels during the course of a day. This is a significant source of error and can only be corrected as long as all of the detector-crystals drift in the same way.

The calibration procedure is based on the assumption that prominent photopeaks have discrete positions in the observed spectra. Usually, the spectra are summed along each line and then the peak positions of the summed spectra are determined. These peak positions are then used to calibrate each of the individual spectra.

4.1.4 Aircraft and cosmic background removal

[Minty et al. 1997]; [IAEA 2003]

The aircraft background spectrum is due to trace amounts of radionuclides in the helicopter and the detector and is a constant. The cosmic background spectrum is due to cosmic radiation, which reacts with molecules of the upper atmosphere. In the lower atmosphere the shape of the cosmic background spectrum is nearly constant and its amplitude changes with altitude. For removing cosmic background it's also important to know that radiation at energies higher than 3 MeV all is cosmic in origin and that this cosmic window count rate is linearly related to the count rate in the i^{th} channel. Therefore, plotting the cosmic window count rate at different heights (1000, 1500, ..., 3500m) against the corresponding count rates in the i^{th} channel should show a linear trend. The slope of the linear regression line then yields the cosmic sensitivity and the zero-intercept corresponds to the aircraft background.

Aircraft and cosmic background are estimated as follows:

$$n_i = a_i + b_i n_{cos}$$

n_i ... aircraft and cosmic background count rate in the i^{th} channel

n_{cos} ... cosmic window count rate

a_i ... aircraft background in the i^{th} channel

b_i ... cosmic background in the i^{th} channel normalised to unit counts in the cosmic window

Better results will be achieved by using window count rates instead of channel count rates for K, U and Th, respectively. An example of a regression plot for aircraft- and cosmic-background correction is shown in Fig. 4.1. The calibration strategy for aircraft and cosmic background correction has been discussed in subsection 3.2.1.

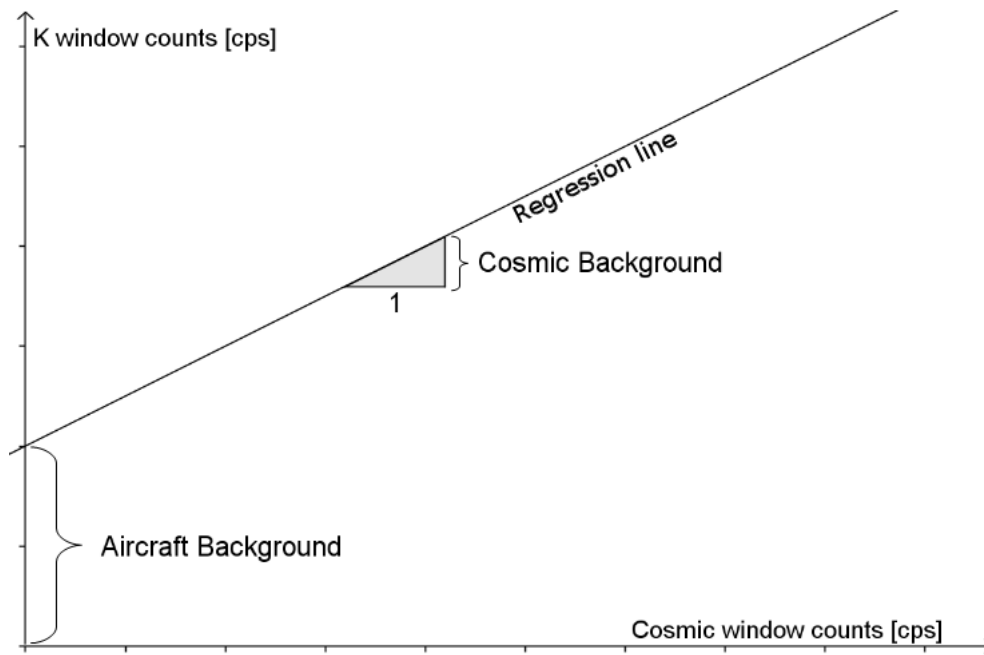


Figure 4.1: Cosmic window-counts vs. Potassium window-counts: Regression plot for aircraft- and cosmic-background determination

The aircraft background can also be determined from flights over water at common survey altitudes. As there is no gamma-radiation emitted from the sea-surface, count rates detected over the ocean mainly originate from radioelements in the helicopter and only few are due to cosmic radiation at these low altitudes. The determination of the aircraft background from flights over the ocean is demonstrated in Fig. 4.2 - Fig 4.7. The aircraft background of each radioelement-window corresponds to the zero-intercept in each diagram.

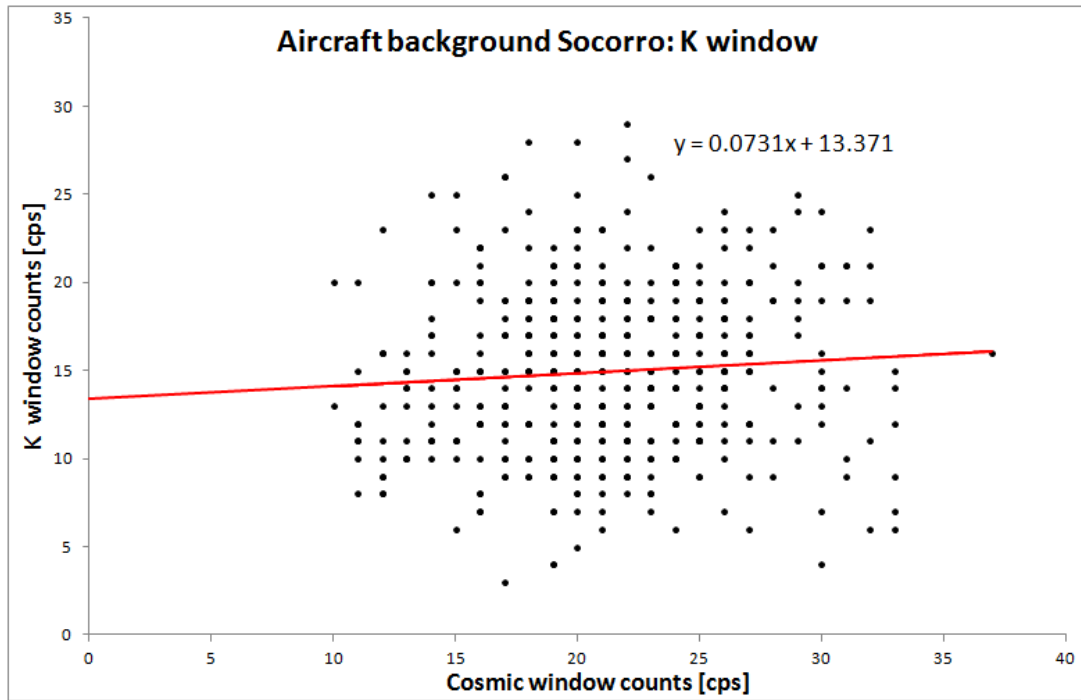


Figure 4.2: Cosmic window-counts vs. Potassium window-counts for a flight over the ocean near Socorro Island

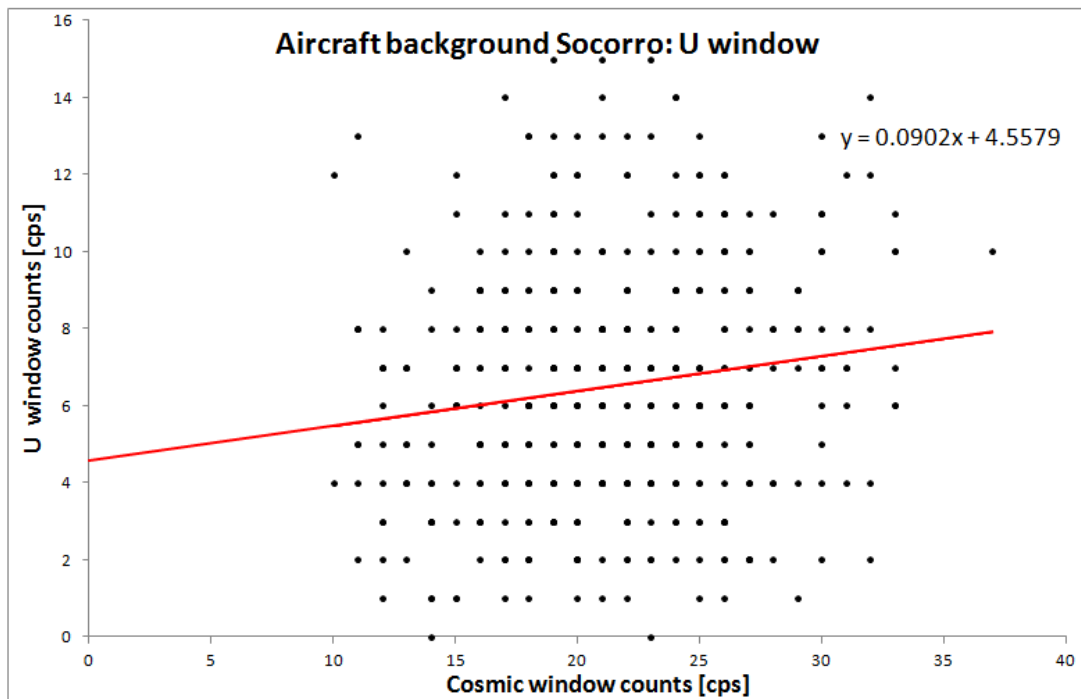


Figure 4.3: Cosmic window-counts vs. Uranium window-counts for a flight over the ocean near Socorro Island

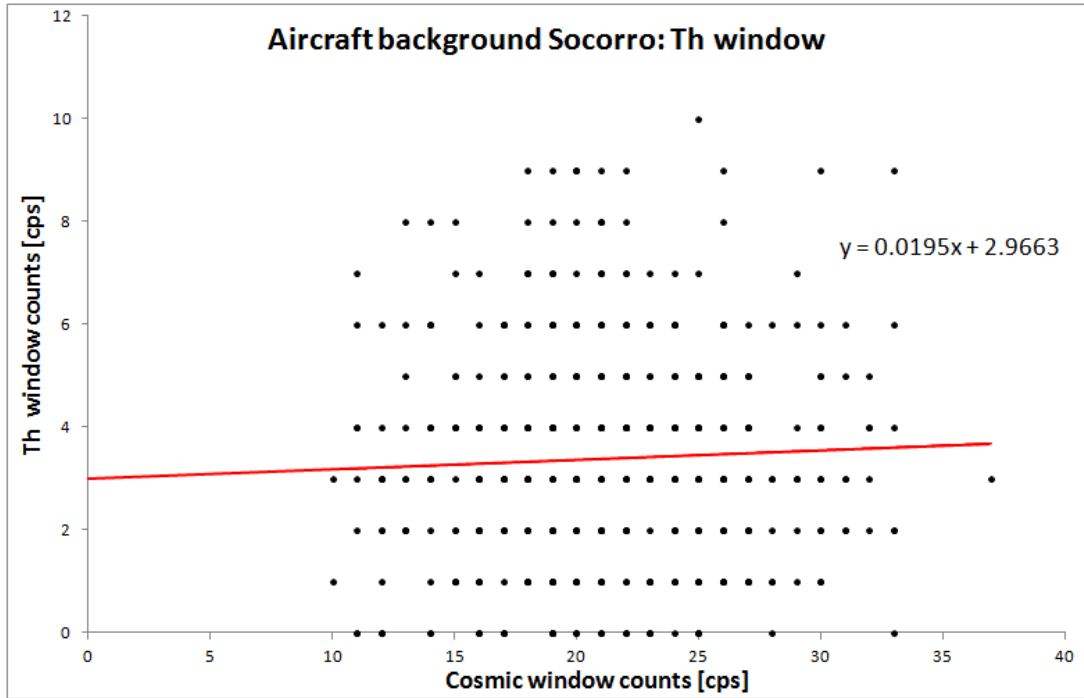


Figure 4.4: Cosmic window-counts vs. Thorium window-counts for a flight over the ocean near Socorro Island

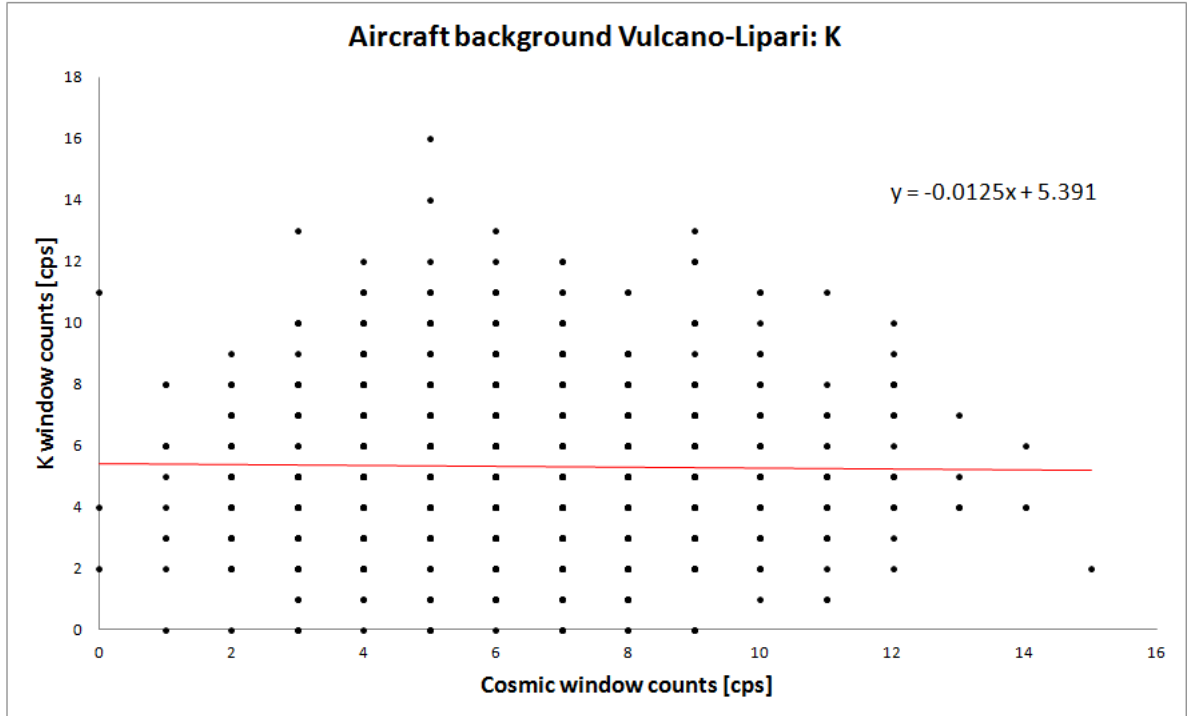


Figure 4.5: Cosmic window-counts vs. Potassium window-counts for a flight over the ocean near Vulcano Island

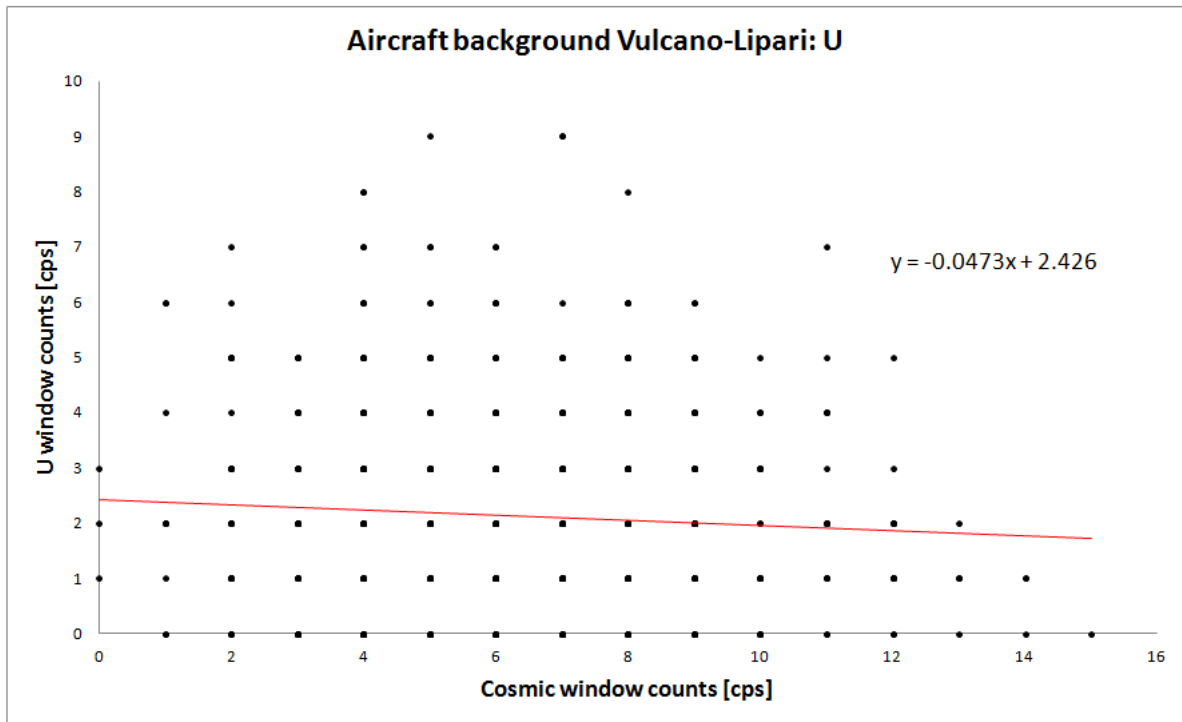


Figure 4.6: Cosmic window-counts vs. Uranium window-counts for a flight over the ocean near Vulcano Island

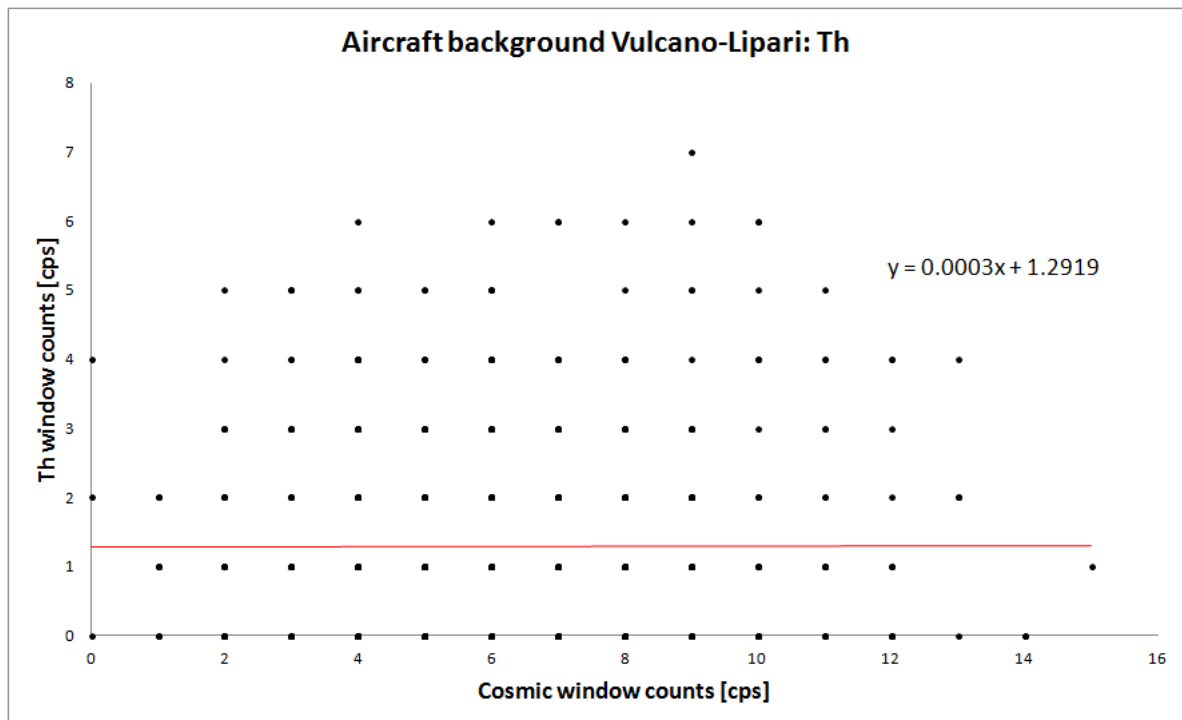


Figure 4.7: Cosmic window-counts vs. Thorium window-counts for a flight over the ocean near Vulcano Island

4.1.5 Radon background removal

Radon gas (^{222}Rn), a radioactive daughter nuclide of ^{238}U , is very mobile and can escape into the atmosphere from soils and rock fissures. This poses a big problem to the count rates of the uranium window, since the most prominent gamma-ray emitter (^{214}Bi) occurs below ^{222}Rn in the ^{238}U decay chain. A big problem for radon background removal is that it is unevenly distributed in the lower atmosphere and under special conditions it can be trapped close to the Earth's surface. Radon background can be removed by one of the three following procedures:

- **The spectral ratio method:** [Praga Manual, IAEA 2003]

The relative contribution of primary and secondary radiation to the observed spectra changes with distance from the source. For a close source, the lower energy part of the spectrum is far less attenuated as it would be for a distant source. The spectrum of atmospheric radon is that of a close radioactive source (around the helicopter), while the spectrum of terrestrial radiation is that of a distant source. The spectral ratio method uses the fact that the lower energy photopeaks are more affected by interaction of gamma-rays with matter than the higher energy peaks. The two ^{214}Bi photopeaks at 0.609 and 1.76 MeV are inspected with regard to their attenuation, as the peak at 0.609 MeV is less attenuated relative to the peak at 1.76 MeV for atmospheric radon than this would be the case for radon from the ground. The radon detection stage requires the Compton continuum to be removed and therefore requires a high degree of noise reduction, especially for the low energy part of the spectrum. A fourth energy window (L) has to be monitored, which represents the counts above the Compton continuum in the 0.609 MeV photopeak. The radon count rate in the low energy uranium window can be computed as follows:

$$L_R = \frac{L_{Ob} - C_2 U_{Ob} - C_3 Th_{Ob}}{1 - \frac{C_2}{C_1}}$$

The radon count rate in the standard uranium window is:

$$U_R = Q_R * \frac{L_{Ob} - C_2 U_{Ob} - C_3 Th_{Ob}}{C_1 - C_2}$$

L_{Ob}, U_{Ob}, Th_{Ob} ... window count rates calculated from observed spectrum after aircraft/cosmic background removal

C_1 ... L/U ratio for radon spectrum

C_2 ... L/U ratio for uranium spectrum

C_3 ... Th into L stripping value

Q_R ... ratio of uranium window count rates: (standard-window)/(above Compton continuum)

The success of the method strongly depends on the quality of C_1 and C_2 ratios, which should be derived during over water flights in the presence of radon. An alternative version of the spectral ratio method uses the ^{214}Pb photopeak at 0.352 MeV, which is independent from Cs and Th sources. The disadvantage is the high noise content in this lower energy part of the spectrum, and therefore the use of spectral smoothing techniques is strongly recommended.

- **The full spectrum method:** [Praga Manual, IAEA 2003]

The full spectrum method uses spectrum fitting techniques (usually LSQ fitting) to find contributions of atmospheric radon. This method requires full spectrum background removal. The observed spectrum can be expressed as a linear sum of K, U, Th and atmospheric radon as follows:

$$I_{obs} = |K| f_K + |U| f_U + |Th| f_{Th} + |Rn| f_{Rn}$$

I_{obs} ... observed spectrum

$|K|, |U|, |Th|, |Rn|$... elemental count rates due to K, U, Th, Rn

f_K, f_U, f_{Th}, f_{Rn} ... normalised component spectra due to K, U, Th, Rn

- **The upward looking detector method:** [IAEA 2003]

An additional crystal pack (the upward looking detector) is mounted on the other crystals of the spectrometer in a way that it is partially shielded from radiation from the ground. As a result, the spectrometer obtains some directional sensitivity and can now discriminate between radiation from the ground and from the atmosphere. A disadvantage of this method is the high degree of noise in the upward uranium window. This method is the only choice on the northern hemisphere, where there is high contamination of ^{137}Cs . The other two methods don't take Cs-window count-rates into account when computing the radon correction and are therefore influenced by high contamination of ^{137}Cs .

4.1.6 Stripping/ channel interaction correction

[IAEA 2003]

This correction is used to correct the K, U and Th window count rates for gamma-rays not originating from the radioelements or decay series being monitored. "For example, thorium series gamma rays appear in both the uranium and the potassium windows, and uranium series gamma rays appear in the potassium window." [IAEA 2003]

This effect can be corrected as follows:

$$\begin{aligned} n_{th(corr)} &= \frac{n_{th} - \alpha n_u}{1 - \alpha} \\ n_{u(corr)} &= \frac{n_u - \alpha n_{th}}{1 - \alpha} \\ n_{k(corr)} &= n_k - \beta n_{th(corr)} - \gamma n_{u(corr)} \end{aligned}$$

α ... counts in the U window per unit count in the Th window for a pure Th source
 β ... counts in the K window per unit count in the Th window for a pure Th source
 γ ... counts in the K window per unit count in the U window for a pure U source
 a ... counts in the Th window per unit count in the U window for a pure U source

Formula: [IAEA 2003]

The "stripping ratios" α , β , γ and a can be calculated from calibration experiments over specially constructed radioactive pad sources. The calibration procedure has been discussed in subsection 3.2.2.

In airborne surveying, height correction factors also have to be considered. They are given by the IAEA as increase in the stripping ratios with increasing altitude:

Stripping ratio	Increase per meter
α	0.00049
β	0.00065
γ	0.00069

[IAEA 2003]

4.1.7 Height correction

[Minty et al. 1997]

In airborne gamma-ray spectrometry it is essential to correct the collected data to a constant survey height (= nominal survey height), because variations in altitude during a survey result in varying attenuation of gamma-rays. The change of attenuation with altitude depends on the geometry of the source and on the energy of the radiation. An algorithm which is adequate for typical survey heights (50-250 m), broad sources (this is the most common source type), and subdued topography can be obtained by considering an exponential fall-off of radiation with increasing height:

$$N = N_0 e^{-\mu(H-h)}$$

μ ... height attenuation coefficient

N_0 ... observed count rate for height at standard temperature (273.15°K) and pressure (101.325 kPa), h

N ... corrected count rate for the nominal survey height H

In areas of rugged topography, other algorithms should be considered.

The STP height h used in the previous formula, can be calculated from the observed height h_{obs} by:

$$h = h_{STP} = \frac{273.15 \times P \times h_{obs}}{(T + 273.15) \times (101.325)}$$

The calibration strategy for determining the height attenuation coefficients has been discussed in subsection 3.2.3. By considering an exponential fall-off of radiation

with increasing height, the height attenuation coefficients can be derived from an exponential fit-curve when plotting the window count rates of K, U and Th against height. The determination of the height attenuation coefficients from the exponential fit-curve is demonstrated in Fig. 4.8 - Fig. 4.15. The height attenuation coefficients can be found in the exponent of the fit-curve-equation.

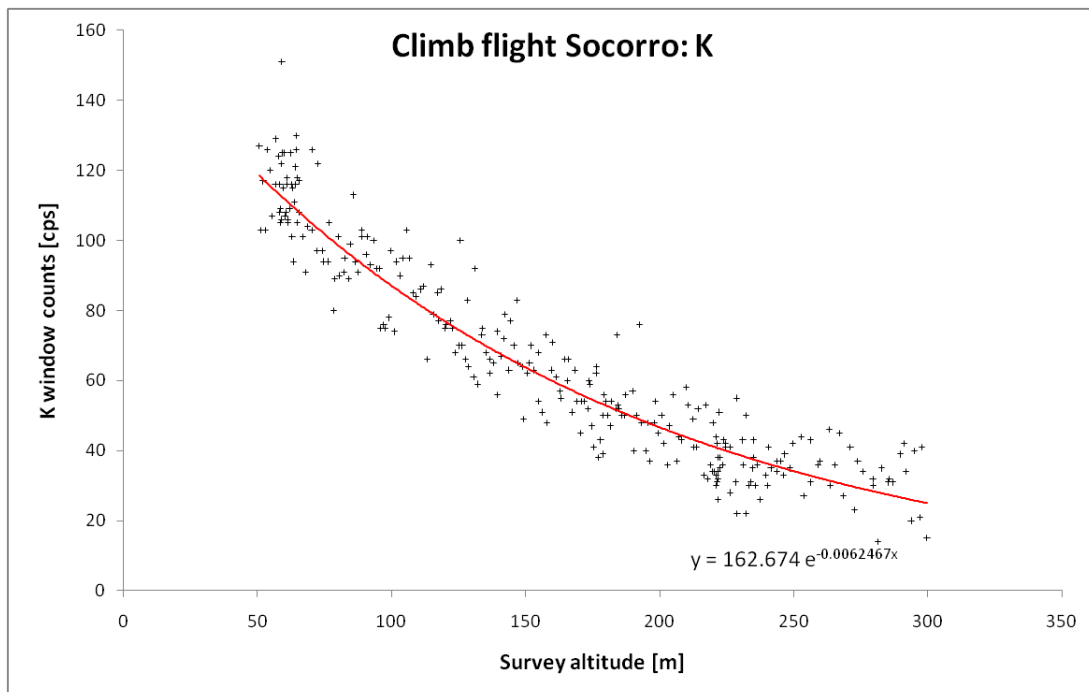


Figure 4.8: Flight altitude vs. Potassium window-counts for a climb-flight over Socorro Island

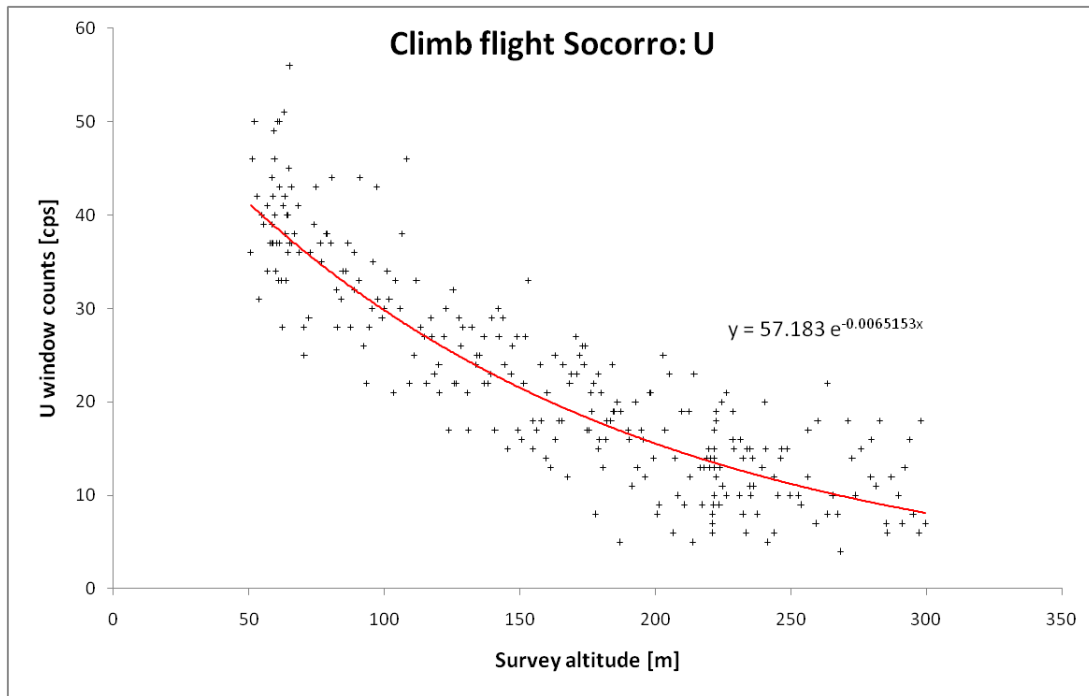


Figure 4.9: Flight altitude vs. Uranium window-counts for a climb-flight over Socorro Island

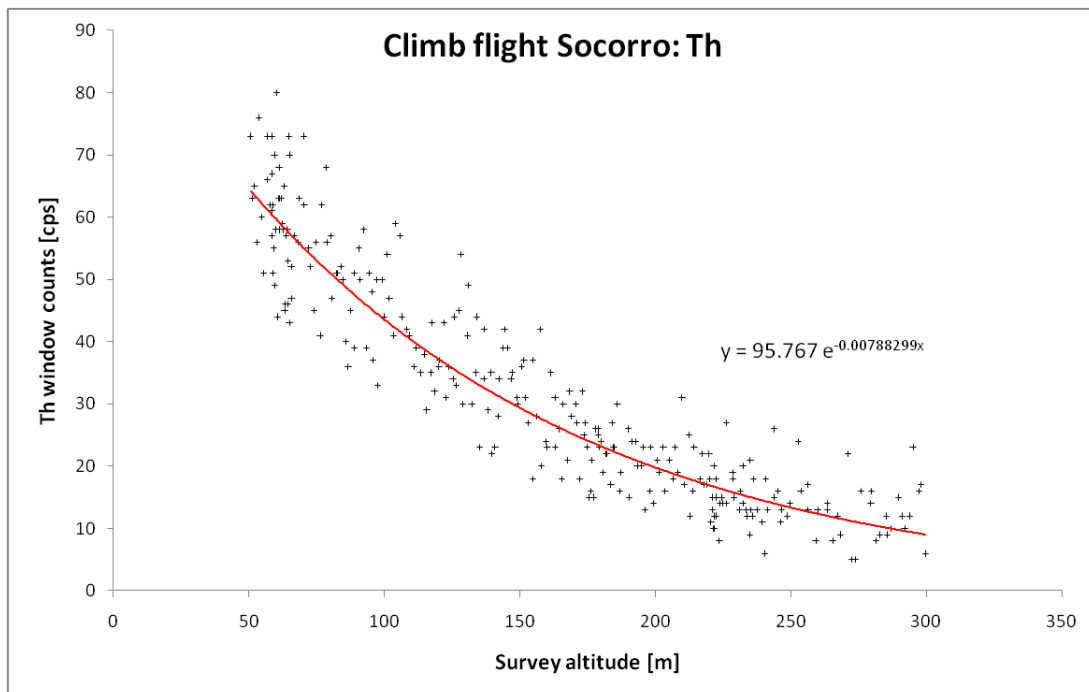


Figure 4.10: Flight altitude vs. Thorium window-counts for a climb-flight over Socorro Island

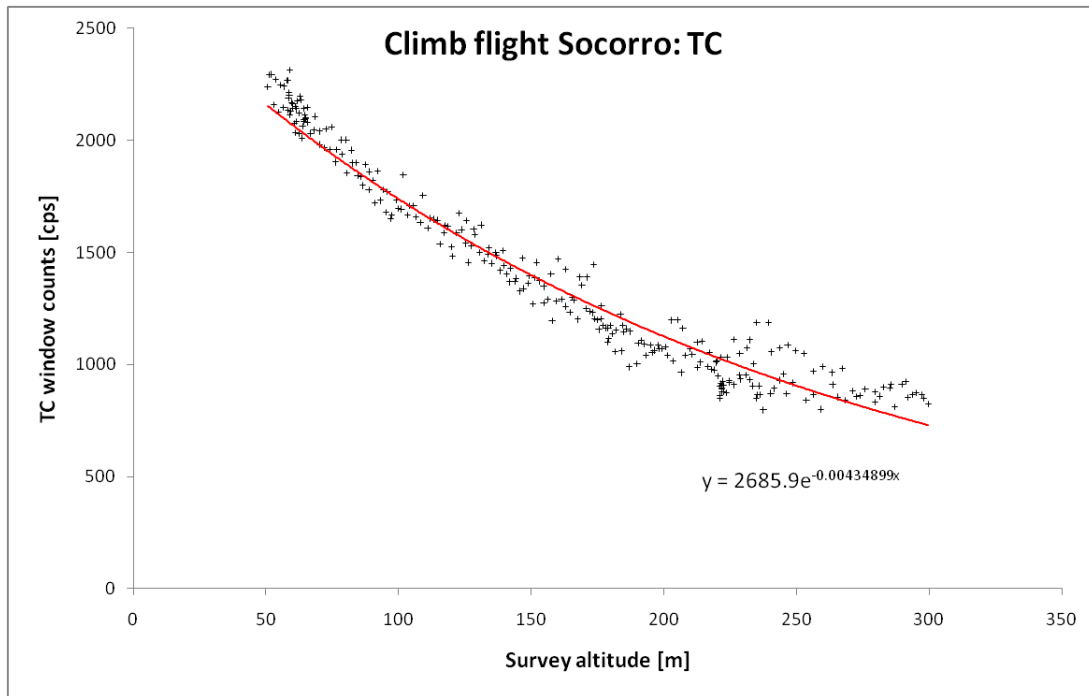


Figure 4.11: Flight altitude vs. Total Count window counts for a climb-flight over Socorro Island

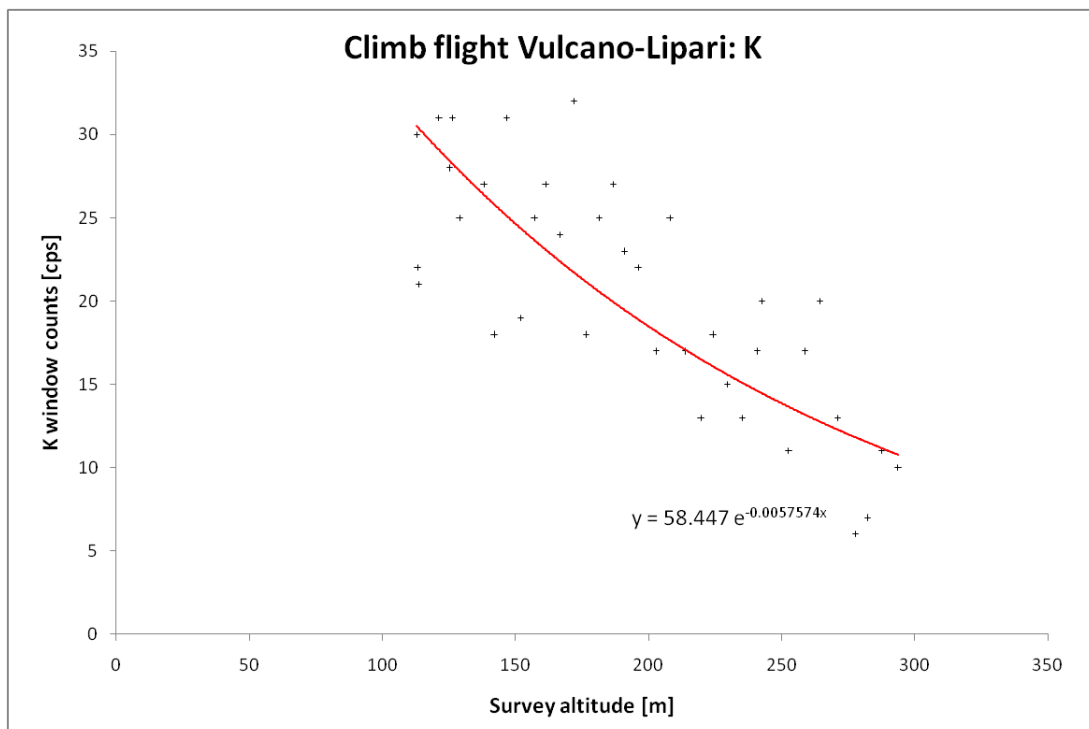


Figure 4.12: Flight altitude vs. Potassium window-counts for a climb-flight over Vulcano Island

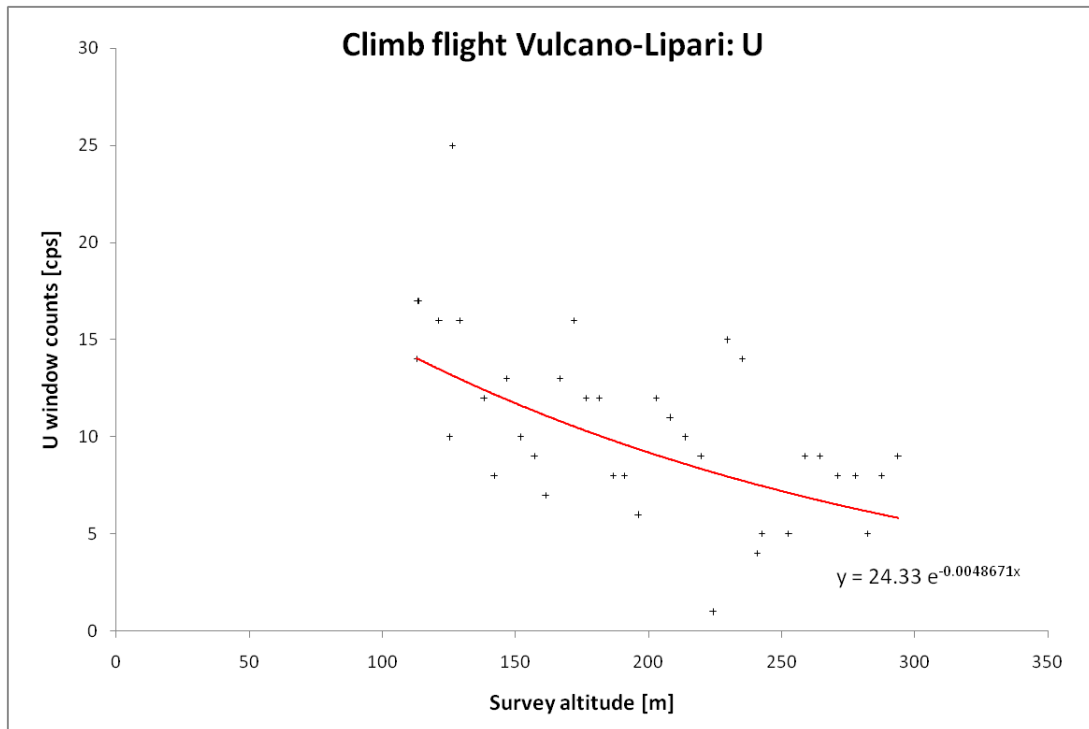


Figure 4.13: Flight altitude vs. Uranium window-counts for a climb-flight over Vulcano Island

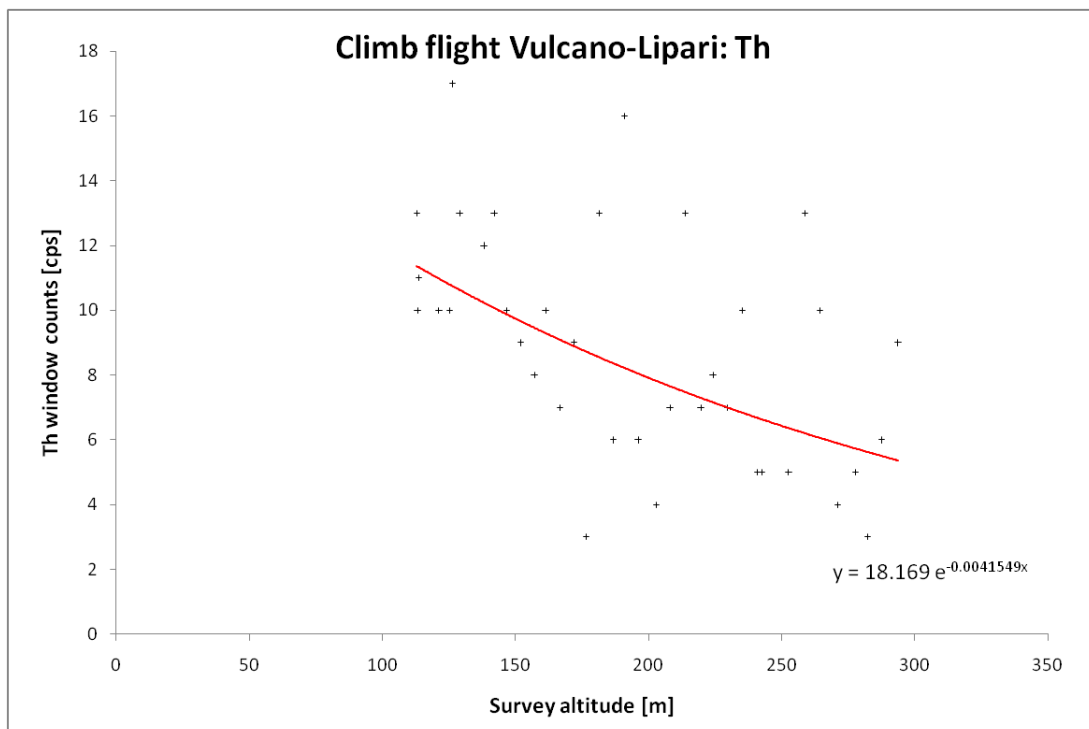


Figure 4.14: Flight altitude vs. Thorium window-counts for a climb-flight over Vulcano Island

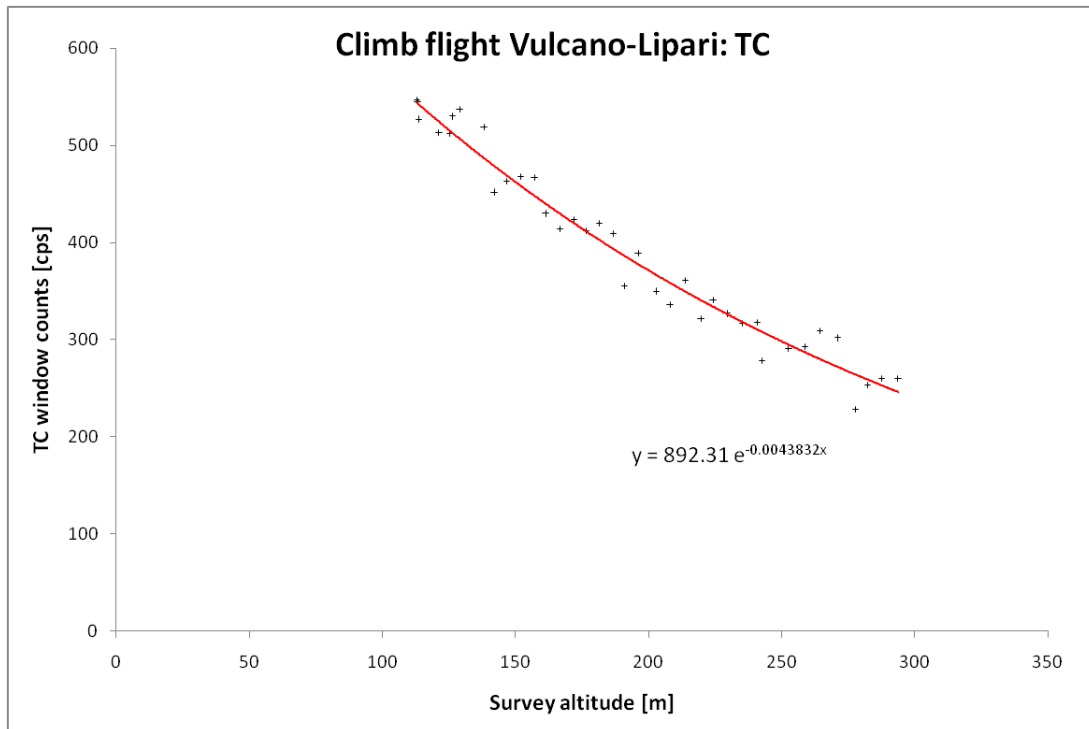


Figure 4.15: Flight altitude vs. Total Count window-counts for a climb-flight over Vulcano Island

4.1.8 Reduction to elemental concentrations

[IAEA 2003]; [Minty et al. 1997]

Count rates from gamma-ray spectrometric surveys depend not only on the concentration of the radioelements on the ground, but also on crystal volume, detector efficiency and nominal height of the particular survey. To make data from different surveys comparable, it is necessary to reduce the airborne count rates to mean ground-level abundances of the radioelements. This can be derived by dividing each of the corrected channel count rates by a sensitivity coefficient, which can be determined by measuring concentrations of the radioelements over a calibration range. The determination of the sensitivity coefficients has been discussed in subsection 3.2.2.

4.1.9 Levelling the data

[Minty et al. 1997]

Changes in the radiation output from the Earth's surface during the course of a survey, as well as all assumptions that have to be taken during the preceding processing steps, cause unwanted changes in the measured radiation both along and between lines. This results in long-wavelength "level-shift" errors, which can be corrected by one or more of the following three methods:

- **Crossover ties:** Tie lines are flown perpendicular to the flight lines and are used to correlate the data and minimise differences at their intersection points.
- **Between-channel correlation** information is used to remove residual background estimation errors from the uranium window. This works only with the assumption of a good correlation between U and Th concentrations in nature.
- **Microlevelling:** With the use of directional grid filtering techniques, residual errors can be removed from gridded data and then the filtered grids can be used to correct the line data.

4.2 Data Processing with Praga 4 radiometric processing software

[Praga Manual]

4.2.1 Setting the project

Praga 4 radiometric processing software is basically programmed for the processing of data collected by Pico Envirotec Inc. spectrometers and expects data to have a resolution of at least 256 channels. Furthermore, radiometric processing requires additional data values such as life time and STP (standard temperature and pressure) altitude. If one of these is missing, Praga 4 uses default values. After a Praga project has been created, some additional inputs have to be entered. Else, Praga will not provide accurate results.

At first, the range of valid spectrum channels has to be defined. This is especially important, as data containing other than radiometric information can have high impact on the results or can even completely disable processes like Compton removal. It is also advisable to browse through spectra and check if all values (like XY-position, altitude, temperature, pressure and cosmic counts) are as expected. In the next step, parameters which influence the processing have to be entered. These are calibration constants like sensitivity coefficients, stripping coefficients, altitude increase of the stripping coefficients, attenuation coefficients, and cosmic- and aircraft background counts in each of the spectrum windows. Calibration constants should be determined at regular intervals and anyway, if the equipment is modified. Praga 4 expects the calibration constants to be entered as for a detector system with 8 downward-crystals. If less than 8 crystals were used, the detector volume has to be changed in the Input/Output settings dialog. The quality of any processing-results strongly depends on the quality of the calibration constants!

4.2.2 Channel to energy calibration

Almost all processing steps require proper channel-to-energy calibration. The calibration is achieved as follows: At first, a smooth averaged spectrum has to be computed, which represents the whole dataset. Afterwards, the peak positions of the averaged spectrum are compared to those of a model spectrum. Peak positions of the averaged spectrum and of the model spectrum should match each other. If they don't, channel-to-energy calibration has to be performed by one of two different methods. Input spectra can either be physically stretched to fit the model spectrum or the model spectrum is stretched to fit input spectra. The second method implies that peak positions change and that the channel width does not necessarily have constant value across the spectrum. It's the method which is recommended by Pico Envirotec Inc.

As a result of proper channel-to-energy calibration, input and model spectra should match each other and peak positions should be at the expected positions of natural nuclides. To investigate the energy-calibrated spectra and to identify photopeaks of natural and man-made nuclides, spectra should be sufficiently stacked.

Praga provides different tools to control the effects of energy calibration and to identify the presence of man-made nuclides in the spectra. For example the residual spectrum (difference between input and fitted model spectrum) can be computed. Strong deviations of the residual spectrum from values close to zero can be an indication of the presence of man-made nuclides. Furthermore it should be checked if peak positions of major photopeaks fall into standard windows.

The presence of man-made nuclides can also be tested in the spectrum analysis mode, where three different tasks are offered:

- **R/Compton** shows spectra with the Compton continuum removed.
- **PeakDeco** approximates the spectrum photopeaks by Gaussian functions and photopeak positions as well as stability of the spectrum photopeaks across the dataset can be investigated.
- **Peak Plot** is based on the **PeakDeco** functionality, with the difference that only a small dash is plotted at the photopeak position. When browsing through spectra, the previous dashes remain on the screen, resulting in a scatter-plot where major photopeaks stand out.

All three tasks are better used in combination with the "Nuclide Info" tool, which shows expected peak positions of natural and man-made nuclides as well as the position of the standard windows.

4.2.3 Principal component analysis and spectrum restoration (smoothing)

Principal component analysis and spectrum restoration can be performed in two steps. If one has decided upon the type of PCA (NASVD or MNF or both) and the range of

valid spectrum channels has been selected, eigenvalues and eigenvectors will be computed in the next processing job. In the interactive mode, results of the PCA process can be examined. This serves as a perfect tool for quality control since any signatures, which are not caused by natural radioactive sources, will be included in eigenvectors. By browsing through eigenvectors, data can be examined for example for signs of spectrometer drift (eigenvectors would reveal peak movement) or unexpected (man-made) radionuclides. It is faster to search through 256 (or 512) eigenvectors, than to investigate all spectra of the whole dataset.

If the results of principle component analysis are satisfying and the eigenvectors are found to be correct, spectra can be recomputed and smoothed by selecting the required eigenvectors. A rule of thumb is to use $1 + 2 \cdot N$ eigenvectors, where N is the number of radionuclides present in the data (usually K, U, Th, Rn). Generally, the first eigenvector represents the average spectrum, the next N eigenvectors are mixtures of responses at main altitude and the following N eigenvectors represent response variations due to changes in altitude. Therefore, in a natural geologic environment, at least 9 eigenvectors should be included in the restoration process, and 11, if Cs fall-out is present. However, in the case of bad data quality, it is recommended to use more eigenvectors to prevent signal loss.

Since PCA restoration reduces noise especially in the low-energy channels, some radon detection techniques profit from the use of PCA smoothed spectra as primary input spectra.

4.2.4 Standard window based processing

Standard window based processing is done during any processing job and there is no possibility to switch off any part of this process. Praga 4 processing software is designed for full-spectrum processing and therefore the full spectrum must be the input of any processing task. Standard window processing can also be applied on PCA smoothed spectra.

Before starting a processing job, required outputs must be selected in the Input/Output settings dialog. The following outputs are possible:

- Raw window count-rates of the four standard windows (TC, K, U and Th) in [cps]
- Corrected window count-rates of the four standard windows in [cps], which are corrected for background, stripping and altitude
- Corrected window count-rates of the three radioelement windows (K, U and Th) which are converted to radioelement concentrations in [%] for K and [ppm] for U and Th or to activities in [Bq/kg]; the corrected TC-window is converted to the dose rate
- Absorbed dose rate in air in [nGy/h] or [pGy/s] and exposure rates in [μ R/h] or [pA/kg], 1m above the ground; these are computed using the K, U and Th concentrations.

4.2.5 Radon detection and removal

Since the performance of a radon removal technique strongly depends on the dataset, the spectrometer and the survey area, none of the methods seems to be universally valid. For this reason, Praga 4 offers several different radon detection methods:

- Full-spectrum method
- Spectral-ratio method using the ^{214}Bi 609 keV photopeak
- Spectral-ratio method using the ^{214}Pb 352 keV photopeak
- Spectral-ratio with combination of ^{214}Bi and ^{214}Pb methods
- Upward looking detector method

The radon removal process can be run in two stages, the analysis stage and the removal stage. In the analysis stage, radon contribution to the individual spectra is computed and the radon anomaly along the whole dataset is output into database. Depending on the chosen radon detection method, different degree of stacking or the use of PCA smoothed spectra can enhance the quality of the results. During the next standard window processing task, radon anomaly is loaded from database into memory, smoothed along the flight line, approximated by a polynomial, and is then removed as part of the background correction.

4.3 Basic models

The modelling of gamma-ray fields provides an important insight into the physics of the gamma-ray spectrometric method and the understanding of this method is necessary for proper data processing and interpretation. Two basic types of models are used in gamma-ray spectroscopy:

4.3.1 Physical models

[Minty et al. 1997], [IAEA 2003]

The simplest assumption for modelling gamma-rays is based on mono-energetic (un-scattered) radiation and a two-layer model with the Earth as an infinite homogeneously radioactive half space which is overlain by non-radioactive air. Both, Earth and air are assumed to have constant density. Based on the radiation output of an elementary point source, a radiation intensity law can be computed for various source types by integrating over the corresponding source geometries.

The amount of radiation dI that is absorbed by an absorber of thickness dx is given by:

$$dI = -\mu I dx$$

$$I = I_0 e^{-\mu x}$$

μ ... linear attenuation coefficient

I ... radiation intensity

Additionally, gamma-rays are subject to the inverse square law of attenuation of point sources of electromagnetic radiation.

$$I \propto \frac{e^{-\mu r}}{r^2}$$

r ... distance between source and detector

For our two-layer model and with the assumption that the detector has no directionally dependent sensitivity we get [cp. Minty et al. 1997]:

$$dI = \frac{A\epsilon}{4\pi R^2} e^{-\mu_e r_e} e^{-\mu_a r_a} N dV$$

A ... effective cross-sectional area of a spherical detector

$N dV$... number of γ -rays of energy E_0 emitted per second by the volume element dV

ϵ ... photopeak efficiency of the detector for γ -rays of energy E_0

μ_e, μ_a ... linear attenuation coefficients for the Earth and air respectively

r_e, r_a ... distances through the Earth and air that the γ -rays travel ($R = r_e + r_a$)

To obtain the photopeak responses due to particular source types, the preceding equation is integrated over the corresponding source geometries.

4.3.2 Statistical models

[Minty 1997]

Statistical models are used to estimate or predict errors. Radioactive decay is a statistical process since each atomic disintegration occurs independently of every other decay event. Therefore, the number of measured gamma-rays resulting from radioactive decay in the source rock follows a Poisson statistical distribution with the special property that the standard deviation σ is equal to the square root of the mean count rate n :

$$\sigma = \sqrt{n}$$

The variance v , in turn, is the mean square deviation, which is equal to the square of the standard deviation:

$$v = \sigma^2 = n$$

The standard deviation of a function $f(x, y)$ of two variables x and y , with known standard deviations σ_x and σ_y associated with the variables, can be computed by:

$$\sigma_f = \sqrt{\left|\frac{\partial f}{\partial x}\right|^2 (\sigma_x)^2 + \left|\frac{\partial f}{\partial y}\right|^2 (\sigma_y)^2}$$

In gamma-ray spectroscopy, we assume that all errors are due to the statistical nature of radioactive decay and with the help of the preceding equations we can estimate errors in our measurements. During processing, counting errors are propagated into the estimates of elemental abundances and errors in raw data are thus amplified by the processing procedures.

4.4 Data presentation and interpretation

After processing of gamma-ray survey data has been completed, results can be presented in a multitude of ways to facilitate interpretation. None of the methods is universally applicable and it's often necessary to test several different gridding- and image presentation techniques to find the most suitable.

To prepare the processed data for interpretation, the general procedure during this work was to interpolate data to a regular grid with Golden Software Surfer (gridding, contouring and surface mapping software), load the grids to ArcMap (ArcGIS, ESRI Software), create pseudo-colour- and ternary radioelement maps and compare these with satellite images and geologic maps to find dominant geologic structures and shapes. A more detailed description of the individual image rendition and interpretation steps is given in the following subsections.

4.4.1 Gridding

[IAEA 2003]

Gridding is the interpolation of original, unevenly distributed, data to a regular rectangular mesh of values. A multitude of different gridding algorithms is available, but only few of them are able to deal with the inherent anisotropy of airborne survey data. The problem in airborne surveying is the high sample density along the flight lines (~ 30 m sample interval) compared to the low sample density across the flight lines (100 - 250 m sample interval). Two gridding algorithms are proposed by the IAEA [IAEA 2003] to be the most suitable for airborne surveying:

- **Bi-directional gridding** uses spline interpolation both, along and across the flight lines in combination with a low pass filter along the flight lines, to avoid aliasing. As this method is not included in the gridding selection of Surfer, it was not possible to test the performance of the technique for the present dataset.

- **Minimum curvature gridding** uses two-dimensional spline interpolation to fit the survey data to a grid surface, with the constraint that the curvature of the surface has to be a minimum. Only samples which lie within a predefined search radius are included in the interpolation and an inverse distance function is used to give them distance-dependant weights. At least two adjacent flight lines should lie within the search radius. A disadvantage of this method is its tendency to extrapolate extremely high or low values in areas of no data. For this reason, Surfer offers the special option to define a "fault". A "fault" is a polygon or polyline, acting as barrier when gridding.

A third algorithm, **Kriging**, seems to be very well suited for gamma-ray spectrometric data, but has its problems with the anisotropy in sample density of airborne data [IAEA 2003]:

Kriging is ideally suited for gamma ray data as it considers three separate components: a regional trend, a spatially dependent component and a noise component [IAEA 2003]. It is able to deal with the stochastic nature of radioactive decay, as it separates the randomly distributed noise from the spatially dependent signal.

For the present data, Kriging yielded better results than Minimum Curvature gridding. It turned out that the ideal setting for gridding was Kriging with grid node spacing in the range of flight line spacing and a search radius, which exceeds the grid node spacing by approximately 50m.

4.4.2 Pseudo-colour radioelement maps

[IAEA 2003]

Pseudo-colour radioelement maps display the spatial distribution of radioelement abundance as coloured shades. The colours should be chosen in a way that the variation in colour is intuitively related to variations in radioelement concentration. A good colour bar would, for example, be shaded from blue over green, yellow and orange to red, whereas blue displays the lowest and red the highest radioelement concentrations.

Pseudo-colour images can be easily created in ArcMap. A histogram can be computed, which displays the occurrence of concentrations over the whole range of values. Different settings then allow classification (e.g. equal interval, natural breaks, quantiles,...), exclusion of data values and change of colour-bar.

4.4.3 Ternary radioelement maps

[IAEA 2003]

Ternary radioelement maps are colour composite images and are commonly used to display the relation of K-Th, K-U, U-Th or K-U-Th in one image. The red, green and blue phosphors of the display device are modulated in proportion to the respective radioelement concentrations, whereas red is used to display the potassium channel, green for thorium and blue for uranium. Combinations of the radioelement concentrations are displayed as combinations of the red, green and blue phosphors. If all phosphors are

off, the resulting colour is black, if all phosphors reach their maximum, the resulting colour is white. Equal amounts of K, U and Th result in grey shades ranging from black to white. Same amounts of K and Th but no U is displayed as yellow, while same amounts of K and U but no Th is displayed as magenta and same amounts of Th and U but no K is displayed as cyan.

Figure 4.16 shows the RGB colour-cube, a model to display the generation of colours out of red, green and blue.

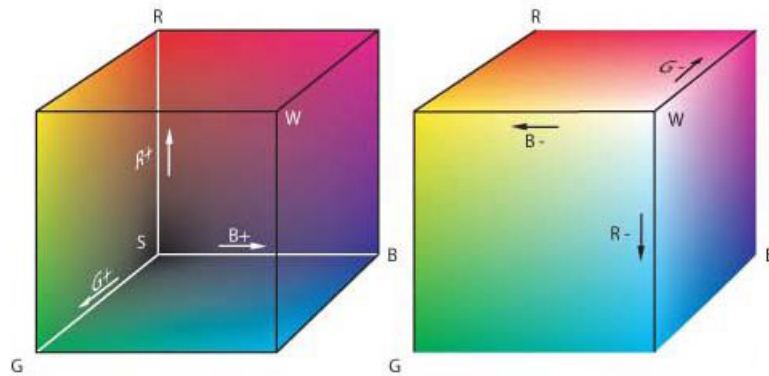


Figure 4.16: RGB colour-cube; creator: Horst Frank

Ternary radioelement maps often show contours and shapes, which could not be identified from the pseudo-colour image alone.

4.4.4 Georeferencing and map projections

Prior to interpreting gamma-ray spectrometric data, it may be necessary to transform it to another coordinate system, to render comparison with other datasets, geologic maps, topographic maps and satellite images.

For the present project, all datasets and maps were projected to the Universal Transverse Mercator System (UTM) on the base of the WGS84-ellipsoid. The World Geodetic System 1984 (WGS 84) is a geocentric datum where the centre of the Earth is defined as the true centre of gravity. The UTM system uses a series of 60 zones around the Earth, each referring to 6° of longitude. The UTM zone for the Aeolian Islands is 33N; the UTM zone for Socorro Island is 12N.

4.4.5 Integration with other datasets

As with every other geophysical method, it's impossible to interpret gamma-ray spectrometric data without any other additional information. The integrated interpretation with complementary datasets is therefore strongly recommended:

- **Aeromagnetic data:** The residual magnetic anomaly field measured at airborne survey heights is caused by sources which can be located in great depths up to

10 km [IAEA 2003]. Thus, the magnetic anomaly data does not reflect surface geology and therefore magnetic anomaly patterns generally won't coincide with radiometric anomalies. Anyhow, a joint interpretation of airborne magnetic and radiometric data of volcanoes can provide a bulk of useful information about the volcano, as magnetic data reflects the inner structure of the edifice and radiometric data reflects the eruptive products at the surface.

- **Airborne electromagnetic data:** Airborne electromagnetic data reflects the conductivity of the ground with a penetration range of several cm up to hundreds of m, depending on frequency of the survey and conductivity of the subsurface. Penetration depth decreases with increasing frequency and increasing conductivity and therefore high-frequency surveys reflect near-surface conductivities. Thus, electromagnetic anomalies may correlate with radiometric anomalies and consequently with surface geology.
- **Ground radiometric surveys:** Ground radiometric surveys are performed with equipment, which is quite similar to airborne equipment, apart from that it is smaller. Airborne and ground radiometric surveys can complement each other, as airborne surveying provides a good overview of radioelement distribution over the whole survey area and ground surveying serves as verification of airborne results.
- **Pre-existing geologic maps:** For the interpretation of gamma-ray spectrometric data it's particularly important to compare intermediate results with pre-existing geologic maps. Deviations of gamma-ray anomalies from geologic units can be a sign of disequilibrium, weathering, mineralisation or mobilisation, but it's also possible, especially in remote areas, that the assignment of geologic units has to be reconsidered.
- **Satellite imagery:** Satellite images are detailed renditions of the surface and can be quite useful for delineating unit boundaries. Furthermore, they are a great help in interpreting gamma-ray data, as they also display vegetation and human settlement.

4.4.6 Creating Shapefiles

After the gridded gamma-ray spectrometric data has been displayed in a way that variations in radioelement concentration are emphasized and easily visible, the dataset can be investigated for unit boundaries and dominant shapes and structures of geologic origin.

Generally, areas of similar radioelement concentration can be considered to belong to the same geologic unit. It's important to investigate variation of all three radioelements, to test different colour-codes, compute band ratios (ratio of two radioelement grids), compare ternary- and pseudo-colour-maps and examine radioelement concentrations for strong deviations from mean crustal abundances. Once some dominant shapes have been identified, discrete units can be manually delimited with the ArcMap Editor

tool by creating vector polygons. In some cases it may be difficult to find the exact course of unit boundaries and it's therefore strongly recommended to compare the radiometric maps to pre-existing geologic maps, satellite images or aerial photographs. In ArcMap, the polygons can be saved into a single shapefile, where they can later be distinguished by attributes which can be entered into the "Attribute table". Such attributes are for example a specific number of the polygon, the name of the feature, the name of the unit to which it belongs, mean, standard deviation, minimum and maximum of radioelement concentrations within the polygon, and so on.

4.4.7 Statistical analysis

Once the whole survey area has been subdivided into polygons, which correlate with geologic units and areas of similar radioelement characteristic, the radiometric properties of each polygon can be investigated by intersecting the survey data with the polygons. It's better to use original data instead of gridded data for intersection, because gridding may produce data values which exceed the range of the original data. As a result of the intersection, data samples are resorted according to the polygons and so a statistical analysis is possible for each polygon.

The main part of statistical analysis is the computation of mean and standard deviation, what can be easily done with any spreadsheet software. Furthermore, it can be useful to investigate radioelement concentrations for minima and maxima within each polygon.

4.4.8 Reassignment of geologic units

After mean and standard deviation have been computed for each polygon, polygons with similar values for mean and standard deviation of all three radioelements can be assigned to the same radiometric cycle and, with caution, to the same geologic unit. In this stage of interpretation it's especially important to compare intermediate results with results of other surveys and pre-existing geologic maps. In the special case of interpreting gamma-ray spectrometric data of volcanoes, conclusions can be drawn concerning eruptive cycles, changes in magma composition, magma differentiation and spreading of eruptive products.

4.4.9 Reconsideration of results with ternary radioelement diagrams

A ternary radioelement diagram is an equilateral triangular diagram, where each side of the triangle gives the percentage of K, U and Th, respectively. A sum-normalization

is used to compute relative concentrations of K, U and Th [IAEA 2003]:

$$K_n = \frac{K}{K + U + Th}$$

$$U_n = \frac{U}{K + U + Th}$$

$$Th_n = \frac{Th}{K + U + Th}$$

K ... potassium ground concentration [%]
U ... uranium ground concentration [ppm]
Th ... thorium ground concentration [ppm]

As the relative abundance of thorium is usually higher than the abundance of potassium and uranium, a slightly different normalization technique can be used, which scales the radioelement abundances to approximately equal range [cp. IAEA 2003]:

$$K_n = \frac{K}{K + U + \frac{Th}{4}}$$

$$U_n = \frac{U}{K + U + \frac{Th}{4}}$$

$$Th_n = \frac{\frac{Th}{4}}{K + U + \frac{Th}{4}}$$

Relative concentrations can be computed for the mean ground concentrations of K, U and Th within each Polygon and are then plotted at the respective positions in the ternary diagram. As a result, each dot (or cross) in the diagram represents mean radioelement concentrations of the respective polygon and polygons, which have been assigned to the same geologic unit, should lie close together in the ternary diagram.

An example of a ternary diagram is shown in Figure 4.17. All ternary radioelement diagrams in this work have been created with Tri-plot, a Microsoft® Excel spreadsheet by David Graham and Nicholas Midgley [Graham & Midgley 2000].

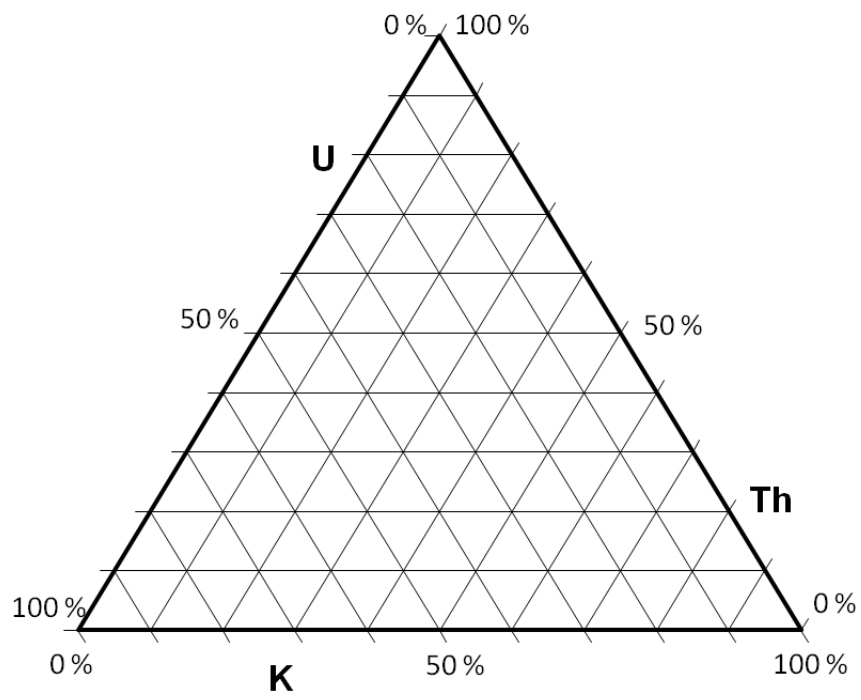


Figure 4.17: Ternary radioelement diagram

Chapter 5

Gamma-rays and Volcanoes

5.1 Volcán Evermann, Socorro Island, Mexico

Socorro Island is located in the eastern Pacific Ocean at 18°47'N and 110°58'W, 700 km off the coast of mainland Mexico at the intersection of the Clarion Fracture Zone and the Mathematician Ridge System. With an extent of 130 km² it is the largest island of the Revillagigedo Archipelago, which consists of the four islands Socorro, Clarión, San Benedicto and Roca Partida, all of them being volcanic in origin. These four islands as well as a group of several seamounts make up the Mathematician Ridge, an abandoned mid-ocean ridge spreading centre which was active from 6.5 Ma to 3.15 Ma before present [Siebe et al. 1995].

Socorro Island is the emergent portion of a large shield volcano, Volcán Evermann, which rises from the seafloor at a depth of about 3 km to the summit of the volcano at 1050 m above sea level [Carballido-Sanchez 1994] and has a submarine slope of a little less than 10 degrees [Siebe et al. 1995]. With a basal radius of 24 km and the assumption that the volcano is a perfect cone, the total volume of the volcano makes up approximately 2400 km³. Hence the subaerial portion of Volcán Evermann makes up about 2 vol. % of the total edifice.

Volcanism in the Revillagigedo Archipelago produced primarily alkali olivine basalts, followed by eruptions of soda-rich rhyolite [Siebe et al. 1995]. Therefore, Volcán Evermann could be better described as a composite volcano, with an early shield-building stage, characterised by basaltic effusive eruptions, and late extensive pyroclastic peralkaline eruptions [Carballido-Sanchez 1994]. The domination of subaerial silicic peralkaline eruptions makes Socorro Island virtually unique in the Pacific Ocean. Peralkaline volcanic rocks show a molar excess of $(Na_2O + K_2O)$ over Al_2O_3 whereas the opposite characteristic is usual in the Earth's crust [Carballido-Sanchez 1994]. Samples from Socorro Island taken by *Bohrson and Reid* showed a peralkalinity index $(= (Na_2O + K_2O)/Al_2O_3)$ of 1.1 - 2.2 [Bohrson & Reid 1998]. According to *Carballido-Sanchez*, almost 90 % of the peralkaline products on Socorro Island

are of pantelleritic¹ composition. Examples of other islands that have erupted peralkaline lavas are Pantelleria, the Canary Islands and the Azores among others [Carballido-Sanchez 1994].

It is supposed that peralkaline rocks make up 80- 90 % of the total subaerial volume of rocks exposed on Socorro Island. With the assumption that the submarine portion of the volcano is composed mainly of basalts, peralkaline rhyolitic rocks make up only 1.5 vol. % of the volcanic edifice. Only little is known about the submarine part of the volcano.

The eruptive history of Socorro Island has been divided into pre-, syn- and post-caldera stages [cp. Bohrson et al. 1996], whereas the postcaldera stage has been subdivided by *Bryan* into Cerro Evermann eruptives and Lomas Coloradas eruptives [cp. Carballido-Sanchez 1994]. A sketch-map of the classification made by *Bryan* is shown in figure 5.1.

The bulk of the volcanic edifice, which is submarine, erupted before the formation of a small caldera and is basaltic in origin. The precaldra units on Socorro Island erupted in two episodes of activity. The first episode of eruptions was mainly effusive. The volcano built up from the seafloor, which corresponds to the shield-building stage of volcanism. The second stage of precaldra eruptions was dominated by explosive eruptions and deposition of peralkaline pyroclastics. [Carballido-Sanchez 1994]

The oldest subaerially exposed units of Socorro Island are precaldra alkaline basalts to comendites², which are confined to the base of a sea cliff at the eastern part of the island [Taran et al. 2002, Bohrson & Reid 1998] and range in age between 540 and 370 ka. Most of the subaerially exposed pre- and syncaldra rocks are silicic peralkaline ignimbrites, which are commonly holocrystalline (= completely crystalline), nonfragmental (= not composed of fragments of pre-existing rocks and minerals), nonvesicular lava-like deposits that lack inclusions or lithic fragments [Bohrson et al. 1996]. *Bohrson et al.* found some evidence, that silicic pre- and syncaldra phases on Socorro Island were dominated by explosive eruptions with low eruption columns.

The remainder of a former caldera wall can be found on the southeastern side of the summit at approximately 600m elevation. The size of the steep escarpment is consistent with a former caldera dimension of about 4.5 x 3.8 km, which is typical for peralkaline volcanoes [cp. Bohrson et al. 1996]. Caldera formation occurred probably between 370 and 182 ka and was followed by up to 200 kyr of quiescence. "The presence of a small summit caldera on Socorro suggests that the silicic magma reservoir was shallow, probably located within the volcanic edifice or the upper oceanic crust." [Bohrson et al. 1996]

Caldera formation was followed by a change in eruptive style from predominantly explosive to predominantly effusive. [Bohrson et al. 1996]

Rocks of the postcaldera stage had been subdivided into the Cerro Evermann- and Lomas Coloradas Formation, which erupted contemporaneously between 180 and 15

¹Pantellerite: Peralkaline rhyolite, more mafic than comendite

²Comendite: Peralkaline rhyolite, more felsic than pantellerite

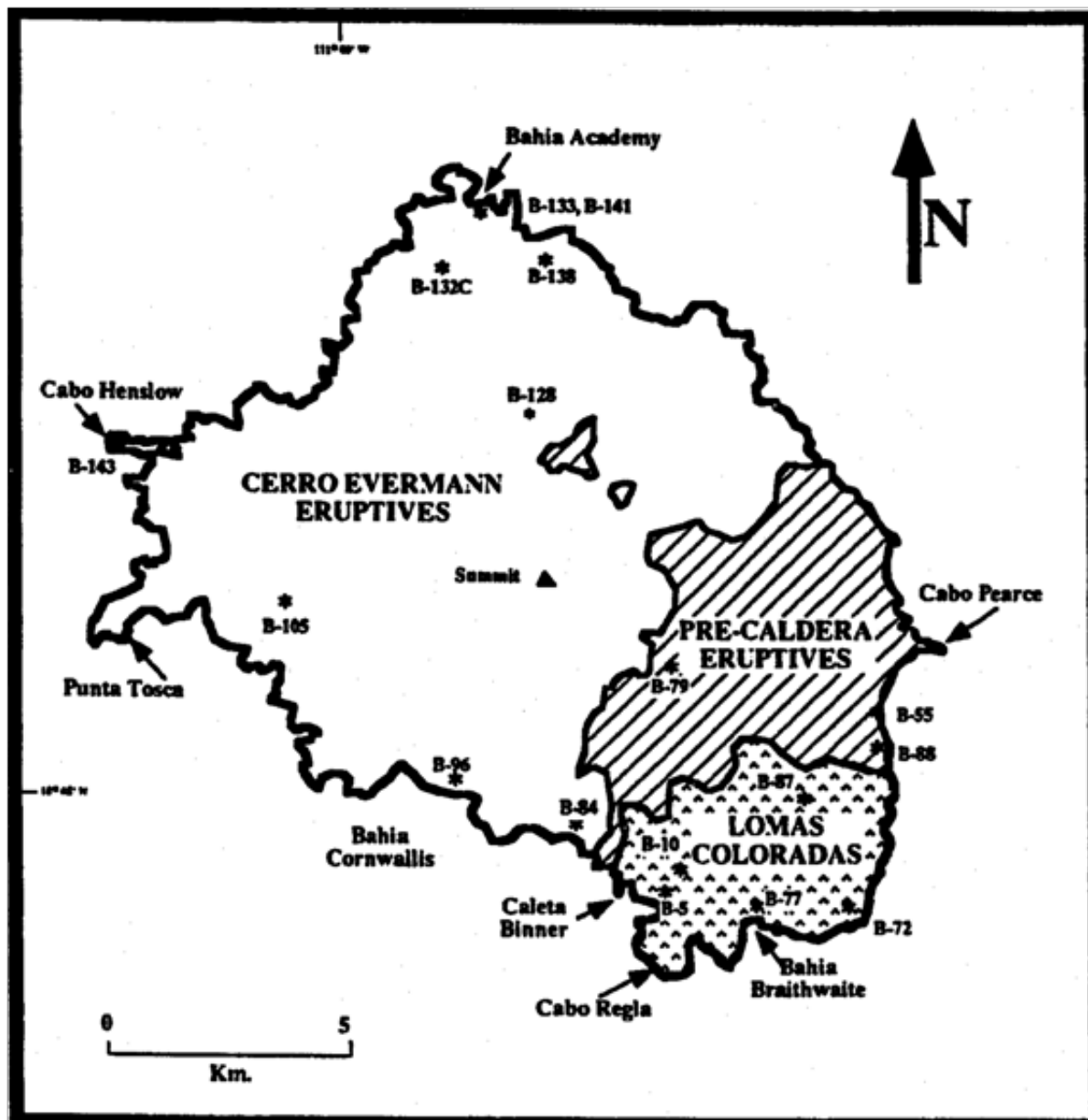


Figure 5.1: Geologic sketch-map of Socorro Island after Bryan [cp. Carballido-Sanchez 1994]

ka (Cerro Evermann) and 150 and 70 ka (Lomas Coloradas), respectively [Bohrson et al. 1996]. Rocks of the Cerro Evermann Formation are pyroclastics, lava flows, and lava domes of peralkaline composition, which are exposed in the caldera and at the northern, western and southern flanks of the volcano. These are primarily trachytes, comendites and pantellerites [Carballido-Sanchez 1994]. The lava flows and cinder cones of the Lomas Coloradas formation are exposed at the south-eastern part of the island and are composed of basalt, mugearite and hawaiite [Carballido-Sanchez 1994]. "Contemporaneous eruption of peralkaline-rhyolitic and basaltic magmas during the post-caldera phase can best be explained by a stratified magma chamber composed of soda-rhyolite overlying a column of basaltic magma." [Siebe et al. 1995]

Morphologically, the subaerially exposed rocks on Socorro Island can be classified as lava-flows, domes, pyroclastic flows, air-fall pyroclastics and cinder cones. The lava-flows on Socorro Island can be of both, basaltic and peralkaline composition, whereas the pyroclastic flows are exclusively peralkaline [Carballido-Sanchez 1994]. Cinder cones all are basaltic in composition (except for one) and are confined to the Lomas Coloradas unit. The domes, on the other hand, are exclusively peralkaline. Air-fall pyroclastics are both, peralkaline and basaltic, whereas the basaltic ash, cinder, spatter and bomb deposits are all (except for one deposit in the Bahia Academy area) restricted to the Lomas Coloradas area. [Carballido-Sanchez 1994]

Bryan [cp. Carballido-Sanchez 1994] identified three major zones of fractures that intersect on Socorro Island. One zone has a north-south orientation and extends from the summit of Volcán Evermann to Bahia Academy, which is located in the northern part of the island. A second zone is orientated in east-west direction and extends from the western coast of the island (Cabo Henslow, Punta Tosca, Caleta Grayson) to the summit area of Volcán Evermann. The third zone is located in the southern part of the island and shows approximately northwest-southeast orientation.

According to *Bohrson and Reid*, three different conditions are required for the formation of silicic peralkaline magmas: a mildly extensional tectonic setting, a shallow magma reservoir and availability of parental transitional to mildly alkalic basalt [Bohrson & Reid 1997]. The formation of silicic peralkaline magmas can be explained by three different mechanisms: Fractional crystallization of transitional to mildly alkalic basalt, partial melting of mafic intrusive rock and volatile complexing and transport in association with one of these [Bohrson & Reid 1997]. The most likely mechanism of formation for Socorro Island is a moderate degree of partial melting of intrusive alkalic basalt and associated crystal cumulates followed by crystal fractionation.

Calculation of eruption rates for the submarine and the subaerial parts of the volcanic edifice suggests that either subaerial eruption rates are less than submarine eruption rates or that the growth of the volcano has continued to be dominantly submarine. Comparison of eruption rates of other isolated ocean islands suggest, that the source of alkaline magmatism associated with Socorro may be consistent with a mantle plume. [Bohrson et al. 1996]

Volcanic activity on Socorro Island has continued to the present. The first his-

torically reported eruption took place in 1848 [Carballido-Sanchez 1994], but no detailed description of the event exists. Another eruption was observed in 1896 [Carballido-Sanchez 1994], but also no further information on the eruption is available. Further small eruptions are reported for 1947 and 1951. The so long last eruption occurred in 1993 and was submarine [Siebe et al. 1995]. At the moment, fumarolic activity can be observed near the summit of Volcán Evermann.

The first visit to Socorro, which was of geologic importance, was made in 1925 by the California Academy of Science Expedition led by *G. Dallas Hanna*. Wrong determination of surface rocks led to the assumption that the archipelago was underlain by continental crust. In 1959 *Wilfried Bryan* wrote his dissertation on the geology and petrology of Clarion and Socorro Islands and later published a series of papers on the same topic. Further works were done in the 1970s and 1980s by several scientists. In 1989 *Enrique A. Carballido-Sanchez* spent some days on the island collecting rock samples. His intention was to construct a detailed geologic map at a 1:24,000 scale, with the use of vertical aerial photographs and a series of 34 samples of representative rock units. [Carballido-Sanchez 1994]

In 1995 *Claus Siebe* [Siebe et al. 1995] published a geochemical study on the 1993 submarine eruption near Socorro Island. Further works were done by *Wendy A. Bohrsen* and *Mary R. Reid* between 1995 and 1998 [Bohrson et al. 1996, Bohrson & Reid 1997, Bohrson & Reid 1998], who tried to investigate the genesis of silicic peralkaline magmas. In 1999, a seismic survey was carried out in the south-eastern part of Socorro Island with the use of five portable broadband seismometers [Valenzuela et al. 2005]. The intention was to install a seismic T-phase station on Socorro, as part of the International Monitoring System (IMS) of the Comprehensive Nuclear-Test-Ban Treaty Organization (CTBTO). Probably the so long last publication was made by *Y. A. Taran* in 2010, who analyzed the geochemistry of hydrothermal fluids on Socorro [Taran et al. 2010].

According to this short literature study, the airborne geophysical and ground geoelectric survey of the Geological Survey of Austria (GSA) in 2009 was the first detailed geophysical survey on Socorro Island.

The amount of scientific work on Socorro Island is limited by the remoteness of the island and the fact that access to the island is only possible under special permissions, which are only provided upon a formal request at least two months in advance [Carballido-Sanchez 1994]. Furthermore, when on Socorro, access to some remote places is hardly possible because of dense vegetation and lack of possibilities of transportation.

5.1.1 Geophysical survey at Socorro

[Supper et al. 2010]

Field work on Socorro Island was performed in February 2009 by the GSA in order to open up new resources for local groundwater supply. This was necessary because the

5.1.2 Processing of gamma-ray spectrometer data

Prior to processing, data was inspected for incorrect values and in particular all samples, which were taken at altitude higher than 400 m were deleted. The calibration constants and coefficients, which were used for the processing of gamma-ray data of Socorro Island are presented in table 5.1. The sensitivity and stripping coefficients, as well as the cosmic-background coefficients were determined by the GSA several years ago. The aircraft-background coefficients and the height attenuation coefficients have to be determined for each survey and in that case have been determined in subsections 4.1.4 and 4.1.7, respectively. The change of stripping coefficients with altitude is given by the IAEA [cp. IAEA 2003].

	^{40}K	^{238}U	^{232}Th	TC
Aircraft Background	26.8	9.2	6.0	40.0
Cosmic Background	0.083	0.043	0.059	1.9
Attenuation by air	-0.0062	-0.0065	-0.0079	-0.0043
Sensitivity	47.2	7.3	3.4	29.5
Stripping Coefficients	0.2	0.26	0.74	0.05
SC altitude increase	0.00049	0.00065	0.00069	0

Table 5.1: Calibration constants and coefficients for Socorro Island

The average gamma-ray spectrum of the whole survey over Socorro Island is presented in Fig. 5.3. The average spectrum was calculated by computing the mean count rate of each channel over the whole dataset.

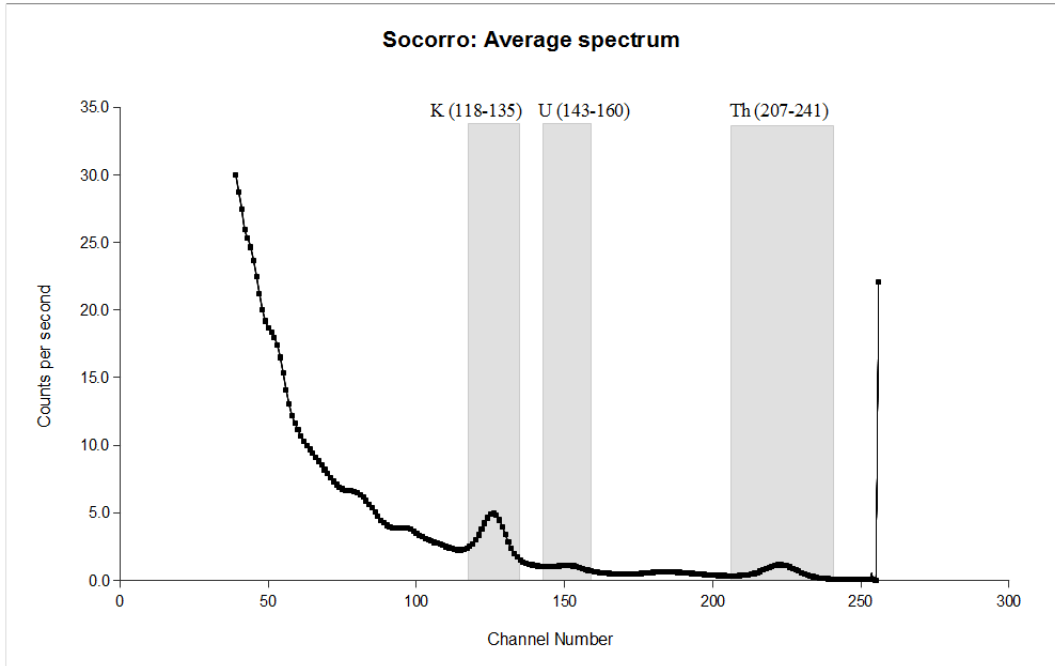


Figure 5.3: Average gamma-ray spectrum of Socorro Island

Processing was performed both, with and without the use of PCA smoothed spectra [cp. e.g. Fig. 5.7 and 5.10]. Radon removal was first run with the full-spectrum method [cp. Fig. 5.6], but this seemed to remove too much and so radon removal was run for a second time with the spectral-ratio method.

In some parts of the island (especially in the south-western part), the height-correction did not work well due to large differences in flight altitude of the helicopter between adjacent flight lines. This results in lower ground concentrations for high flight altitudes and higher ground concentrations for low flight altitudes, what can be seen as parallel stripes in the radioelement maps [cp. Fig. 5.4 and Fig. 5.8].

The best gridding results could be achieved with the gridding-method kriging. Since flight line spacing at Socorro was approximately 100 m, the grid-node spacing was also chosen to be 100 m, with a search radius of 150 m.

Interpretation of gamma-ray data of Socorro Island was performed with the combined use of radioelement maps [Fig. 5.4 - 5.10], ternary maps [Fig. 5.11 - 5.14], a detailed satellite image and several pre-existing geologic maps. Main geologic maps used for interpretation were the detailed geologic map of *Carballido-Sanchez* [Fig. 5.35], the geologic map of *Bryan* [Fig. 5.1] and the map of the Lomas Coloradas area designed by *Bohrson and Reid* [Fig. 5.36].

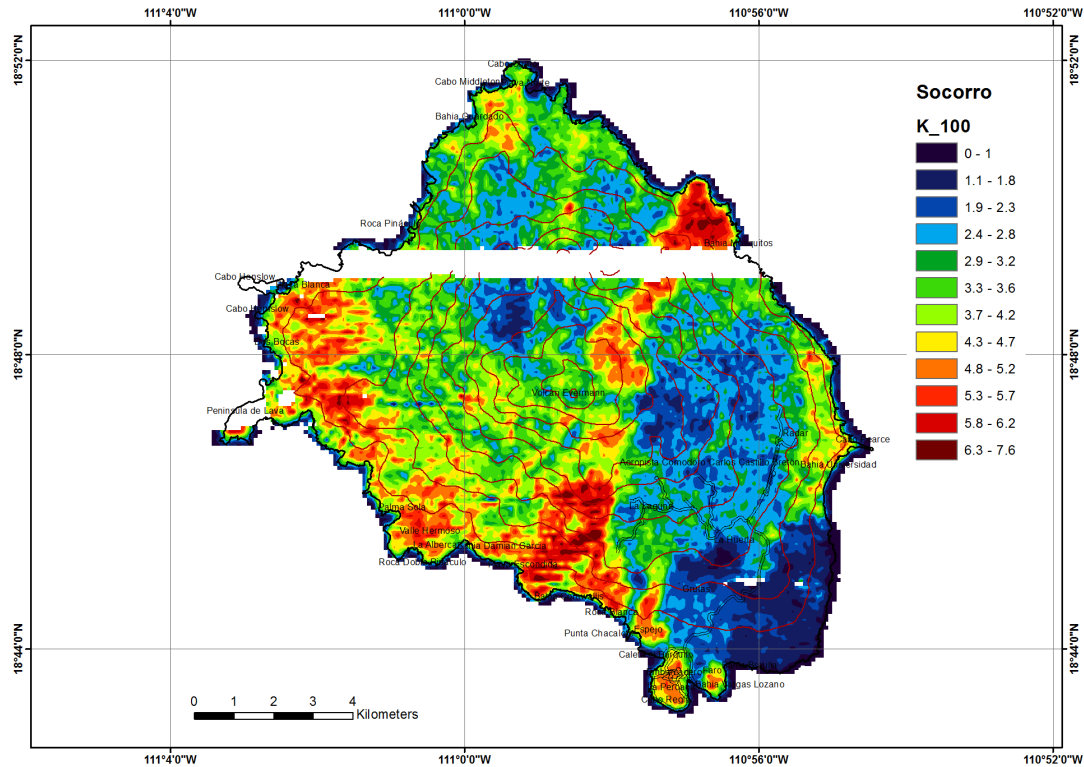


Figure 5.4: Radioelement map of Socorro Island (100 m grid); standard window based processing: Potassium [%]

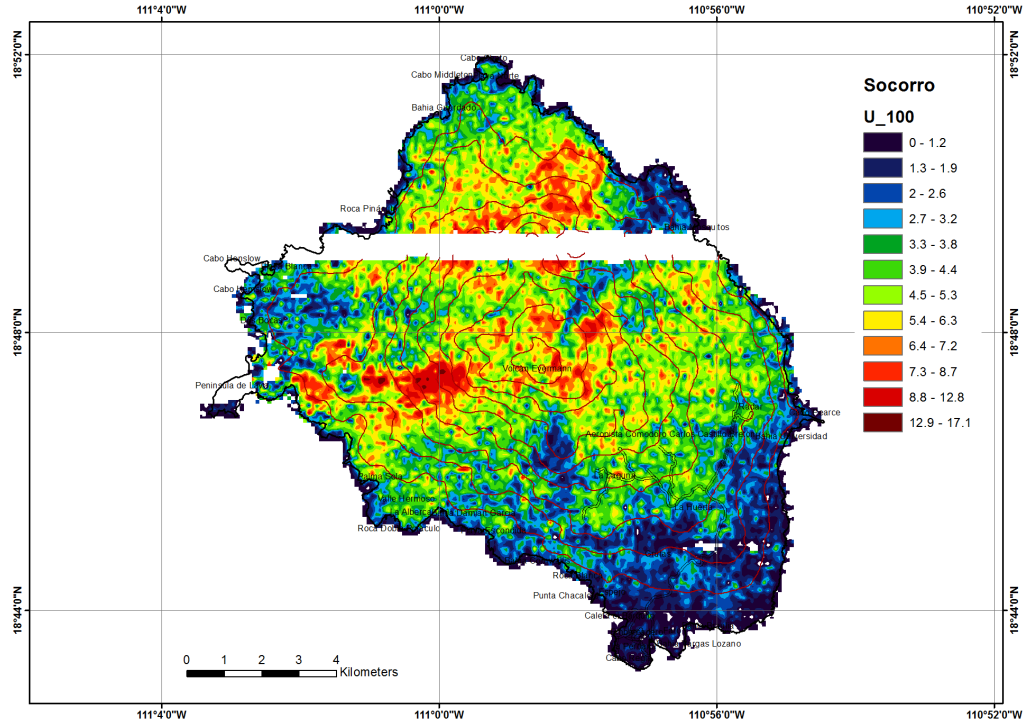


Figure 5.5: Radioelement map of Socorro Island (100 m grid): Uranium [ppm]. Radon correction performed with the Spectral-Ratio method

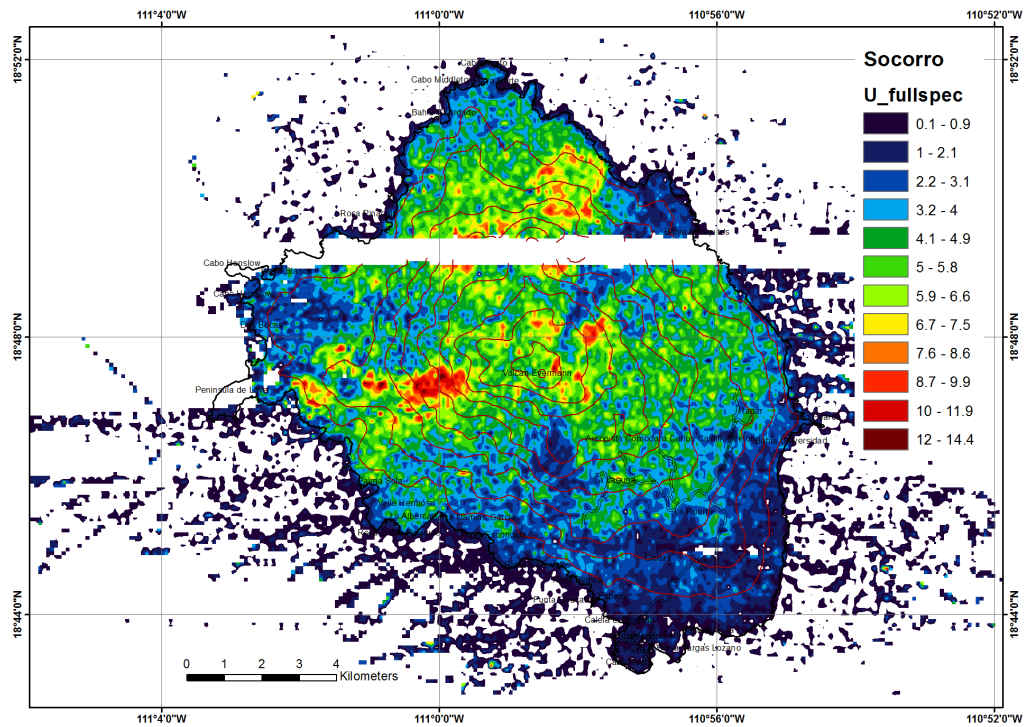


Figure 5.6: Radioelement map of Socorro Island (100 m grid): Uranium [ppm]. Radon correction performed with the Full-Spectrum method

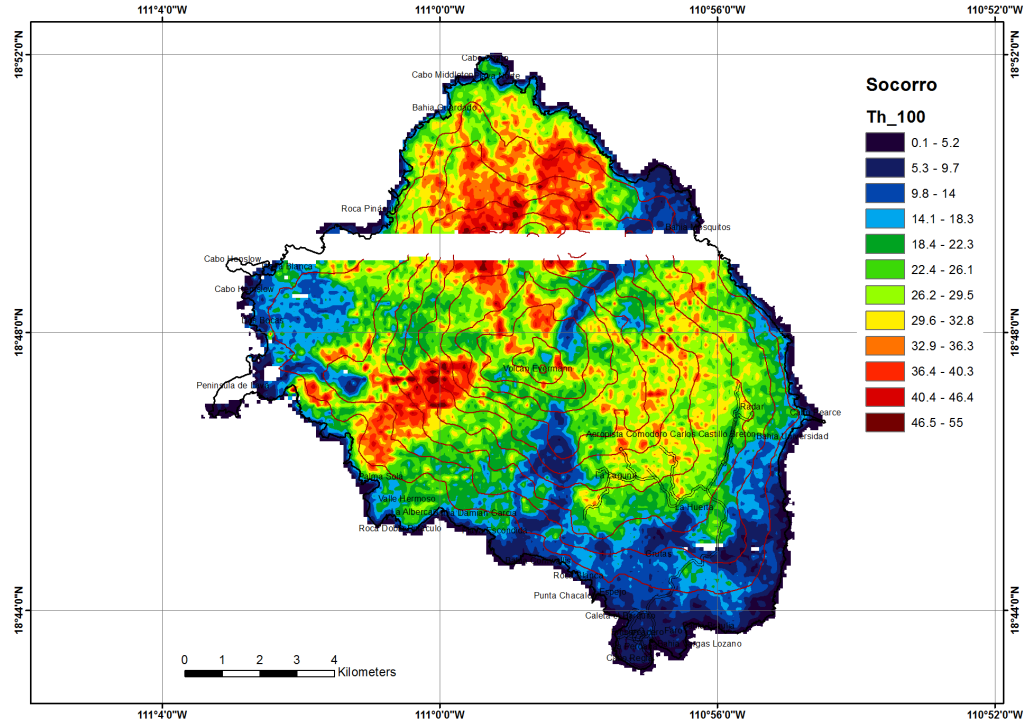


Figure 5.7: Radioelement map of Socorro Island (100 m grid); standard window based processing: Thorium [ppm]

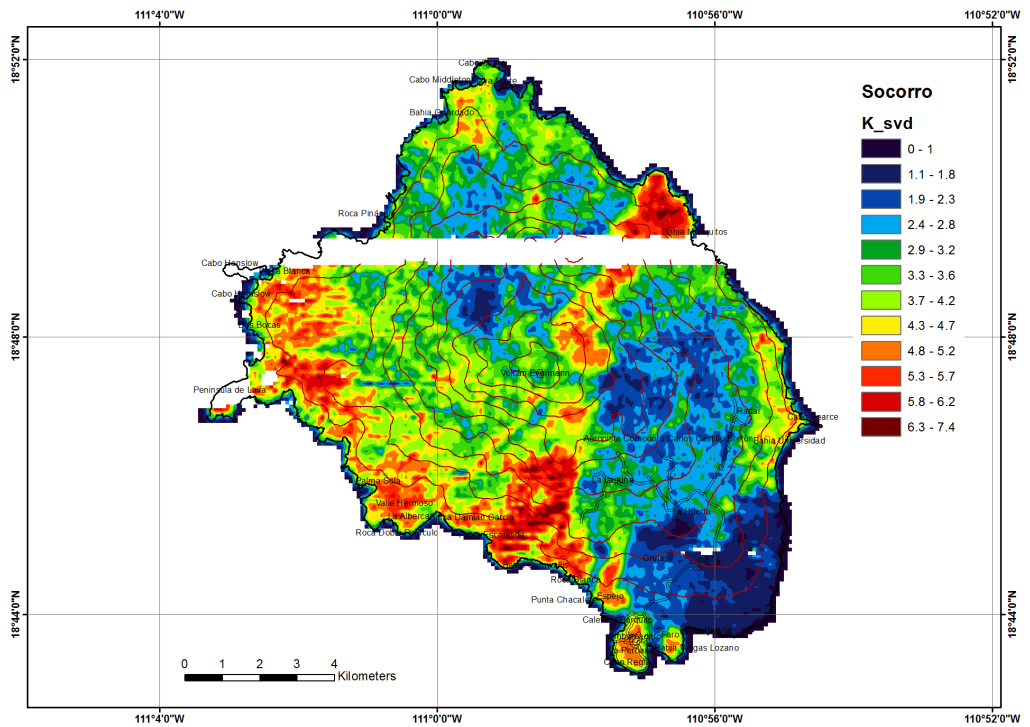


Figure 5.8: Radioelement map of Socorro Island (100 m grid); processing performed with the use of NASVD smoothed spectra: Potassium [%]

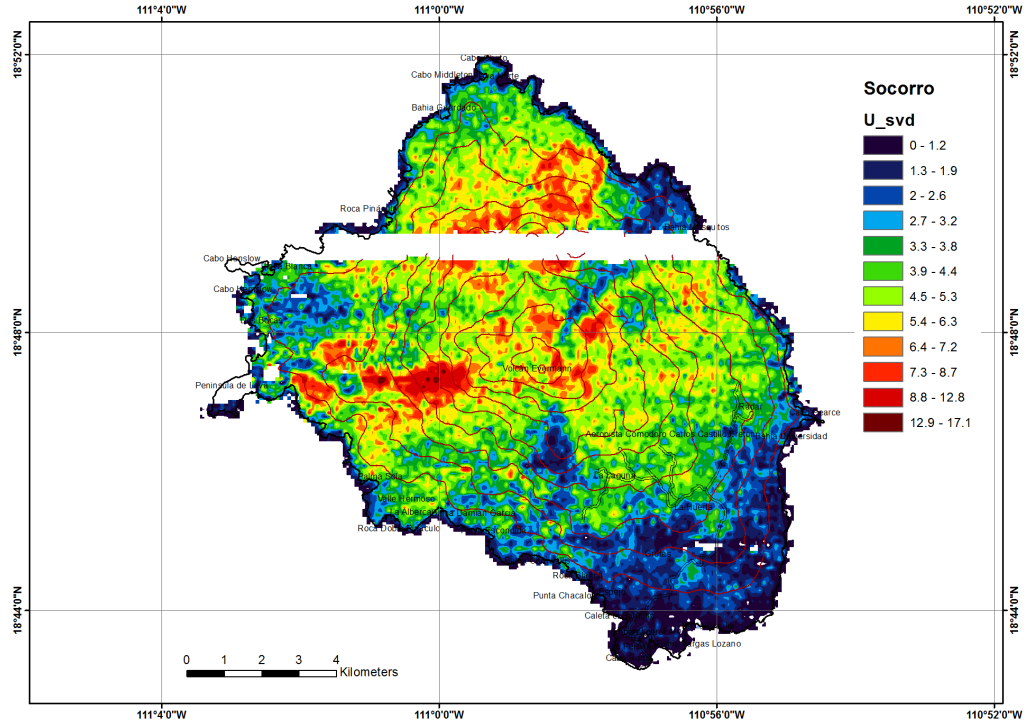


Figure 5.9: Radioelement map of Socorro Island (100 m grid) with NASVD smoothing: Uranium [ppm]. Radon correction performed with the Spectral-Ratio method

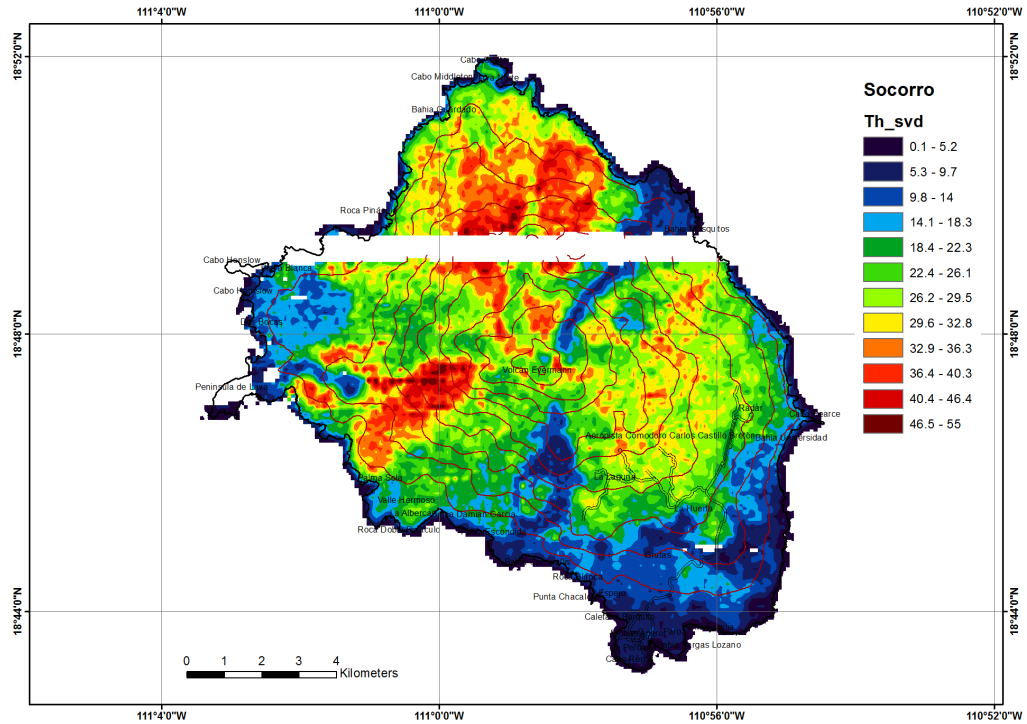


Figure 5.10: Radioelement map of Socorro Island (100 m grid); processing performed with the use of NASVD smoothed spectra: Thorium [ppm]

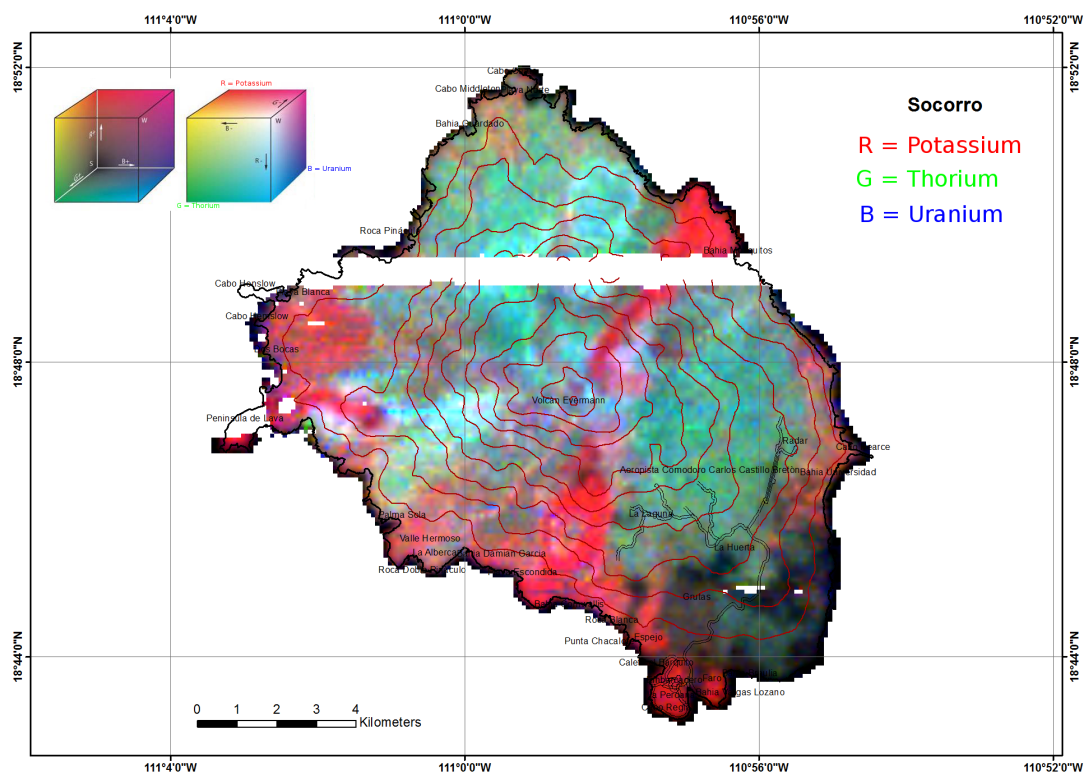


Figure 5.11: Ternary Radioelement map of Socorro Island: K-Th-U

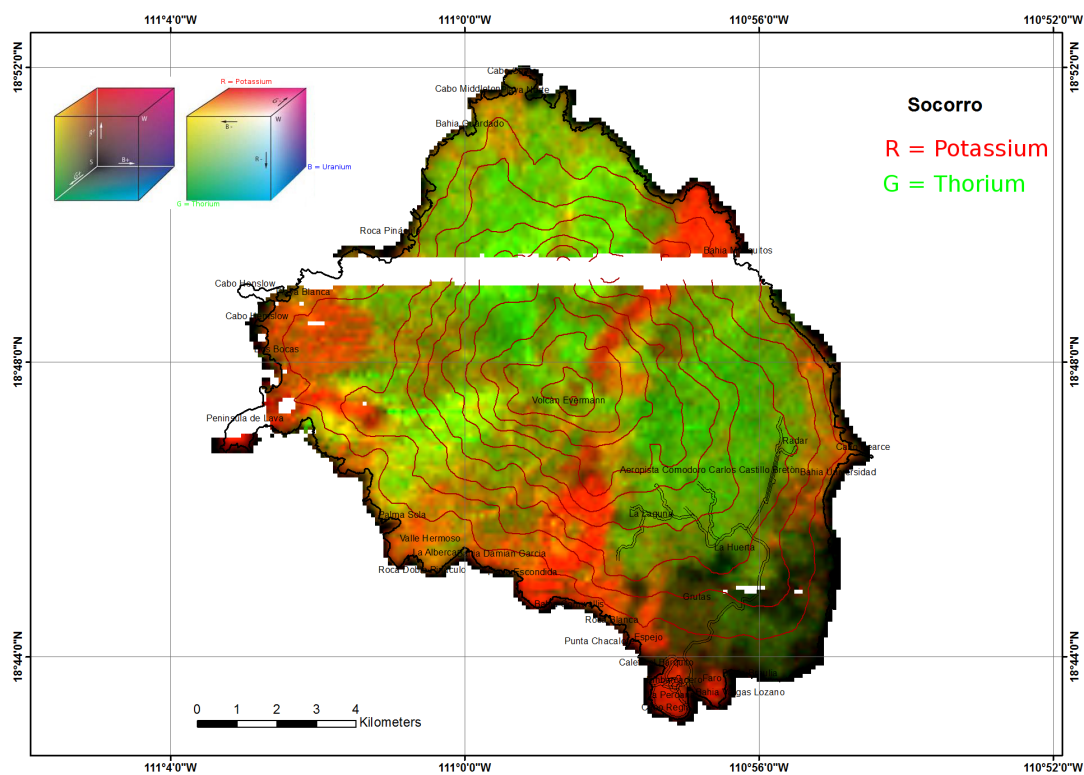


Figure 5.12: Ternary Radioelement map of Socorro Island: K-Th

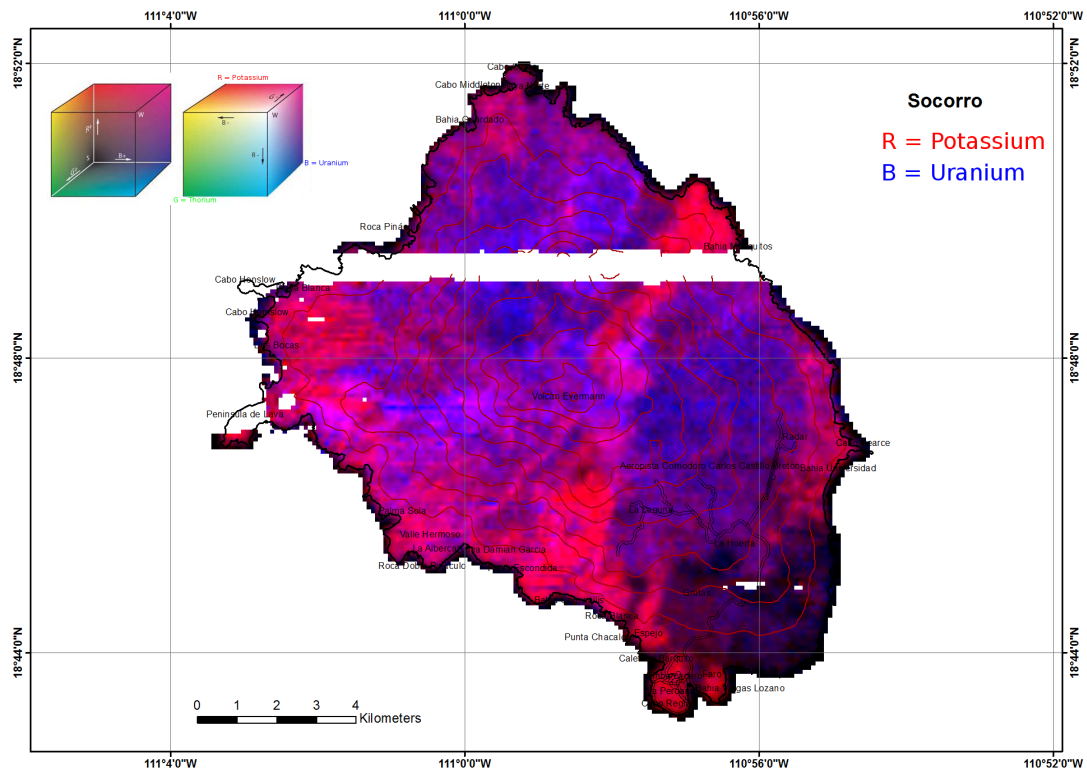


Figure 5.13: Ternary Radioelement map of Socorro Island: K-U

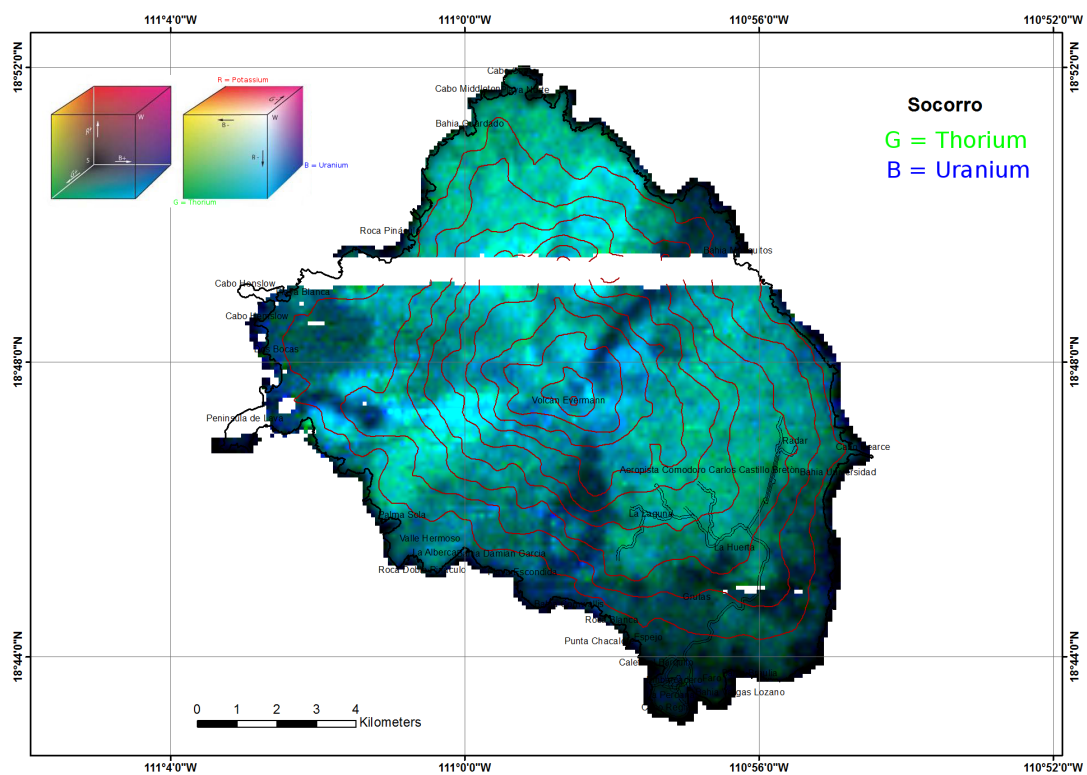


Figure 5.14: Ternary Radioelement map of Socorro Island: Th-U

5.1.3 Description of Geologic Units

As mentioned previously, subaerially exposed units on Socorro Island have been divided into pre-, syn- and postcaldera units by *Bryan* [cp. *Carballido-Sanchez* 1994]. *Carballido-Sanchez* identified several geologic units, which can be found in his map [Fig. 5.35]. The names of the units, which have been identified in the present study are related to the study of *Carballido-Sanchez*. Fig. 5.15 gives an overview of the chronology of these units.

Precaldera		El Muerto members	~ 530 - 480 ka
		Playa Blanca members	~ 430 - 420 ka
		Playa Norte members	pre- or syncaldera
Syncaldera		El Bosque members	~ 370 - 180 ka
Postcaldera	Cerro Evermann eruptives 180 - 15 ka	Felipe members	
		Palma Sola members	
		Volcán Evermann eruptives	
		Peralkaline Domes	
	Lomas Coloradas eruptives 150 - 70 ka	Basalt lava flows	
		Cinder Cones	
		Lozano	

Figure 5.15: Timescale of the subaerial eruptive products on Socorro Island

Pre- and syncaldera deposits

El Muerto members:

The El Muerto member in the Cabo Pearce area represents the oldest crystalline tuff and is therefore probably the oldest exposed precaldera peralkaline pyroclastic flow deposit. Deposits can be found about 4 km along the eastern shoreline of the island, partly capped by younger pyroclastic units. [Carballido-Sanchez 1994]

Carballido-Sanchez identified further members of the El Muerto unit along the coast in the Bahia Academy, Punta Tosca and Punta Judith areas, but these could not be clearly identified by radiometric signatures of the present study. Even though, two further deposits, which could probably belong to the El Muerto unit, have been identified by their radiometric properties. These are located along the shoreline between Punta Tosca and Palma Sola, in the western part of the island. The three deposits of the El Muerto unit, which are plotted in Fig. 5.32, show increased radioelement concentrations in the range of 3.8 - 4.0 % K, 4.7 - 5.5 ppm U and 18.8 - 23.0 ppm Th [cp. Appendix A].

The bar chart in Fig. 5.16 shows the radioelement distributions of the different features which have been assigned to the El Muerto members. The position of these features can be found in Fig. 5.19.

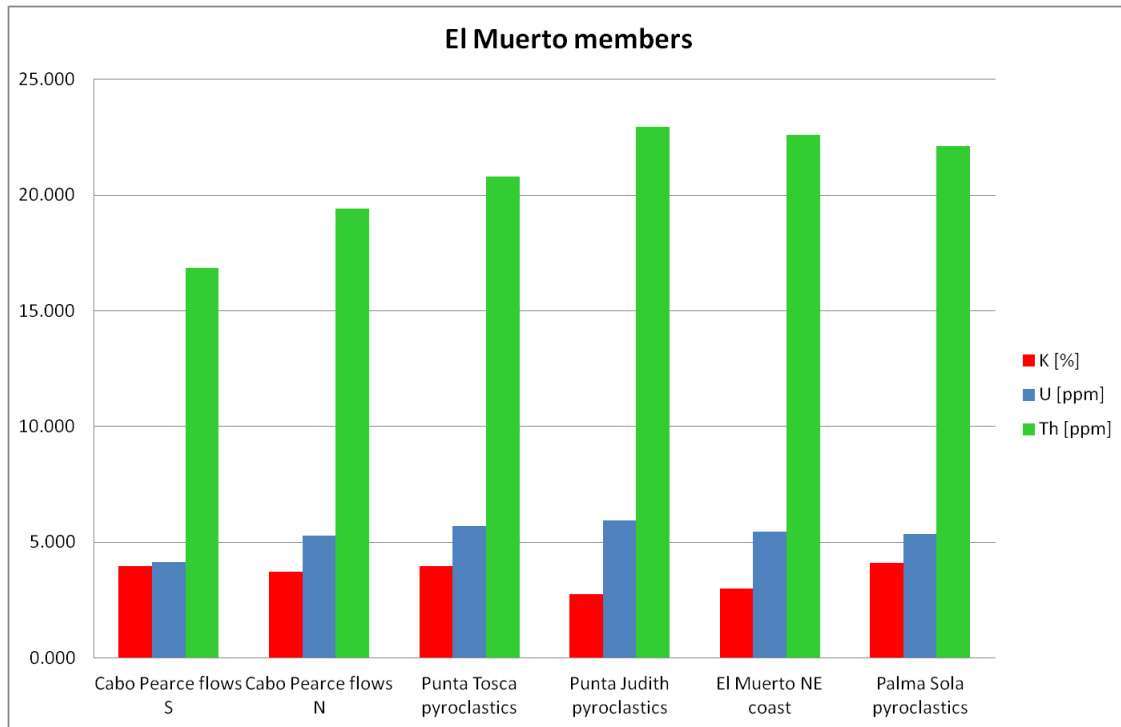


Figure 5.16: Radioelement distribution for the El Muerto members

Playa Blanca members:

The peralkaline pyroclastic flow deposits of the Playa Blanca unit are crystalline tuffs, which are slightly younger than the tuffs of the El Muerto unit. *Carballido-Sanchez* classified them as pantelleritic trachytes and found several deposits all over the island. On the basis of radiometric results, only three deposits could be clearly identified. One of the deposits is located in the Cabo Henslow area, while the other two are located in the area of Caleta Binner and are separated by a basalt lava flow of the Lomas Coloradas sequence. *Wendy A. Bohrson* [Bohrson et al. 1996] determined the $^{40}\text{Ar}/^{39}\text{Ar}$ ages of the two deposits in the Caleta Binner area to be between 433 and 420 ka, and therefore assigned them to the latest stage of precaldera eruptions.

Their mean radioelement concentrations are in the range of 4.4 - 4.6 % K, 3.8 - 4.5 ppm U and 12.3 - 14.7 ppm Th [cp. Appendix A] and they are located within a small circumference in the ternary radioelement diagram. Two further deposits, which correlate with deposits found by *Carballido-Sanchez*, are imaged in the detailed map [Fig. 5.33], but they have not been delineated by their radioelement signatures. The bar chart in Fig. 5.17 shows the radioelement distributions of the different features which have been assigned to the Playa Blanca members. The position of these features can be found in Fig. 5.19.

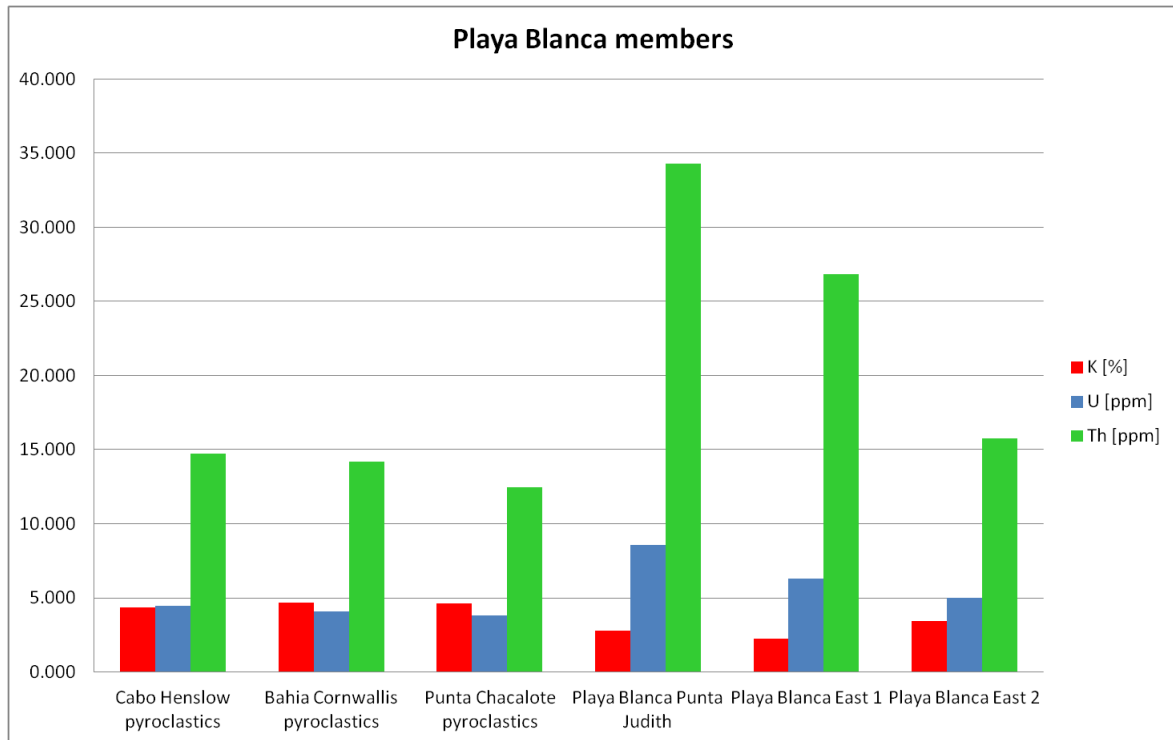


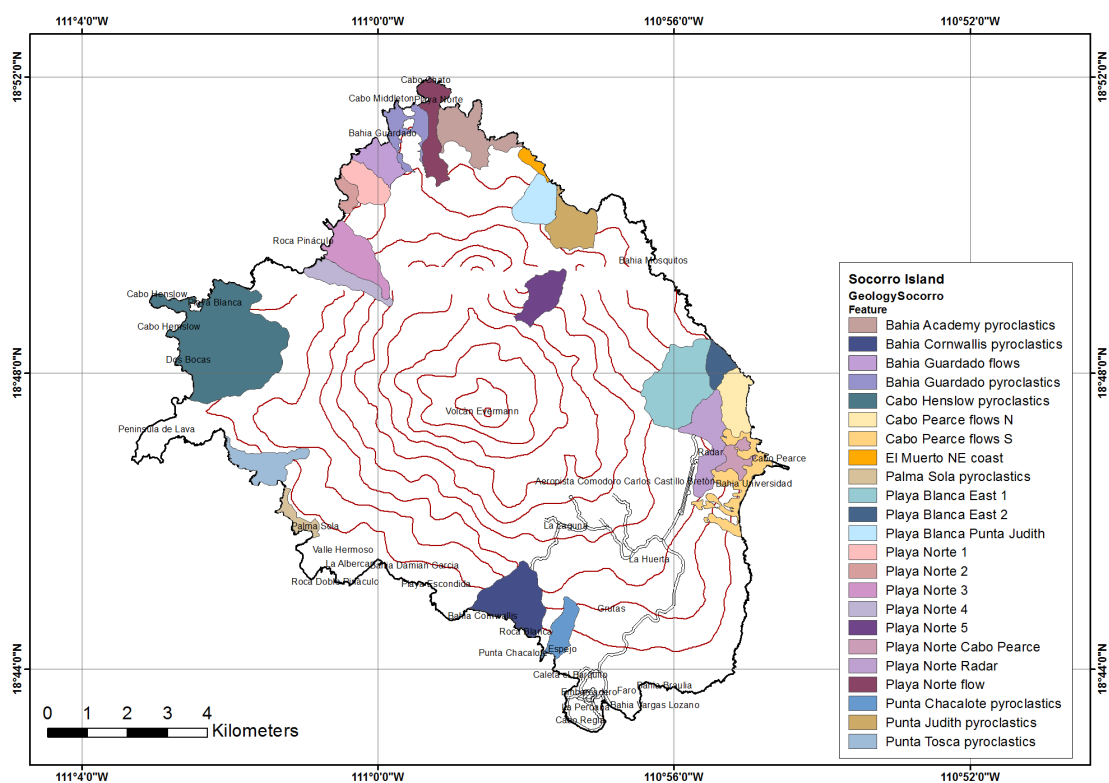
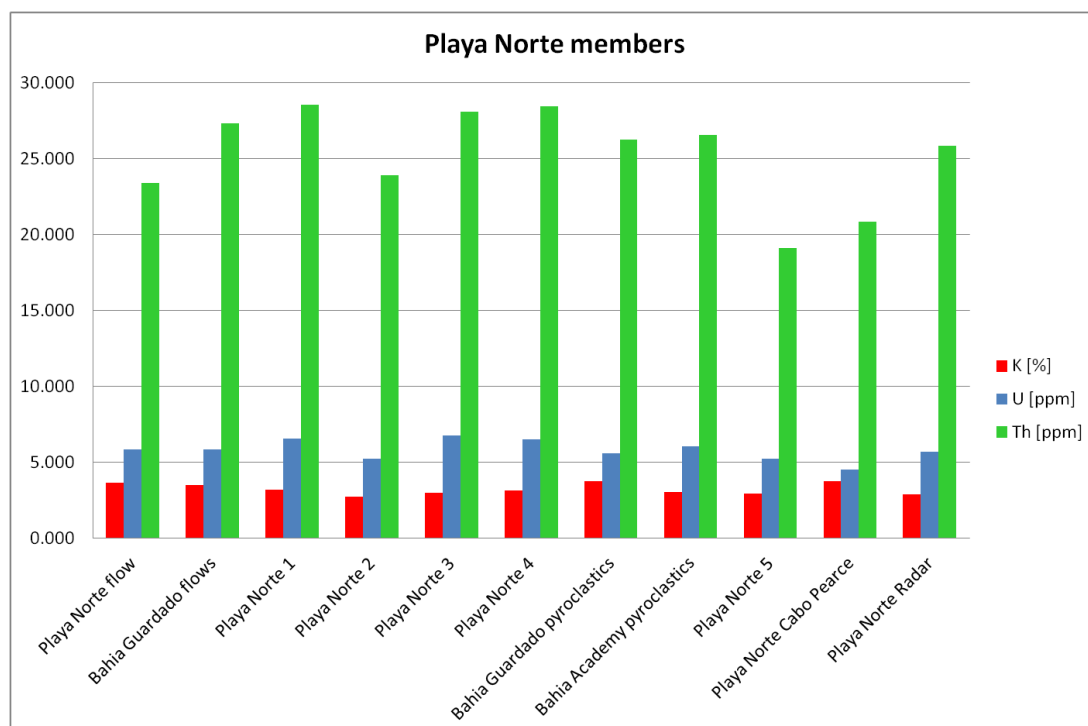
Figure 5.17: Radioelement distribution for the Playa Blanca members

Playa Norte members:

Playa Norte members are peralkaline lava flows which were sampled by *Carballido-Sanchez* in the eastern sector of the island (Barranca del Muerto, Cabo Pearce) and in the Bahia Academy area. Further members were defined by the interpretation of aerial photographs, but weren't sampled by him. He interpreted the Playa Norte members to be either pre- or syncaldera. [Carballido-Sanchez 1994]

The Playa Norte members found in the present work were plotted only in the detailed map [Fig. 5.33], since they could not be identified by their radioelement signature alone. Their distribution was determined by comparing the radioelement maps with the satellite image and the geologic map of *Carballido-Sanchez*. Deposits in the north-western sector of the island show mean radioelement concentrations in the range of 2.7 - 3.8 % K, 5.3 - 6.8 ppm U and 23.4 - 28.6 ppm Th whereas deposits from the eastern sector have concentrations in a similar range (2.9 - 3.8 % K, 4.5 - 5.7 ppm U, 19.1 - 25.9 ppm Th)[cp. Appendix A]. In the rough map of Socorro Island [Fig. 5.32], the Playa Norte members are not plotted as a separate unit, but are part of the Palma Sola members and Precaldera eruptives, respectively.

The bar chart in Fig. 5.18 shows the radioelement distributions of the different features which have been assigned to the Playa Norte members. The position of these features can be found in Fig. 5.19.



El Bosque members:

Crystalline peralkaline pyroclastics of the El Bosque unit are younger than the Playa Blanca members. Exposures found by *Carballido-Sanchez* make up large parts of the caldera wall and therefore the unit could possibly be syncaldera. Due to dense vegetation and lack of trails, only the outcrops east of the caldera had been sampled and their distribution had been defined by means of morphological similarities in aerial photographs. [Carballido-Sanchez 1994]

The only outcrops which can be identified by means of the present data and which coincide with El Bosque outcrops defined by *Carballido-Sanchez* can be found east of the caldera and to the southeast of the large lava-flow that makes up Punta Judith. The two members of the El Bosque unit differ from the surrounding precaldera eruptives by their lower thorium concentration. Their mean radioelement concentrations are in the range of 2.4 - 2.9 % K, 5.0 - 6.4 ppm U and 16.5 - 20.0 ppm Th [cp. Appendix A]. In the ternary diagram the El Bosque members have no exposed position and therefore their distribution and maybe also their existence should be considered with care. The bar chart in Fig. 5.20 shows the radioelement distributions of the two features which have been assigned to the El Bosque unit. The position of these features can be found in Fig. 5.21.

Other precaldera eruptives:

Precaldera eruptives defined in the present work, have a positional relation to the precaldera eruptives in *Bryans* work and were named after them. In the geologic map of *Carballido-Sanchez* the corresponding area includes El Muerto, El Bosque, Playa Blanca and Playa Norte members, but these could not be clearly identified by their radiometric properties. This could be possibly due to dense vegetation in some parts of the area, but this would only explain the lack of dominant radiometric features in the northern part of the area in question. Other possible explanations could be that large parts of the area are affected by weathering and rheomorphism or they are covered with products of explosive eruptions.

Mean radioelement concentrations of the precaldera eruptives were computed to be 2.5 % K, 6.2 ppm U and 26.3 ppm Th. [cp. Appendix A]

The bar chart in Fig. 5.20 shows the radioelement distributions of the different features which have been assigned to the Precaldera eruptives. The position of these features can be found in Fig. 5.21.

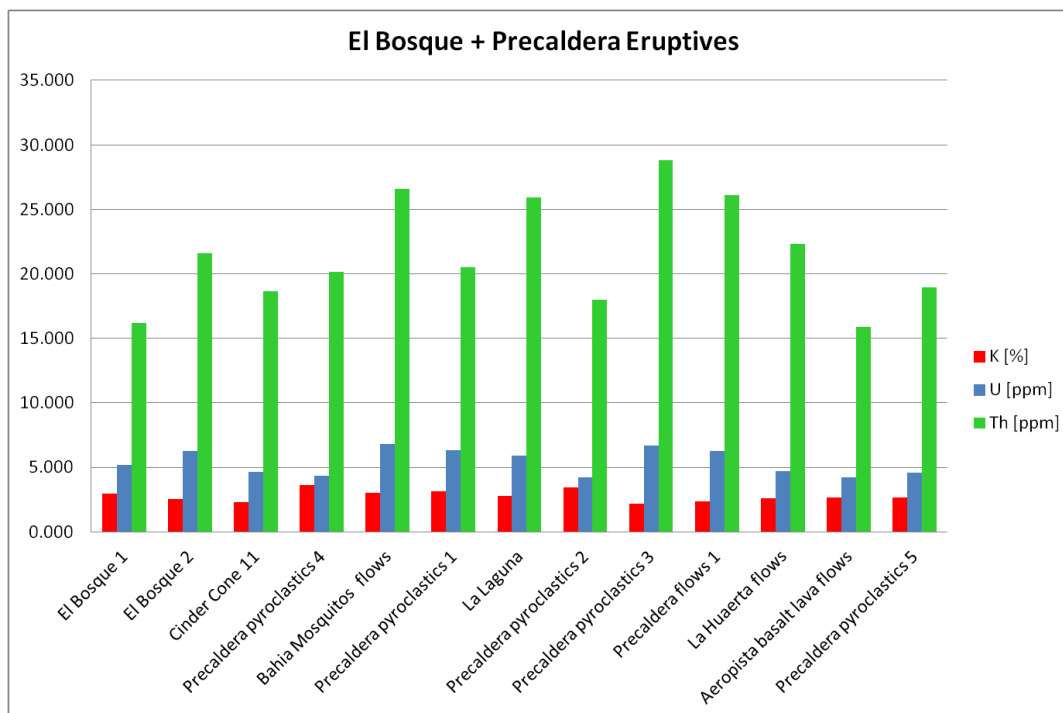


Figure 5.20: Radioelement distribution for the Precaldera eruptives

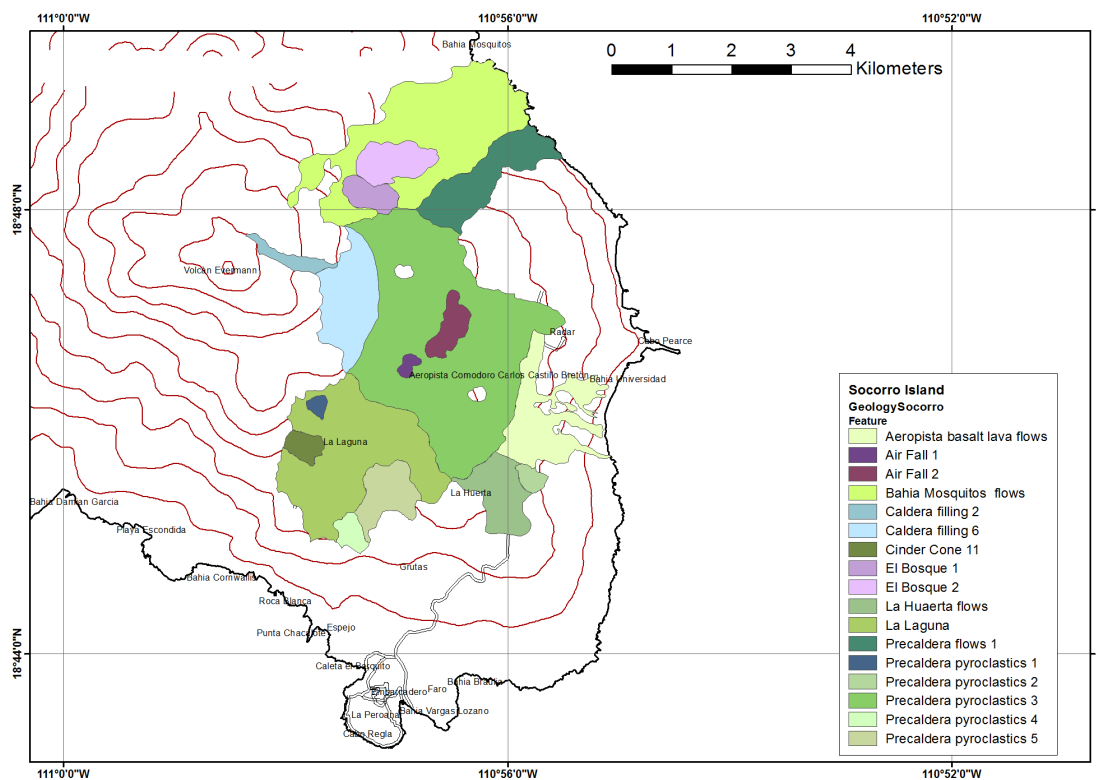


Figure 5.21: Position of the El Bosque members and of the features, which have been assigned to the Precaldera eruptives

Caldera Filling:

The Caldera wall or the caldera filling could not be identified by radiometric signatures and for that reason they could be accidentally assigned to the precaldern eruptives. However, it seemed reasonable to mark the remnant of the caldera as own unit, as the flows and pyroclastics that fill the caldera can only be postcaldera in age. According to the geologic map of *Carballido-Sanchez* these deposits belong to the Palma Sola unit and this is also attended by radiometric data, although the thorium content of the caldera fillings is slightly lower than that of the other Palma Sola members. Mean radioelement concentrations were computed to be 3.5 % K, 7.8 ppm U and 25.3 ppm Th [cp. Appendix A]. Examination of the ternary radioelement diagram yielded Palma Sola and El Bosque as possible units, but El Bosque could possibly be excluded because of age relations.

Cerro Evermann eruptives

Felipe members:

Enrique A. Carballido-Sanchez found at least ten peralkaline lava flows, which he assigned to the Felipe unit. These included evidently visible lava-flows of Punta Tosca, Punta Judith, Bahia Cornwallis, Caleta Grayson and the summit area.

Investigation of the present dataset only allowed a delineation of the lava-flows that form Punta Tosca and Punta Judith, respectively, as they are clearly visible as negative thorium and positive potassium anomalies. Surprisingly, the lava-flow that reaches the coast at Playa Escondia [cp. Appendix A: feature Playa Escondia Twinflow], and which *Carballido-Sanchez* assigned to the Lomas Coloradas unit, shows the same radiometric signature as the two peralkaline lava-flows of Punta Tosca and Punta Judith. Supported by the results of *Wendy A. Bohrsen* [Bohrson et al. 1996], who determined this flow to be composed of peralkaline trachyte and dated it at approximately 15 ka, it can perhaps be assigned to the Felipe members. These three peralkaline lava-flows have very similar radioelement concentrations in the range of 4.2 - 5.2 % K, 4.2 - 4.7 ppm U and 10.2 - 11.1 ppm Th and therefore they lie close together in the ternary radioelement diagram.

Furthermore, because of the map of *Carballido-Sanchez*, their location and their radioelement signatures, three other peralkaline lava flows can be characterized as Felipe members, but this classification has to be handled with care. These three flows are all located in the summit area and filled the caldera or partly overflow the caldera wall. They seem to be older than the three other Felipe members, as they are partly covered by them. While their potassium concentration is pretty close to that of the other Felipe members (3.9 - 4.4 % K), they show distinctly higher concentrations in uranium and thorium (5.1 - 10.5 ppm U and 13.5 - 28.2 ppm Th) [cp. Appendix A and Fig. 5.22]. The bar chart in Fig. 5.22 shows the radioelement distributions of the different features which have been assigned to the Felipe members. The position of these features can be found in Fig. 5.26.

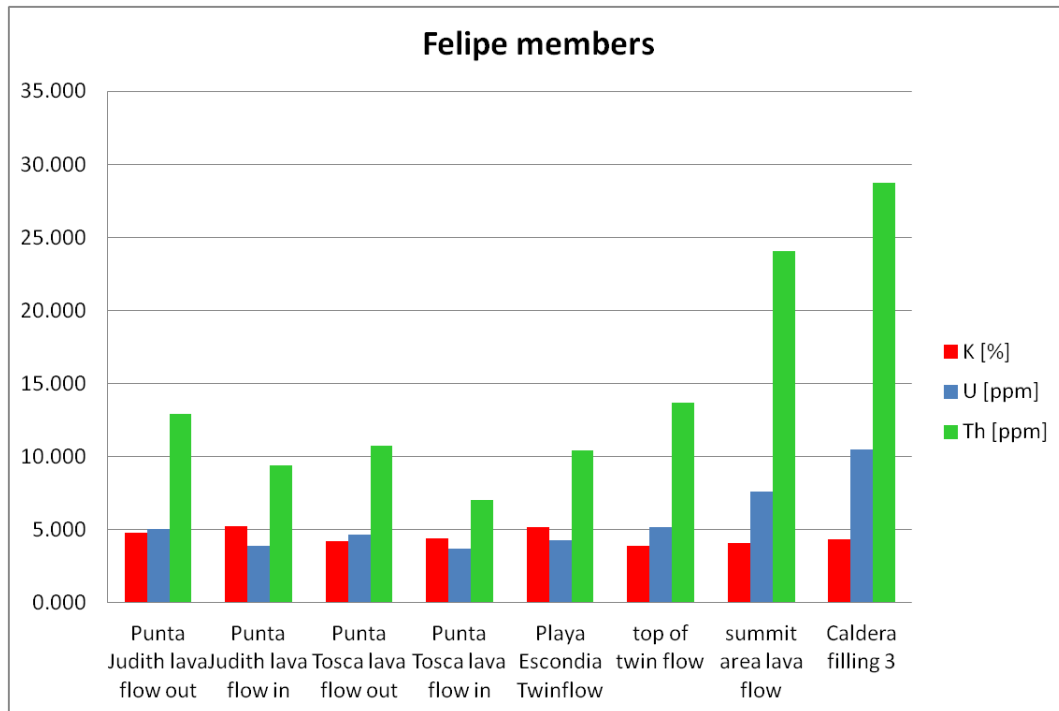


Figure 5.22: Radioelement distribution for the Felipe members

Palma Sola members:

The Palma Sola unit is the most recent unit of peralkaline crystalline pyroclastics and partly correlates with *Bryans* Cerro Evermann eruptives. It is the only crystalline pyroclastic unit, which can be considered unequivocally postcaldera in age. [Carballido-Sanchez 1994]

The Palma Sola members found in the present study are restricted to two large areas. The area to the west of the island appears in the radioelement maps (especially in the thorium map) as elongated oval anomaly, which runs from close to the summit area to the coast of Palma Sola. The second area in the northern sector was assigned to the Palma Sola unit because of its similarity in radioelement concentrations to the area in the West. All members of the Palma Sola unit lie close together in the ternary radioelement diagram. Mean radioelement concentrations of the Palma Sola unit are in the range of 2.9 - 3.9 % K, 7.1 - 10.9 ppm U and 30.2 - 37.2 ppm Th [cp. Appendix A]. The bar chart in Fig. 5.23 shows the radioelement distributions of the different features which have been assigned to the Palma Sola members. The position of these features can be found in Fig. 5.24.

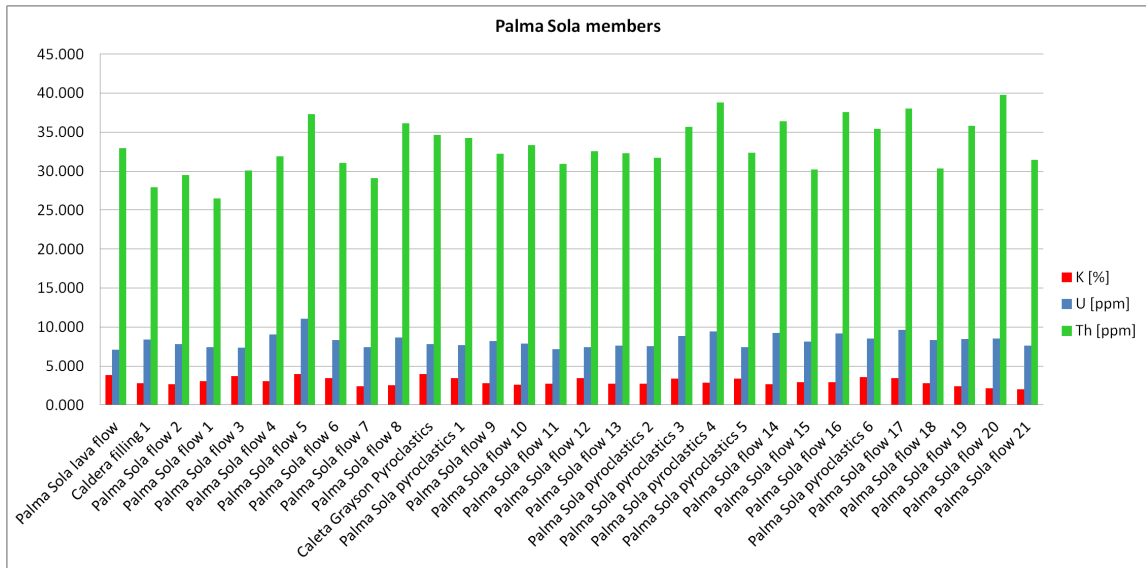


Figure 5.23: Radioelement distribution for the Palma Sola members

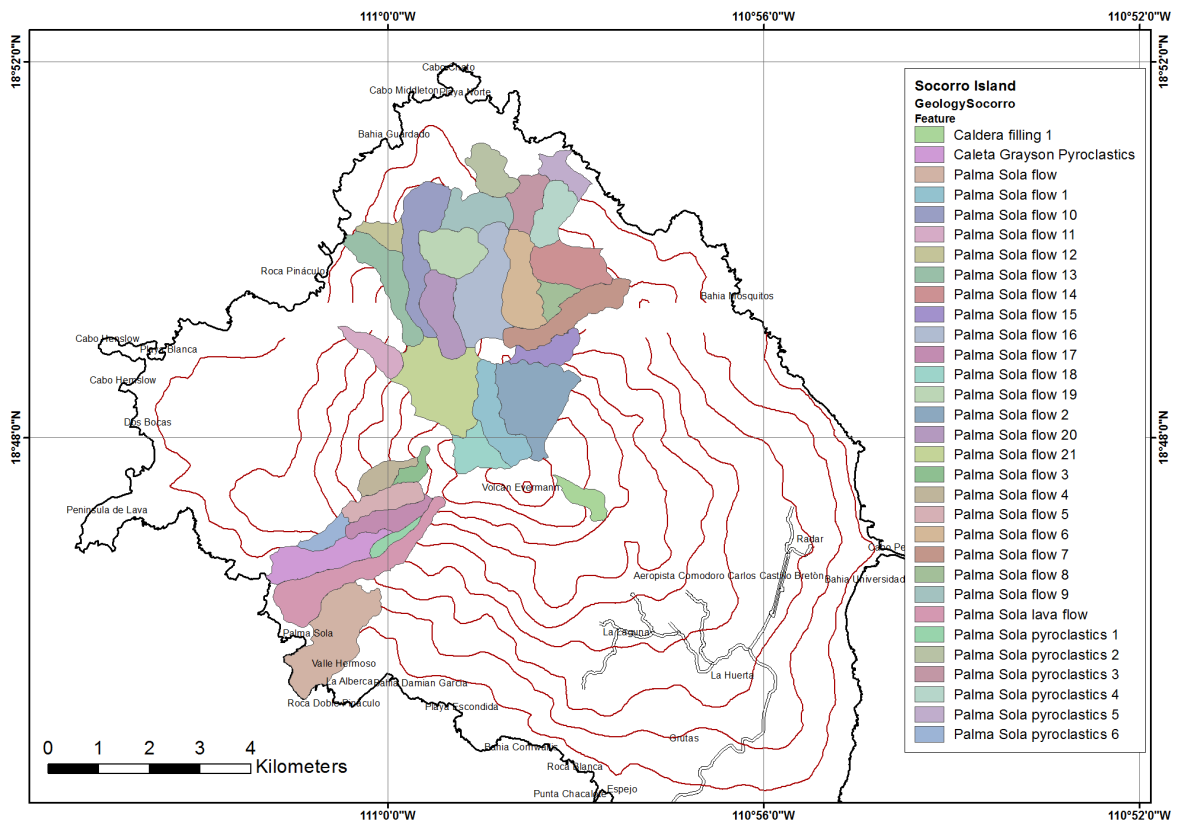


Figure 5.24: Position of the features, which have been assigned to the Palma Sola members

Peralkaline Domes:

Peralkaline domes on Socorro Island are either comenditic or pantelleritic in composition. They appear as endogenous³ and exogenous⁴ types, whereas generally the endogenous can be found at higher elevations and are smaller in size than the exogenous, which have been formed from vents near sea level. Domes are typical for late stages of volcanic activity. A good exposure, which demonstrates the age relationship of peralkaline domes and the surrounding deposits, can be found in the Lomas Coloradas area east of Caleta Binner, where a comenditic dome is emplaced on top of a basalt lava flow of the Lomas Coloradas sequence. *Bryan* found similarities between comenditic domes on Socorro Island concerning composition, structure and degree of weathering and *Carballido-Sanchez* hence concluded that most comenditic domes formed in the latest stage of activity of Volcán Evermann. [Carballido-Sanchez 1994]

At least six domes could be identified by their gamma-ray signatures, especially because of their positive potassium anomaly. Further domes which are plotted in the detailed map [Fig. 5.33] could only be identified by means of the satellite image of Socorro, because they were too small to appear as anomalies in the radioelement maps or the surrounding deposits had similar radioelement concentrations. Mean radioelement concentrations of the peralkaline domes are in the range of 3.3 - 4.9 % K, 4.7 - 8.7 ppm U and 21.6 - 32.3 ppm Th [cp. Appendix A]. The bar chart in Fig. 5.25 shows the radioelement distributions of the different domes. Their positions can be found in Fig. 5.26.

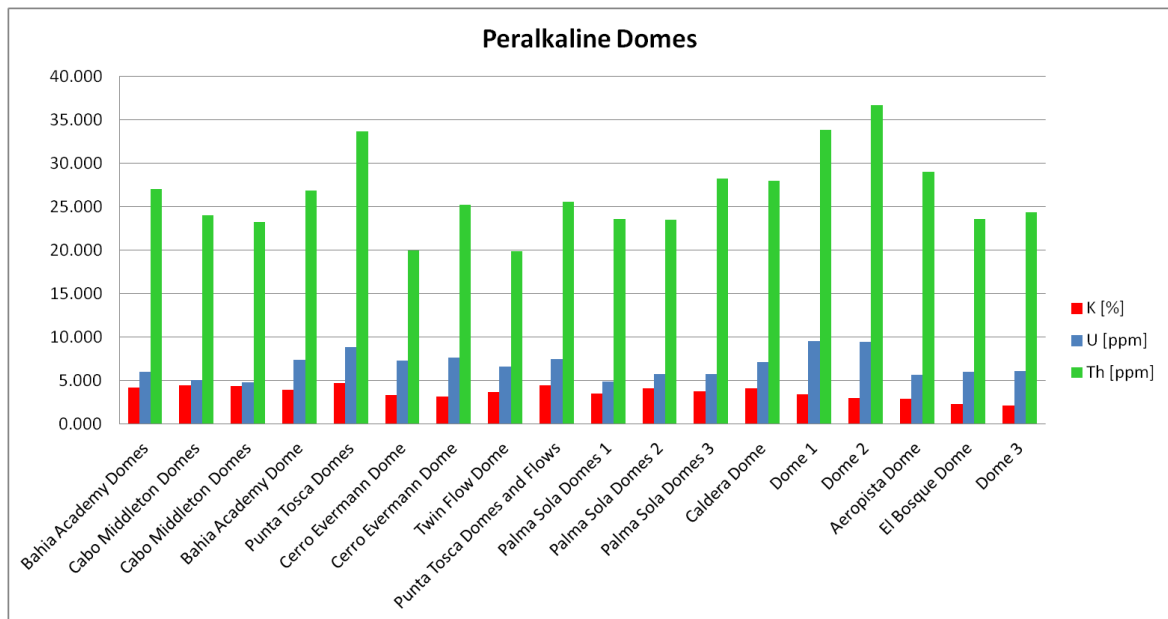


Figure 5.25: Radioelement distribution for the peralkaline domes

³interior expansion of the dome, when new lava arrives

⁴dome expands from surface when new lava stratifies over the dome

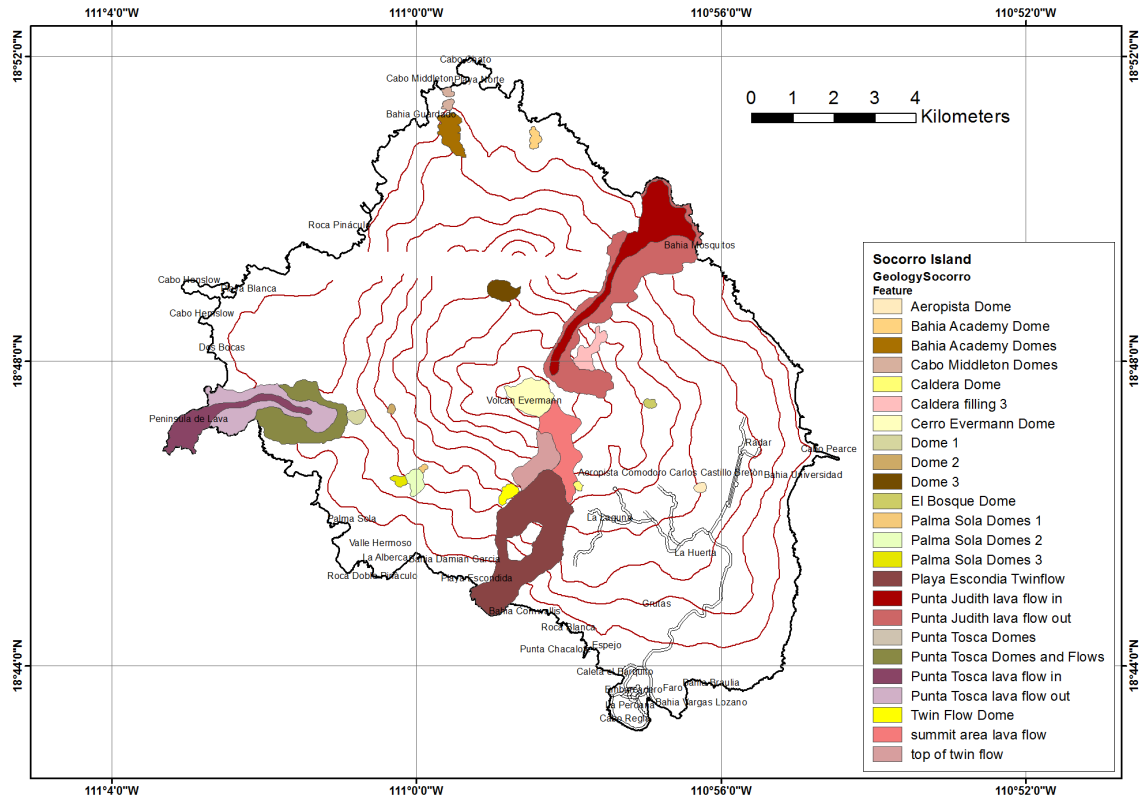


Figure 5.26: Position of the peralkaline domes and of the features, which have been assigned to the Felipe members

Volcán Evermann eruptives:

The Volcán Evermann eruptives found in the present study are the second unit which could possibly correlate with *Bryans* Cerro Evermann eruptives. Because of their lower uranium and thorium concentrations compared to the Palma Sola members these deposits were assigned to an own unit. Volcán Evermann eruptives are peralkaline lava flows and pyroclastics, which are confined to the western sector of the island. Two large areas were delineated as Volcán Evermann eruptives, showing mean radioelement concentrations in the range of 3.2 - 3.9 % K, 5.7 - 6.7 ppm U and 19.3 - 21.7 ppm Th [cp. Appendix A]. A third small area has been assigned to the Volcán Evermann eruptives, which *Carballido-Sanchez* suggested to be a Playa Blanca member. For the present purpose it was called the Playa Escondia "Eye" as it is the central part of the Playa Escondia "Twinflow". Although it cannot be clearly assigned to a unit by its radioelement signature, it was integrated in the Volcán Evermann eruptives, as it was supposed to be postcaldera in age by *Bohrson et al.* The bar chart in Fig. 5.27 shows the radioelement distributions of the different features which have been assigned to the Volcán Evermann eruptives. The position of these features can be found in Fig. 5.28.

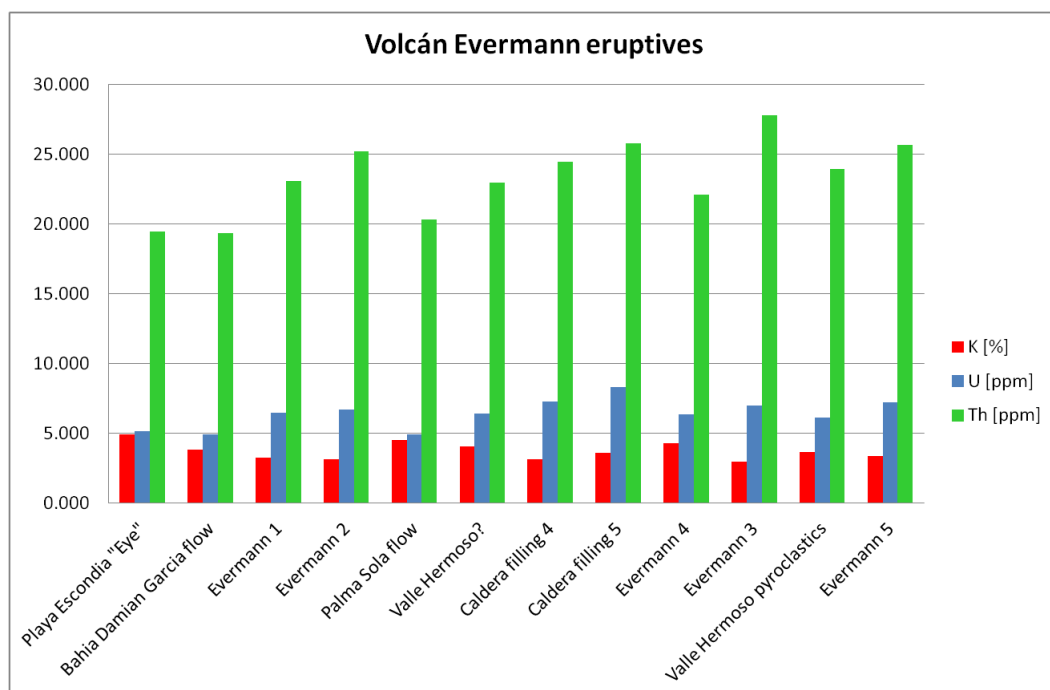


Figure 5.27: Radioelement distribution for the Volcán Evermann eruptives

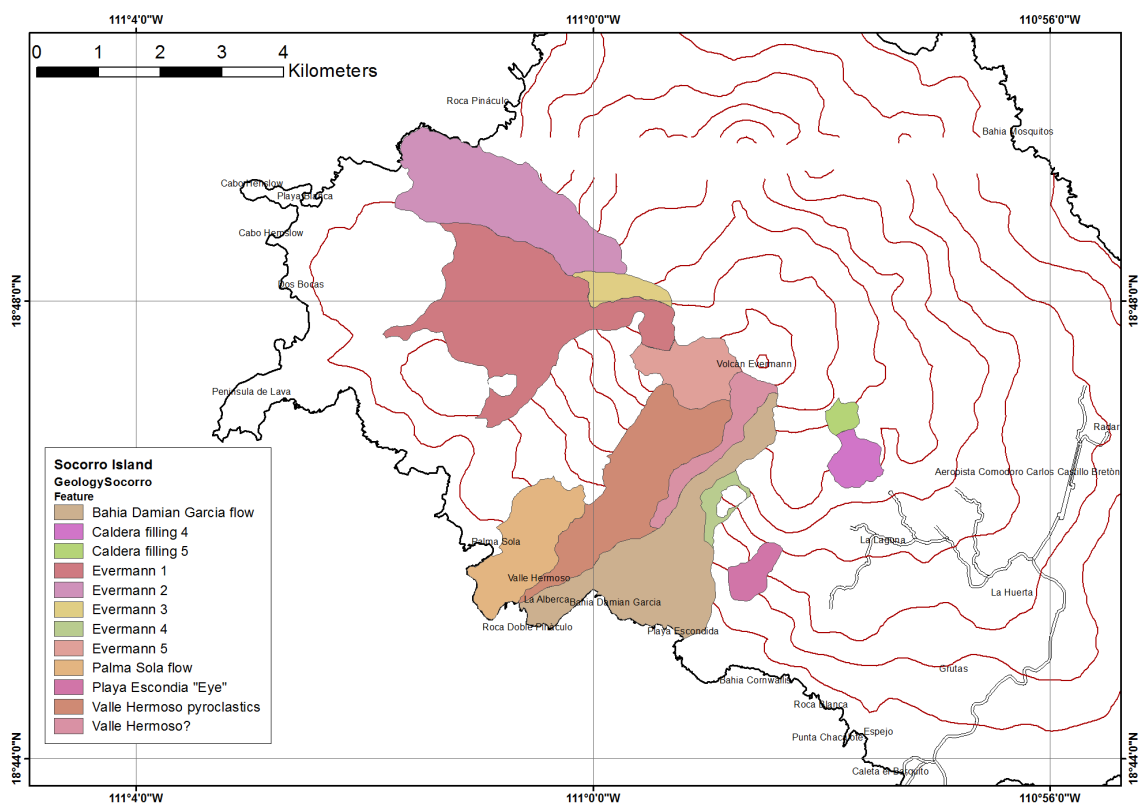


Figure 5.28: Position of the features, which have been assigned to the Volcán Evermann eruptives

Lomas Coloradas Area

The Lomas Coloradas area is the most accessible part of the whole island and covers approximately 20 % of the surface area of Socorro. It is probably the youngest unit on the island and consists of lava flows and cinder cones of basaltic, mugearitic and hawaiitic composition [Carballido-Sanchez 1994]. Most of the previous geologic and geochemical studies on Socorro Island have been confined to this area and therefore a lot of information is available. Radiometrically, this area shows the lowest radioelement concentrations of all three radioelements and can be clearly identified by gamma-ray spectrometry.

Lomas Coloradas basalt lava flows:

Although Socorro Island is believed to be composed mainly of basalts, the Lomas Coloradas alkaline basalts, which are confined to the south-eastern part of the island, are the only basalts exposed at the surface. The basalts have erupted from fissures on the flanks or at the base of cinder cones and show typical pahoe-hoe morphology [Carballido-Sanchez 1994].

Contacts between basalts and pre- and syncaldera deposits show that the basalts are younger, whereas contacts between Lomas Coloradas basalts and domes and flows of the Cerro Evermann Formation demonstrate, that these two formations erupted contemporaneously [Bohrson et al. 1996].

The Lomas Coloradas basalt lava flows are characterized by low radioelement concentrations in the range of 1.4 - 2.5 % K, 2.8 - 3.8 ppm U and 8.8 - 10.3 ppm Th [cp. Appendix A]. Only one section within the Lomas Coloradas area [cp. Appendix A: feature Bahia Braithwaite flows] is silhouetted against the rest of the basalt lava flows, as it shows slightly higher Th concentrations of 14.3 ± 4.7 ppm.

The bar chart in Fig. 5.29 shows the radioelement distributions of the different features which have been assigned to the Lomas Coloradas basalts. The position of these features can be found in Fig. 5.30.

Lomas Coloradas Cinder Cones:

Basaltic air-fall pyroclastics and cinder cones show the lowermost radioelement concentrations of the island. Because it is difficult to distinguish between ash, cinder, spatter and bomb deposits without taking field samples, they all have been assigned to the Cinder Cone unit. At least ten deposits could be identified by their gamma-ray signatures. According to *Carballido-Sanchez* more than 18 cinder cones can be found in the Lomas Coloradas area, who also considered that they have been emplaced contemporaneously.

The cinder cones have mean radioelement concentrations of 1 - 1.4 % K, 2 - 3 ppm U and 4 - 9 ppm Th, whereas especially the thorium concentrations are significantly smaller than those from the surrounding Lomas Coloradas basalt lava flows [cp. Appendix A].

The bar chart in Fig. 5.29 shows the radioelement distributions of the different cinder cones in the Lomas Coloradas area. The position of these cinder cones can be found in Fig. 5.30.

Lozano:

This unit is made up of three peralkaline trachyte domes and one cinder cone. According to the map of *Carballido-Sanchez*, these deposits would belong to the Lomas Coloradas basalt lava flows and cinder cones, but the results of the radiometric studies show a clear difference in the radiometric characteristics. The results rather coincide with the studies of *Bohrson and Reid* [e.g. Bohrson et al. 1996], who assigned these deposits to the postcaldera silicic stage and determined their $^{40}\text{Ar}/^{39}\text{Ar}$ ages to lie between 60 and 70 ka.

The deposits show high potassium concentrations of 4.1 - 4.7 %, low uranium concentrations of 1.7 - 3.0 ppm and low thorium concentrations of 5.8 - 9.0 ppm [cp. Appendix A]. In the ternary diagram [Fig. 5.34] they are located clearly apart and it's because of this position in the ternary diagram, why they have been assigned to a distinct unit.

The bar chart in Fig. 5.29 shows the radioelement distributions of the three different features which have been assigned to the Lozano unit. The position of these features can be found in Fig. 5.30.

The bar chart in Fig. 5.31 gives an overview over the radioelement distributions (average concentrations) of the different units on Socorro Island.

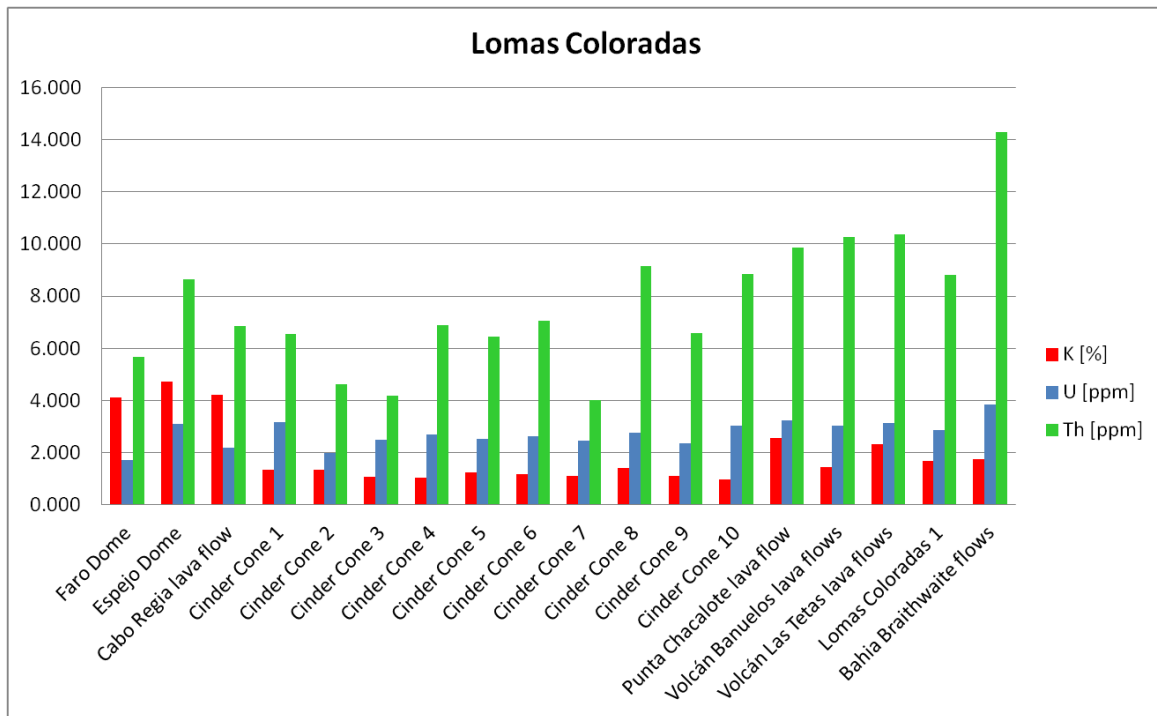


Figure 5.29: Radioelement distribution for the Lomas Coloradas area

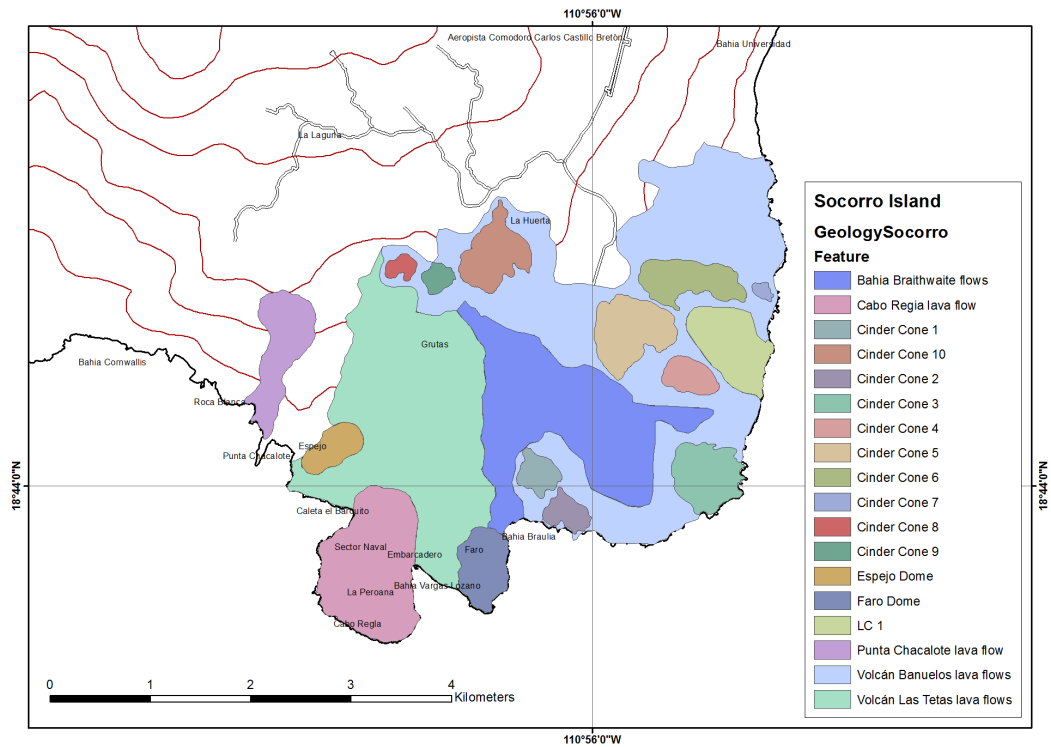


Figure 5.30: Position of the features, which have been assigned to the Lomas Coloradas area

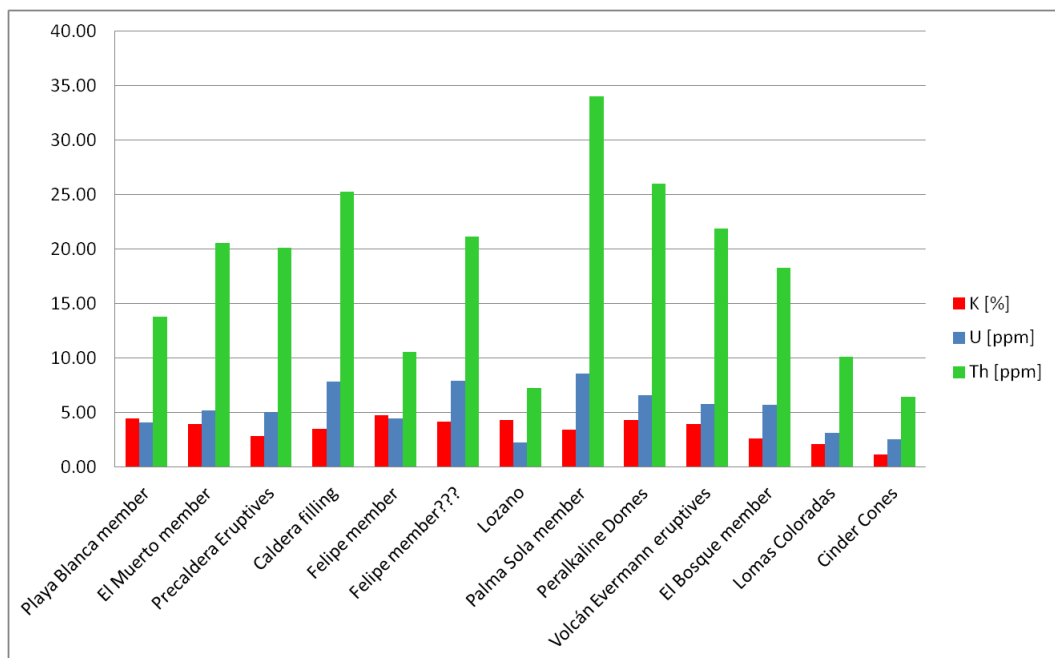


Figure 5.31: Radioelement distribution (average concentrations) for the the different units on Socorro Island

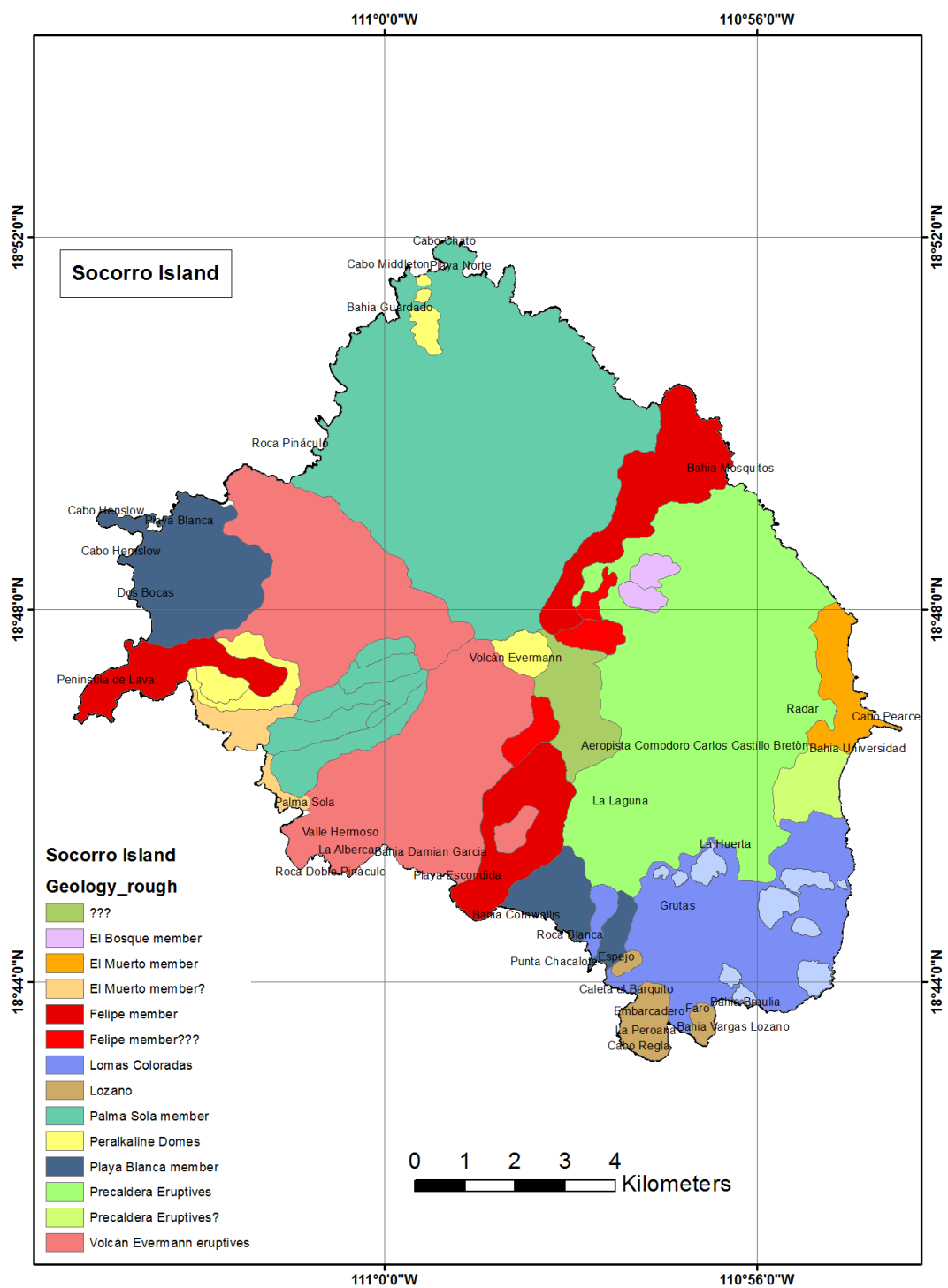


Figure 5.32: Map of Socorro Island showing units that have been delineated on the basis of the radiometric studies

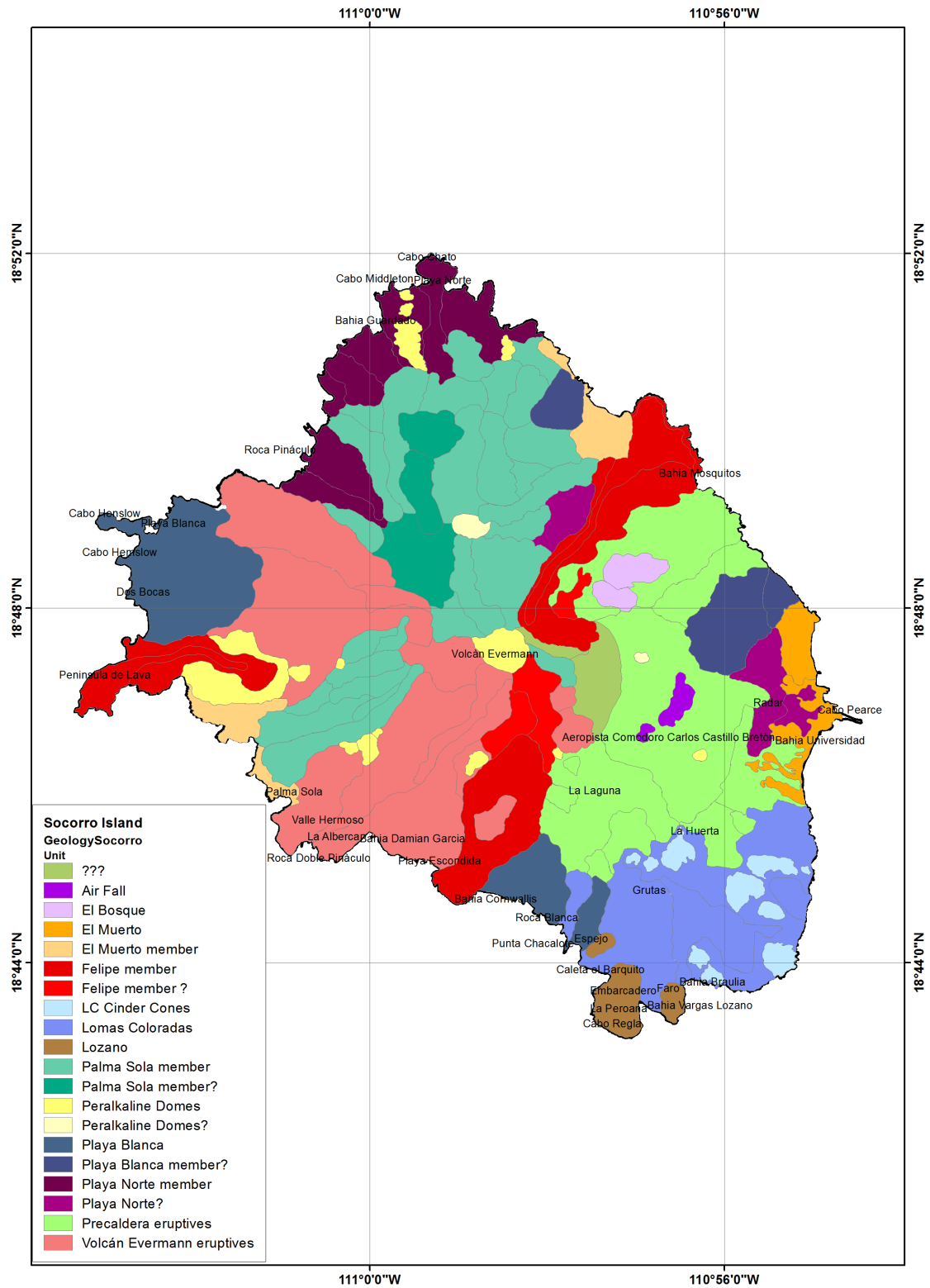


Figure 5.33: Detailed map of Socorro Island showing units that have been delineated on the basis of the radiometric studies

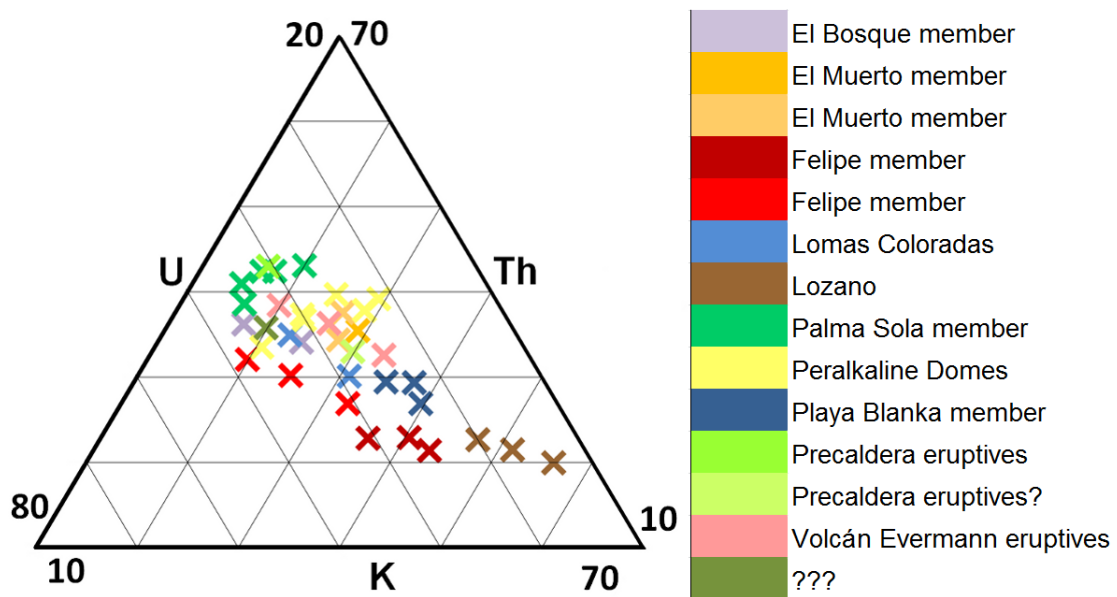


Figure 5.34: Ternary radioelement diagram showing the geologic units of Socorro Island

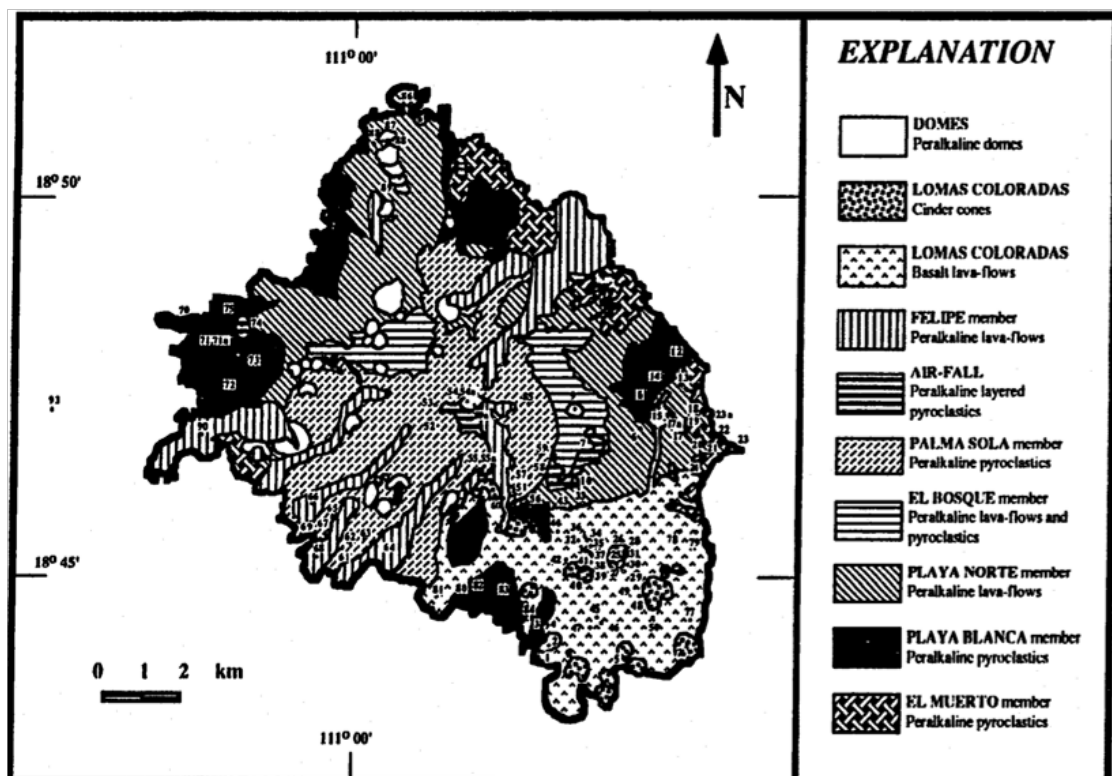


Figure 5.35: Geologic map of Socorro Island designed by *Carballido-Sanchez* [Carballido-Sanchez 1994]

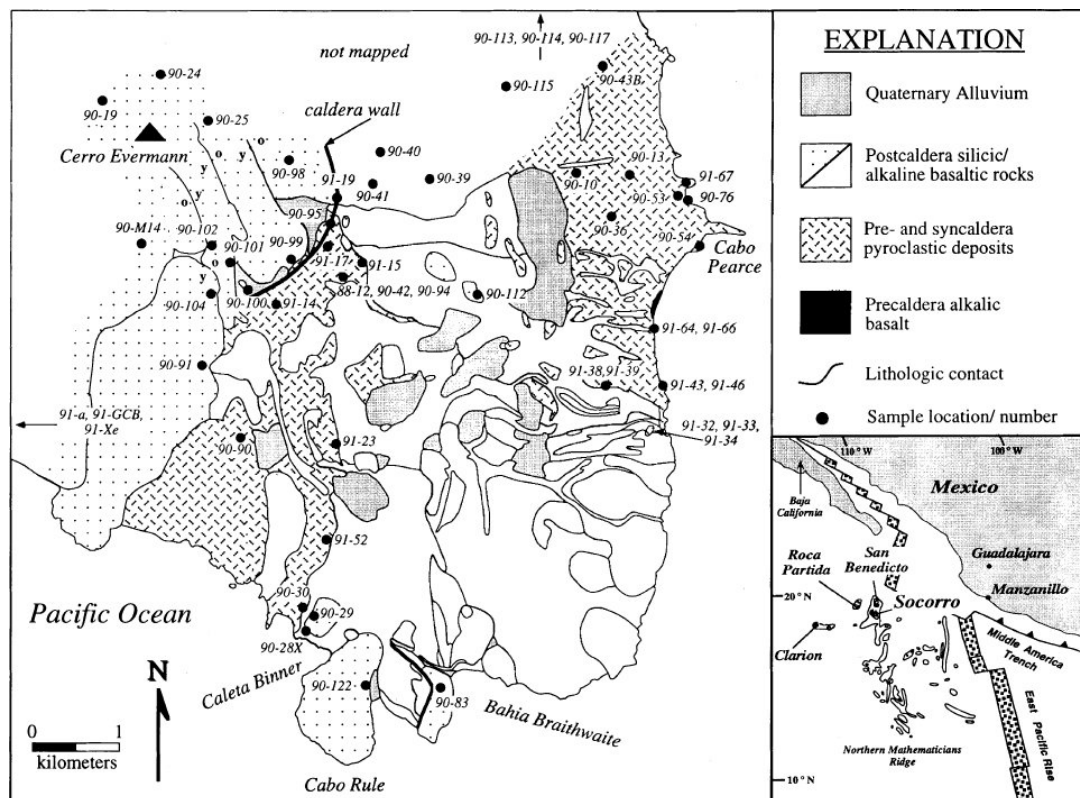


Figure 5.36: Geologic map of the south-eastern sector of Socorro Island designed by Bohrson *et al.* [Bohrson & Reid 1997]

5.2 The Aeolian Archipelago

The Aeolian arc consists of seven islands, all of them being volcanic in origin. From West to East the islands are: Alicudi, Filicudi, Salina, Lipari, Vulcano, Panarea, and Stromboli.

Furthermore, the Tyrrhenian Sea hides at least 23 submarine volcanoes (seamounts), which rise from the seafloor at a depth of approximately 3200 m below sea level and reach heights of 700 - 2900 m above the sea bottom [Pichler & Pichler 2007]. Nine of these seamounts belong to the Aeolian volcanic district [De Astis *et al.* 1997], whereas three are located NW of Alicudi and the others are located NE of the island arc. The Aeolian Archipelago is located between the Marsili oceanic basin and the Calabrian arc and is emplaced on a thinned (~ 20 km) continental crust [Ventura *et al.* 1999]. The origin of the arc is related to the subduction of the African plate under Eurasia, or especially under the Italian peninsula [De Astis *et al.* 1997]. Evidence for this is the observation of seismic events, which indicate the existence of a narrow Wadati-Benioff zone [De Astis *et al.* 1997]. A more detailed delineation of the events having contributed to the genesis of volcanism in this area will not be discussed here.

The Aeolian arc was formed in two main stages of volcanic activity [cp. Gehring 2001]:

The first stage of activity built the islands of Panarea, Alicudi, Filicudi and parts of Salina and Lipari. The second stage of activity formed the islands of Stromboli and Vulcano and completed the islands of Salina and Lipari.

The islands of Lipari and Vulcano deviate from the arc structure and, together with the island of Salina, are affected by the Tindari-Letojanni fault system, a NNW - SSE trending dextral strike slip fault, which further extends to the north-eastern sector of Sicily [Ventura et al. 1999]. Along this fault, volcanic activity started at Salina (430 - 13 ka) and then shifted southwards towards Lipari (223 ka 580 AD) and Vulcano (113 ka - 1890 AD) [Ventura et al. 1999].

Figure 5.37 shows the location of the islands in the Southern Tyrrhenian Sea and their basic volcanic composition.

With an average SiO_2 content of 55 - 57 % the plagioclase-rich lava-flows and pyroclastics of the Aeolian Islands are more acidic than those of Mt. Etna [Pichler & Pichler 2007]. Accordingly, their viscosity is very high and degassing is hindered, resulting in a higher degree of explosivity. If the SiO_2 content further increases up to 63 %, the highly dangerous dacites are formed, which can be found for example on Mt. Sant'Angelo (594 m) in the central part of Lipari Island [Pichler & Pichler 2007].

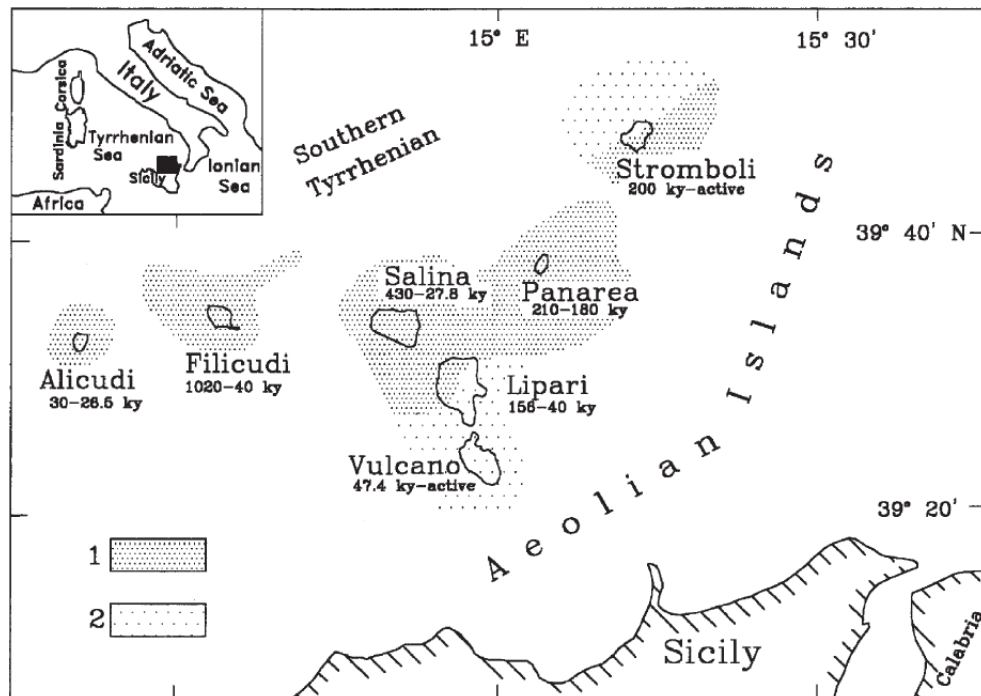


Figure 5.37: Position and age of the islands of the Aeolian volcanic arc. (1) Calc-alkaline to high-K calc-alkaline and (2) shoshonitic products [Chiozzi et al. 2003]

5.2.1 Vulcano

With an extent of 21.2 km² Vulcano (38° 23' N, 14° 58' E) is the third largest island of the Aeolian Archipelago. It is the top of a much larger structure, which has its base at a depth of 1000 m below sea level with a basal diameter of approximately 15 km [De Astis & Dellino 2006]. Volcanic activity on the island started at approximately 120 ka and continued till present. The eruption of various lava flows, domes, and scoriae, ranging in composition from high-K calc-alkaline and shoshonitic⁵ mafic rocks to more evolved intermediate to rhyolitic rocks, formed the island to a NW-SE elongated composite structure. Furthermore, explosive phreatic and phreatomagmatic eruptions produced wet and dry pyroclastic surges, pumice fall deposits, and highly viscous lava flows [Revil et al. 2008]. At the surface, mainly volcanic rocks and pyroclastic material are exposed, confirming the volcanic origin of the island.

Two overlapping volcanotectonic structures stand out on the island: The 2.5-km-wide Piano Caldera and the 3-km-wide Fossa Caldera, which were formed at about 98 - 77 ka and 24 - 13 ka, respectively [Revil et al. 2008]. The Piano Caldera is located in the central to south-eastern part of the island. Its base lies at an altitude of approximately 350 m and the crater rims reach their maximum at 500 m above sea level (Mt. Aria). The Fossa Caldera is located in the central part of the island. In its centre has grown the Fossa Cone, which is responsible for most historic eruptions of the island.

Eruptive history on Vulcano Island has been subdivided into six eruptive stages [Santacroce et al. 2003]: Primordial Vulcano, Caldera del Piano, La Fossa Caldera, Lentia Complex, La Fossa Cone, and Vulcanello. Subaerial volcanism at Vulcano started in the South, with the eruption of basaltic and shoshonitic lavas and scoriae, dated between 120 and 100 ka [Santacroce et al. 2003]. This first volcanic stage, which refers to the formation of a stratovolcano, was called Primordial Vulcano. The collapse of the summit of the cone between 98 and 78 ka formed the Caldera del Piano, which was then progressively filled with lava flows and pyroclastics between 77 and 21 ka [Santacroce et al. 2003]. The remnants of the stratovolcano (Primordial Vulcano) and its caldera (Caldera del Piano) now form the southern part of the island. At the end of this volcanic stage activity shifted towards NW and formed the southern part of La Fossa Caldera (55 - 24 ka). The following period between 24 and 13 ka produced intermediate to rhyolitic magmas. These were deposited as lava domes in the northern part of the island and formed the Lentia Complex. At approximately 15 ka the largest explosive eruption at Vulcano occurred, forming the Tufi di Grotte dei Rossi deposits and probably triggering the collapse of the western part of La Fossa Caldera [Santacroce et al. 2003]. The succeeding volcanic stage refers to the activity of La Fossa Cone, which grew within the Fossa Caldera and started its activity at 6 ka before present. The Fossa Cone formed six volcanic successions with different vent locations, each of them following the same evolution starting with pyroclastic surges and ending with the eruption of highly viscous lava flows [Revil et al. 2008]. The six successions are: Punte Nere, Palizzi, Caruggi, Forgia Vecchia, Pietre Cotte, and Gran Cratere. All these products of La Fossa Cone are characterized by high potassium

⁵Shoshonite: a potassic trachyandesite

content and show a range from trachytic to rhyolitic composition [Revil et al. 2008]. *I. Gehring* described only five successions of La Fossa and described them as various pyroclastic deposits, lava flows and fall-out deposits, ranging from alkali-rich trachytic to rhyolitic in composition. The five successions from oldest to youngest are: Punte Nere, Tufi Varicolori, Palizzi, Commenda, and Cratere Attuale [Gehring 2004].

La Fossa di Vulcano at 391 m above sea level, which can still be considered to be active, is a potentially very dangerous volcano, what becomes apparent by considering the so far last eruption, which took place between 1888 and 1890. It was a heavy eruption with a 4 km high eruption column and volcanic bombs falling down within a radius of 3 km around the volcano. The source of this phreatic eruption was ground- and seawater, which could move to the depth along cracks and fissures and was then vaporised under high tension [Pichler & Pichler 2007]. This kind of explosive activity with high eruption columns and volcanic bombs was called "vulcanian type eruption" by Giuseppe Mercalli and is now eponymous for eruptions of this distinct type. Most "vulcanian" eruptions are due to interaction of water and magma (usually with increased silica content), and are characterized by numerous eruptive pulses within irregular time intervals [De Astis & Dellino 2006].

The youngest products of the last eruptive stage, which erupted between 183 BC and the 16th century AD, build the northernmost part of the island. This structure is called Vulcanello and was formed as a new island in 183 BC. Successive eruptions in the 6th and 16th century then connected it to Vulcano Island. [De Astis et al. 1997]

At present, fumarolic activity can be found inside La Fossa crater and on the flanks of the cone and also degassing activity can be found, which is mainly restricted to the northern sector of the island [De Astis & Dellino 2006]. A special feature of the fumaroles at La Fossa Cone is a periodically occurring increase in temperature, accompanied by shallow seismicity [cp. Revil et al. 2008]. The last of these so called "crises" occurred between 2004 and 2006 [Revil et al. 2008].

Volcanic deposits on Vulcano Island can also be classified by their different petrochemical characteristics. They consist of high-K calc-alkaline and shoshonitic to potassic rocks, varying in their degree of evolution from basalt to rhyolites [Chiozzi et al. 2001]. Three different volcanic cycles can be characterised and within these cycles two temporal and geochemically distinct series can be recognized [Chiozzi et al. 2001]: The first and oldest cycle, which produced trachyandesite-trachybasalt, corresponds mainly with the first eruptive stage (Primordial Vulcano) and is therefore dated from 120 to 98 ka. The second cycle, which produced trachybasalt, largely corresponds with the formation of Piano caldera and lasted from 98 to 50 ka. Both, the first and the second cycle consist of lava flows and pyroclastics with high-K calc-alkaline and shoshonitic affinity [Chiozzi et al. 2001] and can be combined to the first geochemical series. The third cycle lasted from 15 ka until present and shows a higher K_2O content and much wider variation of SiO_2 than the other two [Chiozzi et al. 1999]. Volcanics of this cycle belong to the second series and range in composition from leucitic-tephritic rocks (Caldera della Fossa) to felsic lava flows, with associated pyroclastites (Lentia Complex) and rhyolitic obsidians (La Fossa) and also rocks of leucitic-tephritic to trachytic composition, which can be found on Vulcanello [Chiozzi et al. 1999].

Previous radiometric surveys

Ground based gamma-ray spectrometric surveys were performed at Vulcano by *I. Gehring* [Gehring 2001, Gehring 2004] and *P. Chiozzi* [Chiozzi et al. 1999], [Chiozzi et al. 2001]. The ground radiometric equipment is rather similar to the airborne detector, with minor differences in that it is smaller and more appropriate for carrying it in the field. Concentrations of the radioelements K, U and Th were taken at a number of sites representing the different structural units on Vulcano [Chiozzi et al. 1999]. Outcrops affected by weathering were either cleaned or avoided and the surface was made as flat as possible to simulate 2π geometry [Gehring 2004, Chiozzi et al. 2001].

Based on the ground radiometric data, two series or radiometric districts can be identified. Generally, the older mafic volcanic series shows lower radioelement concentration than the younger felsic series. The lowest eU values (1 - 5 ppm) could be found in trachyandesite-trachybasalt lava-flows in the southern part of the island, the highest values (20 - 25 ppm) in turn were detected over rhyolitic obsidians of La Fossa [Chiozzi et al. 1999]. Uranium values measured at Vulcanello varied between 5 - 15 ppm, confirming the leucitic-tephritic composition of the peninsula. Thorium showed the same increase in concentration from the first and second to the third cycle and also the potassium concentration of the third cycle is higher than that of the first two cycles. The lowest K values (2.4 %) were observed in the southern part of the island. K concentration increases in the central part of the island (4.5 %) [Chiozzi et al. 1999] and, like uranium, shows the maximum concentration (6.1 %) in the rhyolitic obsidians. Lower potassium concentration (3.8 %) was measured at Vulcanello, again correlating with the leucitic-tephritic composition of the Vulcanello platform.

Only the concentration values of Caldera della Fossa (third cycle) depart from the general trend, as they show mean values similar to those of the first and second cycle [Chiozzi et al. 2001].

The radioelement ratios Th/U, K/Th and K/U show a general decrease from the first and second to the third volcanic cycle.

Table 5.2 lists the results of the ground radiometric survey performed by *P. Chiozzi*. The numbers in brackets quote the standard deviations.

Structural unit	Rock type	eU (ppm)	eTh (ppm)	K (%)
Primordial Vulcano (first cycle)	lava flow	2.9 (0.8)	10.3 (2.7)	2.5 (0.7)
	pyroclastite	3.4 (0.2)	11.2 (1.4)	2.1 (0.1)
Caldera del Piano (second cycle)	pyroclastite	3.0 (0.6)	10.0 (1.6)	1.9 (0.5)
Lentia (third cycle)	lava flow	15.7 (3.0)	49.5 (7.3)	4.8 (0.7)
Caldera della Fossa (third cycle)	lava flow	3.1 (0.7)	9.9 (0.6)	3.0 (0.7)
	pyroclastite	5.9 (2.7)	22.7 (5.6)	3.0 (0.8)
La Fossa (third cycle)	lava flow	19.2 (5.0)	65.9 (18.9)	6.1 (0.5)
	pyroclastite	9.9 (4.2)	31.5 (12.7)	3.8 (1.2)
Vulcanello (third cycle)	lava flow	10.6 (1.5)	27.6 (5.0)	3.7 (0.5)
	pyroclastite	9.3 (3.6)	22.7 (10.5)	4.0 (1.5)

Table 5.2: cp. Chiozzi et al. 1999

5.2.2 Lipari

With an extent of 37 km², the main island Lipari (38° 29' N, 14° 57' E) is the largest island of the Aeolian Archipelago and is located in the southern Tyrrhenian Sea 30 km off the northern coast of Sicily. Lipari was formed by Strombolian-type eruptions with first andesitic-basaltic volcanism dated at 223 ka.

The eruption of gases with relatively little melt, at regular intervals is called Strombolian eruption. Low eruption columns and low eruption energies are typical. [Schmincke 2004]

Eruptive history on Lipari Island has been subdivided into 4 main cycles of activity. The oldest products were dated to have erupted between 223 - 150 ka before present. Those eruptive products were mainly submarine basaltic lava flows and hyaloclastites⁶, which are now exposed in the western part of the island, and basaltic to andesitic lava flows and pyroclastics, which are exposed in the northern and eastern part of the island [Chiozzi et al. 2001]. The second stage of eruption lasted from 127 - 92 ka and is characterised by high-K andesitic lava flows and pyroclastics, which were produced by the activity of the Mt. S. Angelo and Costa d'Agosto volcanoes within the central part of the island [Ventura et al. 1999]. This second eruptive stage was followed by a long period of quiescence and volcanism was reactivated 50 kyr later in the southern and eastern sector of the island. During the following third stage of activity, resumed volcanism between 42 - 20 ka produced rhyolitic lava domes and rhyolitic to shoshonitic pyroclastics. The fourth stage of eruption lasted from 11.4 - 1.41 ka and was confined to the Gabletto-, Forgia Vecchia- and Pilato- rhyolitic eruptive centers on the northern sector of the island, with rhyolitic obsidian lava flows and pyroclastics [Bruno et al. 2000]. In the 6th century AD, the last known volcanic activity on Lipari Island formed the rhyolitic pumice cone Monte Pilato, which showed several explosive eruptions, ending with the extrusion of the Rocche Rosse obsidian lava flow [Dellino & La Volpe 1994].

⁶Hyaloclastite is a hydrated tuff-breccia, which is formed by volcanic eruptions under water or ice.

Currently only low-temperature fumaroles and hot springs confirm volcanic activity on Lipari [Bruno et al. 2000].

P. Chiozzi gave a good description of the main mineral content of investigated rocks exposed on Lipari and Vulcano Island:

Basaltic andesites on Lipari and Vulcano contain mainly phenocrysts of plagioclase, clinopyroxene and orthopyroxene in a fine-grained groundmass. Furthermore, biotite, red-brown hornblende phenocrysts and olivine relics can be found. Andesites also contain mainly phenocrysts of plagioclase, clinopyroxene and orthopyroxene. Additionally cordierite, silimanite and garnet can be found. In trachybasalts, tephrites and trachytes, plagioclase is the dominant phenocryst, which is joined to K-feldspar in the groundmass.

Rhyolites show low abundance of plagioclase, clinopyroxene and K-feldspar, which can be found either in a spherulitic fine-grained groundmass welded by brown glass or in a densely packed spherulitic groundmass, indicating hydrothermal alteration processes. [Chiozzi et al. 2001]

Volcanic deposits on Lipari Island can also be classified by their different petrochemical characteristics. Four different volcanic cycles can be characterised and within these cycles two temporal and geochemically distinct series can be recognized [Chiozzi et al. 1998]:

The first two volcanic cycles are mainly characterized by basaltic-andesitic lava flows, cropping out in the western and north-western part of the island. The other two cycles are characterized by rhyolitic domes, obsidian lava flows and pumice deposits in the southern and north-eastern part of the island.

Previous radiometric surveys:

[Chiozzi et al. 2001, Chiozzi et al. 1998]

A ground radiometric survey was carried out by *P. Chiozzi et al.* during two campaigns in June and September 1996. Gamma-ray spectra were acquired at 177 sites on Lipari and Vulcano, whereas 117 samples were recorded on Lipari. The results of this survey allow the delineation of two radiometric districts, whereas the first corresponds to the earlier mafic stage of the first and second volcanic cycle (223 - 50 ka) and the second corresponds to the felsic stage of the third and fourth cycle (< 50 ka) [cp. Fig. 5.38]. Samples of the first radiometric district show low eU concentrations, with the highest values for lava flows of the second volcanic cycle (5.2 ppm). In felsic rocks of the second cycle, the eU concentrations are approximately four times higher, with the maximum in rhyolitic obsidians (20.0 ppm). Furthermore the studies showed that eU is generally spatially related to both, eTh and K. Thus, the lowest K concentrations could be found within the first two volcanic cycles (mean concentration 2.3 %), with the lowest value in the basaltic-andesite pyroclastite (1.8 %). The highest K concentrations were found in rocks of the third and fourth cycle, with a mean value of 5.1 %. Mean concentrations of eTh range from 10.1 ppm in pyroclastites of the first and second cycle to 57.8 ppm in lava-flows of the third and fourth cycle.

The air absorbed dose rate, which was calculated for each sample, ranges between 20

and 470 nGy/h. The minimum was calculated for pyroclastites of basaltic composition and the maximum was found over rhyolitic obsidians. A general decrease could be found for the Th/U, K/Th and K/U ratios from the oldest to the more recent volcanic cycles. The calculated ratios range between 3.1 - 3.5 for Th/U, 1140 - 2355 for K/Th and 3465 - 8090 for K/Th.

High radioelement abundance in felsic rocks demonstrates the tendency of uranium and thorium to segregate from other rock-forming constituents during magma evolution.

Magmatic series	Rock type (volcanic cycle)		Site number	U (ppm)	Th (ppm)	K (%)	Dose rate (n Gy h ⁻¹)
Calc-alkaline High-K calc-alkaline(Lipari)	Basaltic andesite (I)	Lava flow	9	3.8 (1.3)	12.4 (4.5)	2.7 (0.8)	89.0 (28.6)
		Pyroclastite	21	2.7 (2.1)	9.2 (7.2)	1.8 (1.1)	63.2 (43.0)
	Andesite (II)	Lava flow	15	5.2 (1.5)	16.6 (4.8)	3.0 (1.0)	112.7 (32.3)
		Pyroclastite	11	3.5 (1.5)	11.9 (4.5)	2.0 (1.0)	76.8 (26.7)
	Rhyolite (III)	Lava flow	10	15.9 (5.1)	48.3 (13.9)	4.9 (1.3)	279.0 (81.1)
		Pyroclastite	11	18.1 (5.5)	57.7 (17.2)	5.3 (1.1)	322.2 (87.4)
		Pumice	23	16.4 (3.7)	51.1 (11.5)	4.9 (1.0)	290.7 (60.1)
	Rhyolitic obsidian (III)	Lava flow	17	20.0 (3.5)	63.4 (10.0)	5.5 (1.0)	350.1 (57.8)
	Trachyandesite-trachybasalt (I)	Lava flow	12	2.9 (0.8)	10.3 (2.7)	2.5 (0.7)	75.3 (19.4)
		Pyroclastite	2	3.4 (0.2)	11.2 (1.4)	2.1 (0.0)	75.6 (5.0)
Shoshonite(Vulcano)	Trachybasalt (II)	Pyroclastite	5	3.0 (0.6)	10.0 (1.6)	1.9 (0.5)	68.1 (14.1)
	Tephrite (III)	Lava flow	2	3.1 (0.1)	9.9 (0.6)	3.0 (0.1)	81.6 (0.2)
	Trachyte (III)	Lava flow	12	10.6 (1.0)	27.6 (3.0)	3.7 (0.5)	179.9 (18.2)
		Pyroclastite	20	8.9 (3.8)	26.2 (11.1)	3.6 (1.3)	165.8 (64.2)
	Rhyolite (III)	Lava flow	4	15.7 (3.0)	49.5 (7.3)	4.8 (0.7)	280.9 (44.0)
	Rhyolitic obsidian (III)	Lava flow	3	19.2 (5.0)	65.9 (18.9)	6.1 (0.5)	360.9 (84.0)

Figure 5.38: Radioelement concentrations for different rock-types on Lipari and Vulcano Island [Chiozzi et al. 2001]

5.2.3 The airborne geophysical survey of the GSA

The airborne geophysical surveys on the Aeolian Islands were performed as a cooperation work of the Geological Survey of Austria, the Geological Survey of Japan and the Istituto Nazionale di Geofisica e Vulcanologia of Rome. The surveys were financially supported by the European Commission, the Austrian Science Foundation, the Geological Survey of Japan, the Istituto Nazionale di Geofisica e Vulcanologia and the Austrian Exchange Service (ÖAD). Between 1999 and 2004 several airborne geophysical surveys were conducted on the Aeolian Islands, including Vulcano, Lipari, Salina, Panarea and Stromboli. In the frame of the surveys, aeromagnetic -, laser altimeter -, and gamma-ray - data were collected.

The survey in 1999 included 19 profiles in NW-SE direction, which covered the whole island of Vulcano, the sea between Vulcano and Lipari, and the south-western part and the submerged flanks of Lipari Island. Flight line spacing was chosen to be 250 m and tie lines were flown with a separation of approximately 3000 m. Due to rugged topography and with respect to densely populated areas, average ground clearance was 150 m. Radiometric data of this survey has not been inspected in the

frame of this work.

In 2002, a regional airborne geophysical survey was flown over a large area covering the islands of Stromboli and Panarea. The survey was flown with an AS350 B2 helicopter and included 17 lines, which were orientated in NE-SW direction, at a spacing of 1500 m and an average survey altitude of 100 m. Some of the lines were extended to cover parts of Lipari and Salina.

In 2002 a second survey was conducted over the island of Vulcano and the southwestern part of Lipari. 19 flight-lines were flown in NW-SE direction, at an average line spacing of 250 m and a ground clearance of approximately 150 m. The whole survey of 2002 was impaired by heavy rainfall, what influenced not only the survey altitude, but also the amount of gamma-radiation detected by the spectrometer.

In 2004 a more detailed survey was conducted over Stromboli, including 10 survey lines in NE-SW direction at a spacing of 750 m and one single spiral line. Over the island of Panarea and its surroundings a survey was conducted at approximately 250 m line spacing. 11 lines with an average ground clearance of 150 m covered the island of Panarea in WNW-ESE direction. A third survey in 2004 was flown over the islands of Salina, Lipari and Vulcano. The islands of Vulcano and Lipari were covered by a dense pattern of flight lines with an average spacing of 100 - 125 m. The lines were flown in NW-SE direction at an average ground clearance of 150 m. Each fourth line was further extended to the north-west, covering the island of Salina at a line spacing of 400 - 500 m.

The locations of the flight lines over the islands of Vulcano and Lipari for the two surveys in 2002 and 2004 are presented in Fig. 5.39 and 5.40.

For all of the surveys, horizontal and vertical orientation and navigation of the helicopter was rendered by the use of a GPS receiver and a laser altimeter, respectively. It also has to be mentioned that only one NaI(Tl) crystal was installed on board of the helicopter and therefore the detected count rates were pretty small.

The aeromagnetic surveys were performed with the use of an optically pumped magnetometer (Scintrex CS-2), which was towed 30 m below the helicopter. Both, short- and long-wavelength anomalies could be identified, whereas short wavelengths characterise shallow rocks and long wavelengths characterise deeper bodies and the regional character of tectonic features [Supper et al. 2004].

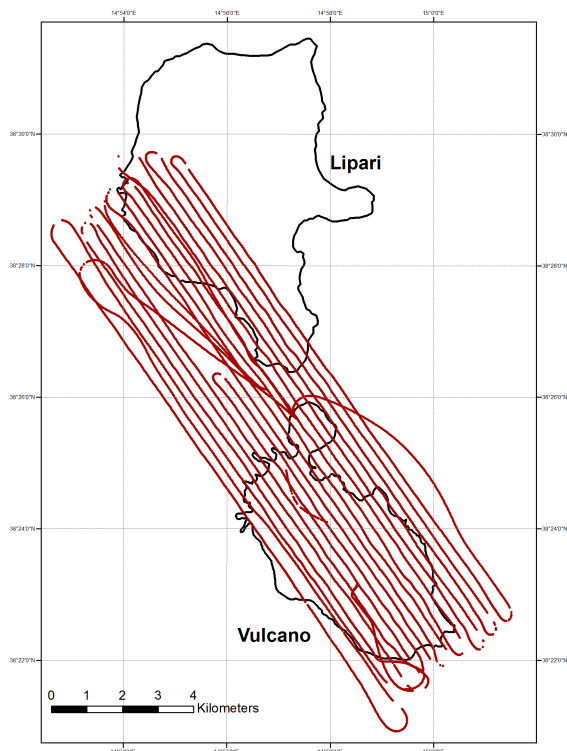


Figure 5.39: Flight lines of the Vulcano-Lipari survey in 2002

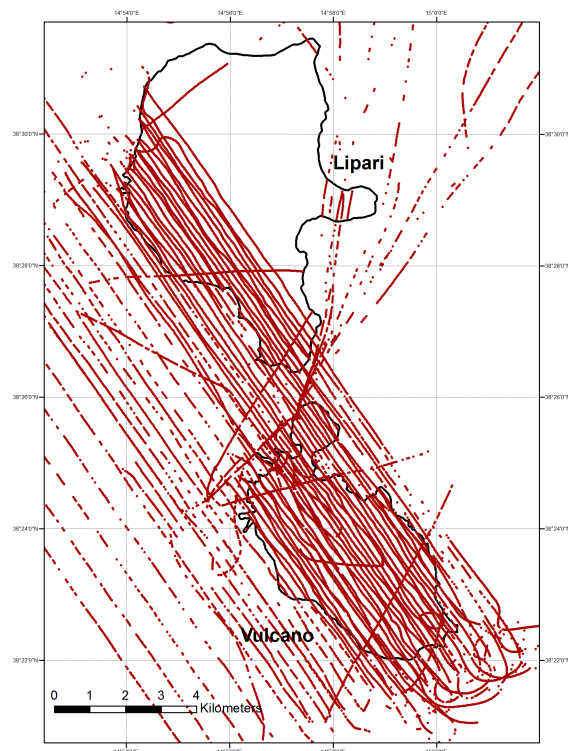


Figure 5.40: Flight lines of the Vulcano-Lipari survey in 2004

5.2.4 Processing of gamma-ray spectrometer data

Prior to processing, data was inspected for incorrect values and in particular all samples, which were taken at altitude higher than 400 m were deleted.

The calibration constants and coefficients, which were used for the processing of gamma-ray data of the Aeolian Islands are presented in table 5.3. The sensitivity and stripping coefficients, as well as the cosmic-background coefficients were determined by the GSA several years ago. The aircraft-background coefficients and the height attenuation coefficients have to be determined for each survey and in that case have been determined in subsections 4.1.4 and 4.1.7, respectively. The height attenuation coefficients have been determined from the climb-flight in 2002 and therefore, the height-correction did not work properly for the survey in 2004. This can be seen as parallel stripes in the radioelement maps [cp. especially Fig. 5.53]. The change of stripping coefficients with altitude is given by the IAEA [cp. IAEA 2003].

The average gamma-ray spectrum of the whole survey over Vulcano and Lipari Island is presented in Fig. 5.41. The average spectrum was calculated by computing the mean count rate of each channel over the whole dataset.

	^{40}K	^{238}U	^{232}Th	TC
Aircraft Background	43.2	19.2	10.4	71
Cosmic Background	0.083	0.043	0.059	1.9
Attenuation by air	-0.0057	-0.0048	-0.0041	-0.0044
Sensitivity	47.2	7.3	3.4	29.5
Stripping Coefficients	0.2	0.26	0.74	0.05
SC altitude increase	0.00049	0.00065	0.00069	0

Table 5.3: Calibration constants and coefficients for the Aeolian Islands

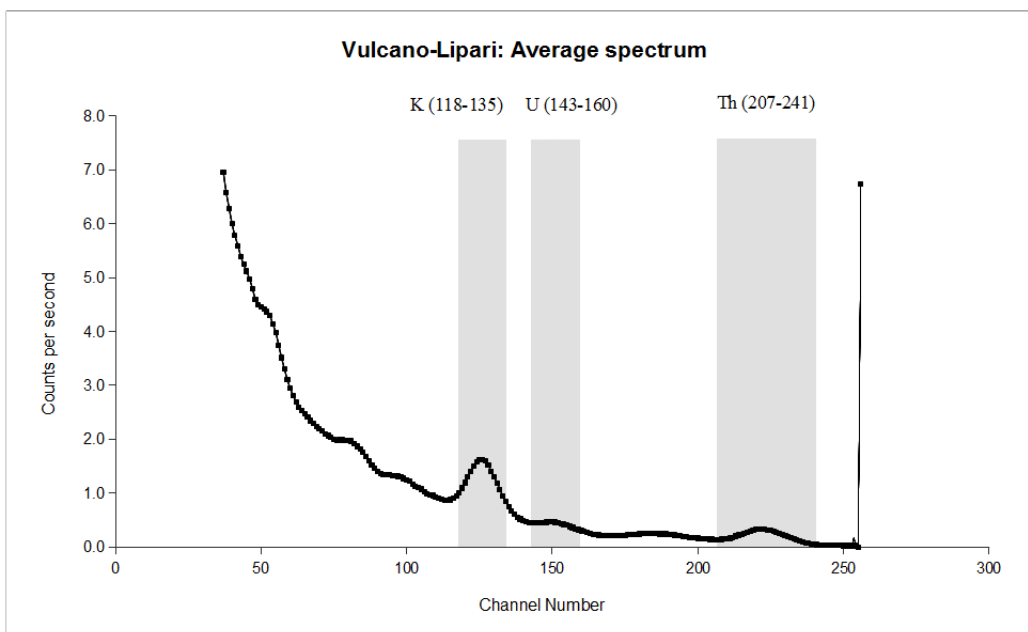


Figure 5.41: Average gamma-ray spectrum of Vulcano and Lipari Island

Gamma-ray data of the survey in 2004 was first processed in one single processing job and then separately for each sub-survey. Stromboli and Panarea were processed separately. Salina, Lipari and Vulcano had to be processed in common, as they belonged to the same sub-survey.

Processing was performed both, with and without the use of PCA smoothed spectra. Radon removal was run with the spectral-ratio method.

The best gridding results for all surveys of the Aeolian Islands could be achieved with the gridding-method kriging. It was pretty challenging to find the appropriate grid-node spacing for each of the surveys, as they were all flown at different line-spacing. Data from the Stromboli-survey in 2004 has been gridded at a 750 m grid and with a search radius of 1000 m. As the resulting radioelement maps were too rough to identify any geologic structures, data has not been further investigated. Radiometric data from the Stromboli-survey in 2002 was even worse, as gamma-radiation had been attenuated by heavy rainfall. The radioelement maps of the Stromboli-survey in 2004 are shown in Fig. 5.42.

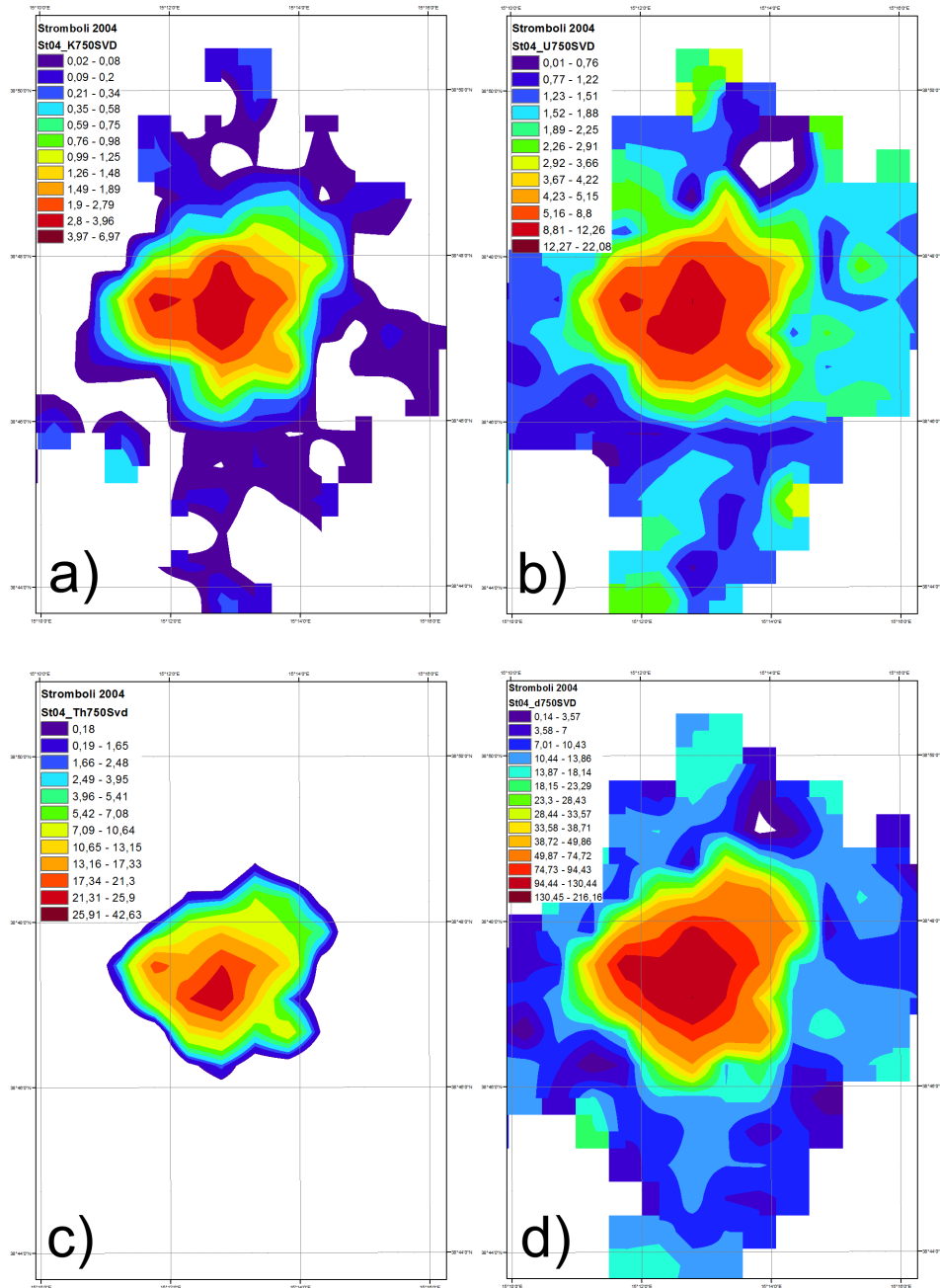


Figure 5.42: Concentrations detected at the Stromboli survey in 2004 (750 m grid): a) K [%], b) U [ppm], c) Th [ppm], d) dose [nGy/h]; Processing performed with the use of NASVD smoothed spectra

Data from the Panarea-survey was gridded on a 250 m grid with a search radius of 300 m. Although the island was covered by 11 flight-lines and data quality was pretty good, it was difficult to identify any geologic structures because of the small size of the island (2.5 km²). The radioelement maps of the Panarea-survey in 2004 are shown in Fig. 5.43.

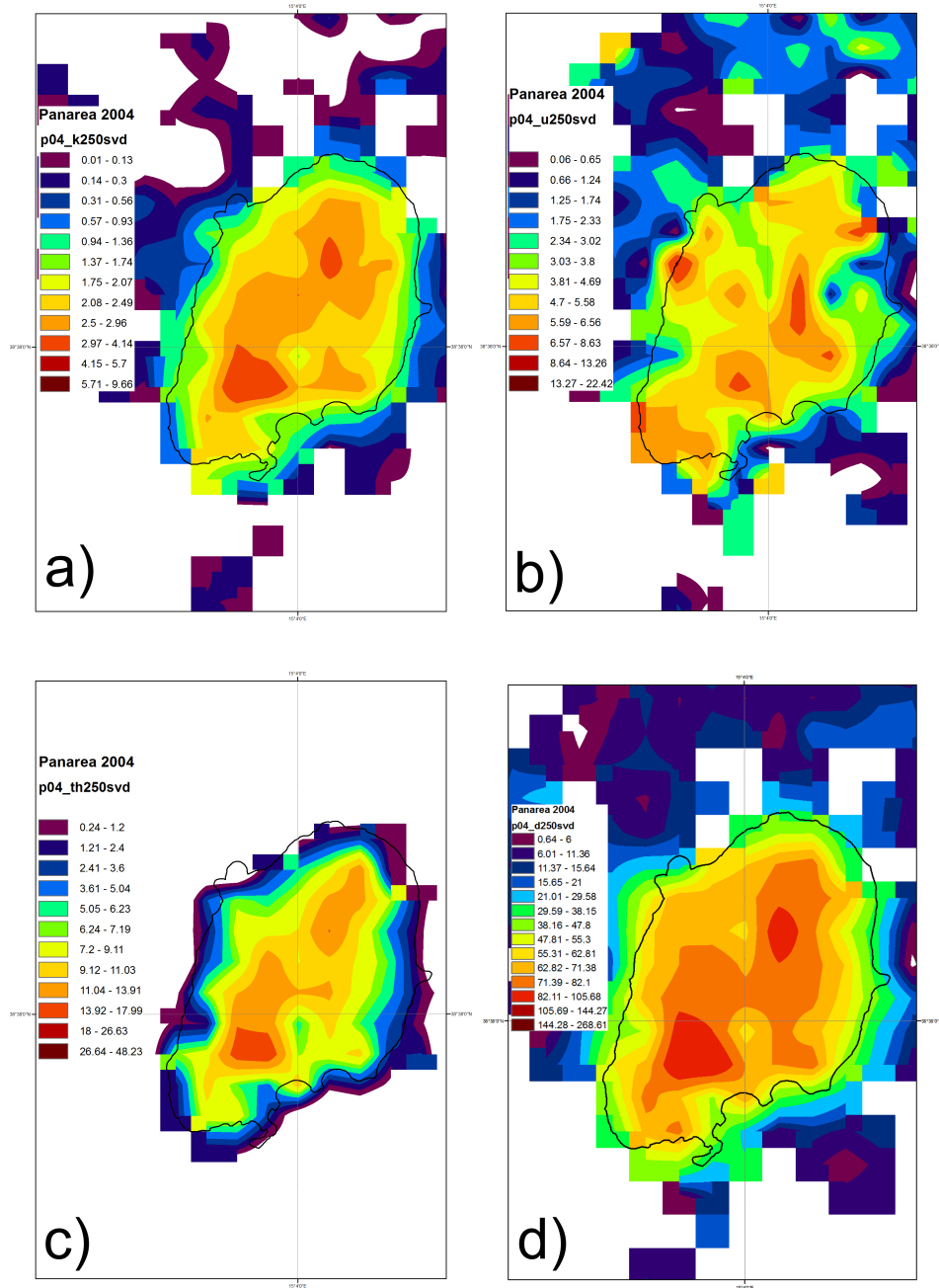


Figure 5.43: Concentrations detected at the Panarea survey in 2004 (250 m grid): a) K [%], b) U [ppm], c) Th [ppm], d) dose [nGy/h]; Processing performed with the use of NASVD smoothed spectra

Data from the Salina-survey was gridded on a 500 m grid. Because of the low flight-line density and the low radioactivity of the rocks on Salina, data from this survey was sparse and the identification of geologic units was hardly possible. No interpretation of gamma-ray data from Salina has been made. The radioelement maps of the Salina-survey in 2004 are shown in Fig. 5.44.

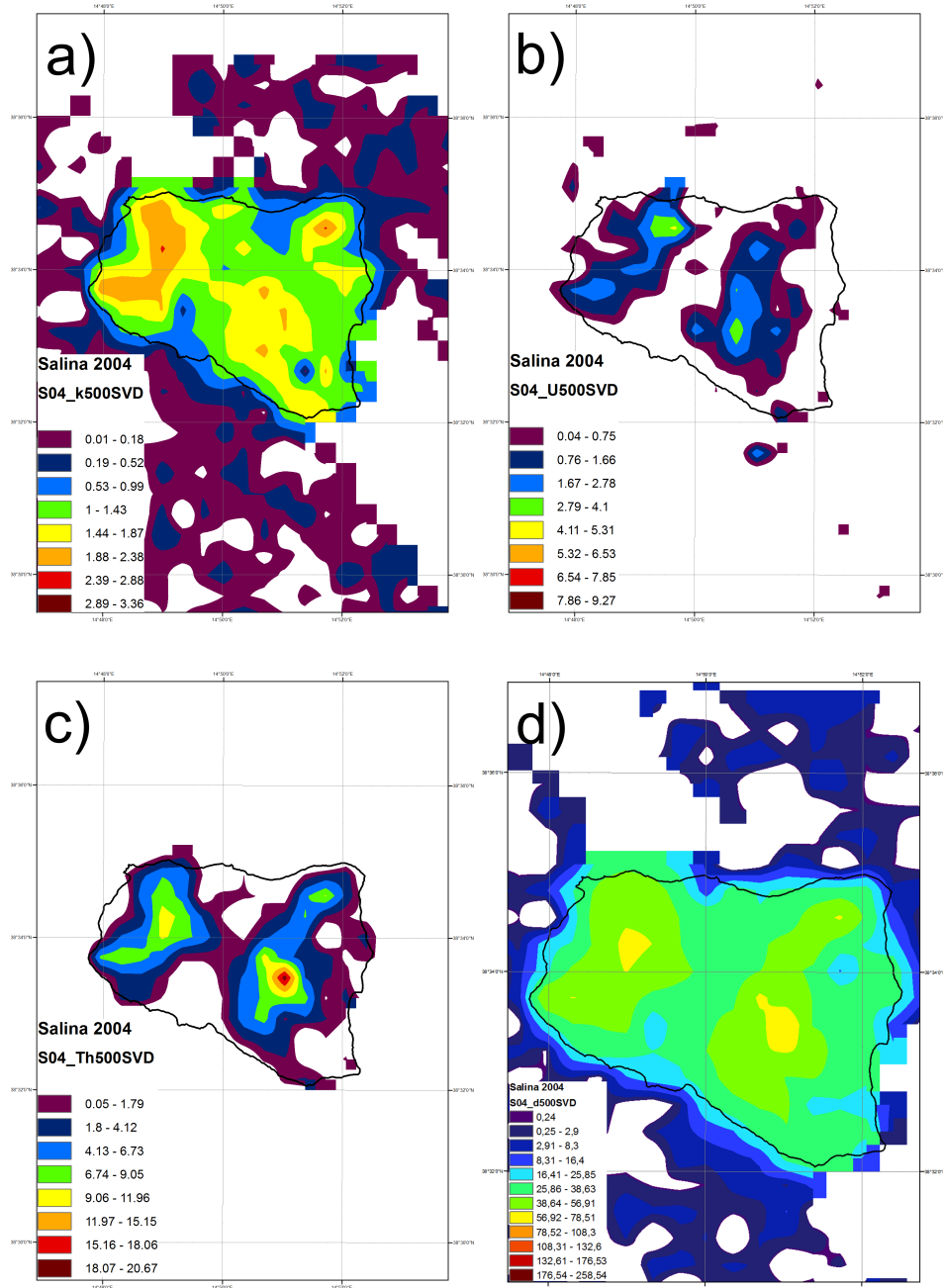


Figure 5.44: Concentrations detected at the Salina survey in 2004 (500 m grid): a) K [%], b) U [ppm], c) Th [ppm], d) dose [nGy/h]; Processing performed with the use of NASVD smoothed spectra

Data from the Vulcano-Lipari-survey in 2004 was gridded on a 125 m grid with a search radius of 175 m. From all surveys on the Aeolian Islands, this survey yielded the most detailed dataset and the best results. Data from the survey in 2002 was gridded on a 175 m grid with a search radius of 200 m. Due to heavy rainfall during the survey, ground concentrations of the radioelements K, U and Th were reduced by about their

half. The radioelement maps of the Vulcano- and Lipari-survey in 2002 are shown in Fig. 5.45 and Fig. 5.46. The radioelement maps of the Vulcano- and Lipari-survey in 2004 are shown in Fig. 5.47 to Fig. 5.52.

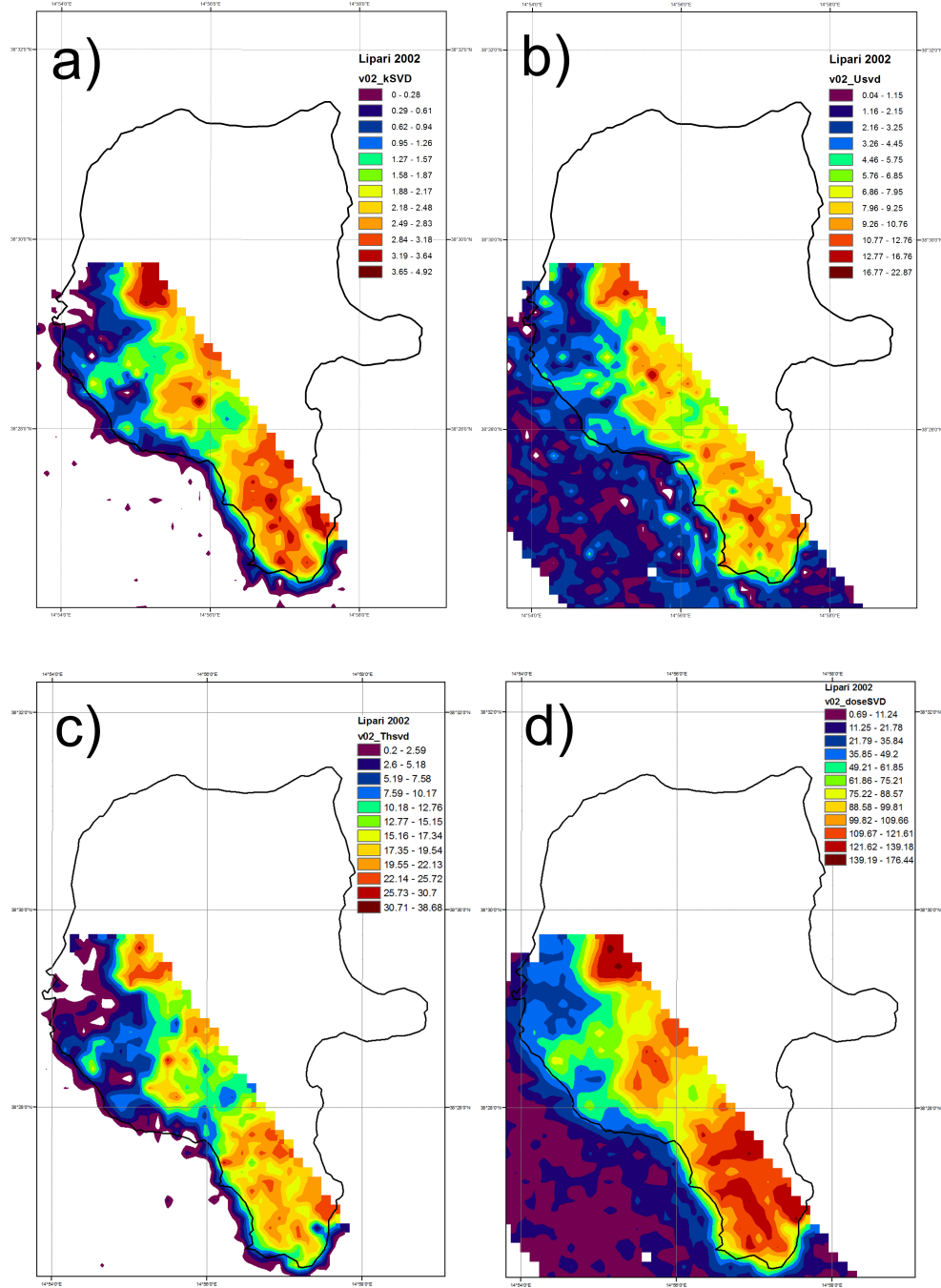


Figure 5.45: Concentrations detected at the Lipari survey in 2002 (175 m grid): a) K [%], b) U [ppm], c) Th [ppm], d) dose [nGy/h]; Processing performed with the use of NASVD smoothed spectra

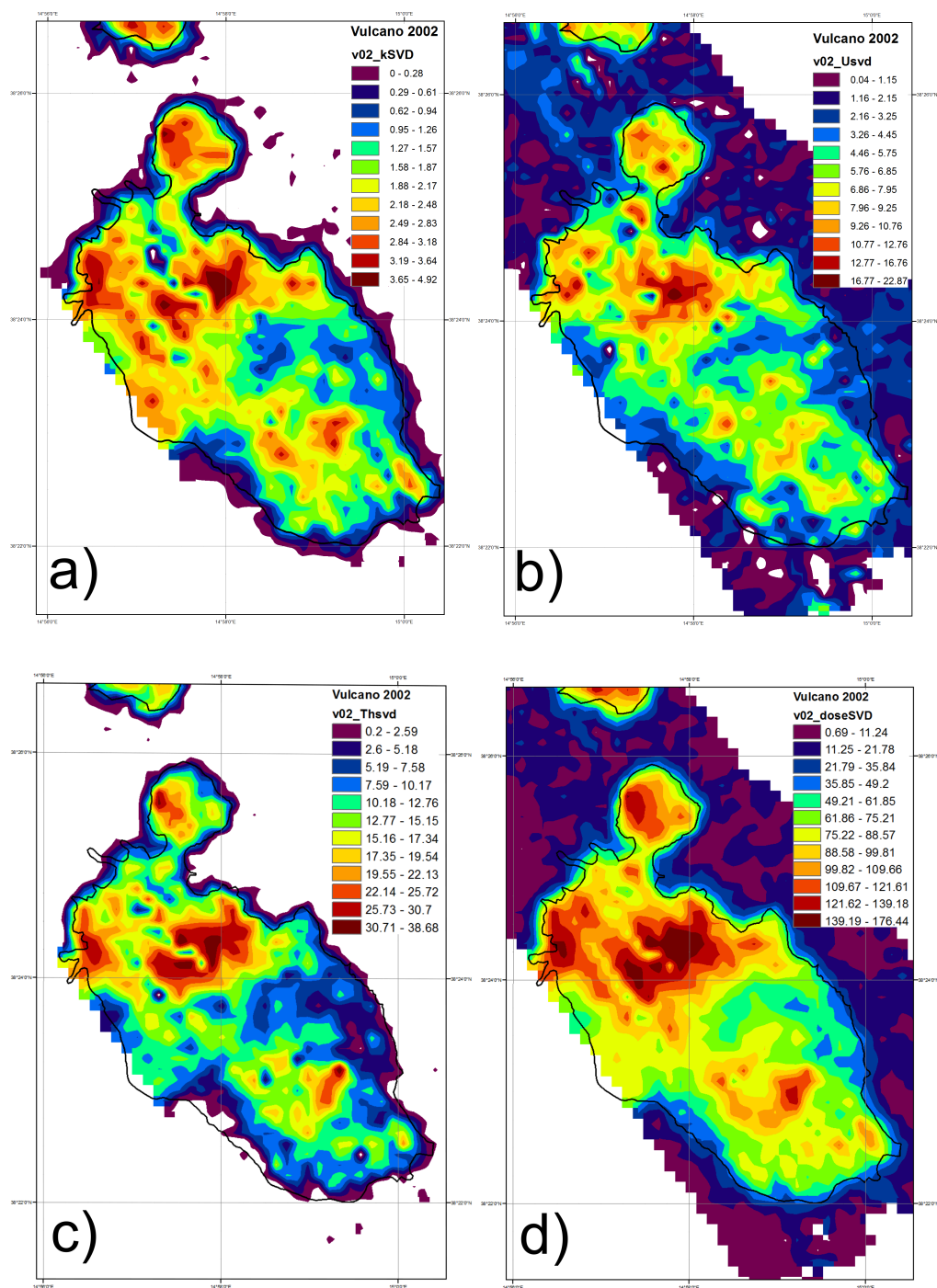


Figure 5.46: Concentrations detected at the Vulcano survey in 2002 (175 m grid): a) K [%], b) U [ppm], c) Th [ppm], d) dose [nGy/h]; Processing performed with the use of NASVD smoothed spectra

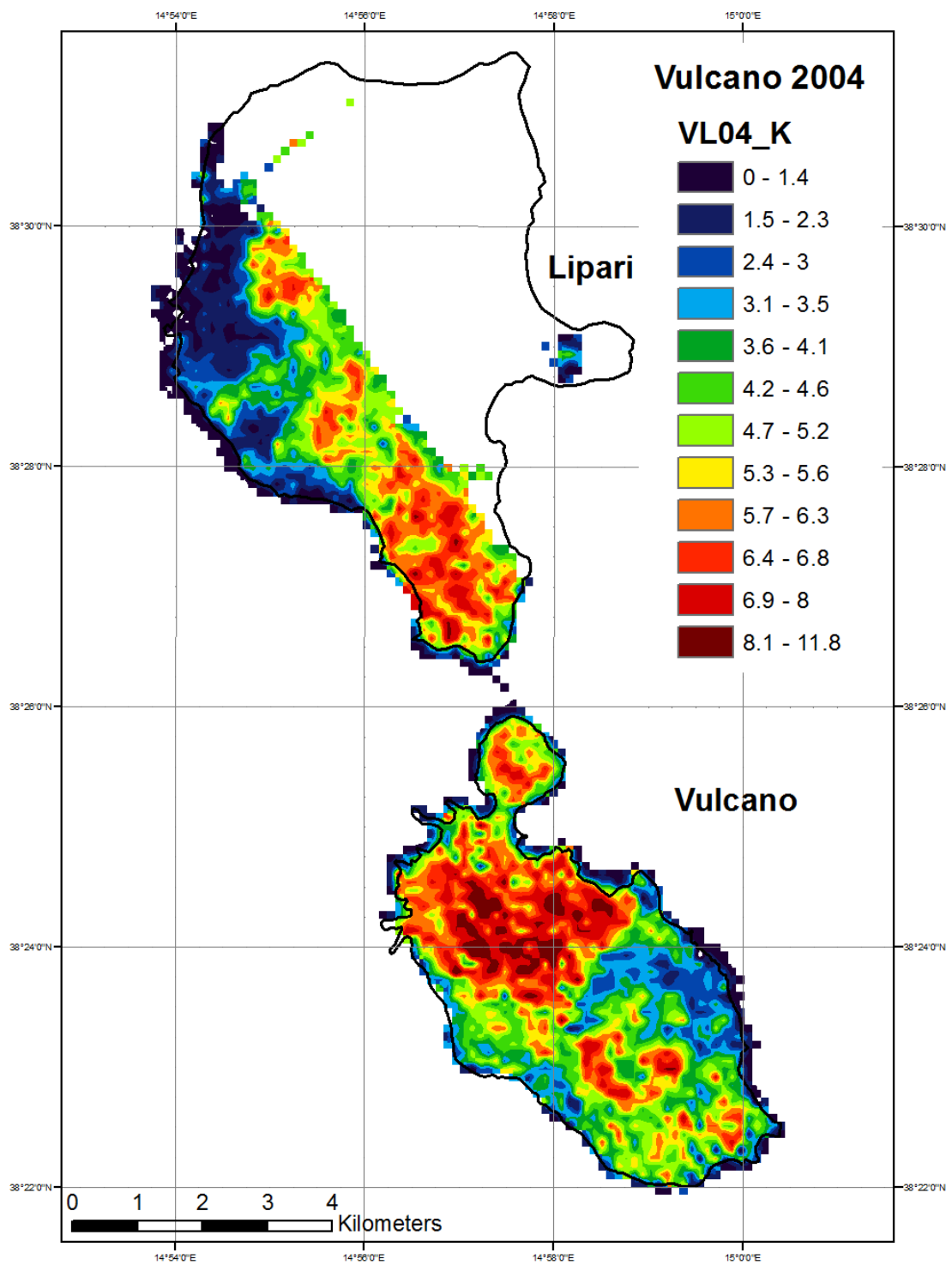


Figure 5.47: Ground concentrations detected at the Vulcano-Lipari survey in 2004 (125 m grid); Standard window based processing: K [%]

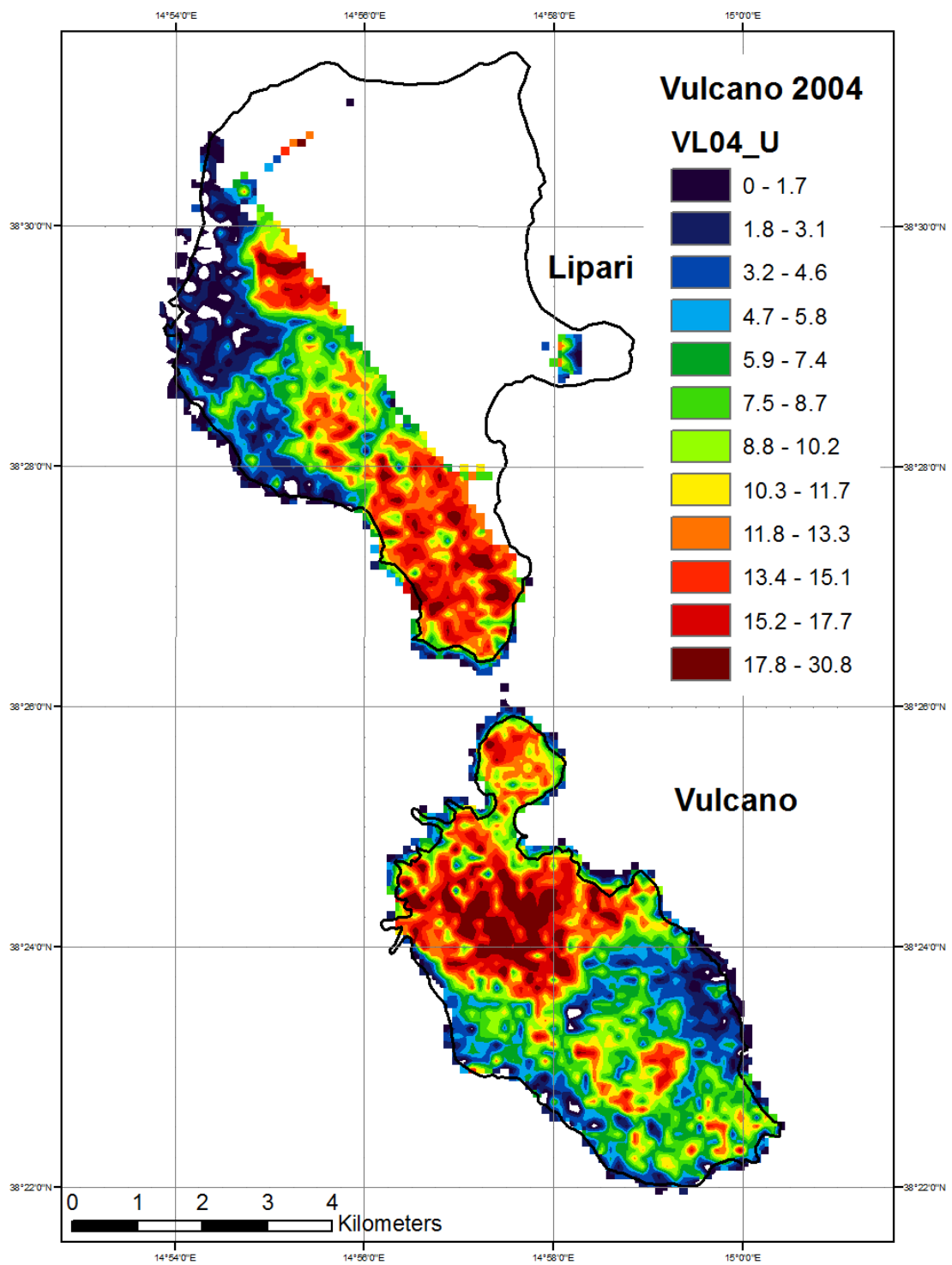


Figure 5.48: Ground concentrations detected at the Vulcano-Lipari survey in 2004 (125 m grid); Standard window based processing: U [ppm]

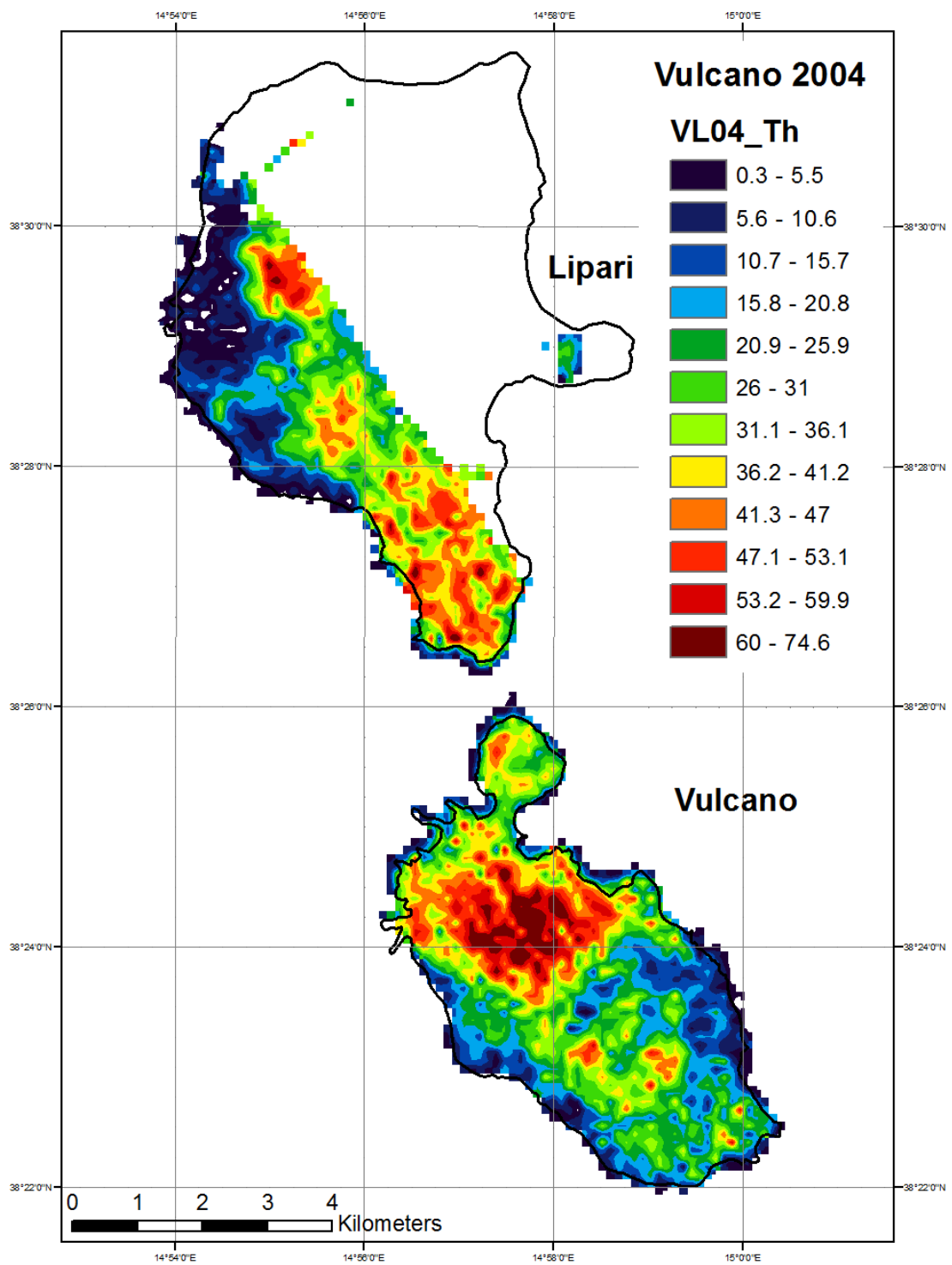


Figure 5.49: Ground concentrations detected at the Vulcano-Lipari survey in 2004 (125 m grid); Standard window based processing: Th [ppm]

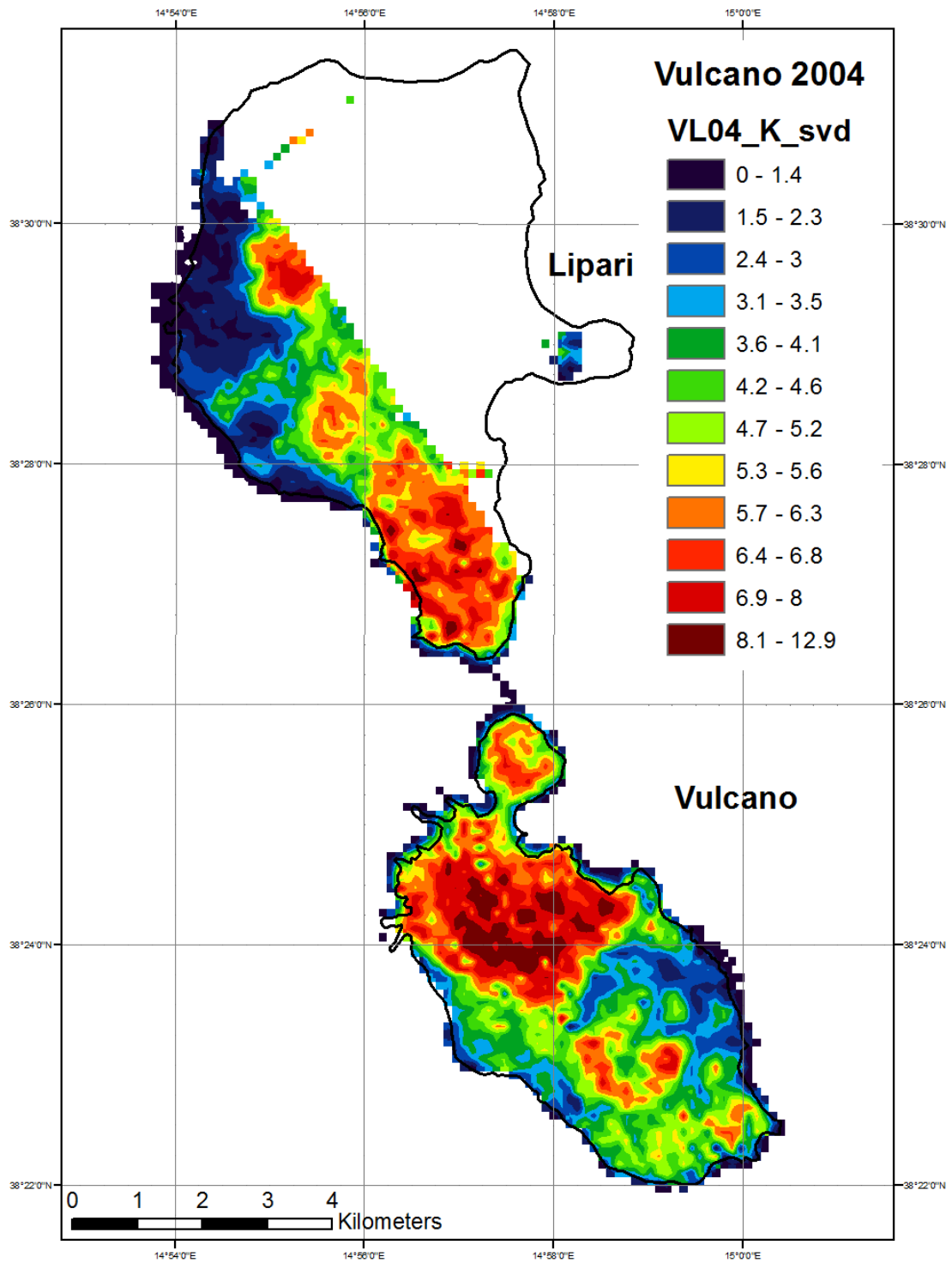


Figure 5.50: Ground concentrations detected at the Vulcano-Lipari survey in 2004 (125 m grid); Processing performed with the use of NASVD smoothed spectra: K [%]

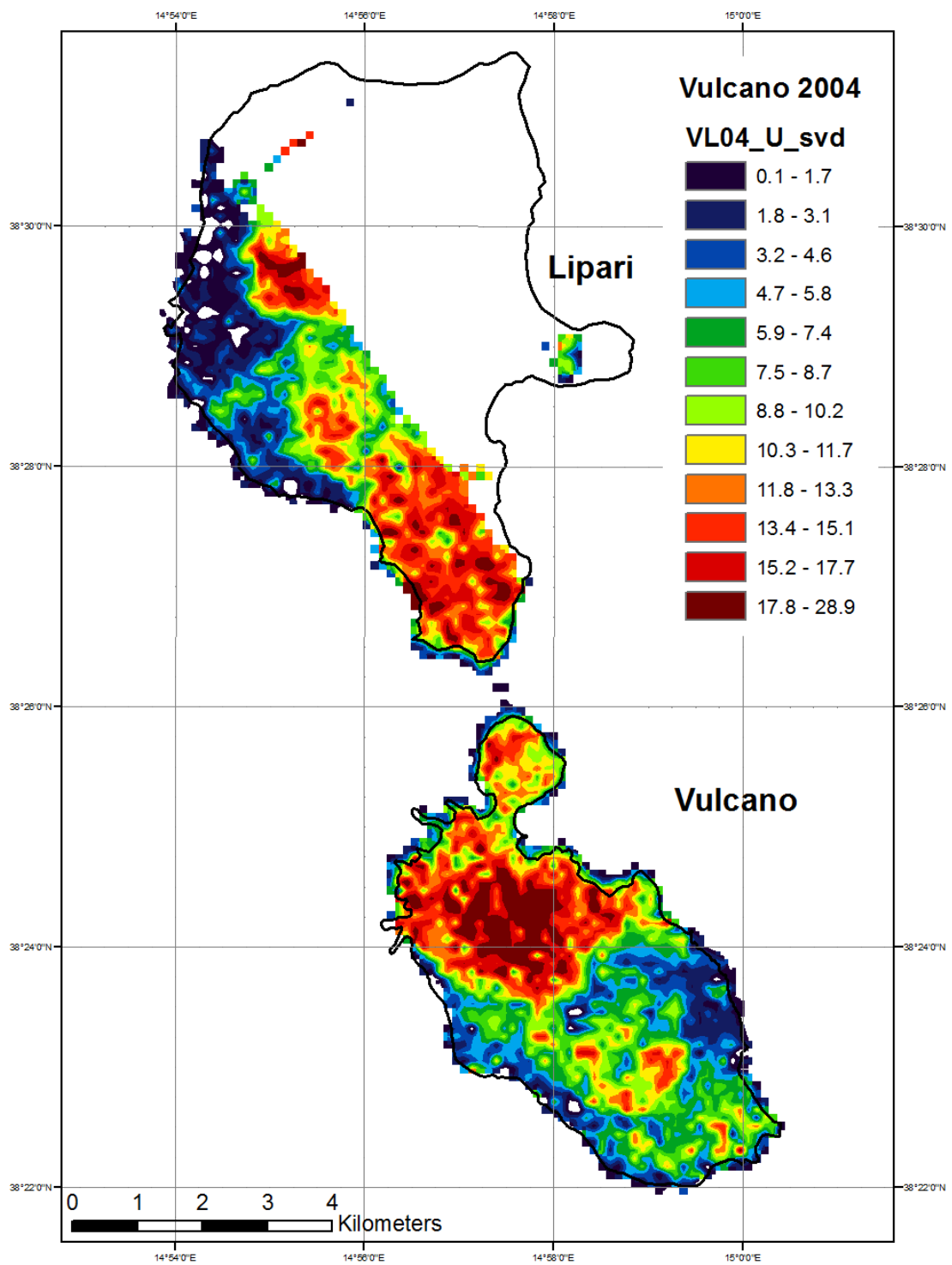


Figure 5.51: Ground concentrations detected at the Vulcano-Lipari survey in 2004 (125 m grid); Processing performed with the use of NASVD smoothed spectra: U [ppm]

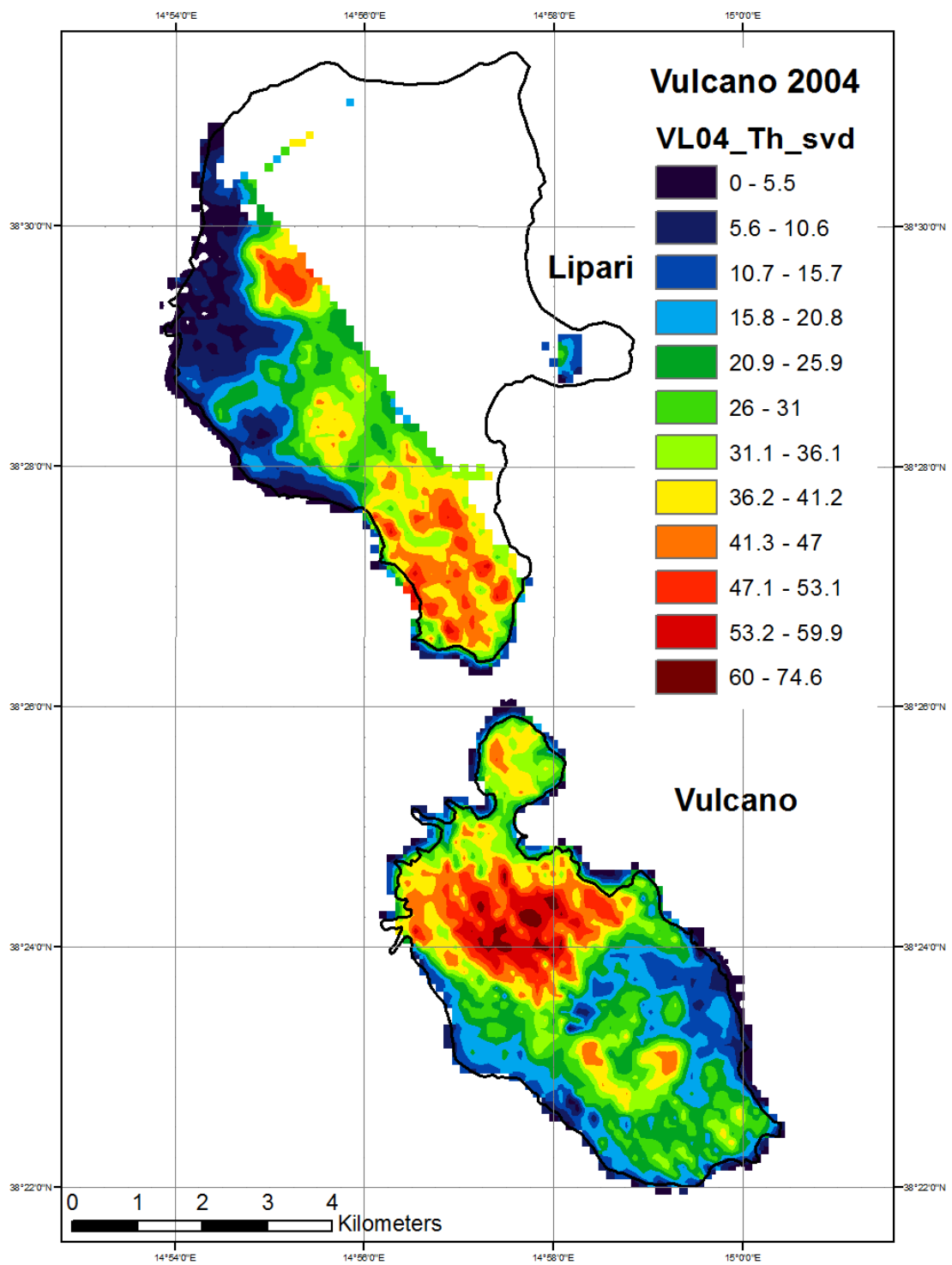


Figure 5.52: Ground concentrations detected at the Vulcano-Lipari survey in 2004 (125 m grid); Processing performed with the use of NASVD smoothed spectra: Th [ppm]

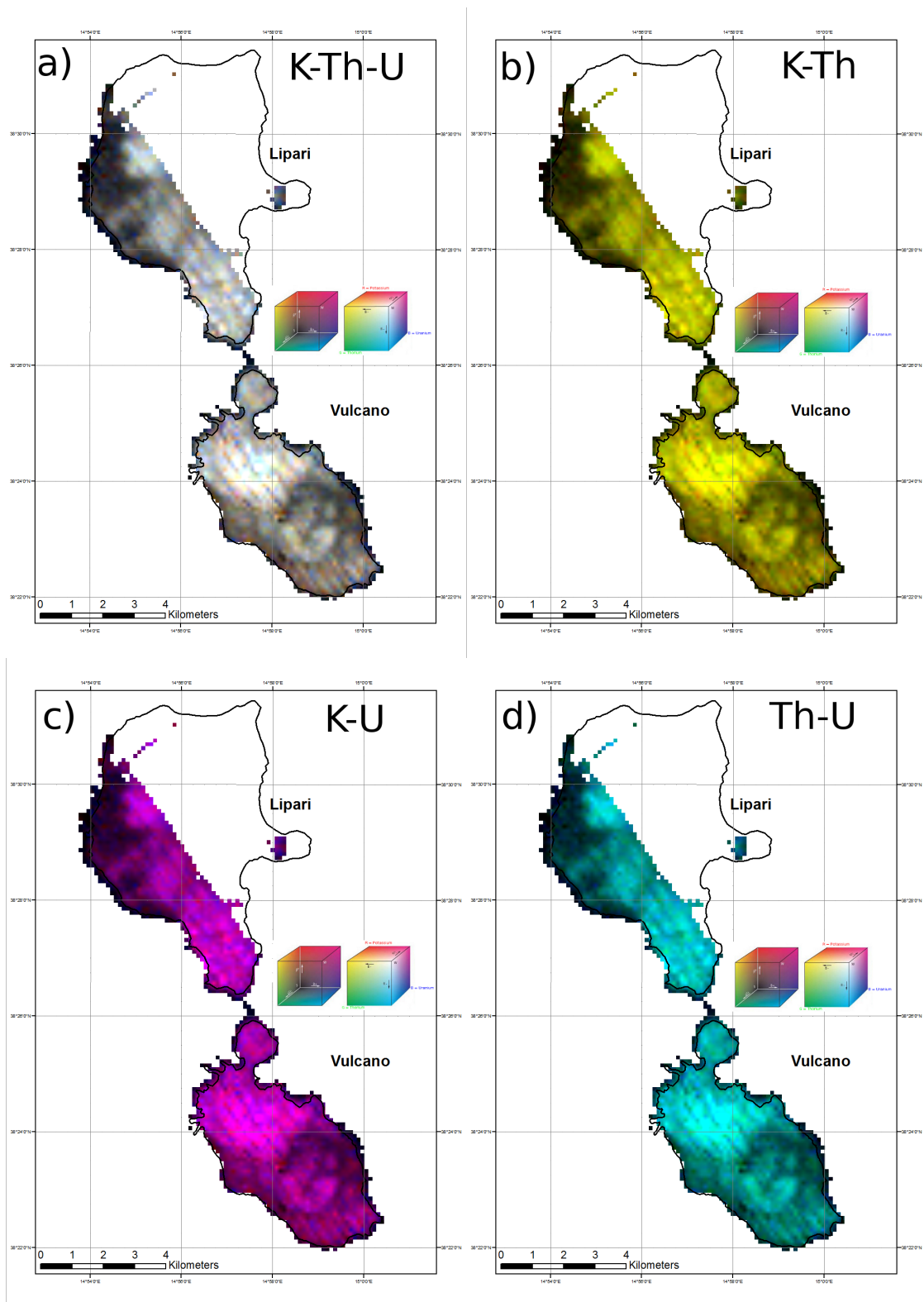


Figure 5.53: Ternary radioelement maps of the Vulcano-Lipari survey in 2004: a) K-Th-U, b) K-Th, c) K-U, d) Th-U

Interpretation of gamma-ray data of the Aeolian Islands was performed with the combined use of radioelement maps, ternary maps, detailed satellite images and several pre-existing geologic maps. The ternary radioelement maps of Lipari and Vulcano are shown in Fig. 5.53. As the radioelements seem to be positively correlated over all geologic units of the two islands, only a kind of light/dark differentiation - corresponding to low radioactivity and high radioactivity - can be made. Thus, the ternary maps were no great help for interpretation. Main geologic maps used for interpretation were the detailed geologic map of *J. Keller* [Keller 1970] for Vulcano and the geologic map of *C.A. Tranne* [Tranne et al. 2002] for Lipari.

5.2.5 Description of Geologic Units

Vulcano

Vulcano Primordiale:

Vulcano Primordiale is the remnant of a composite cone with a central summit caldera (Piano Caldera). It is the oldest structure on Vulcano Island (120 - 100 ka) and is mainly composed of lava flows and scoriae deposits. Subordinately, fine grained pyroclastic units occur. [De Astis et al. 1997]

The tuffs of Monte Aria region, which were deposited on the south-eastern flanks of Primordial Vulcano, represent the final activity of the stratovolcano [Keller 1970].

On the K_2O - SiO_2 classification diagram, rocks of this unit plot in the fields of high-K calc-alkaline series and to a minor extent in the shoshonitic field. [De Astis et al. 1997]

Trachybasaltic to trachyandesitic lavas of Vulcano Primordiale show the lowest ground concentrations of K, U and Th. With 2.9 - 3.8 % K, 3.6 ppm U and 14.0 - 15.2 ppm Th, the mean radioelement concentrations are slightly higher than the average crustal abundances. The air absorbed dose rate over this unit is between 75 and 86 nGy/h in average [cp. Appendix B, Vulcano 2004, Id 10]. Three areas could be delineated and assigned to the Primordial Vulcano unit, whereas only two of them show similar radioelement concentrations (Primordiale SW, Primordiale SE). Those two features have a rather exposed position in the ternary radioelement diagram, distinctly showing the highest relative concentrations of K [cp. Fig. 5.54]. A third area (Primordiale S) which eventually belongs to the Primordiale Vulcano unit, shows higher radioelement concentrations in the range of 4.3 % K, 6.4 ppm U and 22.3 ppm Th. These higher ground concentrations are probably due to lava flows and pyroclastics of the second and third volcanic cycle that partly overlay lavas of Primordial Vulcano.

The airborne survey in 2002 shows significantly lower radioelement concentrations of 1.3 - 1.4 % K, 1.6 - 2.8 ppm U and 6.5 - 6.9 ppm Th for Primordiale SW and Primordiale SE, and 1.7 % K, 4.1 ppm U and 12.6 ppm Th for Primordiale S. [cp. Appendix B, Vulcano 2002, Id 10 and 8]

Compared to ground-radiometric data from *P. Chiozzi* the radioelement concentrations computed from the aero-radiometric survey in 2004 are slightly higher, but in the same range [cp. table 5.2].

Piano Caldera:

This unit refers to volcanic products erupted between 98 and 20 ka. These are lava flows and pyroclastic deposits emplaced inside the caldera and on the flanks of Primordial Vulcano. Between 98 and 78 ka, a thick lava flow sequence erupted from ring faults and was followed by tuff and scoriae deposits. Between 50 and 20 ka, activity shifted from SE to NW and formed the south-eastern sectors of the Fossa Caldera. Volcanism also reassumed on the southern and western flanks of Primordial Vulcano between 25 and 20 ka. Rocks of Caldera del Piano are geochemically similar to Vulcano Primordiale, even though rocks composing the Piano Caldera show larger variations of several compositional parameters. This is probably due to the presence of trachytes. [De Astis et al. 1997]

Due to the larger variation in compositional parameters, rocks of Caldera del Piano also show larger variation in radioelement concentration. Therefore, two classes of rocks belonging to the Caldera del Piano unit have been delineated by their radioelement concentration. The first class shows low radioelement concentrations, comparable to those of Vulcano Primordiale. Two features have been delineated: The pyroclastics of "Monte Molineddo" are mainly composed of stratified lapilli-tuffs and scoriae. The mean radioelement concentrations of this feature are 3.5 % K, 5.5 ppm U and 19.0 ppm Th, and the air absorbed dose rate is approximately 94 nGy/h. Sandy tuffs and welded scoriae of "Piano di Luccia" erupted along the caldera fault and show mean radioelement concentrations of 3.2 % K, 4.5 ppm U and 17.0 ppm Th. The air absorbed dose rate over this feature is 85 nGy/h. [cp. Appendix B, Vulcano 2004, Id 9]

The survey in 2002 shows distinctly lower K- and Th-concentrations for these two features, which are in the range of 1.2 - 1.4 % K, 3.1 - 3.6 ppm U and 9.5 - 11.0 ppm Th. [cp. Appendix B, Vulcano 2002, Id 9]

The second class shows slightly higher radioelement concentrations, which are comparable to those of the Fossa Caldera. Three features have been delineated: "La Sommata" refers to an intracalderical cinder cone of trachybasaltic composition, which shows mean radioelement concentrations of 4.5 % K, 7.4 ppm U and 25.1 ppm Th, and an air absorbed dose rate of 120 nGy/h. "Spiaggia Lunga" and "Quadrara" refer to intensely welded blankets of scoriae and pyroclastic flow deposits of trachyandesitic composition. They show mean radioelement concentrations of 4.4 and 4.9 % K, 6.7 and 7.2 ppm U, and 23.0 and 25.5 ppm Th, respectively. [cp. Appendix B, Vulcano 2004, Id 8]

The airborne survey in 2002 shows significantly lower radioelement concentrations of 1.8 - 2.1 % K, 3.8 - 5.1 ppm U and 10.1 - 15.7 ppm Th for the three features. [cp. Appendix B, Vulcano 2002, Id 8]

Compared to data of the ground-radiometric survey of *P. Chiozzi*, both classes of the airborne survey in 2004 show significantly higher ground concentrations of all radioelements [cp. table 5.2].

One feature, which actually belongs to another unit, has been assigned to the second Piano Caldera class, due to its radioelement signature. Primordiale S shows significantly higher radioelement concentrations than the other two features of Primordial Vulcano. The higher radioelement concentrations of Primordiale S are probably due

to lava flows and pyroclastics of Caldera del Piano and Caldera della Fossa, which overlay Vulcano Primordiale.

La Fossa Caldera:

Volcanics that formed the south-eastern sectors of La Fossa Caldera erupted between 55 and 24 ka [Santacroce et al. 2003]. The collapse of the caldera was probably triggered by the shallow submarine eruption of Tufi di Grotte dei Rossi at 15 ka, the largest explosive eruption on Vulcano [De Astis et al. 1997]. Fossa Caldera deposits, which erupted between 15 and 8 ka were pyroclastic and effusive. Volcanostratigraphic units of this stage of activity tend to become more mafic and alkaline towards the top [De Astis et al. 1997].

Rocks erupted between 55 and 8 ka are related to various volcanic centres and different types of activity. In the K_2O - SiO_2 classification diagram, samples of this unit plotted in the shoshonitic field. Some had a potassic affinity. [De Astis et al. 1997]

Volcanic products of the Fossa Caldera show increased ground concentrations of the radioelements K, U and Th compared to average crustal abundances. Three features have been delineated, two of them having approximately the same mean air absorbed dose rate of 120 nGy/h. Their mean radioelement concentrations are in the range of 4.4 - 4.6 % K, 7.5 - 7.7 ppm U and 25.4 - 27.2 ppm Th. "Piano d'Alighieri" is built by hyaloclastitic lapilli-tuffs and an extended scoriae deposit, which erupted from a fissure system with NS direction. "Tufi di Luccia" refers to a small anomaly, which is probably caused by a small deposit of Tufi di Grotte dei Rossi. The third feature is "Piano Grotte dei Rossi", a large deposit of Tufi di Grotte dei Rossi. Over the fine, brown earthy tuffs of this unit, an air absorbed dose rate of 130 nGy/h was detected. The mean radioelement concentrations of "Piano Grotte dei Rossi" are 4.8 % K, 8.7 ppm U and 27.8 ppm Th. [cp. Appendix B, Vulcano 2004, Id 6]

The survey in 2002 shows lower radioelement concentrations of 1.7 - 1.9 % K, 3.7 - 5.0 ppm U and 11.1 - 15.9 ppm Th. [cp. Appendix B, Vulcano 2002, Id 6]

Compared to data of the ground-radiometric survey by *P. Chiozzi*, ground concentrations computed from the airborne survey in 2004 are higher [cp. table 5.2].

Alluvial and beach deposits:

Alluvial and beach deposits on Vulcano Island show high radioelement concentrations in the range of 5.9 % K, 12.6 ppm U and 35.9 ppm Th, and a mean air absorbed dose rate of approximately 168 nGy/h [cp. Appendix B, Vulcano 2004, Id 4]. These high radioactivity values probably result from the influence of la Fossa di Vulcano, which is very close to Porto di Levante. This area is the most populated area on Vulcano. Thus, radioelement concentrations could also be distorted by radioelements contained in construction materials.

The survey in 2002 shows lower radioelement concentrations of 2.0 % K, 5.9 ppm U and 18.2 ppm Th. [cp. Appendix B, Vulcano 2002, Id 4]

Lentia Complex:

The Lentia Complex is the remnant of a once larger structure, which formed between 24 and 15 ka. It is sited north-east of the Piano Caldera and east of la Fossa Caldera.

It is mainly composed of rhyolitic lava flows and minor extrusive domes, which overlie a sequence of explosive and effusive latitic products. Furthermore, two trachytic lava flows can be found on top of Mt. Lentia. On the $K_2O - SiO_2$ diagram, samples of the Lentia Complex plotted in the fields of latite and rhyolites. [De Astis et al. 1997]

The Lentia Complex shows high ground concentrations of radioelements of 5.9 % K, 13.3 ppm U and 36.9 ppm Th, and an air absorbed dose rate of 170 nGy/h [cp. Appendix B, Vulcano 2004, Id 2]. These high radioactivity values confirm the rhyolitic composition of this unit. The potassium concentration of this feature is higher than that computed from the ground-radiometric survey by *P. Chiozzi*, the thorium- and uranium concentrations are slightly lower [cp. table 5.2].

The airborne survey in 2002 shows distinctly lower radioelement concentrations of 2.9 % K, 7.1 ppm U and 22.5 ppm Th. [cp. Appendix B, Vulcano 2002, Id 2]

La Fossa Cone:

La Fossa Cone is a composite volcanic edifice which is located in the centre of La Fossa Caldera. It was built over the past 6 kyr by successive eruption of pyroclastic products and minor lava flows from different vents. [De Astis et al. 1997]

The Fossa Cone is mainly composed of intermediate-felsic magmas. The most mafic products are scoriaceous bombs and ash-lapilli. Trachytic products can be found as lavas and pyroclastics. Furthermore, rhyolitic lavas and trachy-rhyolitic pumices can be found. Volcanic deposits which crop out at the cone and inside the crater of la Fossa di Vulcano are mainly products of the most recent period of eruption between 1888 and 1890. A large part of the cone is covered by ash-tuffs of the Fossa Rossa formation, which erupted after the 6th century A.D. Furthermore, trachytic and rhyolitic obsidian lava flows can be found on the flanks of La Fossa. [Keller 1970]

La Fossa di Vulcano shows the highest ground concentrations of the radioelements K, U and Th on Vulcano Island. Since the crater of the Fossa Cone has distinctly higher ground concentrations than the flanks of the cone, concentrations of the two areas are named separately. The flanks of the Fossa Cone show mean radioelement concentrations of 7.4 % K, 15.9 ppm U and 46.3 ppm Th, and an air absorbed dose rate of 210 nGy/h. The crater shows higher concentrations of 7.5 % K, 19.2 ppm U and 52.7 ppm Th, and an air absorbed dose rate of 230 nGy/h [cp. Appendix B, Vulcano 2004, Id 0]. However, ground concentrations of thorium computed from the ground-radiometric survey by *P. Chiozzi* are even higher than those of the airborne survey in 2004. The potassium concentrations of the ground survey, in turn, are lower than that of the airborne survey. [cp. table 5.2]

The airborne survey in 2002 shows also a great difference in radioelement concentration between the crater and the flanks of the cone. Mean ground concentrations of 3.0 and 3.4 % K, 8.0 and 10.6 ppm U, and 24.0 and 29.7 ppm Th were computed for the cone and the crater, respectively. [cp. Appendix B, Vulcano 2002, Id 0]

The Fossa Cone is a still active volcanic edifice with the last eruption between 1888 and 1890, and presently intense fumarolic activity in the summit area. Therefore, these extremely high ground concentrations could be possibly due to disequilibrium conditions.

Six further deposits of earlier eruptions of La Fossa di Vulcano could be identified by

their radiometric signature and have been subdivided into two radiometric classes, each being composed of three features. One of the deposits of the first class is located in the Piano Caldera, the other two build the rims of the Fossa Caldera. These features show mean radioelement concentrations in the range of 6.4 - 6.8 % K, 12.4 - 13.6 ppm U and 37.6 - 39.7 ppm Th, and an air absorbed dose rate of 176 - 186 nGy/h [cp. Appendix B, Vulcano 2004, Id 1]. Concentrations computed from the survey in 2002 are in the range of 3.0 % K, 5.7 - 6.9 ppm U and 18.7 - 23.6 ppm Th. [cp. Appendix B, Vulcano 2002, Id 1].

The deposits of the second class show lower radioelement concentrations in the range of 4.0 - 5.0 % K, 8.4 - 10.0 ppm U and 26.2 - 26.9 ppm Th, and air absorbed dose rates in the range of 125 - 131 nGy/h [cp. Appendix B, Vulcano 2004, Id 7]. Three features have been delineated, which all refer to products of earlier Fossa eruptions: Monte Luccia, Capo Grillo and Gelso pyroclastics, the latter two being composed of products of la Fossa di Vulcano, which are superimposed on the eastern and southern flanks of Vulcano Primordiale, respectively. Radioelement concentrations computed from the survey in 2002 are lower and are in the range of 1.9 - 2.1 % K, 4.8 - 5.4 ppm U and 12.2 - 14.3 ppm Th. [cp. Appendix B, Vulcano 2002, Id 7]

One further feature has been delineated by its radioelement signature, which could not be unequivocally assigned to one distinct unit. It is located within the Piano Caldera and includes deposits of Monte Sommata, Tufi di Grotte dei Rossi and of the earlier Fossa I eruption. It shows high radioelement concentrations of 5.8 % K, 11.1 ppm U and 34.6 ppm Th, and an air absorbed dose rate of 160 nGy/h [cp. Appendix B, Vulcano 2004, Id 3]. According to these comparatively high ground concentrations, it seems to be mainly influenced by products of la Fossa di Vulcano.

Vulcanello:

Vulcanello was built as a new island in 183 B.C. and consists of a composite lava platform and three volcanic cones, mainly composed of scoriae, tuffs and tuff-breccias. Successive eruptions in the 6th and 16th century gradually connected the small island to Vulcano. [De Astis et al. 1997]

New data from archeo-magnetic measurements by *Simone Arrighi* suggests the peninsula to be more than a millennium younger than previously believed from historical descriptions. Following this data the oldest pyroclastic cone on Vulcanello erupted at 1050 AD and most of the lava platform and probably the second cone were built through successive eruptions between 1100 and 1250 AD. If this dating is correct, Vulcanello could have been possibly built contemporaneously with the eruption of the Rocche Rosse obsidian lava flow on Lipari Island. [Arrighi et al. 2006]

The Vulcanello platform was built by at least 8 leucite-tephritic lava flows, followed by the eruption of trachytic lavas from the third tuff cone [Arrighi et al. 2006]. It shows high radioelement concentrations of 5.8 % K, 11.9 ppm U and 34.9 ppm Th, and an air absorbed dose rate of 160 nGy/h. These ground concentrations are similar to those detected over pyroclastic deposits of La Fossa di Vulcano outside the Caldera [cp. Appendix B, Vulcano 2004, Id 3]. Ground concentrations computed from the survey in 2002 are 3.3 % K, 8.4 ppm U, and 23.6 ppm Th. Here, the concentrations are closer to those of La Fossa Cone. [cp. Appendix B, Vulcano 2002, Id 1]

The pyroclastic cones of Vulcanello have slightly lower radioelement concentrations of 5.3 % K, 10.9 ppm U and 31.1 ppm Th, and an air absorbed dose rate of 148 nGy/h [cp. Appendix B, Vulcano 2004, Id 5]. Compared to the concentrations computed from the ground-radiometric survey of *P. Chiozzi*, radioelement concentrations derived from the airborne survey in 2004 are higher [cp. table 5.2].

The survey in 2002 shows lower radioelement concentrations, which are in the range of 2.6 % K, 7.3 ppm U and 15.90 ppm Th. [cp. Appendix B, Vulcano 2002, Id 5]

The bar chart in Fig. 5.55 gives an overview over the radioelement distributions (average concentrations) of the different units on Vulcano Island. The position of the different features can be found in Fig. 5.56.

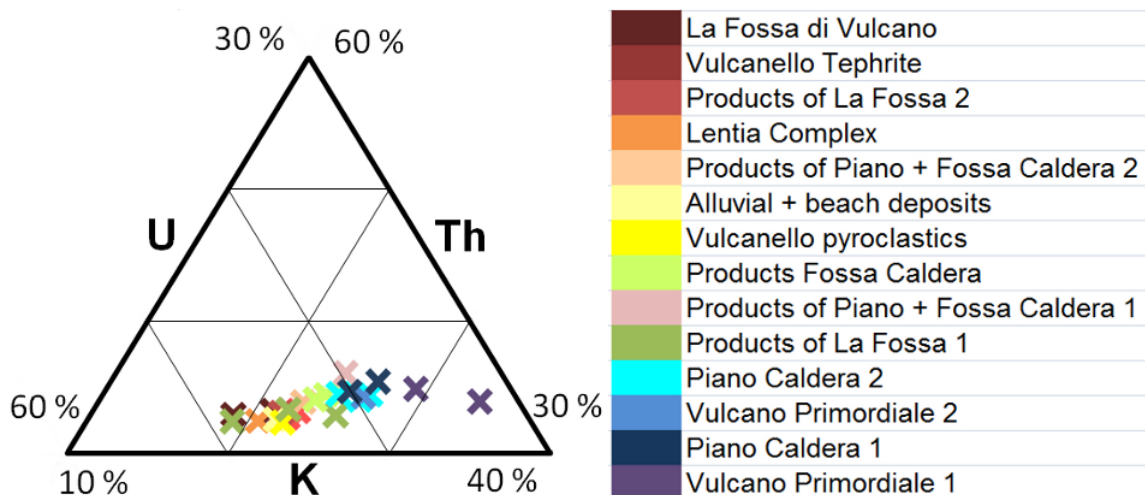


Figure 5.54: Ternary radioelement diagram showing the geologic units of Vulcano Island

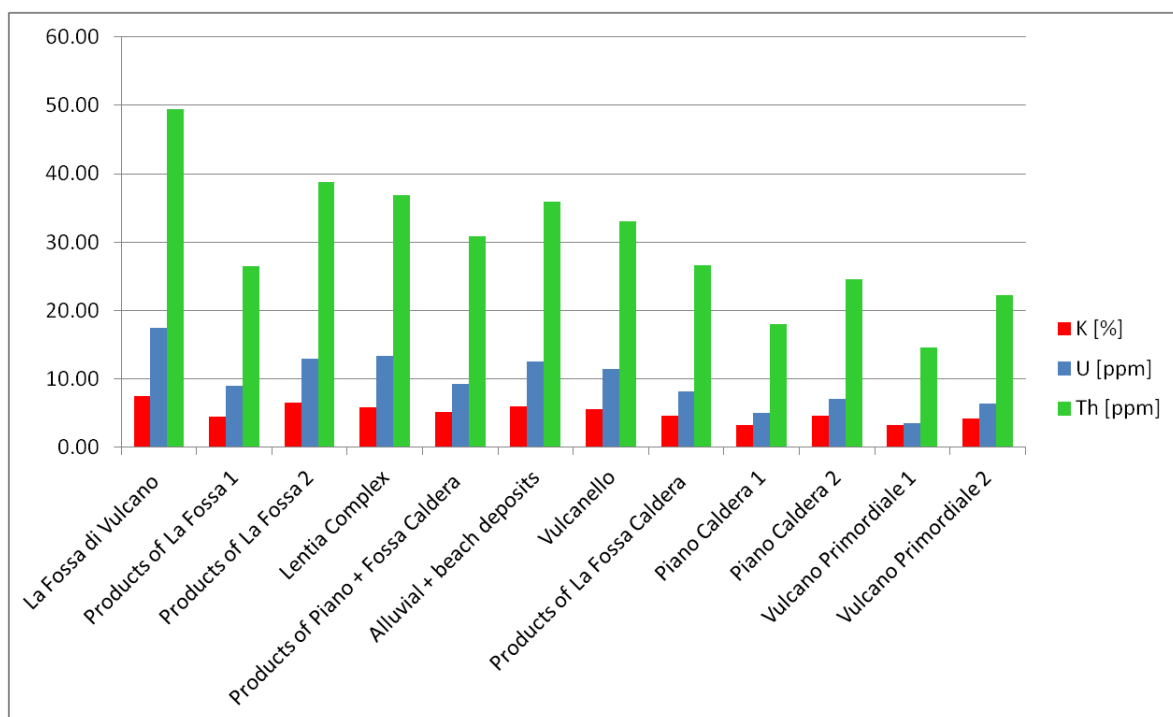


Figure 5.55: Radioelement distribution (average concentrations) for the the different units on Vulcano Island

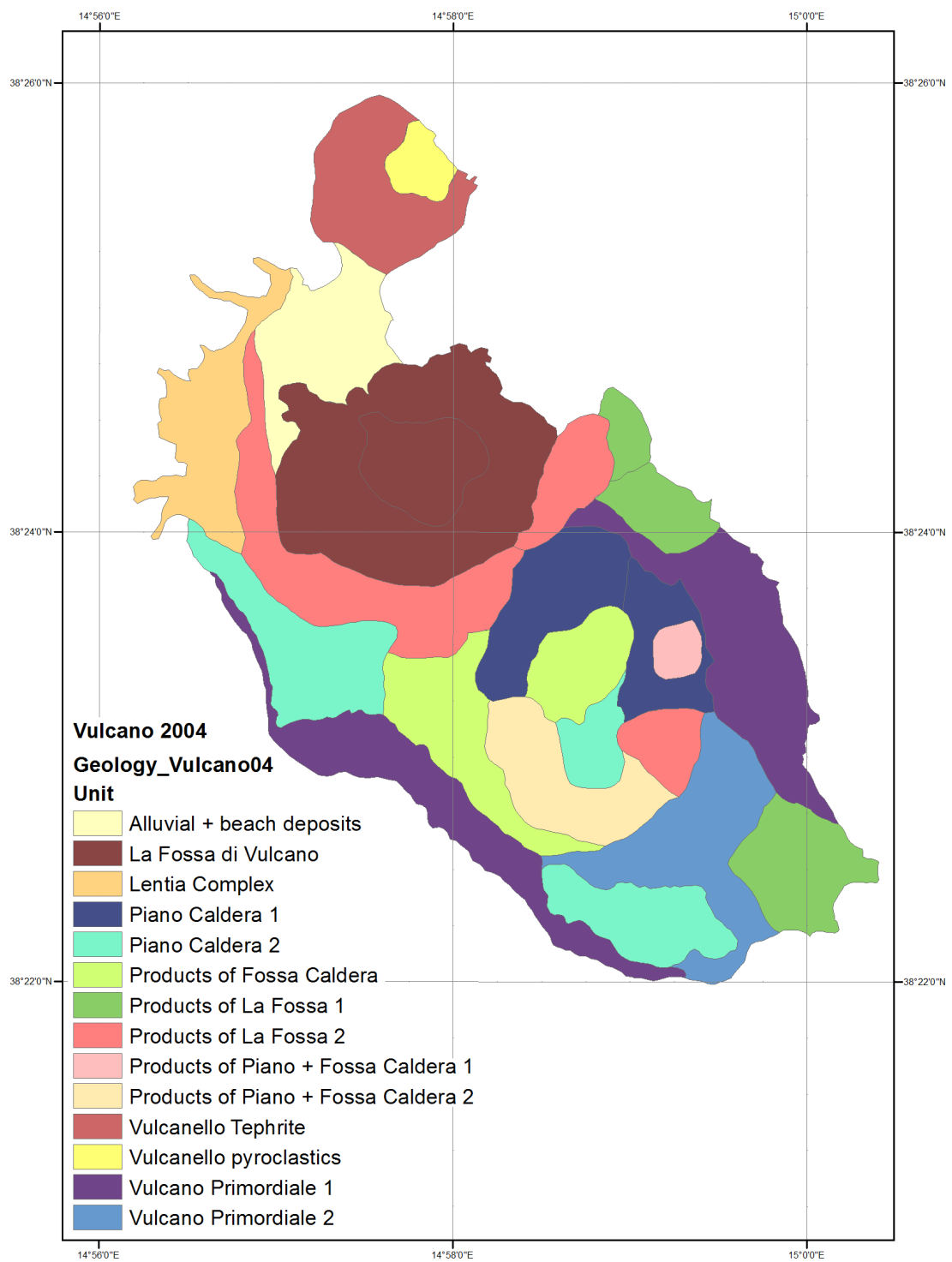


Figure 5.56: Map of Vulcano Island showing units that have been delineated on the basis of the radiometric studies

Lipari

Paleolipari:

Paleolipari is the oldest unit on Lipari Island and corresponds to the first volcanic cycle. It is mainly composed of calc-alkaline basaltic-andesites, which erupted from different centres between 223 and 150 ka. Outcrops are largely confined to the western part of Lipari, except for the base of Monterosa, which builds the easternmost part of the island. Five features have been delineated, which are largely composed of products of Paleolipari.

Mt. Mazzacaruso and Timpone Ospedale: Volcanic products of the Monte Mazzacaruso and Timpone Ospedale formations are thickly bedded, massive pyroclastic breccias, which contain thin, discontinuous lava flows and thinly bedded lapilli tuff layers [Tranne et al. 2002]. The products are mainly calc-alkaline basaltic andesites, which accordingly show very low radioelement concentrations of 1.9 % K, 1.7 ppm U and 6.9 ppm Th, and an air absorbed dose rate of 48 nGy/h [cp. Appendix C, Lipari 2004, Id 8]. Radioelement concentrations, which were computed from the survey in 2002, are 0.5 % K, 1.4 ppm U and 3.7 ppm Th [cp. Appendix C, Lipari 2002, Id 8].

Bonanno: Bonanno is located along the north-western coast of the island and is largely composed of products of the Bertaccia and Bonanno formations. Furthermore, some smaller deposits of the Pianoconte, Mauro and Inzolfato formations are present. The Bertaccia formation is composed of calc-alkaline andesites, appearing as lava flows and pyroclastics. The pyroclastic succession is mainly composed of lapilli tuffs, which are in some parts strongly fumarolized. The massive blocky lavas of the Bonanno formation are of high-K calc-alkaline composition. They are strongly brecciated along the coastal sector, and thinly bedded hydromagmatic lapilli tuffs are frequently intercalated to the unit. [Tranne et al. 2002]

This feature shows low radioelement concentrations of 2.2 % K, 2.0 ppm U and 7.9 ppm Th, and an air absorbed dose rate of 56 nGy/h. The radioelement concentrations are comparable to those of Mt. Mazzacaruso and Timpone Ospedale and therefore these two features have been assigned to the same radiometric class [cp. Appendix C, Lipari 2004, Id 8].

The previous two features have a very exposed position in the ternary radioelement diagram, clearly showing the lowest relative concentrations of U and high relative concentrations of K [cp. Fig. 5.57].

Mt. Rosa: Mt. Rosa represents the easternmost part of Lipari and is largely composed of volcanic products of the Monterosa formation. Only some small deposits of the Pianoconte, Mauro and Vallone del Gabellotto formations are emplaced on top of it. The basal portion of Monterosa is built by a thinly bedded tuff layer, the more widespread upper portion, in turn, is built by scoriaceous lapilli-tuffs. Furthermore, at least three massive lava flows can be found. All products of the Monterosa formation are calc-alkaline basaltic andesites. [Tranne et al. 2002]

Mt. Rosa shows low radioelement concentrations of 2.0 % K, 6.0 ppm U and 9.0 ppm Th, and an air absorbed dose rate of 77 nGy/h.

Mt. Rosa shows a very exposed positions in the ternary radioelement diagram, showing the lowest relative concentration of Th and the highest relative concentration

of U [cp. Fig. 5.57].

Fossa di Fuardo: Fossa di Fuardo is a small feature in the south-western part of the island, which is surrounded by outcrops of the Pulera formation. It is composed of calc-alkaline basaltic andesites of the Scoglio Bianco lavas and the Vallone dei Laci formation. The latter is composed of medium-bedded, plane parallel stratified lapilli tuffs building brecciated massive lavas, which are in some parts strongly fumarolized. [Tranne et al. 2002]

Fossa di Fuardo shows low radioelement concentrations of 2.3 % K, 3.2 ppm U and 10.6 ppm Th, which are similar to the concentrations of Mt. Rosa. Therefore, these two features have been assigned to the same radiometric class. [cp. Appendix C, Lipari 2004, Id 7]

The survey in 2002 yielded lower radioelement concentrations of 0.9 % K, 2.1 ppm U and 5.9 ppm Th. [cp. Appendix C, Lipari 2002, Id 7]

Timpone Carubbo: Timpone Carubbo is located in the southern part of the island and is built by the Belvedere and Scoglio Bianco formation. The Belvedere formation is calc-alkaline andesitic in composition and is built by a massive lava flow and a pyroclastic succession of tuff breccias and lapilli tuffs. The Scoglio Bianco formation is built by a pyroclastic succession of calc-alkaline andesitic composition and massive blocky lavas of calc-alkaline basaltic andesite. The pyroclastic succession consists of poorly sorted, thickly and plane parallel bedded tuff breccias, passing upwards to thinly, plane parallel and cross-stratified lapilli tuffs. [Tranne et al. 2002]

Timpone Carubbo shows the highest radioelement concentrations of the features composing Paleolipari. With 2.9 % K, 4.0 ppm U and 14.0 ppm Th, it shows radioelement concentrations in the range of mean crustal abundances. [cp. Appendix C, Lipari 2004, Id 6]

Concentrations computed from the airborne survey in 2002 are in the range of 1.2 % K, 3.0 ppm U and 7.7 ppm Th. [cp. Appendix C, Lipari 2002, Id 6]

P. Chiozzi computed radioelement concentrations for basaltic andesites of the first cycle [cp. Fig. 5.38]. The radioelement concentrations of the ground-radiometric survey are similar to those of Timpone Carubbo, Fossa di Fuardo and Mt. Rosa computed from the airborne survey in 2004.

Piano Grande:

Piano Grande refers to products, which erupted from Mt. Chirica and Mt. St. Angelo at approximately 127 ka. Most of the deposits are covered by younger volcanic products, except for some outcrops of the Vallone di Bezzotti pyroclastics in the north-western part of the island and two outcrops of the Timpone Ricotta formation, which erupted from Mt. St. Angelo in the central part of Lipari [Tranne et al. 2002]. Only one feature has been delineated.

Timpone Croci: Timpone Croci is located in the eastern part of the island, north of Lipari town. It is mainly composed of calc-alkaline basaltic andesites to andesites of the Timpone Ricotta formation. This is a thinly to medium plane parallel bedded pyroclastic succession consisting of an alteration of massive tuff layers and cross-stratified tuff layers. [Tranne et al. 2002]

Only a small area of this feature has actually been covered by flight lines and therefore

the radioelement concentrations of this feature should be considered with care. Slightly elevated ground concentrations of 4.4 % K, 6.5 ppm U and 20.6 ppm Th, and an air absorbed dose rate of 111 nGy/h have been calculated. [cp. Appendix C, Lipari 2004, Id 5]

A second outcrop of Timpone Ricotta has been assigned to the Mt. Mazzacarusio feature, as it showed a similar radioelement signature.

The outcrops of Vallone di Bezzotti in the north-western part of the island have not been covered by flight lines and therefore no feature has been delineated.

Cala Fico:

Products of the Cala Fico unit were deposited during a second and third stage of activity of Mt. St. Angelo and a second stage of activity of Mt. Chirica at approximately 104 and 92 ka.

Two features have been delineated, which can be assigned to the second volcanic cycle: Fontanelle: Fontanelle is an arc like feature in the south-western part of the island. It is mainly built by two lava flows of the Pulera formation, which are of high-K calc-alkaline andesitic to dacitic composition. To a minor extent, also deposits of the Serra Pierra and Timpone Pataso formations are present, which are mainly pyroclastics of high-K calc-alkaline andesitic composition. All three formations were deposited during the second stage of activity of Mt. St. Angelo at 104 ka and belong to the Bruca Synthem. [Tranne et al. 2002]

Fontanelle shows mean radioelement concentrations of 3.8 % K, 6.0 ppm U and 19.8 ppm Th, and an air absorbed dose rate of 99 nGy/h. The concentrations are comparable to those of Timpone Croci and therefore the two features have been assigned to the same radiometric class. [cp. Appendix C, Lipari 2004, Id 5]

The survey in 2002 shows lower radioelement concentrations of 1.5 % K, 3.5 ppm U and 10.6 ppm Th [cp. Appendix C, Lipari 2002, Id 5].

Mt. St. Angelo: Mt. St. Angelo is a large feature located in the central part of the island. It is largely composed of products of the Cala Fico unit, which have been partly covered by younger products of the Valle Muria and Vallone Fiume Bianco units. Deposits of the Serra Pierra, Chiappe Lisce and Pulera formations are present, partly covered by products of the Pianoconte and Mauro formations. The Serra Pierra and Pulera formations are products of the second stage of activity of Mt. St. Angelo and their composition has been described previously. The high-K calc-alkaline andesites of the Chiappe Lisce formation erupted during the third stage of activity of Mt. St. Angelo. They appear as two lava flows and a large pyroclastic succession, building the upper portion of Mt. St. Angelo cone. [Tranne et al. 2002]

The mean radioelement concentrations of this feature are 4.4 % K, 8.1 ppm U and 25.6 ppm Th. The air absorbed dose rate is 121 nGy/h. [cp. Appendix C, Lipari 2004, Id 4]

The survey in 2002 yielded lower radioelement concentrations of 1.9 % K, 5.6 ppm U and 14.2 ppm Th. [cp. Appendix C, Lipari 2002, Id 4]

Inzolfato formation, which is composed of three massive lava flows of high-K calc-alkaline composition, erupted during the second stage of activity of Mt. Chiriza. It crops out at the north-western coast of the island and has been assigned to the

Bonanno feature.

Radioelement concentrations computed from the ground radiometric survey of *P. Chiozzi* for andesites of the second volcanic cycle are lower than those of the survey in 2004 [cp. Fig. 5.38].

Valle Muria:

The Valle Muria Synthem refers to widespread pumiceous hydromagmatic pyroclastics of high-K calc-alkaline rhyolitic composition, which erupted between 70 and 13 ka. Outcrops are largely confined to the southern part of the island, as deposits to the north are covered by products of the younger Vallone Fiume Bianco Synthem. Three features have been delineated, which are largely composed of products of Valle Muria and can be assigned to the third volcanic cycle.

Monte Guardia: Monte Guardia is a large feature in the south-eastern part of the island and is composed of products of the Mauro formation and the Urnazzo subsynthem. Urnazzo is built by the Mt. Guardia, Mt. Giardina, and Punta di Costa formations. Mt. Guardia is a widespread pyroclastic succession, which is mainly composed of tuff breccias and lapilli tuffs of high-K calc-alkaline rhyolitic composition. The Mt. Giardina and Punta di Costa formations each are built by three endogenous lava domes, which are aligned in NNW-SSE direction. The Mauro formation erupted between 20.5 and 13.0 ka and is composed of pale reddish-brown thickly bedded, massive ash tuffs of high-K calc-alkaline rhyolitic composition. [Tranne et al. 2002]

Monte Guardia shows high radioelement concentrations of 6.3 % K, 14.2 ppm U and 40.0 ppm Th, and an air absorbed dose rate of 183 nGy/h. The concentrations are comparable to those of the Vallone del Gabellotto feature, which is composed of products of the Mauro and Vallone del Gabellotto formations. Thus, the features have been assigned to the same radiometric class. [cp. Appendix C, Lipari 2004, Id 1]

The survey in 2002 shows lower radioelement concentrations of 3.0 % K, 7.7 ppm U and 21.2 ppm Th [cp. Appendix C, Lipari 2002, Id 1]

Pianoconte: Pianoconte is a small feature in the central to southern part of the island, which is largely composed of products of the Mauro and Pianoconte formations. The Mauro formation has been described previously (Mt. Guardia). The Pianoconte formation is mainly composed of tuff layers of white to reddish-brown colour, which correlated locally to the "Lower Pollara Tuffs", the "Ischia Layer" or the "Lesser Brown Tuffs". Their composition ranges from calc-alkaline basaltic andesites to andesites. [Tranne et al. 2002]

Pianoconte shows high radioelement concentrations of 5.6 % K, 11.8 ppm U and 34.9 ppm Th, and an air absorbed dose rate of 160 nGy/h. [cp. Appendix C, Lipari 2004, Id 2]

Radioelement concentrations computed from the survey in 2002 are 2.7 % K, 7.4 ppm U and 18.4 ppm Th [cp. Appendix C, Lipari 2002, Id 2].

Santa Margherita: Santa Margherita is located north of Pianoconte and is composed of products of the Mauro, Pianoconte and Mt. Guardia formations. Those have already been described previously. Radiometrically, this feature is similar to Pianoconte and therefore the two features have been assigned to the same radiometric class. Mean radioelement concentrations of 5.6 % K, 10.3 ppm U and 33.2 ppm Th, and an air

absorbed dose rate of 153 nGy/h were calculated. [cp. Appendix C, Lipari 2004, Id 2] The survey in 2002 shows lower radioelement concentrations of 2.7 % K, 6.7 ppm U and 20.5 ppm Th [cp. Appendix C, Lipari 2002, Id 2].

Radioelement concentrations computed from the ground radiometric survey of *P. Chiozzi* for rhyolite of the third volcanic cycle are higher, except for the K concentrations, which are approximately in the same range as those computed from the airborne survey. [cp. Fig. 5.38].

Vallone Fiume Bianco:

Vallone Fiume Bianco is the youngest unit on Lipari and covers the whole north-eastern sector of the island. Pyroclastics and lavas of this unit are of high-K calc-alkaline rhyolitic composition and erupted during several phases of volcanic activity between 11.4 to 1.3 ka. Three features have been delineated, which can all be assigned to the third volcanic cycle.

Vallone del Gabellotto: Vallone del Gabellotto is located in the central to western part of the island and is mainly composed of products of the Vallone del Gabellotto and Mauro formations. The Vallone del Gabellotto formation refers to a thick pumiceous pyroclastic succession consisting of medium and thickly bedded cross-stratified lapilli tuffs and tuff breccias, which erupted approximately at 11.4 ka. [Tranne et al. 2002]

The feature shows high radioelement concentrations of 6.0 % K, 14.0 ppm U and 39.6 ppm Th, and an air absorbed dose rate of 178 nGy/h. The concentrations are comparable to those of Monte Guardia and therefore the two features have been assigned to the same radiometric class. [cp. Appendix C, Lipari 2004, Id 1]

Radioelement concentrations computed from the survey in 2002 are 2.9 % K, 8.4 ppm U and 22.5 ppm Th [cp. Appendix C, Lipari 2002, Id 1].

Costa d Agosto: Costa d Agosto is located in the north-western part of Lipari and is mainly composed of products of the Sciarra dell' Arena formation. This is a pumiceous succession of high-K calc-alkaline rhyolites which erupted approximately at 1.4 ka. The deposits consist of lapilli tuffs and tuff layers. [Tranne et al. 2002]

This feature shows high radioelement concentrations of 5.4 % K, 13.7 ppm U and 35.6 ppm Th, and an air absorbed dose rate of 167 nGy/h. Since the radioelement concentrations are comparable to those of Pianoconte and Santa Margherita, the three features have been assigned to the same radiometric class. [cp. Appendix C, Lipari 2004, Id 2]

Mt. Pilato: Mt. Pilato is located in the north-eastern part of the island and was emplaced during the last eruption on Lipari at approximately 1.3 ka. It is formed by the Fossa delle Rocche Rosse formation, which forms a tongue-like, obsidian-rich flowing dome of high-K calc-alkaline rhyolitic composition. [Tranne et al. 2002]

Mt. Pilato was only covered by one flightline. Mean radioelement concentrations of 4.2 % K, 11.5 ppm U and 31.3 ppm Th, and an air absorbed dose rate of 141 nGy/h were calculated [cp. Appendix C, Lipari 2004, Id 3]. The comparatively low radioelement concentrations can be due to the lack of data.

The bar chart in Fig. 5.58 gives an overview over the radioelement distribu-

tions (average concentrations) of the different units on Lipari Island. The position of the different features can be found in Fig. 5.59.

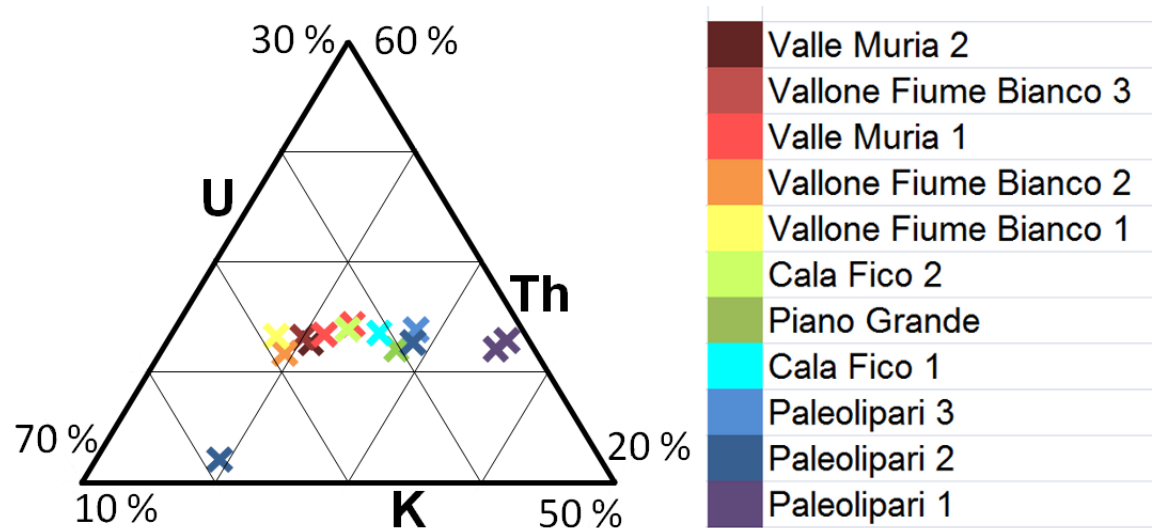


Figure 5.57: Ternary radioelement diagram showing the geologic units of Lipari Island

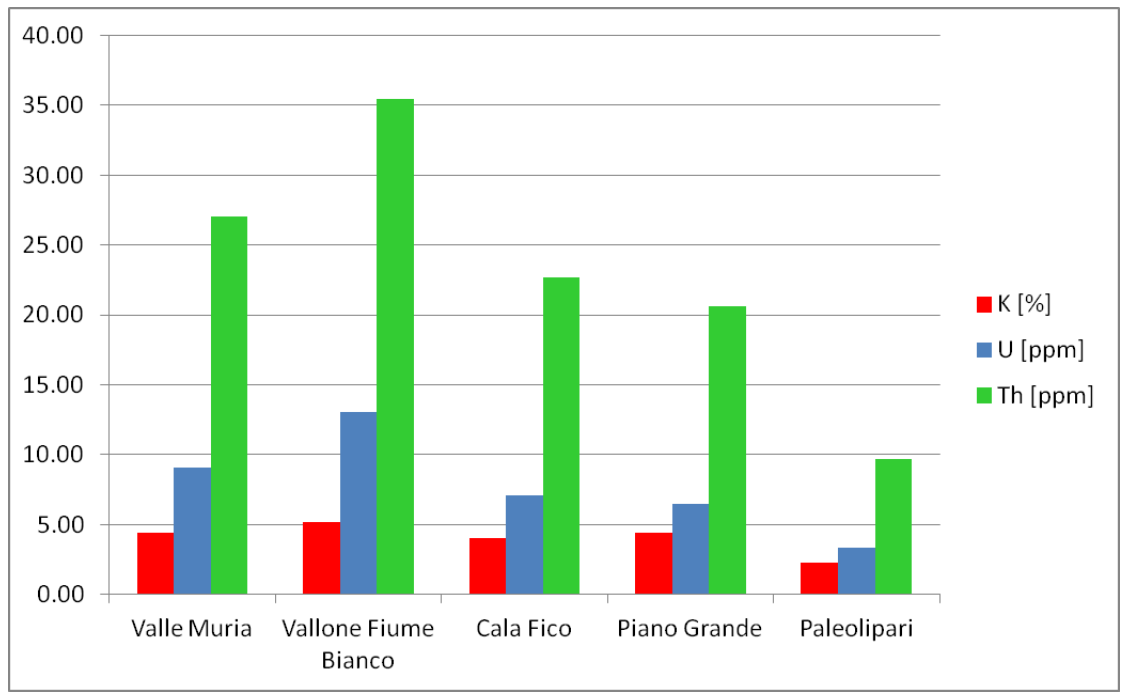


Figure 5.58: Radioelement distribution (average concentrations) for the the different units on Lipari Island

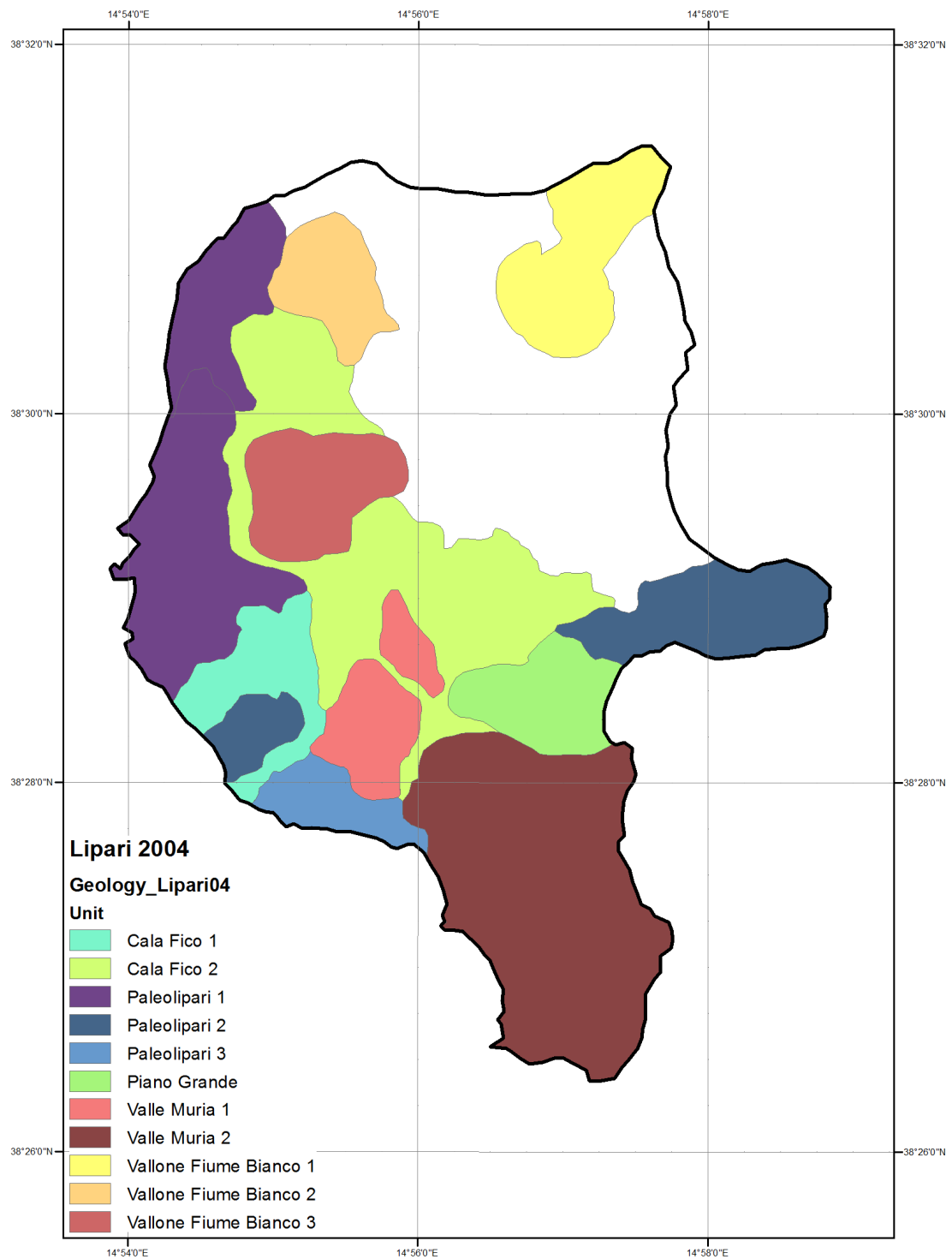


Figure 5.59: Map of Lipari Island showing units that have been delineated on the basis of the radiometric studies

Chapter 6

Discussion and Conclusion

Within the frame of this work, the potential of gamma-ray measurements for mapping volcanic areas was tested. Volcanic areas are often associated with high radioelement concentrations. For example, the mean absorbed dose rate over felsic rocks of the Aeolian Islands is approximately twice as high as that measured over non-volcanic regions in Italy [Chiozzi et al. 2001]. As volcanoes are also often associated with rough topography and inaccessible areas, the airborne measurements of gamma-radiation seem to be especially adequate as an additional mapping tool.

Two different volcanic areas have been tested for the applicability of airborne gamma-ray spectroscopy: An isolated volcanic island in the Pacific Ocean and the Aeolian Island Arc north of Sicily. Both areas are characterised by high ground concentrations of natural radioelements and show a large variety of rocks exposed on the surface. The low population density was an additional advantage of those two areas.

The best results could be achieved from the survey over Socorro Island in 2009. Due to the primary intention of an electromagnetic survey for searching groundwater, the survey altitude had to be kept as low as possible ($< 100\text{m}$) and flight-line spacing was chosen to be 100 m. Four NaI(Tl) crystals were used for the radiometric survey. On the basis of the radiometric processing results it was possible to delineate the main geologic units described by *W. Bryan* [cp. Fig. 5.1]. Furthermore, it was possible to clearly identify the major lava flows of the Felipe unit, the three peralkaline trachyte domes and the cinder cone of the Lozano unit, some of the larger peralkaline domes, some of the Playa Blanca members, and some of the basalt cinder cones in the Lomas Coloradas area. Two maps have been drawn: One is exclusively based on the results of the radiometric studies. Only those features, which could be clearly identified on the basis of the radioelement- and ternary maps, have been delineated. The exact shapes of the features have been determined with the help of the satellite image of Socorro Island. The second map has been drawn on the basis of the radiometric results in combination with two pre-existing geologic maps [cp. Fig. 5.35 and 5.36] and, of course, the satellite image. Furthermore, more topographic details have been taken into account.

It was largely possible to confirm the studies of *W. Bohrson* and *M. Reid*, which were

unfortunately confined to the Lomas Coloradas area. In contrast, the radiometric results partly disagree with the classification of *E.A. Carballido-Sanchez*.

Main differences are as follows:

- The three peralkaline trachyte domes and the cinder cone of the Lozano unit have been assigned to the Lomas Coloradas basalt lava flows and cinder cones by *E.A. Carballido-Sanchez*. In the potassium concentration map [cp. Fig. 5.4] these features clearly stand out as positive anomalies. This fact coincides with the studies of *W. Bohrson and M. Reid*, who described the features as members of the postcaldera silicic stage.
- The Playa Escondia "Twinflow" has also been assigned to the Lomas Coloradas unit by *E.A. Carballido-Sanchez*. In turn, *W. Bohrson and M. Reid* assigned it to the postcaldera silicic stage of volcanism. The radiometric studies showed a clear similarity of the Playa Escondia "Twinflow" and the two lava flows that make up Punta Tosca and Punta Judith. Thus, it has been assigned to the Felipe members on the basis of the radiometric results.
- Apart from the three previously mentioned Felipe members, no other Felipe members were clearly identified on the basis of the radiometric survey. Six further Felipe members had been identified by *E.A. Carballido-Sanchez*, but those showed no comparable radioelement signature.
- Referring to *E.A. Carballido-Sanchez*, several members of the Playa Blanca unit are spread all over the island. On the basis of the gamma-ray survey, only three features of this unit could have been clearly identified.
- According to the geologic map of *E.A. Carballido-Sanchez* [cp. Fig. 5.35], several members of the El Bosque unit can be found along the coastline of Socorro. Only the outcrop in the Cabo Pearce area could have been clearly identified on the basis of the radiometric results.
- Radiometric data of the whole northern, eastern and south-western part of the island was difficult to interpret. According to *E.A. Carballido-Sanchez* this area is largely composed of rocks of the Palma Sola, Playa Norte and El Bosque units. Differences between the three units or typical radioelement signatures could not have been identified within the present studies. Therefore, another classification has been made on the basis of the radiometric results, or actually on the basis of the Th ground concentrations. Two areas of high Th concentration ($\sim 30 - 37$ ppm Th), which were assumed to mainly coincide with the Palma Sola members of *E.A. Carballido-Sanchez*, and two areas of lower Th concentration ($\sim 19 - 24$ ppm Th), which were simply denoted as Volcán Evermann eruptives, have been identified. Only a small area of *E.A. Carballido-Sanchez's* El Bosque members has been identified by its especially low Th concentration ($\sim 16 - 20$ ppm Th) in relation to the surrounding Precaldera Eruptives.

Interpreting gamma-ray data of Socorro Island was particularly interesting as only few is known about eruptive products in the large inaccessible part of the island. Most of the previous studies have been confined to the Lomas Coloradas area and the geologic map of *E.A. Carballido-Sanchez* is partly based on aerial photographs. Therefore, the airborne geophysical survey of the GSA was the first detailed survey covering (almost) the whole island.

The airborne survey over the islands of Vulcano and Lipari in 2004 yielded also quite good results, even though the spatial resolution was not as good as for Socorro Island. Flight line spacing was approximately 125 m and the survey altitude was between 80 and 150 m. Only one NaI(Tl) crystal was used for the radiometric survey and thus, the detected count rates were low. Nevertheless, data quality was pretty good and it was possible to identify the main geologic units by means of the radioelement distribution maps. In contrast to Socorro Island, the radioelements showed a positive correlation for all geologic units of Vulcano and Lipari, hence units with higher K concentrations also showed higher U and Th concentrations. Thus, the ternary radioelement maps and the ternary radioelement diagram were no big help for delineating the individual features. The units identified on Vulcano and Lipari showed a general tendency of increasing radioelement concentrations for more recent eruptive products.

As has already been indicated by *P. Chiozzi*, two radiometric districts could be delineated. The two radiometric districts can be easily identified in the ternary radioelement maps. The district of higher radioactivity is plotted in white, yellow, magenta or cyan within the K-Th-U, K-Th, K-U and Th-U maps, respectively, while the district of lower radioactivity is plotted in grey-scale.

The Vulcano-Lipari survey in 2002 was impaired by heavy rainfall. It was interesting to see the effect of rainfall on the detected count rates. Compared to the survey in 2004, ground concentrations of K, U and Th were reduced by about their half. This strong influence of rainfall emphasises the importance of good weather conditions during the airborne survey. Only few scientific papers can be found on the effect of soil humidity on gamma-ray spectra, what increases the need of further research on this topic.

The gamma-ray survey over Salina in 2004 was part of the Vulcano-Lipari survey. As only each fourth line of the survey was extended to cover the island of Salina, spatial resolution was pretty bad. Furthermore, the island showed significantly lower radioelement concentrations than Vulcano and Lipari. As a result, the quality of the radioelement maps of Salina was too bad to identify any geologic units.

The airborne survey over Panarea in 2004 was flown at an average line spacing of 250 m and an altitude of 150 m. At an altitude of 150 m, the radius of the circle from which 90 % of the gamma-rays originate, is approximately 280 m [cp. Fig. 3.2]. This makes up an area of about 0.25 km². Hence, the circle from which the gamma-rays originate makes up approximately one tenth of the whole surface area of Panarea. It is therefore not surprising that data quality of the Panarea survey was too bad to identify any geologic units.

Likewise it was not possible to make any reasonable interpretation of the survey over

Stromboli volcano.

The following conclusions can be drawn concerning the production of high-quality gamma-ray spectrometric data:

- The use of 4 or more crystals is strongly recommended. Data derived from measurements with only one crystal shows bad quality, especially in areas of low radioactivity.
- Due to the exponential fall-off of radiation with increasing survey altitude, it is important to keep the survey altitude as low as possible (< 100 m). Furthermore, strong variations in survey altitude during a survey impair data quality and complicate the processing, as this strongly depends on the quality of the attenuation coefficients.
- As has been shown by the survey over the Aeolian Islands in 2002, rainfall has a strong impact on data quality and on the detected count rates. Therefore, dry weather conditions should be chosen for the gamma-ray survey and additional measurement of soil humidity would be helpful.
- The determination of calibration constants at regular intervals is very important. Aircraft background should be determined for each helicopter type and cosmic background and height attenuation coefficients should be determined for each region. Furthermore, the sensitivity coefficients should be determined regularly, as these affect the accuracy of the conversion to ground concentrations of the radioelements.

The following conclusions can be drawn concerning the interpretation of gamma-ray data:

- No interpretation would be possible without additional information like geologic maps, satellite images and topographic maps.
- It is important to know details about the survey, like weather conditions. In the special case of interpreting gamma-ray data of volcanoes, it may be important to be informed about current activity of the volcano during the survey.
- Prior to interpreting the results of radiometric processing, data is usually interpolated to a regular grid. One must be aware, that extremely high or low values can be due to missing data and therefore, the resulting radioelement maps should always be interpreted in combination with the original (non-gridded) data.
- When interpreting gamma-ray data of volcanic areas, one can generally assume that an increase in SiO_2 content is associated with an increase in K concentration and that more differentiated volcanic products show higher concentrations of U and Th.

List of Figures

2.1	Uranium decay series [Minty 1997]	10
2.2	Thorium decay series [Minty 1997]	12
3.1	Effect of flying altitude on spatial resolution	21
3.2	Radius of the circle that contributes 90% of the signal as a function of detector height [Billings 1998]	22
3.3	Reduction in the observed signal with height [Billings 1998]	22
3.4	Potassium line spectrum [Minty 1997]	23
3.5	Simulated potassium flux at 300m altitude [Minty 1997]	23
3.6	Uranium line spectrum [Minty 1997]	23
3.7	Simulated uranium flux at 300m altitude [Minty 1997]	23
3.8	Thorium line spectrum [Minty 1997]	23
3.9	Simulated thorium flux at 300m altitude [Minty 1997]	23
4.1	Cosmic window-counts vs. Potassium window-counts: Regression plot for aircraft- and cosmic-background determination	30
4.2	Cosmic window-counts vs. Potassium window-counts for a flight over the ocean near Socorro Island	31
4.3	Cosmic window-counts vs. Uranium window-counts for a flight over the ocean near Socorro Island	31
4.4	Cosmic window-counts vs. Thorium window-counts for a flight over the ocean near Socorro Island	32
4.5	Cosmic window-counts vs. Potassium window-counts for a flight over the ocean near Vulcano Island	32
4.6	Cosmic window-counts vs. Uranium window-counts for a flight over the ocean near Vulcano Island	33
4.7	Cosmic window-counts vs. Thorium window-counts for a flight over the ocean near Vulcano Island	33
4.8	Flight altitude vs. Potassium window-counts for a climb-flight over So- corro Island	37
4.9	Flight altitude vs. Uranium window-counts for a climb-flight over So- corro Island	38
4.10	Flight altitude vs. Thorium window-counts for a climb-flight over So- corro Island	38
4.11	Flight altitude vs. Total Count window counts for a climb-flight over Socorro Island	39

4.12	Flight altitude vs. Potassium window-counts for a climb-flight over Vulcano Island	39
4.13	Flight altitude vs. Uranium window-counts for a climb-flight over Vulcano Island	40
4.14	Flight altitude vs. Thorium window-counts for a climb-flight over Vulcano Island	40
4.15	Flight altitude vs. Total Count window-counts for a climb-flight over Vulcano Island	41
4.16	RGB colour-cube; creator: Horst Frank	49
4.17	Ternary radioelement diagram	53
5.1	Geologic sketch-map of Socorro Island after Bryan [cp. Carballido-Sanchez 1994]	57
5.2	Flight lines of the Socorro survey in 2009	60
5.3	Average gamma-ray spectrum of Socorro Island	61
5.4	Radioelement map of Socorro Island (100 m grid); standard window based processing: Potassium [%]	62
5.5	Radioelement map of Socorro Island (100 m grid): Uranium [ppm]. Radon correction performed with the Spectral-Ratio method	63
5.6	Radioelement map of Socorro Island (100 m grid): Uranium [ppm]. Radon correction performed with the Full-Spectrum method	63
5.7	Radioelement map of Socorro Island (100 m grid); standard window based processing: Thorium [ppm]	64
5.8	Radioelement map of Socorro Island (100 m grid); processing performed with the use of NASVD smoothed spectra: Potassium [%]	64
5.9	Radioelement map of Socorro Island (100 m grid) with NASVD smoothing: Uranium [ppm]. Radon correction performed with the Spectral-Ratio method	65
5.10	Radioelement map of Socorro Island (100 m grid); processing performed with the use of NASVD smoothed spectra: Thorium [ppm]	65
5.11	Ternary Radioelement map of Socorro Island: K-Th-U	66
5.12	Ternary Radioelement map of Socorro Island: K-Th	66
5.13	Ternary Radioelement map of Socorro Island: K-U	67
5.14	Ternary Radioelement map of Socorro Island: Th-U	67
5.15	Timescale of the subaerial eruptive products on Socorro Island	68
5.16	Radioelement distribution for the El Muerto members	69
5.17	Radioelement distribution for the Playa Blanca members	70
5.18	Radioelement distribution for the Playa Norte members	71
5.19	Position of the El Muerto members, the Playa Blanca members and of the features, which have been assigned to the Playa Norte members	71
5.20	Radioelement distribution for the Precaldera eruptives	73
5.21	Position of the El Bosque members and of the features, which have been assigned to the Precaldera eruptives	73
5.22	Radioelement distribution for the Felipe members	75
5.23	Radioelement distribution for the Palma Sola members	76

5.24	Position of the features, which have been assigned to the Palma Sola members	76
5.25	Radioelement distribution for the peralkaline domes	77
5.26	Position of the peralkaline domes and of the features, which have been assigned to the Felipe members	78
5.27	Radioelement distribution for the Volcán Evermann eruptives	79
5.28	Position of the features, which have been assigned to the Volcán Evermann eruptives	79
5.29	Radioelement distribution for the Lomas Coloradas area	81
5.30	Position of the features, which have been assigned to the Lomas Coloradas area	82
5.31	Radioelement distribution (average concentrations) for the the different units on Socorro Island	82
5.32	Map of Socorro Island showing units that have been delineated on the basis of the radiometric studies	83
5.33	Detailed map of Socorro Island showing units that have been delineated on the basis of the radiometric studies	84
5.34	Ternary radioelement diagram showing the geologic units of Socorro Island	85
5.35	Geologic map of Socorro Island designed by <i>Carballido-Sanchez</i> [Carballido-Sanchez 1994]	85
5.36	Geologic map of the south-eastern sector of Socorro Island designed by <i>Bohrson et al.</i> [Bohrson & Reid 1997]	86
5.37	Position and age of the islands of the Aeolian volcanic arc. (1) Calc-alkaline to high-K calc-alkaline and (2) shoshonitic products [Chiozzi et al. 2003]	87
5.38	Radioelement concentrations for different rock-types on Lipari and Vulcano Island [Chiozzi et al. 2001]	93
5.39	Flight lines of the Vulcano-Lipari survey in 2002	95
5.40	Flight lines of the Vulcano-Lipari survey in 2004	95
5.41	Average gamma-ray spectrum of Vulcano and Lipari Island	96
5.42	Concentrations detected at the Stromboli survey in 2004 (750 m grid): a) K [%], b) U [ppm], c) Th [ppm], d) dose [nGy/h]; Processing performed with the use of NASVD smoothed spectra	97
5.43	Concentrations detected at the Panarea survey in 2004 (250 m grid): a) K [%], b) U [ppm], c) Th [ppm], d) dose [nGy/h]; Processing performed with the use of NASVD smoothed spectra	98
5.44	Concentrations detected at the Salina survey in 2004 (500 m grid): a) K [%], b) U [ppm], c) Th [ppm], d) dose [nGy/h]; Processing performed with the use of NASVD smoothed spectra	99
5.45	Concentrations detected at the Lipari survey in 2002 (175 m grid): a) K [%], b) U [ppm], c) Th [ppm], d) dose [nGy/h]; Processing performed with the use of NASVD smoothed spectra	100

5.46	Concentrations detected at the Vulcano survey in 2002 (175 m grid): a) K [%], b) U [ppm], c) Th [ppm], d) dose [nGy/h]; Processing performed with the use of NASVD smoothed spectra	101
5.47	Ground concentrations detected at the Vulcano-Lipari survey in 2004 (125 m grid); Standard window based processing: K [%]	102
5.48	Ground concentrations detected at the Vulcano-Lipari survey in 2004 (125 m grid); Standard window based processing: U [ppm]	103
5.49	Ground concentrations detected at the Vulcano-Lipari survey in 2004 (125 m grid); Standard window based processing: Th [ppm]	104
5.50	Ground concentrations detected at the Vulcano-Lipari survey in 2004 (125 m grid); Processing performed with the use of NASVD smoothed spectra: K [%]	105
5.51	Ground concentrations detected at the Vulcano-Lipari survey in 2004 (125 m grid); Processing performed with the use of NASVD smoothed spectra: U [ppm]	106
5.52	Ground concentrations detected at the Vulcano-Lipari survey in 2004 (125 m grid); Processing performed with the use of NASVD smoothed spectra: Th [ppm]	107
5.53	Ternary radioelement maps of the Vulcano-Lipari survey in 2004: a) K-Th-U, b) K-Th, c) K-U, d) Th-U	108
5.54	Ternary radioelement diagram showing the geologic units of Vulcano Island	114
5.55	Radioelement distribution (average concentrations) for the the different units on Vulcano Island	115
5.56	Map of Vulcano Island showing units that have been delineated on the basis of the radiometric studies	116
5.57	Ternary radioelement diagram showing the geologic units of Lipari Island	122
5.58	Radioelement distribution (average concentrations) for the the different units on Lipari Island	122
5.59	Map of Lipari Island showing units that have been delineated on the basis of the radiometric studies	123
A.1	Radioelement concentrations of the Lomas Coloradas area	131
A.2	Radioelement concentrations of Socorro Island part 1	132
A.3	Radioelement concentrations of Socorro Island part 2	133
B.1	Radioelement concentrations of the Vulcano survey in 2002	135
B.2	Radioelement concentrations of the Vulcano survey in 2004	136
C.1	Radioelement concentrations of the Lipari survey in 2002	137
C.2	Radioelement concentrations of the Lipari survey in 2004	138

Appendix A

Geologic units and radioelement concentrations of Socorro Island

Feature	Geology	Unit		K	U	Th
Cinder Cone 1	Cinder Cones	LC Cinder Cones	Mean/Sigma Min/Max	1,32 ± 0,43 0,38 - 2,38	3,16 ± 1,06 1,54 - 6,01	6,56 ± 2,75 0,99 - 12,09
Cinder Cone 2	Cinder Cones	LC Cinder Cones	Mean/Sigma Min/Max	1,34 ± 0,36 0,52 - 2,13	1,97 ± 1,53 0,00 - 7,01	4,62 ± 2,44 0,00 - 8,93
Cinder Cone 3	Cinder Cones	LC Cinder Cones	Mean/Sigma Min/Max	1,08 ± 0,39 0,00 - 1,91	2,48 ± 1,17 0,00 - 6,19	4,19 ± 2,80 0,00 - 12,71
Cinder Cone 4	Cinder Cones	LC Cinder Cones	Mean/Sigma Min/Max	1,03 ± 0,36 0,27 - 1,94	2,70 ± 1,13 0,24 - 4,77	6,87 ± 3,02 1,03 - 13,32
Cinder Cone 5	Cinder Cones	LC Cinder Cones	Mean/Sigma Min/Max	1,25 ± 0,38 0,25 - 2,40	2,53 ± 1,47 0,00 - 6,62	6,46 ± 3,42 0,08 - 20,26
Cinder Cone 6	Cinder Cones	LC Cinder Cones	Mean/Sigma Min/Max	1,18 ± 0,40 0,27 - 2,24	2,61 ± 1,22 0,00 - 6,25	7,05 ± 3,41 0,00 - 16,75
Cinder Cone 7	Cinder Cones	LC Cinder Cones	Mean/Sigma Min/Max	1,11 ± 0,46 0,47 - 1,84	2,46 ± 0,92 0,62 - 3,74	4,02 ± 2,56 0,00 - 9,42
Cinder Cone 8	Cinder Cones	LC Cinder Cones	Mean/Sigma Min/Max	1,41 ± 0,56 0,52 - 2,48	2,75 ± 1,60 0,00 - 5,42	9,16 ± 3,13 4,29 - 14,45
Cinder Cone 9	Cinder Cones	LC Cinder Cones	Mean/Sigma Min/Max	1,11 ± 0,47 0,15 - 2,19	2,35 ± 1,40 0,00 - 6,73	6,59 ± 3,24 0,50 - 15,89
Cinder Cone 10	Cinder Cones	LC Cinder Cones	Mean/Sigma Min/Max	0,98 ± 0,45 0,15 - 2,19	3,03 ± 1,62 0,00 - 7,61	8,86 ± 4,10 0,50 - 25,53
Volcán Banuelos lava flows	basalt lava flows	Lomas Coloradas	Mean/Sigma Min/Max	1,44 ± 0,58 -0,78 - 3,23	3,02 ± 1,73 -0,30 - 9,51	10,28 ± 5,40 -0,25 - 29,45
Volcán Las Tetras lava flows	basalt lava flows	Lomas Coloradas	Mean/Sigma Min/Max	2,30 ± 0,72 0,29 - 6,09	3,15 ± 1,56 -0,16 - 9,89	10,36 ± 4,17 0,00 - 26,58
Lomas Coloradas 1	basalt lava flows	Lomas Coloradas	Mean/Sigma Min/Max	1,67 ± 0,67 0,13 - 3,30	2,85 ± 1,59 0,00 - 7,63	8,81 ± 4,21 0,00 - 19,38
Bahia Braithwaite flows	basalt lava flows	Lomas Coloradas	Mean/Sigma Min/Max	1,75 ± 0,50 0,45 - 4,08	3,83 ± 1,66 -0,16 - 9,90	14,30 ± 4,75 0,00 - 31,63

Figure A.1: Radioelement concentrations of the Lomas Coloradas area

Cycle	Feature	Geology	Unit		K [%]	U [ppm]	Th [ppm]	dose [nGy/h]
1	Punta Chacalote pyroclastics	precaldera peralkaline pyroclastics	Playa Blanca member	Mean/Sigma Min/Max	4,55 ± 0,90 1,87 - 6,48	3,84 ± 0,10 0,10 - 9,18	12,35 ± 4,27 -0,61 - 26,42	95,65 ± 7,71 63,10 - 117,60
1	Bahia Cornwallis pyroclastics	precaldera peralkaline pyroclastics	Playa Blanca member	Mean/Sigma Min/Max	4,62 ± 0,95 1,52 - 7,56	4,05 ± 1,99 -0,82 - 13,91	14,31 ± 5,05 -1,34 - 32,68	106,11 ± 18,63 66,80 - 192,10
1	Cabo Henslow pyroclastics	peralkaline pyroclastics	Playa Blanca member	Mean/Sigma Min/Max	4,36 ± 1,07 -1,25 - 7,71	4,47 ± 2,38 -2,71 - 21,00	14,71 ± 5,61 -5,63 - 43,11	115,92 ± 17,55 86,30 - 227,60
1	Cabo Pearce pyroclastics	oldest precaldera peralkaline	El Muerto member	Mean/Sigma Min/Max	3,87 ± 0,96 0,32 - 7,85	4,71 ± 2,30 -1,84 - 15,54	18,83 ± 7,03 -2,80 - 40,08	115,44 ± 21,66 57,70 - 222,20
1	Punta Tosca Pyroclastics	peralkaline pyroclastics	El Muerto member?	Mean/Sigma Min/Max	4,02 ± 1,16 0,52 - 6,99	5,49 ± 2,60 -4,22 - 15,09	19,87 ± 7,04 -0,57 - 53,39	122,43 ± 24,21 71,00 - 224,50
1	Palma Sola Coast	peralkaline pyroclastics	El Muerto member?	Mean/Sigma Min/Max	4,06 ± 0,71 2,32 - 5,93	5,49 ± 2,30 0,53 - 11,08	22,98 ± 7,59 2,77 - 41,68	115,92 ± 16,60 66,70 - 155,30
1	Precaldera eruptives	peralkaline trachytes and rhyolites	Precaldera Eruptives	Mean/Sigma Min/Max	2,52 ± 0,81 -0,52 - 6,09	6,19 ± 2,45 -3,54 - 19,35	26,28 ± 7,03 -3,23 - 64,50	112,45 ± 15,49 67,40 - 200,40
2	Bahia Universidad pyroclastics	peralkaline pyroclastics	Precaldera Eruptives?	Mean/Sigma Min/Max	3,21 ± 0,92 0,57 - 6,23	3,95 ± 1,65 -1,91 - 9,81	14,05 ± 4,89 1,84 - 34,51	90,46 ± 13,06 65,30 - 164,60
2	Caldera filling	peralkaline rhyolite flows	???	Mean/Sigma Min/Max	3,51 ± 0,98 0,64 - 6,81	7,84 ± 2,54 0,04 - 18,21	25,28 ± 6,99 8,31 - 58,01	127,41 ± 16,71 96,90 - 192,90
3	Playa Escondia Twinflow	peralkaline trachyte dome + flow	Felipe member	Mean/Sigma Min/Max	5,17 ± 1,11 1,69 - 8,23	4,23 ± 1,89 -1,25 - 14,45	10,21 ± 4,60 -3,93 - 28,74	106,20 ± 16,52 63,00 - 174,80
3	Punta Judith flow	peralkaline lava flow	Felipe member	Mean/Sigma Min/Max	4,92 ± 0,93 1,73 - 7,36	4,45 ± 2,07 -1,28 - 14,67	11,10 ± 5,12 -0,88 - 35,65	103,67 ± 12,18 56,70 - 154,50
3	Punta Tosca flow	peralkaline lava flow	Felipe member	Mean/Sigma Min/Max	4,19 ± 1,26 0,00 - 7,80	4,69 ± 2,75 -3,24 - 17,94	10,52 ± 7,13 -8,98 - 41,74	125,16 ± 25,67 60,90 - 214,00
3	Caldera filling	peralkaline lava flow	Felipe member???	Mean/Sigma Min/Max	4,38 ± 0,84 2,00 - 6,41	8,02 ± 2,55 2,48 - 15,71	21,69 ± 6,44 6,40 - 45,45	128,74 ± 11,35 95,10 - 161,90
3	Little Felipe	peralkaline lava flow	Felipe member???	Mean/Sigma Min/Max	4,37 ± 0,90 1,94 - 6,57	10,56 ± 2,37 3,94 - 15,23	28,21 ± 5,38 15,19 - 40,56	147,32 ± 8,22 132,50 - 178,20
3	Top of Twinflow	peralkaline lava flow	Felipe member???	Mean/Sigma Min/Max	3,92 ± 0,79 2,05 - 5,98	5,12 ± 2,13 0,78 - 13,45	13,55 ± 5,00 2,71 - 28,51	100,03 ± 10,98 78,20 - 146,40
3	Cabo Regia Dome + Cinder Cone	peralkaline trachyte dome + cinder cone	Lozano	Mean/Sigma Min/Max	4,16 ± 0,83 1,61 - 6,15	2,17 ± 1,43 -1,69 - 7,14	6,94 ± 3,67 -1,33 - 21,65	80,55 ± 8,20 55,90 - 109,20
3	Faro Dome	peralkaline trachyte dome	Lozano	Mean/Sigma Min/Max	4,13 ± 0,91 1,82 - 6,24	1,70 ± 1,50 -1,32 - 6,13	5,80 ± 3,61 -3,07 - 17,32	83,85 ± 7,96 61,80 - 107,10
3	Northern sector	peralkaline lava flows + pyroclastics	Palma Sola member	Mean/Sigma Min/Max	2,88 ± 0,90 -0,40 - 7,10	7,39 ± 2,75 -1,56 - 23,72	30,21 ± 8,40 -0,66 - 62,74	123,27 ± 16,66 56,20 - 227,10

Figure A.2: Radioelement concentrations of Socorro Island part 1

3	Palma Sola flow	lava flow	Palma Sola member	Mean/Sigma Min/Max	3,83 ± 0,86 1,50 - 6,75	7,08 ± 2,17 -1,65 - 14,16	33,02 ± 6,13 16,13 - 54,26	127,31 ± 9,91 100,60 - 167,00
3	High Dose Flow	lava flow	Palma Sola member	Mean/Sigma Min/Max	3,94 ± 1,24 -0,14 - 6,94	10,88 ± 3,19 0,48 - 19,88	37,25 ± 9,42 13,97 - 80,54	174,65 ± 32,53 137,50 - 300,20
3	???	???	Palma Sola member	Mean/Sigma Min/Max	3,09 ± 1,06 0,38 - 5,60	9,20 ± 3,63 0,87 - 20,28	34,13 ± 10,14 12,52 - 72,17	161,77 ± 39,28 113,60 - 250,90
3	Palma Sola pyroclastics	peralkaline pyroclastics	Palma Sola member	Mean/Sigma Min/Max	3,67 ± 0,94 0,92 - 6,85	8,46 ± 3,14 -0,04 - 23,74	35,66 ± 7,40 11,41 - 61,97	145,28 ± 16,97 109,70 - 217,20
3	Punta Tosca domes	peralkaline domes	Peralkaline Domes	Mean/Sigma Min/Max	4,92 ± 0,89 2,92 - 7,70	8,69 ± 2,94 1,97 - 16,93	32,35 ± 7,82 10,51 - 66,88	151,07 ± 16,49 114,40 - 209,00
3	Punta Tosca dome ring	peralkaline domes	Peralkaline Domes	Mean/Sigma Min/Max	4,36 ± 1,09 0,59 - 6,81	7,55 ± 3,04 -0,40 - 18,27	27,63 ± 8,34 9,73 - 55,11	151,99 ± 22,05 104,50 - 241,30
3	Bahia Guardado Domes	peralkaline domes	Peralkaline Domes	Mean/Sigma Min/Max	4,19 ± 0,69 2,18 - 5,91	5,98 ± 1,90 1,52 - 14,46	26,74 ± 5,40 14,09 - 42,10	118,08 ± 9,29 94,90 - 145,50
3	Bahia Guardado Dome	peralkaline domes	Peralkaline Domes	Mean/Sigma Min/Max	4,61 ± 0,80 2,75 - 6,48	5,42 ± 1,54 2,55 - 9,65	24,44 ± 4,20 15,60 - 38,77	115,57 ± 7,54 103,00 - 132,00
3	Cobo Middleton Dome	peralkaline domes	Peralkaline Domes	Mean/Sigma Min/Max	4,38 ± 0,89 2,47 - 6,08	4,69 ± 2,15 -0,64 - 8,12	23,44 ± 3,42 15,25 - 30,19	118,07 ± 10,64 104,10 - 137,10
3	Summit Dome	peralkaline dome	Peralkaline Domes	Mean/Sigma Min/Max	3,32 ± 0,75 1,93 - 5,80	7,41 ± 2,06 2,54 - 13,29	21,63 ± 7,17 10,94 - 51,75	111,51 ± 13,24 92,20 - 144,80
3	Northwestern sector	lava flows and pyroclastics	Volcán Evermann eruptives	Mean/Sigma Min/Max	3,19 ± 0,99 -1,18 - 6,34	6,72 ± 2,89 -3,22 - 24,96	24,80 ± 7,92 -5,99 - 74,60	131,67 ± 27,96 82,10 - 271,40
3	Valle Hermoso	lava flows	Volcán Evermann eruptives	Mean/Sigma Min/Max	3,86 ± 1,00 0,68 - 7,74	5,66 ± 2,48 -2,14 - 19,19	21,70 ± 6,59 -0,34 - 60,26	115,37 ± 15,79 69,00 - 201,40
3	Playa Escondia "Eye"	peralkaline pyroclastics	Volcán Evermann eruptives	Mean/Sigma Min/Max	4,90 ± 1,01 2,13 - 8,18	5,07 ± 2,40 -2,01 - 11,06	19,27 ± 5,35 6,08 - 37,87	121,41 ± 17,48 91,00 - 191,20
3	El Bosque 1	lava flows	El Bosque member	Mean/Sigma Min/Max	2,93 ± 0,78 0,78 - 4,73	5,05 ± 2,08 0,68 - 15,08	16,47 ± 5,77 5,99 - 42,45	100,33 ± 22,57 78,00 - 195,60
3	El Bosque 2	lava flows	El Bosque member	Mean/Sigma Min/Max	2,41 ± 0,60 0,71 - 4,38	6,44 ± 1,95 1,84 - 11,53	20,08 ± 5,52 7,94 - 38,53	102,23 ± 9,34 86,70 - 129,80
4	Espejo Dome	peralkaline trachyte dome	Lozano	Mean/Sigma Min/Max	4,75 ± 0,56 3,54 - 5,83	3,01 ± 1,32 0,21 - 5,14	9,07 ± 3,62 1,24 - 18,72	85,96 ± 7,84 70,60 - 102,90
4	Lomas Coloradas basalts	alkaline basalts	Lomas Coloradas	Mean/Sigma Min/Max	1,66 ± 0,68 -0,78 - 4,73	3,11 ± 1,69 -1,77 - 9,90	10,25 ± 5,25 -4,27 - 31,63	68,70 ± 11,05 27,90 - 122,50
4	Punta Chacalote lava flow	alkaline basalts	Lomas Coloradas	Mean/Sigma Min/Max	2,56 ± 0,73 1,03 - 5,18	3,24 ± 1,55 -0,55 - 7,38	10,04 ± 3,96 1,58 - 23,52	72,56 ± 9,96 44,60 - 97,10

Figure A.3: Radioelement concentrations of Socorro Island part 2

Appendix B

Geologic units and radioelement concentrations of Vulcano Island

Id	Feature	Geology	Unit		Dose	K	U	Th
0	La Fossa Cone	pyroclastic deposits	La Fossa di Vulcano	Mean/Sigma Min/max	125.18 ± 24.85 50.80 - 192.60	2.97 ± 1.57 -5.75 - 6.45	7.95 ± 6.13 -7.75 - 26.37	23.98 ± 11.06 -9.71 - 79.53
0	La Fossa Crater	lava flows + pyroclastics	La Fossa di Vulcano	Mean/Sigma Min/max	143.96 ± 29.38 48.50 - 222.40	3.37 ± 1.39 -2.26 - 6.39	10.61 ± 6.28 -11.28 - 28.94	29.71 ± 10.77 -3.38 - 53.21
1	Caruggi	pyroclastics of Fossa I	Products of La Fossa 2	Mean/Sigma Min/max	108.98 ± 21.95 76.20 - 153.80	2.96 ± 1.44 -0.61 - 5.85	5.79 ± 5.04 -4.69 - 18.25	18.71 ± 7.76 1.07 - 42.95
1	La Fossa Caldera	stratified tuffs or loose sands, Fossa I	Products of La Fossa 2	Mean/Sigma Min/max	110.86 ± 21.40 52.70 - 174.70	3.02 ± 1.41 -3.70 - 5.99	5.71 ± 5.22 -6.27 - 22.65	19.01 ± 9.21 -10.03 - 45.36
1	Piano Caldera 3	stratified tuffs or loose sands, Fossa I	Products of La Fossa 2	Mean/Sigma Min/max	113.30 ± 14.49 79.60 - 140.50	2.97 ± 0.83 0.87 - 4.56	6.86 ± 4.60 -5.71 - 16.73	23.57 ± 7.15 9.92 - 40.04
2	Lentia Complex	rhyolitic lava flows and domes	Lentia Complex	Mean/Sigma Min/max	112.06 ± 26.39 18.80 - 171.10	2.88 ± 1.28 -1.83 - 5.96	7.10 ± 4.87 -3.92 - 29.74	22.50 ± 9.55 -0.14 - 48.18
3	Piano Caldera 2	Fossa I, brown tuffs, trachybasalts	Products of Piano + Fossa Caldera 2	Mean/Sigma Min/max	97.54 ± 18.60 13.20 - 127.90	2.14 ± 1.68 -8.80 - 5.34	6.19 ± 5.41 -13.96 - 28.58	16.90 ± 8.89 -13.47 - 47.75
4	Porto di Levante	alluvial and beach deposits	Alluvial + beach deposits	Mean/Sigma Min/max	99.64 ± 26.50 25.00 - 154.30	2.04 ± 1.68 -4.74 - 7.20	5.89 ± 6.41 -16.08 - 21.48	18.21 ± 9.53 -5.74 - 44.18
5	Vulcanello platform	Leucite-tephritic lava flows	Vulcanello Tephrite	Mean/Sigma Min/max	122.71 ± 32.72 41.30 - 181.90	3.28 ± 1.19 0.04 - 5.92	8.44 ± 4.19 -1.07 - 19.38	23.64 ± 10.29 -1.31 - 47.55
5	Vulcanello pyroclastics	ash tuffs, trachytic lava, scoriae and tuff	Vulcanello pyroclastics	Mean/Sigma Min/max	98.10 ± 11.79 67.00 - 115.70	2.57 ± 0.84 0.12 - 4.36	7.30 ± 3.68 0.05 - 13.50	15.91 ± 6.31 -0.63 - 31.46
6	Piano Grotte dei Rossi	fine brown earthy tuffs	Products of La Fossa Caldera	Mean/Sigma Min/max	82.10 ± 15.04 52.20 - 121.60	1.91 ± 0.76 0.20 - 3.55	4.99 ± 4.00 -5.05 - 14.75	15.83 ± 8.08 -6.29 - 39.67
6	Piano d' Alighieri	hyaloclastitic lapilli tuffs + scoriae	Products of Fossa Caldera	Mean/Sigma Min/max	70.98 ± 14.49 34.60 - 117.50	1.81 ± 0.79 -0.15 - 3.85	3.71 ± 3.34 -5.69 - 10.85	11.08 ± 6.34 -1.87 - 29.28
6	Tufi di Luccia	fine brown earthy tuffs + welded scoriae	Products of Piano + Fossa Caldera 1	Mean/Sigma Min/max	75.34 ± 15.80 45.40 - 96.00	1.74 ± 0.82 0.39 - 3.43	4.79 ± 4.12 -1.84 - 14.22	12.91 ± 5.67 1.71 - 24.06
7	Monte Luccia	pyroclastics of Fossa I	Products of La Fossa 1	Mean/Sigma Min/max	78.72 ± 13.78 46.50 - 100.80	2.06 ± 0.80 0.08 - 3.72	4.76 ± 3.84 -4.14 - 14.81	12.16 ± 4.97 1.12 - 24.19
7	Capo Grillo	pyroclastics of Fossa I	Products of La Fossa 1	Mean/Sigma Min/max	85.88 ± 18.14 52.10 - 134.80	2.10 ± 0.97 -0.70 - 4.10	5.44 ± 3.93 -3.19 - 16.22	13.17 ± 7.04 0.86 - 29.52
7	Gelso pyroclastics	stratified tuffs or loose sands, Fossa I	Products of La Fossa 1	Mean/Sigma Min/max	84.58 ± 26.99 12.60 - 129.90	1.90 ± 1.31 -1.04 - 4.75	5.09 ± 4.71 -8.63 - 16.79	14.30 ± 8.84 -7.89 - 33.68
8	Spiaggia Lunga	pyroclastic flows of trachyandesite	Piano Caldera 2	Mean/Sigma Min/max	77.31 ± 16.29 38.30 - 118.90	2.14 ± 0.71 -0.90 - 3.79	3.81 ± 3.62 -5.47 - 17.97	13.11 ± 6.63 0.02 - 34.55
8	La Somatica	Trachybasalts, Cinder Cone	Piano Caldera 2	Mean/Sigma Min/max	80.80 ± 14.50 51.90 - 111.30	1.77 ± 0.64 0.26 - 3.15	5.09 ± 2.70 -1.14 - 15.40	15.71 ± 5.91 3.46 - 31.74
8	Quadrara	pyroclastic flows of trachyandesite	Piano Caldera 2	Mean/Sigma Min/max	73.95 ± 17.71 27.80 - 102.40	1.82 ± 1.10 -2.54 - 3.84	3.98 ± 4.84 -7.84 - 19.02	10.12 ± 7.05 -4.17 - 30.80
8	Primordiale S	trachyandesitic trachybasaltic lava	Vulcano Primordiale 2	Mean/Sigma Min/max	73.06 ± 16.76 24.00 - 113.80	1.70 ± 0.94 -2.14 - 4.15	4.10 ± 3.90 -5.52 - 14.81	12.58 ± 7.42 -8.71 - 42.61
9	Piano di Luccia	sandy tuffs and welded scoriae	Piano Caldera 1	Mean/Sigma Min/max	56.38 ± 15.39 26.80 - 96.00	1.23 ± 0.69 -0.23 - 2.55	3.08 ± 3.47 -2.46 - 11.36	9.54 ± 6.64 -3.77 - 29.64
9	Monte Molineddo	stratified lapilli-tuffs and scoriae	Piano Caldera 1	Mean/Sigma Min/max	65.08 ± 18.69 34.80 - 125.20	1.36 ± 0.86 -1.06 - 4.14	3.60 ± 4.01 -3.81 - 17.22	10.97 ± 6.53 -3.28 - 32.24
10	Primordiale SW	trachyandesitic trachybasaltic lava	Vulcano Primordiale 1	Mean/Sigma Min/max	56.04 ± 19.85 17.90 - 106.50	1.42 ± 1.20 -2.85 - 4.22	1.56 ± 4.34 -10.70 - 13.79	6.51 ± 8.09 -13.74 - 35.37
10	Primordiale SE	trachyandesitic trachybasaltic lava	Vulcano Primordiale 1	Mean/Sigma Min/max	54.18 ± 16.38 22.10 - 101.40	1.28 ± 0.86 -3.02 - 4.17	2.82 ± 3.69 -11.05 - 19.45	6.85 ± 6.22 -6.22 - 23.08

Figure B.1: Radioelement concentrations of the Vulcano survey in 2002

Id	Feature	Geology	Unit		dose	K	U	Th
0	La Fossa Crater	lava flows + pyroclastics	La Fossa di Vulcano	Mean/Sigma	230.75 ± 31.65	7.51 ± 1.59	19.21 ± 6.05	52.73 ± 8.59
				Min/Max	160.10 - 323.60	3.78 - 12.30	2.69 - 35.42	34.54 - 80.24
0	La Fossa Cone	pyroclastic deposits	La Fossa di Vulcano	Mean/Sigma	209.70 ± 37.68	7.37 ± 1.72	15.86 ± 6.26	46.25 ± 10.44
				Min/Max	-21.70 - 364.80	-0.60 - 16.02	-3.10 - 37.11	-8.58 - 81.88
1	Caruggi	pyroclastics of Fossa I	Products of La Fossa 2	Mean/Sigma	176.58 ± 36.68	6.43 ± 1.88	12.43 ± 6.64	37.61 ± 10.06
				Min/Max	96.00 - 263.10	0.48 - 12.06	-11.58 - 37.20	10.08 - 61.19
1	La Fossa Caldera	stratified tuffs or loose sands, Fossa I	Products of La Fossa 2	Mean/Sigma	185.96 ± 30.92	6.77 ± 1.53	13.59 ± 6.17	39.68 ± 8.60
				Min/Max	85.40 - 251.70	1.35 - 11.50	-6.91 - 31.84	14.05 - 60.92
1	Piano Caldera 3	stratified tuffs or loose sands, Fossa I	Products of La Fossa 2	Mean/Sigma	179.77 ± 23.27	6.50 ± 1.35	13.05 ± 4.81	38.88 ± 6.05
				Min/Max	112.70 - 219.80	3.11 - 10.21	2.60 - 23.72	20.87 - 51.57
2	Lentia Complex	rhyolitic lava flows and domes	Lentia Complex	Mean/Sigma	170.21 ± 37.12	5.86 ± 1.59	13.32 ± 6.26	36.92 ± 9.62
				Min/Max	26.90 - 256.70	0.59 - 10.32	-2.71 - 33.39	1.17 - 63.13
3	Piano Caldera 2	Fossa I, brown tuffs, trachybasalts	Products of Piano + Fossa Caldera 2	Mean/Sigma	159.81 ± 22.43	5.79 ± 1.24	11.07 ± 5.02	34.60 ± 6.29
				Min/Max	108.60 - 218.50	2.57 - 8.66	-2.71 - 28.41	19.20 - 53.52
4	Porto di Levante	alluvial and beach deposits	Alluvial + beach deposits	Mean/Sigma	167.95 ± 33.93	5.94 ± 1.77	12.56 ± 6.15	35.85 ± 9.59
				Min/Max	79.10 - 250.40	0.82 - 10.19	-3.81 - 34.09	10.83 - 60.12
5	Vulcanello platform	Leucite-tephritic lava flows	Vulcanello Tephrite	Mean/Sigma	160.72 ± 29.53	5.75 ± 1.40	11.93 ± 4.82	34.94 ± 7.85
				Min/Max	68.60 - 220.00	1.88 - 9.49	-2.82 - 24.38	13.14 - 53.11
5	Vulcanello pyroclastics	ash tuffs, trachytic lava, scoriae and tuff	Vulcanello pyroclastics	Mean/Sigma	147.85 ± 24.26	5.33 ± 1.24	10.90 ± 4.71	31.11 ± 6.83
				Min/Max	94.00 - 197.60	3.19 - 8.30	0.81 - 24.47	15.74 - 50.97
6	Piano d' Alighieri	hyaloclastic lapilli tuffs + scoriae	Products of La Fossa Caldera	Mean/Sigma	120.14 ± 29.42	4.40 ± 1.33	7.67 ± 4.73	25.42 ± 7.60
				Min/Max	-22.70 - 226.20	-0.62 - 11.42	-3.23 - 22.85	-8.93 - 47.15
6	Tufi di Luccia	fine brown earthy tuffs + welded scoriae	Products of Piano + Fossa Caldera 1	Mean/Sigma	122.24 ± 16.94	4.57 ± 0.91	7.47 ± 3.84	27.22 ± 4.52
				Min/Max	72.40 - 152.40	2.61 - 6.17	-2.64 - 14.06	13.42 - 35.47
6	Piano Grotte dei Rossi	fine brown earthy tuffs	Products of La Fossa Caldera	Mean/Sigma	130.77 ± 16.46	4.76 ± 1.00	8.66 ± 3.89	27.82 ± 4.44
				Min/Max	88.50 - 180.50	2.18 - 7.37	-0.94 - 19.22	16.87 - 42.77
7	Gelso pyroclastics	stratified tuffs or loose sands, Fossa I	Products of La Fossa 1	Mean/Sigma	130.96 ± 29.73	5.03 ± 1.58	8.35 ± 5.91	26.30 ± 8.60
				Min/Max	22.10 - 192.60	-2.40 - 8.99	-13.30 - 36.17	-2.89 - 45.98
7	Monte Luccia	pyroclastics of Fossa I	Products of La Fossa 1	Mean/Sigma	125.02 ± 22.47	3.95 ± 1.36	10.05 ± 5.33	26.91 ± 8.15
				Min/Max	43.00 - 161.00	-1.26 - 6.33	-2.05 - 25.78	8.11 - 43.40
7	Capo Grillo	pyroclastics of Fossa I	Products of La Fossa 1	Mean/Sigma	126.07 ± 27.78	4.34 ± 1.49	8.76 ± 5.90	26.23 ± 7.43
				Min/Max	19.40 - 180.50	-1.23 - 9.59	-10.53 - 21.89	-1.94 - 42.26
8	Spiaggia Lunga	pyroclastic flows of trachyandesite	Piano Caldera 2	Mean/Sigma	113.13 ± 25.93	4.41 ± 1.18	6.71 ± 4.84	23.02 ± 6.56
				Min/Max	60.40 - 179.80	1.73 - 7.52	-7.09 - 28.70	10.18 - 46.61
8	La Sommata	Trachybasalts, Cinder Cone	Piano Caldera 2	Mean/Sigma	120.15 ± 20.15	4.48 ± 0.95	7.43 ± 4.03	25.12 ± 5.52
				Min/Max	82.00 - 179.30	2.37 - 7.32	-1.15 - 17.42	13.34 - 37.53
8	Quadrara	pyroclastic flows of trachyandesite	Piano Caldera 2	Mean/Sigma	125.75 ± 19.51	4.93 ± 1.11	7.21 ± 4.75	25.54 ± 5.88
				Min/Max	64.10 - 172.20	0.53 - 7.79	-4.46 - 27.24	11.61 - 42.59
8	Primordiale S	trachyandesitic trachybasaltic lava flows	Vulcano Primordiale 2	Mean/Sigma	110.57 ± 23.10	4.27 ± 1.34	6.41 ± 4.52	22.32 ± 6.56
				Min/Max	-22.40 - 177.00	-2.48 - 8.53	-6.38 - 31.02	-8.82 - 45.62
9	Piano di Luccia	sandy tuffs and welded scoriae	Piano Caldera 1	Mean/Sigma	84.59 ± 17.51	3.18 ± 0.94	4.54 ± 3.63	16.96 ± 5.33
				Min/Max	43.00 - 130.90	0.54 - 5.90	-3.54 - 13.20	3.99 - 33.86
9	Monte Molineddo	stratified lapilli-tuffs and scoriae	Piano Caldera 1	Mean/Sigma	94.07 ± 22.53	3.45 ± 1.11	5.48 ± 3.89	19.00 ± 5.75
				Min/Max	-31.60 - 159.50	-0.90 - 6.93	-4.41 - 16.49	-12.18 - 36.12
10	Primordiale SW	trachyandesitic trachybasaltic lava flows	Vulcano Primordiale 1	Mean/Sigma	85.77 ± 18.44	3.76 ± 1.11	3.62 ± 4.41	15.17 ± 5.18
				Min/Max	34.60 - 137.50	0.94 - 6.70	-8.56 - 17.87	2.09 - 35.99
10	Primordiale SE	trachyandesitic trachybasaltic lava flows	Vulcano Primordiale 1	Mean/Sigma	75.08 ± 20.61	2.92 ± 1.11	3.58 ± 3.91	13.96 ± 6.02
				Min/Max	-25.40 - 160.50	-1.66 - 7.80	-8.02 - 17.52	-9.93 - 33.92

Figure B.2: Radioelement concentrations of the Vulcano survey in 2004

Appendix C

Geologic units and radioelement concentrations of Lipari Island

Id	Feature	Geology	Unit		dose	K	U	Th
1	Monte Guardia	pyroclastics and domes	Valle Muria 2	Mean/Sigma	115.78 ± 20.61	3.02 ± 1.14	7.65 ± 4.81	21.23 ± 8.55
				Min/Max	60.10 - 180.40	-0.60 - 6.69	-6.90 - 25.17	-2.57 - 55.27
1	Vallone del Gabelotto	pumiceous pyroclastics	Vallone Fiume Bianco 3	Mean/Sigma	115.06 ± 18.38	2.89 ± 0.91	8.42 ± 4.18	22.48 ± 6.51
				Min/Max	65.10 - 154.10	1.09 - 4.94	-0.87 - 22.21	2.79 - 37.92
2	Pianoconte	lapilli tuff layer, scoria + pumice	Valle Muria 1	Mean/Sigma	104.05 ± 13.53	2.67 ± 0.80	7.39 ± 4.13	18.38 ± 6.52
				Min/Max	71.00 - 134.40	0.03 - 5.20	-2.17 - 21.28	0.15 - 42.24
2	Santa Margherita	ash tuffs	Valle Muria 1	Mean/Sigma	103.75 ± 11.72	2.74 ± 0.74	6.72 ± 3.67	20.53 ± 5.64
				Min/Max	75.50 - 126.10	1.48 - 4.11	-1.15 - 14.84	10.71 - 33.33
4	Mt. St. Angelo	pyroclastics	Cala Fico 2	Mean/Sigma	81.52 ± 18.25	1.94 ± 0.86	5.59 ± 3.98	14.23 ± 7.06
				Min/Max	30.80 - 120.70	-0.53 - 4.23	-4.48 - 16.91	-1.24 - 45.42
5	Fontanelle	lava flows, HKCA andesites to dacites	Cala Fico 1	Mean/Sigma	64.84 ± 15.01	1.54 ± 0.84	3.53 ± 3.96	10.60 ± 6.10
				Min/Max	27.70 - 107.30	-1.52 - 3.47	-3.28 - 19.78	-3.60 - 27.41
6	Timpone Carubbo	CA basaltic andesites	Paleolipari 3	Mean/Sigma	54.91 ± 23.03	1.17 ± 1.02	2.97 ± 4.13	7.72 ± 7.19
				Min/Max	13.50 - 127.40	-1.41 - 4.08	-4.62 - 19.70	-6.43 - 26.77
7	Fossa di Fuardo	massive blocky lavas	Paleolipari 2	Mean/Sigma	46.03 ± 17.22	0.86 ± 0.80	2.12 ± 3.63	5.91 ± 6.66
				Min/Max	14.90 - 89.90	-1.63 - 2.65	-4.35 - 14.21	-8.49 - 27.65
8	Mt. Mazzacaruso + Timpone Ospedale	pyroclastic breccia	Paleolipari 1	Mean/Sigma	38.35 ± 16.21	0.51 ± 0.95	1.37 ± 3.69	3.68 ± 6.15
				Min/Max	1.90 - 75.10	-3.44 - 2.73	-10.84 - 19.04	-15.69 - 22.83

Figure C.1: Radioelement concentrations of the Lipari survey in 2002

Id	Cycle	Feature	Geology	Unit		dose	K	U	Th
1	3	Monte Guardia	pyroclastics and domes	Valle Muria 2	Mean/Sigma	183.18 ± 31.69	6.33 ± 1.55	14.22 ± 5.88	40.01 ± 8.50
					Min/Max	91.40 - 285.30	1.41 - 12.45	-2.68 - 36.85	16.17 - 70.68
1	3	Vallone del Gabellotto	pumiceous pyroclastics	Vallone Fiume Bianco 3	Mean/Sigma	178.14 ± 32.45	5.95 ± 1.35	13.95 ± 5.71	39.56 ± 8.85
					Min/Max	86.10 - 233.20	2.37 - 9.38	-0.84 - 26.91	15.57 - 57.11
2	3	Pianoconte	lapilli tuff layer, scoria + pumice	Valle Muria 1	Mean/Sigma	160.47 ± 19.38	5.61 ± 1.09	11.76 ± 4.91	34.89 ± 5.65
					Min/Max	90.00 - 192.70	2.34 - 7.94	-2.98 - 24.42	18.32 - 53.52
2	3	Costa d Agosto	pumiceous succession, lapilli	Vallone Fiume Bianco 2	Mean/Sigma	167.03 ± 25.43	5.43 ± 1.49	13.73 ± 6.35	35.60 ± 7.13
					Min/Max	109.30 - 198.80	1.64 - 7.83	2.68 - 23.58	20.50 - 49.34
2	3	Santa Margherita	ash tuffs	Valle Muria 1	Mean/Sigma	153.10 ± 21.08	5.60 ± 1.03	10.27 ± 4.91	33.21 ± 5.66
					Min/Max	98.60 - 188.20	2.82 - 8.47	-1.50 - 23.30	21.79 - 44.81
3	3	Mt. Pilato	rhyolite obsidian dome + flow	Vallone Fiume Bianco 1	Mean/Sigma	140.95 ± 13.18	4.22 ± 0.96	11.46 ± 4.14	31.29 ± 3.95
					Min/Max	116.40 - 160.30	2.89 - 6.21	6.33 - 18.02	23.19 - 36.39
4	2	Mt. St. Angelo	pyroclastics	Cala Fico 2	Mean/Sigma	121.40 ± 24.07	4.35 ± 1.15	8.14 ± 4.52	25.64 ± 6.60
					Min/Max	45.10 - 197.60	1.01 - 7.47	-2.73 - 20.41	6.36 - 47.95
5	1	Timpone Croci	highly fumarolized and brecciated lavas	Piano Grande	Mean/Sigma	110.75 ± 11.89	4.42 ± 1.54	6.46 ± 5.20	20.58 ± 3.32
					Min/Max	93.50 - 134.20	2.35 - 8.08	-2.73 - 13.04	15.37 - 25.12
5	2	Fontanelle	lava flows, HKCA andesites to dacites	Cala Fico 1	Mean/Sigma	99.09 ± 20.42	3.76 ± 1.04	6.01 ± 4.11	19.77 ± 5.63
					Min/Max	33.20 - 146.00	-0.07 - 6.52	-3.42 - 19.44	-0.15 - 36.15
6	1	Timpone Carubbo	CA basaltic andesites	Paleolipari 3	Mean/Sigma	75.89 ± 32.52	2.93 ± 1.31	3.95 ± 4.80	14.07 ± 8.52
					Min/Max	23.90 - 192.00	-0.22 - 8.90	-4.89 - 26.47	-3.12 - 48.59
7	1	Mt. Rosa	CA basaltic andesite lava flows	Paleolipari 2	Mean/Sigma	77.17 ± 20.55	1.96 ± 1.19	5.97 ± 4.30	9.00 ± 6.47
					Min/Max	36.10 - 130.30	-1.32 - 4.80	-3.04 - 14.99	-4.58 - 33.67
7	1	Fossa di Fuardo	massive blocky lavas	Paleolipari 2	Mean/Sigma	60.95 ± 18.80	2.31 ± 0.95	3.15 ± 3.67	10.63 ± 5.01
					Min/Max	14.00 - 104.60	-0.06 - 5.12	-6.62 - 11.54	-1.24 - 26.97
8	1	Mt. Mazzacaruso + Timpone Ospedale	pyroclastic breccia	Paleolipari 1	Mean/Sigma	48.06 ± 16.52	1.85 ± 1.02	1.65 ± 3.64	6.85 ± 5.18
					Min/Max	-12.40 - 109.80	-3.06 - 5.40	-10.60 - 16.62	-15.28 - 23.55
8	1	Bonanno	HKCA andesites	Paleolipari 1	Mean/Sigma	56.49 ± 26.23	2.15 ± 1.47	2.01 ± 6.18	7.87 ± 7.41
					Min/Max	0.70 - 123.70	-2.81 - 6.44	-15.77 - 22.16	-10.53 - 30.20

Figure C.2: Radioelement concentrations of the Lipari survey in 2004

Bibliography

Arrighi S., Tangui J.-C., Rosi M.: Eruptions of the last 2200 years at Vulcano and Vulcanello (Aeolian Islands, Italy) dated by high-accuracy archeomagnetism.- *Physics of the Earth and Planetary Interiors*, vol. 159, pages 225-233, Italy, 2006.

Aydin I., Aydogan M.S., Oksum E., Kocak A.: An attempt to use aerial gamma-ray spectrometry results in petrochemical assessments of the volcanic and plutonic associations of Central Anatolia (Turkey).- *Geophysical Journal International*, Vol. 167, Issue 2, pages 1044-1052, 2006

Billings S.D.: Geophysical aspects of soil mapping using airborne gamma-ray spectrometry. - Dr. phil Thesis, Univ. of Sydney, Australia, 1998.

Bohrson W.A., Reid M.R., Grunder A.L., Heizler M.T., Harrison T.M., Lee J.: Prolonged history of silicic peralkaline volcanism in the eastern Pacific Ocean.- *Journal of Geophysical Research*, Vol. 101, No. B5, pages 11457-11474, USA, 1996.

Bohrson W.A., Reid M.R.: Genesis of Evolved Ocean Island Magmas by Deep- and Shallow-Level Basement Recycling, Socorro Island, Mexico: Constraints from Th and other Isotope Signatures.- *Journal of Petrology*, Vol. 39, No. 5, Pages 995-1008, USA, 1998.

Bohrson W.A., Reid M.R.: Genesis of Silicic Peralkaline Volcanic Rocks in an Ocean Island Setting by Crustal Melting and Open-system Processes: Socorro Island, Mexico.- *Journal of Petrology*, Vol. 38, No. 9, Pages 1137 - 1166, USA, 1997.

Bruno P. P. G., Paoletti V., Grimaldi M., Rapolla A.: Geophysical exploration for geothermal low enthalpy resources in Lipari Island, Italy.- *Journal of Volcanology and Geothermal Research*, vol. 98, pages 173 - 188, Italy, 2000.

Burnham J.: Radiation Protection - CreateSpace, 2011.

Carballido-Sánchez E.A.: The Geology and Petrology of Socorro Island, Revillagigedo Archipelago, Mexico.- Dr. Phil. Thesis, Tulane University, USA, 1994.

Chiozzi P., De Felice P., Pasquale V., Russo D., Verdoya M.: Field gamma-ray spectrometry on the Vulcano island (Aeolian Arc, Italy).- *Applied Radiation and Isotopes*, Vol. 51, pages 247-253, Italy, 1999.

- Chiozzi P., Pasquale V., Verdoya M., Minato S.: Gamma-ray activity in the volcanic islands of the Southern Tyrrhenian Sea.- *Journal of Environmental Radioactivity*, Vol. 67, pages 235-246, Italy, 2003.
- Chiozzi P., Pasquale V., Verdoya M., Minato S.: Natural gamma-radiation in the Aeolian volcanic arc.- *Applied Radiation and Isotopes*, Vol. 55, pages 737-744, Italy, 2001.
- Chiozzi P., Pasquale V., Verdoya M.: Ground radiometric survey of U, Th and K on the Lipari Island, Italy.- *Journal of Applied Geophysics*, vol. 38, pages 209-217, Italy, 1998.
- De Astis G., Dellino P.: Project V3 Research on active volcanoes, precursors, scenarios, hazard and risk, Sub-Project V3_5 - Vulcano.- *Istituto Nazionale di Geofisica e Vulcanologia*, pages 84-95, Italy, 2006.
- De Astis G., La Volpe L., Peccerillo A., Civetta L.: Volcanological and petrological evolution of Vulcano island (Aeolian Arc, southern Tyrrhenian Sea).- *Journal of Geophysical Research*, Vol. 102, No. B4, pages 8021-8050, Italy, 1997.
- Dellino P., La Volpe L.: Fragmentation versus transportation mechanisms in the pyroclastic sequence of Monte Pilato - Rocche Rosse (Lipari, Italy).- *Journal of Volcanology and Geothermal Research*, vol. 64, pages 211-231, Italy, 1994.
- Demtröder W.: *Experimentalphysik 4 - Kern-, Teilchen- und Astrophysik.* - Springer Lehrbuch, Germany, 2009.
- Dickson B.L., Scott K.M.: Interpretation of aerial gamma-ray surveys - adding the geochemical factors. - *AGSO Journal of Australian Geology & Geophysics*, vol. 17, no 2, pages 187-200, Australia, 1997.
- Gehring I.: Volcanostratigraphy using geophysical methods on La Fossa di Vulcano (S-Italy).- Thesis, Julius-Maximilians-Universität Würzburg, Germany, 2001.
- Gehring I.: The use of grain-size dependent magnetic susceptibility and gamma-ray measurements for the detailed reconstruction of volcanostratigraphy: The case of La Fossa di Vulcano, S. Italy.- *Journal of Volcanology and Geothermal Research*, vol. 138, pages 163-183, Germany, 2004.
- Ghosh D., Deb A., Bera S., Sengupta R., Patra K.K.: Measurement of natural radioactivity in chemical fertilizer and agricultural soil: evidence of high alpha activity. - *Environmental Geochemical Health*, vol. 30, pages 79-86, India, 2008.
- Graham D.J., Midgley N.G.: Graphical representation of particle shape using triangular diagrams: an Excel spreadsheet method. - *Earth Surface Processes and Landforms*, vol. 25, issue 13, pages 1473-1477, 2000.
- Grasty R. L., Kosanke K. L., Foote R. S.: Fields of view of airborne gamma-ray detectors.- *Society of Exploration Geophysicists*, vol. 44, no. 8, pages 1447-1457, Canada, 1979.

Harb S., El-Kamel A. H., Abd El-Mageed A. I., Abbady A., and Negm H. H.: Natural Radioactivity Measurements in Soil and Phosphate Samples from El-Sabaea, Aswan, Egypt. - IX Radiation Physics & Protection Conference, Nasr City - Cairo, Egypt, 15-19 November 2008.

IAEA TECDOC 1363: Guidelines for radioelement mapping using gamma ray spectrometry data.- International Atomic Energy Agency (IAEA), Nuclear Fuel Cycle and Materials Section, Austria, 2003.

Keller J.: Geologic Map of the Island of Vulcano (Aeolian Islands).- Istituto Internazionale di Vulcanologia, Italy, 1970.

Kemski J., Klingel R., Siehl A.: Die terrestrische Strahlung durch natürliche radioaktive Elemente in Gesteinen und Böden.- extraction from „Umweltradioaktivität“ (A. Siehl), Ernst & Sohn, pages 69-96, Germany, 1996.

Minty B. R. S.: Fundamentals of airborne gamma-ray spectrometry. - AGSO Journal of Australian Geology and Geophysics, Vol. 17, no. 2, pages 39-50, Australia, 1997.

Minty B. R. S., Luyendyk A. P. J., Brodie R. C: Calibration and data processing for airborne gamma-ray spectrometry. - AGSO Journal of Australian Geology and Geophysics, Vol. 17, no. 2, pages 51-62, Australia, 1997.

Motschka K.: Aerogeophysics in Austria.- Bulletin of the Geological Survey of Japan, vol. 52 (2/3), pages 83-88, Austria, 2001.

Pichler H., Pichler T.: Vulkangebiete der Erde.- Elsevier, Germany, 2007.

Pico Envirotec Inc.: PRAGA 3, Version 1.3. - Software for processing gamma-ray spectrometry data, User Manual, Canada, 2005.

Revil A., Finizola A., Piscitelli S., Rizzo E., Ricci T., Crespy A., Angeletti B., Balasco M., Barde Cabusson S., Bennati L., Bolève A., Byrdina S., Carzaniga N., Di Gangi F., et al.: Inner structure of La Fossa di Vulcano (Vulcano Island, southern Tyrrhenian Sea, Italy) revealed by high-resolution electric resistivity tomography coupled with self-potential, temperature, and CO₂ diffuse degassing measurements.- Journal of Geophysical Research, vol. 113, B07207, Italy, 2008.

Riedel E.: Allgemeine und Anorganische Chemie, 8. Auflage, de Gruyter, Germany, 2004.

Santacroce R., Cristofolini R., La Volpe L., Orsi G., Rosi M.: Italian active volcanoes.- Episodes, Vol. 26, no. 3, pages 227-234, Italy, 2003.

Schmincke H.-U.: Volcanism.- Springer-Verlag, Germany, 2004.

Siebe C., Komorowski J.-C., Navarro C., McHone J., Delgado H., Cortés A.: Submarine eruption near Socorro Island, Mexico: Geochemistry and scanning electron microscopy studies of floating scoria and reticulite.- Journal of Volcanology and Geothermal Research, Vol. 68, pages 239-271, Mexico, 1995.

- Supper R., Motschka K., Seiberl W., Fedi M.: Geophysical investigations in Southern Italian active volcanic regions.- Bulletin of the Geological Survey of Japan, vol. 52 (2/3), pages 89-99, 2001
- Supper R., De Ritis R., Motschka K., Chiappini M.: Aeromagnetic anomaly images of Vulcano and Southern Lipari Islands (Aeolian Archipelago, Italy).- Annals of Geophysics, vol. 47, Nr. 6, pages 1803-1810, Austria, 2004
- Supper R., Ottowitz D., Motschka K., Ahl A.: A combined airborne and ground geophysical survey to investigate the subsurface structure and hydrology of Socorro Island, Mexico.- Geological Survey of Austria, Final Report, Austria, 2010.
- Taran Y.A., Fischer T.P., Cienfuegos E., Morales P.: Geochemistry of hydrothermal fluids from an intraplate ocean island: Everman volcano, Socorro Island, Mexico.- Chemical Geology, Vol. 88, pages 51-63, Mexico, 2002
- Taran Y.A., Varley N.R., Inguaggiato S., Cienfuegos E.: Geochemistry of H_2 - and CH_4 -enriched hydrothermal fluids of Socorro Island, Revillagigedo Archipelago, Mexico. Evidence for serpentinization and abiogenic methane.- Geofluids, Blackwell Publishing Ltd, Mexico, 2010.
- Telford W. M., Geldart L. P., Sheriff R. E.: Applied Geophysics. Chapter 10 - Radioactivity Method, pages 611-644, Canada, 1990.
- Tranne C.A., Lucchi F., Calanchi N., Lanzafame G., Rossi P.L.: Geological Map of the Island of Lipari (Aeolian Islands).- University of Bologna and INGV, Italy, 2002.
- Valenzuela Raúl W., Galindo M., Pacheco J.F., Iglesias A., Terán L.F., Barreda J.L, Coba C.: Seismic survey in southeastern Socorro Island: Background noise measurements, seismic events, and T phases.- Geofísica Internacional, vol. 44, no. 1, pages 23-38, Mexico, 2005.
- Ventura G., Vilardo G., Milano G., Pino N. A.: Relationships among crustal structure, volcanism and strike-slip tectonics in the Lipari-Vulcano Volcanic Complex (Aeolian Islands, Southern Tyrrhenian Sea, Italy).- Physics of the Earth and Planetary Interiors, vol. 116, pages 31 - 52, Italy, 1999.

Curriculum Vitae

Name: Stefanie Kauer
Anschrift: Alser Straße 16/7
1090 Wien
Telefon: 0650/9880402
E-Mail: stefanie.kauer@gmx.at

Geburtsdaten: 04.02.1988, Linz
Staatsbürgerschaft: Österreich
Familienstand: ledig

Ausbildung

1994 – 1998 Volksschule Puchenau
1998 – 2006 Georg von Peuerbach Gymnasium, Linz
Juni 2006 AHS-Matura mit ausgezeichnetem Erfolg
10.2006 – 07.2007 Studium Meteorologie und Geophysik, Universität Wien
Juli 2007 Abschluss des ersten Studienabschnitts mit der 1. Diplomprüfung
Seit 07.2007 Zweiter Studienabschnitt: Diplomstudium Geophysik, Universität Wien

Bisherige Berufserfahrung im Bereich der Geophysik

2008 Ferialanstellung bei der Rohöl-Aufsuchungs AG im Bereich Seismik
2008 – 2009 Diverse Erschütterungsmessungen für Steinhauser Erschütterungsschutz
2009 – 2011 Ferialanstellung an der Geologischen Bundesanstalt;
Aufgabenbereich: diverse Feldmessungen, Mitarbeit am Aufbau von
Monitoringsystemen (Gschliefgraben, Mölltaler Gletscher), Datenbankarbeit,
Literaturstudie, Prozessing von Radiometrie-Daten, ...
seit 10. 2011 Anstellung an der Geologischen Bundesanstalt, Fachabteilung Geophysik

Fremdsprachen: Englisch, Französisch
EDV-Kenntnisse: Bedienung der Betriebssysteme Microsoft Windows, Linux;
gute Office-Kenntnisse; grundlegende Kenntnisse im Programmieren
mit Fortran 77 und C; Anwenderkenntnisse in ArcGIS, Golden
Software Surfer und Grapher, Praga (radiometric processing software);
Sonstiges: Führerschein B, Sprengbefugnis